UNIVERSITY OF SOUTHAMPTON

FACULTY OF ENGINEERING AND PHYSICAL SCIENCES

School of Electronics and Computer Science

Metal-assisted chemically etched black silicon: morphology and light interaction

by

Tudor Emilian Scheul

Orcid ID: 0000-0003-4517-6096

Supervised by:

Dr. Stuart Boden

Dr. Tasmiat Rahman

Prof. Martin D. B. Charlton

A thesis submitted in partial fulfilment for the degree of Doctor of Philosophy

September 2020

UNIVERSITY OF SOUTHAMPTON

ABSTRACT

FACULTY OF ENGINEERING AND PHYSICAL SCIENCES

School of Electronics and Computer Science

Doctor of Philosophy

METAL-ASSISTED CHEMICALLY ETCHED BLACK SILICON: MORPHOLOGY AND LIGHT INTERACTION

by Tudor Emilian Scheul

An important part of the operation of a silicon solar cell is the ability to capture large amounts of incident light, which is subsequently absorbed in the substrate. Therefore, maximisation of light coupling into the semiconductor is desired for highly efficient devices. The existing texturing processes in the PV industry can be further enhanced by fabrication of nanostructures on the surface of the semiconductor. As such, black silicon (b-Si) becomes an excellent antireflective and light-trapping scheme, which has the potential to optically outperform commercial textured surfaces. Over the last decades, several fabrication methods have been proposed, out of which metal-assisted chemical etching (MACE) has become the most promising for industrial integration, due to its inherently low cost, ease of processing, reproducibility and scalability. This thesis presents an investigation into black silicon fabricated by MACE processes, including the effect of etching parameters, as well as morphological and opto-electronic characterisation of the resulting nanostructures. The black silicon surfaces are shown to consistently outperform their micron-scale pyramids counterparts, both in reduced broadband surface reflectance of 1-2% and in scattering of incident photons towards larger polar angles. These properties of black silicon effectively address challenges related to silicon's large surface reflectance and poor absorption coefficients, particularly for low-energy photons. A trade-off between the optical and electrical performance of the black silicon layers is identified and surface passivation of minority carriers is investigated by means of atomic layer deposition of aluminium oxide. To this end, sufficiently low surface recombination velocities below 30 cm/s are obtained for a range of nanostructure heights, which suggests that black silicon is a suitable and competitive candidate for high-efficiency device integration, especially on back-contacted solar cell architectures.

Publications

Journal research articles

1. **Tudor E. Scheul**, Edris Khorani, Tasmiat Rahman, Martin D.B. Charlton, Stuart A. Boden, *"Wavelength and angle resolved reflectance measurements of pyramidal textures for crystalline silicon photovoltaics",* Progress in Photovoltaics: Research and Applications, 2020; 1-10. https://doi.org/10.1002/pip.3319

2. **Tudor E. Scheul**, Edris Khorani, Tasmiat Rahman, Martin D.B. Charlton, Stuart A. Boden, *"Wavelength and angle resolved reflectance measurements of metal-assisted chemically etched black silicon nanostructures",* Solar Energy Materials and Solar Cells, 2021 (under review)

3. Edris Khorani, **Tudor E. Scheul**, Antulio Tarazona, John Nutter, Tasmiat Rahman, Stuart A. Boden, *"p+ polycrystalline silicon growth via hot wire chemical vapour deposition for silicon solar cells",* Thin Solid Films, volume 705, 2020, https://doi.org/10.1016/j/tsf/2020/137978

4. Edris Khorani, Shona McNab**, Tudor E. Scheul**, Tasmiat Rahman, Ruy Sebastian Bonilla, Stuart A. Boden and Peter R. Wilshaw, *"Optoelectronic properties of ultrathin ALD silicon nitride and its potential as a hole-selective nanolayer for high efficiency solar cells",* APL Materials, 8 (11), 111106. (doi:10.1063/5.0023336).

Conference papers

1. **Tudor E. Scheul,** Edris Khorani, Tasmiat Rahman, Stuart A. Boden, *"Characterization of Atomic Layer Deposited Alumina Thin Films on Black Silicon Textures Using Helium Ion Microscopy",* AIP Conference Proceedings 2147, Silicon PV , Leuven, Belgium, April 2019, https://doi.org/10.1063/1.5123858

2. **Tudor E. Scheul**, Edris Khorani, Tasmiat Rahman and Stuart A. Boden, *"Metal-assisted chemically etched black silicon for crystalline silicon solar cells",* Proceedings of the 14th Photovoltaic Science Application and Technology Conference (PVSAT-14), London, April 2018

3. Edris Khorani, **Tudor E. Scheul,** Tasmiat Rahman and Stuart A. Boden, *"Optimisation of ex-situ annealing process for epitaxial silicon emitters via Hot Wire CVD",* Proceedings of the 14th Photovoltaic Science Application and Technology Conference (PVSAT-14), London, April 2018

4. Edris Khorani, **Tudor E. Scheul**, Jack Tyson, Tasmiat Rahman and Stuart A. Boden, *"Boron-doped silicon growth via Hot Wire CVD towards emitter formation for interdigitated back-contact solar cells",* Proceedings of the 15th Photovoltaic Science Application and Technology Conference (PVSAT-15), Warwick, April 2019

Table of Contents

Declaration of Authorship

I, TUDOR EMILIAN SCHEUL, declare that the thesis entitled *METAL-ASSISTED CHEMICALLY ETCHED BLACK SILICON: MORPHOLOGY AND LIGHT INTERACTION* and the work presented in the thesis are both my own, and have been generated by me as the result of my own original research. I confirm that:

- this work was done wholly or mainly while in candidature for a research degree at this University;
- where any part of this thesis has previously been submitted for a degree or any other qualification at this University or other institution, this has been clearly stated;
- where I have consulted the published work of others, this is always clearly attributed;
- where I have quoted from the work of others, the source is always given. With the exception of such quotations, this thesis is entirely my own work;
- I have acknowledged all main sources of help;
- where the thesis is based on work done by myself jointly with others, I have made clear exactly what was done by others and what I have contributed myself;
- parts of this work have been published as:

1. Tudor E. Scheul, Edris Khorani, Tasmiat Rahman, Martin D.B. Charlton, Stuart A. Boden, *"Wavelength and angle resolved reflectance measurements of pyramidal textures for crystalline silicon photovoltaics",* Progress in Photovoltaics: Research and Applications, 2020; 1-10. https://doi.org/10.1002/pip.3319
2. Tudor E. Scheul, Edris Khorani, Tasmiat Rahman, Stuart A. Boden, *"Characterization of Atomic Layer Deposited Alumina Thin Films on Black Silicon Textures Using Helium Ion Microscopy",* AIP Conference Proceedings 2147, Silicon PV , Leuven, Belgium, April 2019,. https://doi.org/10.1063/1.5123858
3. Tudor E. Scheul, Edris Khorani, Tasmiat Rahman and Stuart A. Boden, *"Metal-assisted chemically etched black silicon for crystalline silicon solar cells",* Proceedings of the 14th Photovoltaic Science Application and Technology Conference (PVSAT-14), London, April 2018

Signed: ……..

Date: ……

Acknowledgments

A special thank-you goes to my supervisors, Dr. Stuart Boden, Dr. Tasmiat Rahman and Prof. Martin Charlton. They have been with me ever since my 3rd year of my Bachelor's degree and have offered me a great opportunity to advance my knowledge and contribute to the field with research of my own. I am especially grateful for their friendly approach, unending patience, keen insights and enthusiasm and for making my whole PhD journey a very enjoyable experience. Many thanks go to my friend and colleague Edris, with whom I have shared much of my academic journey so far, as well as the rest of our research group: Jack, David, Thomas, Chiren, Omesh and Dan. I would like to acknowledge the staff in our cleanroom and labs for helping me with fabrication and characterisation. Everyone's contribution to this project is most appreciated. In addition, I want to thank Prof. Peter Wilshaw's group in Oxford for the useful discussions, suggestions and expertise they have brought to my work.

I would like to thank the picoFIB network for making the trips to the London Centre of Nanotechnology possible. All of the staff involved at LCN has been most helpful, taking me in and providing training and advice whenever needed. In particular, I thank Dr. Suguo Huo for his patience and help, without whom my microscopy work there would have not been successful.

Outside of my PhD, I am grateful for a number of people that have made the almost seven years I have spent in Southampton a great and fun time. Special thanks go to Teo, Alex, Andrei, Antonia and Radu for taking my mind off work when things were not going as planned. In addition, I thank all my friends in Romania for making the holiday trips back home so much more fun and relaxing.

Last, but not least, I am extremely grateful and lucky to have to the most amazing and supportive family of all: thank you to my Mum, Dad, Brother, Uncle and Grandparents for always believing in me and being there for me for all of these years. Special thanks to my partner, Florina, for being very supportive and understanding of my tough times in these last couple of years. I am blessed to have all of you around me.

List of abbreviations

A	Absorption
AFM	Atomic force microscopy
Ag NP	Silver nanoparticle
AM	Air mass
ALD	Atomic layer deposition
ARC	Antireflective coating
b-Si	Black silicon
CB	Conductance band
DI	De-ionised
EVA	Ethylene vinyl acetate
FDTD	Finite difference time domain
FEM	Finite elements method
FEP	Field effect passivation
FF	Fill factor
FGA	Forming gas anneal
G	Generation
HIM	Helium ion microscopy
IBC	Interdigitated back contact
IPA	Isopropyl alcohol
MACE	Metal-assisted chemical etching
MCD	Minority carrier density
NAOS	Nitric acid oxidation of silicon
NIP	Nanoinverted pyramid
PDMS	Polydimethylsiloxane
PECVD	Plasma-enhanced chemical vapour deposition
PERC	Passivated emitter rear contact

PERL	Passivated emitter rear locally-diffused
PESC	Passivated emitter solar cell
PFD	Photon flux density
PTFE	Polytetrafluoroethylene
PV	Photovoltaics
PVB	Polyvinylbutyral
QSSPCD	Quasi steady-state photoconductance decay
R	Reflectance
RCWA	Rigorous coupled-wave analysis
RIE	Reactive ion etching
RP	Random pyramids
RTA	Rapid thermal annealing
SEM	Scanning electron microscopy
SHJ	Silicon heterojunction
SNR	Signal-to-noise ratio
SRH	Shockley-Read-Hall
SRV	Surface recombination velocity
T	Transmittance
TDMASi	Trisdimethylaminosilane
TEM	Transmittance electron microscopy
TIR	Total internal reflection
TMA	Trimethylaluminium
TMM	Transfer matrix method
VB	Valence band
WAH	Weighted average haze
WAR	Weighted average reflectance
WARS	Wavelength and angle resolved scattering

Chapter 1

Introduction

1.1 Evolution and current state of silicon photovoltaics

As the energy demand of our society grows rapidly every year, alternatives to the finite and polluting fossil fuel technologies must be sought, with reduced CO_2 emissions [1]. Photovoltaics (PV) promise to address these issues by providing a route to renewable, green, sustainable, and perhaps most important, infinite energy through means of sunlight absorption. These important criteria meet the current societal crisis demands concerning global warming and greenhouse effects. Due to significant advancements in the microelectronics industry in the early 20th century, photovoltaics was able to borrow a high degree of existent methodology to establish itself as a fast-growing renewable energy alternative. In 2019 alone, 130 GWp of photovoltaic modules were installed across the world, raising the total module

capacity currently available by 20% to almost 700 GWp [2]. The generation of electricity through photovoltaics covers daily 3% of energy demand globally and more than 8% in countries such as Italy, Germany, Australia and Greece [3]. Moreover, the consistent reduction in price every year will ensure accelerate growth of PV technologies for at least the next few decades. It is expected that by 2050, the PV capacity will increase to 5 TWp and will comprise 20% of the global electricity demand [4]. This is due to a strategy involving a combination of steady increase in PV module efficiencies and on-going reduction in fabrication costs. While the price per power unit was more than 100 $/Wp in 1976, it that has since gone down to 0.23 $/Wp in 2019 and a further decrease is predicted, as deduced from the learning curve of Figure 1.1 [2]. This significant price drop is achieved by a continuous reduction of solar cell thicknesses, including the bulk semiconductor material, protecting encapsulants and glass covers, as well as refinement of existing manufacturing processes. The process of price/watt reduction can be further enhanced by fabrication of more efficient devices while maintaining fixed fabrication costs, which is a primary concern of the PV industry and manufacturers.

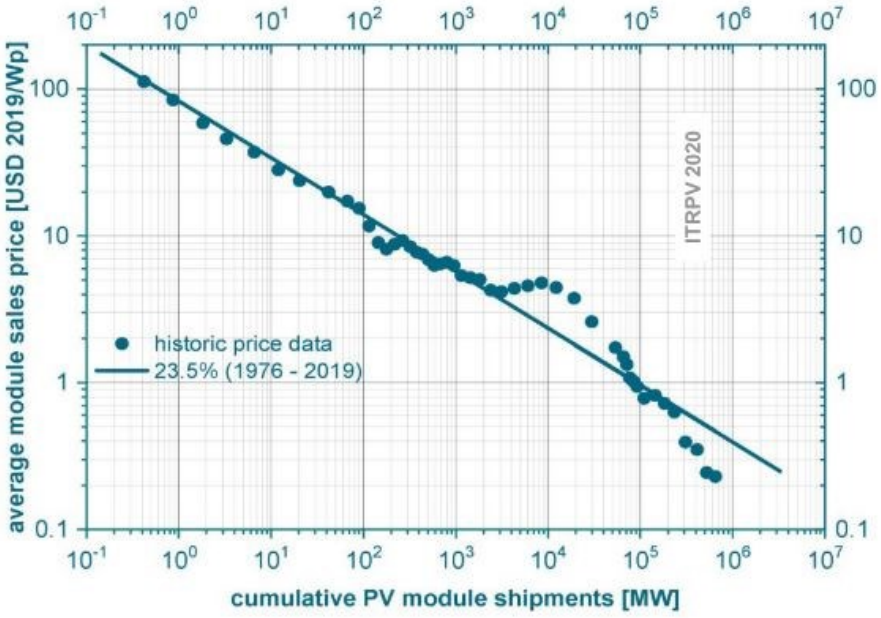

Figure 1.1: Learning curve for module price versus cumulative global shipment for period 1976-2019. Reproduced from Ref. [2].

As in other electronic related fields, the most used semiconductor material is silicon, due to its abundance, non-toxicity and ease of processing. In 2019, it is estimated that silicon PV technologies comprise 95% of the PV world market share, while thin film technologies, based on amorphous silicon (a-Si), cadmium telluride (CdTe) or copper indium gallium selenide (CIGS), make up the rest [2-4]. In research environments, silicon solar cell power conversion efficiencies of more than 26% are possible, while tandem designs and solar cells based on other semiconductors exceed this value, although at a higher cost and more complex fabrication requirements [5]. However, a significantly lower 20-22% figure is currently available on the market for commercial modules, with a wide variety of architectures and absorber material quality. Is it therefore vital for the advancement of photovoltaics to push power conversion efficiencies towards higher values while maintaining acceptable fabrication costs.

1.1.1 Basic operation of a solar cell

A typical semiconductor, such as silicon, becomes conductive at non-zero temperatures. This is due to the random movement of free carriers, which acquire thermal velocity and are free to move within the crystal lattice, scattering off material atoms. When a p-type silicon material, which contains excess holes due to doping with acceptor impurities (such as Boron), is joined with an n-type silicon material, which contains excess electrons due to doping with donor atoms (such as Phosphorus), charge carriers will start moving in an one direction due to the formed charged gradient. This effect is due to the diffusion of the carriers, which move around to fill the free space until equilibrium is reached, ideally. For a p-n junction, this means that majority carriers from the p-type region (holes) diffuse to the n-type region, while the majority carriers from the n-type region (electrons) diffuse to the p-type region. As such, this preferential motion of the charge carriers located close to the junction creates a depletion region, where no carriers are present. This in turn creates a built-in electric potential $\boldsymbol{V_{bi}}$ and field $\boldsymbol{E}$, due to the ion cores that are left behind after charge carrier movement. The electric field gives rise to another type of movement of the carriers, called drift. As such, electrons move in the opposite

direction of the electric field. Figure 1.2 shows the movements of the charge carriers due to diffusion and drift in a silicon p-n junction.

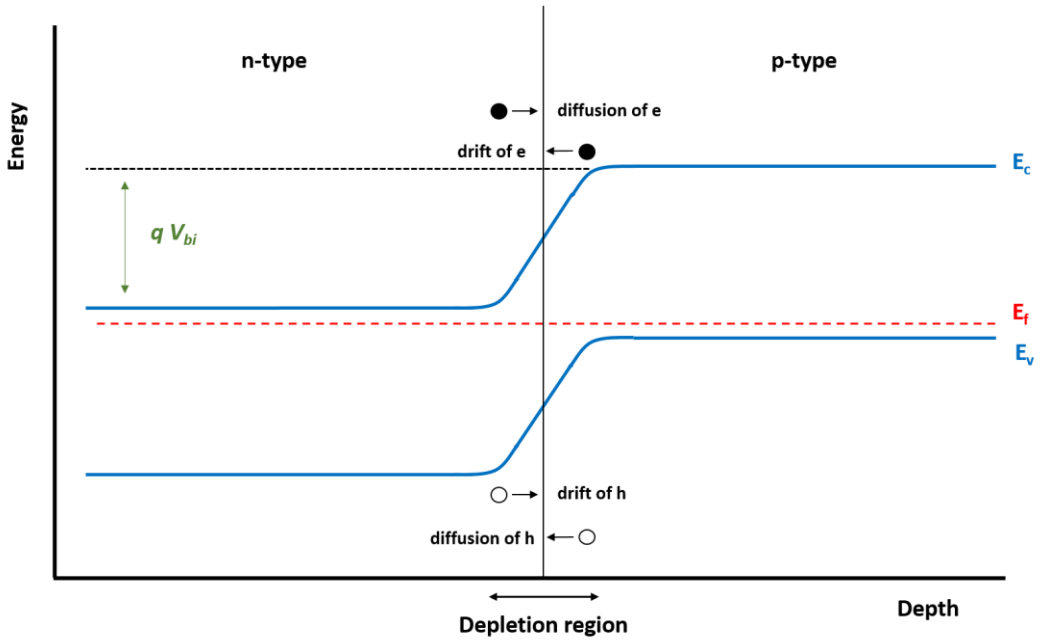

Figure 1.2: Band diagram of a p-n junction under equilibrium, showing charge carrier transport.

Under no illumination, the p-n junction acts as a diode. If metallic contacts are added to extract charge carriers and a bias voltage ***V*** is applied, a current ***I*** will flow through the device, according to Equation (1.1). Depending on the magnitude of the applied bias voltage, the diffusion barrier at the junction can decrease under forward bias, decreasing the built-in voltage and increasing the diffusion current, or increase under negative bias. Under forward bias, large diffusion of minority carriers leads to recombination in the neutral region and the diffusion current becomes the recombination current.

$$I = I_0 \left(e^{\frac{qV}{nkT}} - 1\right) \tag{1.1}$$

- I_0 is the saturation current (A)
- q is the electron charge ($6.02 * 10^{-19}$ C)
- V is the bias voltage (V)
- n is the ideality factor (between 1 and 2)
- k is Boltzmann' constant ($1.38 * 10^{-23}$ J/K)
- T is the temperature (K)

In a p-n junction solar cell device, the absorption of light translates into minority carriers (electron-hole pairs) generated in the semiconductor material. If minority carriers reach the depletion region of the p-n junction, they are swept across by the built-in electric field and thus become majority carriers. The collection probability of the junction is an important parameter for the operation of a solar cell. If minority carriers are generated far away from the junction (more than a diffusion length away), the collection probability becomes very low, as carriers will be more likely to recombine before being collected by the junction. Conversely, carriers generated in the depletion region are instantly collected by the p-n junction and ideally have a unity collection probability. If carriers are generated closer to an unpassivated surface than to the junction, they are more likely to recombine at the surface than be collected by the junction. The flow of the photo-generated carriers across the p-n junction creates a current I_L that modifies the current flowing through the device as in Eq. (1.2). A schematic of the IV curves of a solar cell under no illumination (blue trace) and under illumination (red trace) is shown in Figure 1.3, with the convention that the power quadrant is flipped so that the extracted power is positive. In here, I_{sc} is the short-circuit current at which the voltage across the device is zero and is determined by the rate of generation of carriers and their collection. As such, the optical properties and the collection probability of the device drastically affect I_{sc}. V_{OC} is the open-circuit voltage which occurs when no current flows through the solar cell and is dependent on the saturation current I_0 and thus the recombination of carriers in the semiconductor bulk and surfaces.

$$I = I_0 \left(e^{\frac{qV}{nkT}} - 1\right) - I_L \tag{1.2}$$

- $\boldsymbol{I_0}$ is the saturation current (A)
- $\boldsymbol{q}$ is the electron charge ($6.02 * 10^{-19}$ C)
- $\boldsymbol{V}$ is the bias voltage (V)
- $\boldsymbol{n}$ is the ideality factor (between 1 and 2)
- $\boldsymbol{k}$ is Boltzmann' constant ($1.38 * 10^{-23}$ J/K)
- $\boldsymbol{T}$ is the temperature (K)
- $\boldsymbol{I_L}$ is the light generated current (A).

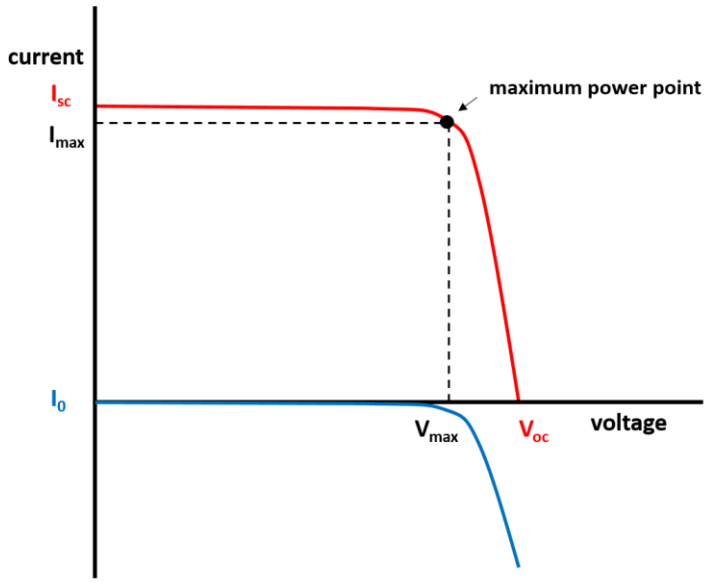

Figure 1.3: IV curve of a diode under no illumination (blue trace) and under illumination (red trace) [6].

The dashed rectangle inside the red trace in Figure 1.3 indicates the actual maximum current I_{max} and voltage V_{max} that can be extracted from the photovoltaic cell. It is desired that the cell operates at the maximum power point, indicated in Figure 1.3. These parameters are used to calculate the fill factor, *FF*, of a device, which describes the quality of the operation of the cell, as in Equation (1.3).

$$FF = \frac{V_{max}I_{max}}{V_{OC}I_{sc}} \tag{1.3}$$

The figure of merit that is generally used to compare solar cells is the power conversion efficiency η, which determines what fraction of incident power can be extracted from the device, as shown in Equation (1.4) [7]. The power obtained from the cell can differ vastly with architecture, size, temperature and other parameters and as such, attention has to be given to the measurement of η, which is usually performed under standard conditions: temperature of 25° C and AM1.5G incident spectrum [7-8]. The incident power is normalised to 100 mW/cm^2, which becomes 24.3 W for a typical solar cell of 156 x 156 mm^2.

$$\eta = \frac{P_{max}}{P_{incident}} = \frac{V_{OC}I_{sc}FF}{P_{incident}} \tag{1.4}$$

1.1.2 Limiting factors

The photogeneration of minority carriers in an illuminated solar cell has a reversible mechanism called recombination. This refers to an electron relaxing from a higher energy state back into a ground state and recombining with a hole. The pair of charge carriers is subsequently lost and cannot be extracted to produce useful work. The three types of recombination encountered in a semiconductor are: radiative (band-to-band) recombination, Auger recombination and trap-assisted recombination. Diagrams for these three types are shown in Figure 1.4.

The ***radiative recombination*** involves the relaxation of an electron across the bandgap to the edge of the valence band, which results in the emission of a photon, and is a strong limiting factor on the efficiency of direct bandgap solar cells, such as GaAs. In indirect bandgap materials, radiative recombination is rarely encountered and the rate of such recombination is four to five orders of magnitude lower than direct bandgap materials [6]. Subsequently, the average radiative lifetime, which describes how long a carrier remains excited before relaxation to a ground state, is five to seven orders of magnitude lower in indirect bandgap materials. Therefore, the improbability of radiative recombination in Si cells leads to the dominance of other, non-radiative mechanisms, such as Auger and trap-assisted recombination.

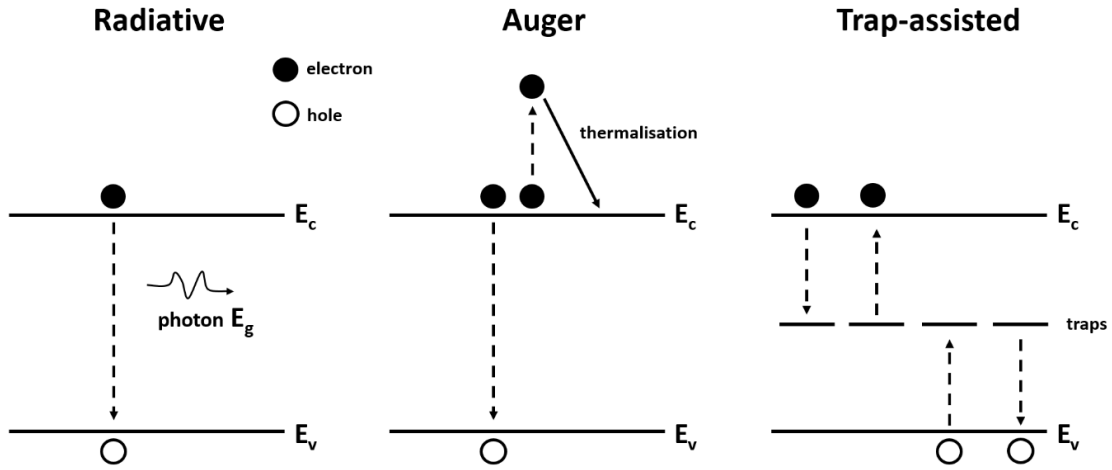

Figure 1.4: Three types of recombination in the semiconductor material [6].

Auger recombination occurs when the relaxation of an electron does not translate into photon emission, but rather into kinetic energy that is given to a second electron, upon collision, for example. The second electron present in the conduction band is excited to even higher energy states, but then quickly relaxes back to the edge of the conduction band through thermalisation processes and phonon emissions. This type of recombination is especially important and dominant for indirect bandgap materials (such as Si and Ge) and places a hard efficiency limit on these devices.

Trap-assisted (Shockley-Read-Hall) recombination is directly connected to the purity of the semiconductor material. As growing high purity materials is difficult and costly, defects in the crystal, such as vacancies and interstitial impurities are known as traps, which essentially form energy levels in the forbidden region (bandgap). These energy levels can be either donor-like or acceptor-like (or both i.e. amphoteric) and capture an electron or a hole that can recombine in this energy region. In most practical cells, this type of recombination often limits the ultimate efficiency and is further detailed in Chapter 3.5 in this thesis.

In addition, many electrical losses in a photovoltaic device affect these parameters and the optimum power extraction. Resistive effects reduce the power conversion efficiency by dissipating power and reduce the fill factor. An equivalent circuit of an actual solar cell is shown in Figure 1.5. Series resistance R_s arises from semiconductor bulk resistance and contact resistance between the metallic contact and the semiconductor material, as well as the metal contact resistance itself. Parallel (shunt) resistance R_p is a contribution of a multitude of manufacturing defects that offer alternative paths for the current to travel (rather than through the external circuit). Equation (1.5) expands equation (1.2) to take into account these electrical losses, as well as the photo-generated current I_L flowing through the device, based on the equivalent solar cell circuit [6].

$$I = I_L - I_0 e^{\frac{q(V+IR_S)}{nkT}} - \frac{V+IR_s}{R_p} \quad (1.5)$$

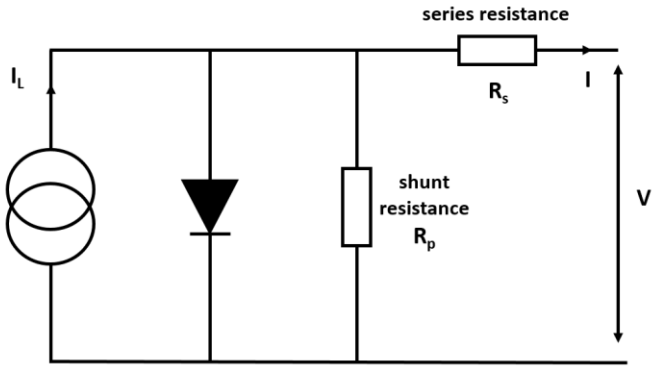

Figure 1.5: Equivalent solar cell circuit with series and parallel resistances [6].

There are a number of intrinsic losses to the ultimate efficiency of a photovoltaic device, which were thoroughly analysed by Shockley and Queisser [9] and later by Teidje [10]. For a semiconductor with a given bandgap, only photons of larger energies than this bandgap can be effectively absorbed (see Chapter 2.1). As such, much of the longer wavelength (lower energy) light in the solar spectrum incident on Earth's surface is not absorbed. Conversely, if the energy of the photons that are successfully absorbed is much larger than the bandgap of the material, thermalisation losses will occur and the excited electrons will relax to the edge of the conduction band, dissipating the excess energy as heat. In addition, recombination of generated charge carriers throughout the entirety of the cell through radiative means further places a limit on the conversion efficiency of the device. By accounteng for these factors, Shockley and Queisser calculated a maximum of approximately 30% in power conversion efficiency, η, for a semiconductor material with bandgap 1.1 eV, such as silicon [11]. The resistive extrinsic effects described earlier further contribute to a reduction in η below this limit. There is an on-going effort to manufacture high-quality substrate materials with large bulk lifetimes, as well as develop surface passivation schemes that prevent recombination processes at various interfaces in a solar cell. Moreover, a combination of large surface reflectance and poor absorption of low-energy photons at the device level remains to hinder the operation of solar cells. Antireflective and light-trapping surfaces can be employed to minimise these optical losses and

enhance carrier photogeneration, as described in more detail in Chapter 2 of this thesis.

1.1.3 Short history of silicon photovoltaic advancements

The history of modern photovoltaics finds its roots in the experimental demonstration of the photovoltaic effect, conducted by Becquerel in 1839, where the excitation of an electron onto a higher energy state in the material was first observed in an electrochemical cell subjected to light irradiation [12-13]. In 1883, Charles Fritts attempted the fabrication of a selenium-based solar cell with modest success, due to the difficulty of manufacturing such a device at the time [14]. The power conversion efficiency is assumed to have been below 1%. Further attempts by Ohl and co-workers in 1941 [15] and 1952 [16] did not result in improvements in the efficiency of the devices, but rather a more methodical approach to their fabrication. At this time, efforts were dedicated to the development of the semiconductor industry for bipolar devices (such as diodes and transistors) and means of fabricating high-purity materials with uniform impurity diffusion processes. It was not until 1954 that more substantial advancements were reported with the work of Bell Laboratories [17], which translated into device efficiencies of 4.5% for lithium diffused junctions and further increase to 6% when the diffusion process used boron species. In the following period, limited applicability of these solar cells was found for satellites, where efficiencies and associated device fabrication costs were not of primary concern. The work of Mandelkorn et al. [18] established conversion efficiencies of 15% for boron diffused cells and 11% for phosphorus diffused p-type substrates. However, at the time, the lower-efficient cells were preferred for space applications, due to the superior radiation resistance of p-type silicon material in space environment, leading to slower degradation of minority carriers.

It was not until the 1970s that more interest and funding was dedicated to terrestrial photovoltaics devices in the pursuit of alternative electricity-generating technologies, following the surge in oil prices in the USA. As such, in 1973, Rittner et

al. [19] presented their Violet Cell, with power conversion efficiencies exceeding 15.5% for terrestrial irradiance. The device successfully made use of the then recently-developed aluminium back surface field (BSF) incorporated via annealing at high temperatures on the rear of the cell, effectively passivating the silicon surface and reducing minority carrier concentration in the region. In combination with a geometrically optimised fine metal grid pattern, shallower diffusion of the phosphorus species and a TaO_x antireflective coating, the cell yielded respectable electrical response in the short wavelength region. After just a couple of years, advancements in the anisotropic etching in the integrated circuit industry led to an expansion of their previous work, and the fabrication of the Non Reflective Cell was reported, shown in Figure 1.6 a). The random pyramidal array formed on the semiconductor surface to expose {111} crystallographic planes further enhanced the optical properties of the solar cell and led to a power conversion efficiency of 17% [20] under an AM2 irradiance spectrum. It was then that society realised the true potential of photovoltaic technology, as well as the concomitant need of efficient devices with reduced fabrication costs.

For almost a decade, the efficiency of research solar cells stabilised under this value, until the Passivated Emitter Solar Cell (PESC) was introduced by Green et al. [21] in 1984 (see Figure 1.6 b). Owing to the excellent passivation of the n^+ emitter with an ultra-thin SiO_2 layer, V_{OC} in the range of 650-675 mV was obtained. Using high-quality Float Zone starting materials, efficiencies of above 19% were reported for the first time ever on such a device. Subsequent work on optimising the top surface metal contacts translated into an efficiency of 19.8% [22], and efficiencies over the 20% mark, which was once thought to be the effective efficiency limit of a silicon solar cell under terrestrial irradiance, were now more feasible than ever. Research at UNSW conducted by Dr. Green managed to break another efficiency record in 1989 with the group's Passivated Emitter Rear Cell (PERC) device [23]. Massive improvements were reported by the use of a passivating dioxide layer on the rear surface of the cell, as well as heavily diffused areas below the top metal contacts. In combination with the inverted pyramidal array on the top of the solar cell, which ensured significantly increased coupling of photons inside the bulk of the

device and more chances for total internal reflections for those travelling upwards upon back-reflection, the efficiency record was raised to 22.8%.

Only two years later, further improvements were reported and a new record-holding device was introduced: the Passivated Emitter Rear Locally-diffused cell (PERL), which combined all of the best features of the previous designs [24-25]. Initial work resulting in efficiencies of 23% was soon expanded in 1996, leading to conversion efficiencies exceeding 24% for the first time [26]. The device underwent additional optimisation of the top-surface grid pattern to ensure metal-silicon contact area below 0.5% to reduce series resistance, thicker high-quality substrates, carefully optimised double antireflection coatings and an improvement to the passivation quality of the thin dioxide layers using hydrogen species. The PERL solar cell is shown in Figure 1.6 c).

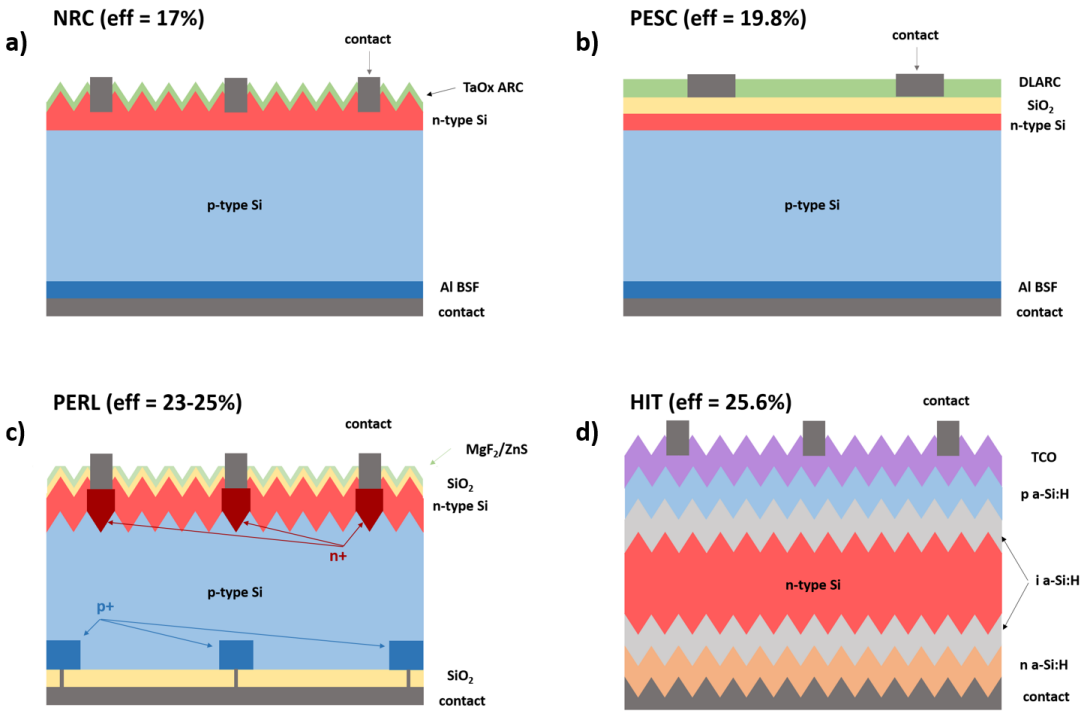

Figure 1.6: Cross-sectional sketches of historical high-efficiency architectures: a) Non-Reflective solar Cell; b) Passivated Emitter Solar Cell; c) Passivated Emitter Rear Locally-diffused; d) Heterojunction with Intrinsic Thin-layer.

Over the following decade, marginal improvements on the PERL architecture translated into efficiencies slightly above 25%. However, the need for locally-diffused regions at the silicon/metal interfaces hindered the industrialisation of such a device, due to complex fabrication steps and large associated costs. In parallel, since the early 1990s, the Sanyo group as part of Panasonic reported massive improvements in their silicon heterojunction solar cell, commercially known as HIT, shown in Figure 1.6 d). The excellent crystalline silicon passivation using thin layers of hydrogenated amorphous silicon (a-Si:H) results in large V_{OC} values. The top half of the device shown in 1.6 d) is the p/n heterojunction, while the BSF effect consists of a thin n-type a-Si layer. A transparent conductive oxide (TCO) is used to conduct minority carriers to the top and bottom contacts, to offset for the high resistivity of the a-Si material. The c-Si n-type base is textured with a random pyramidal structure to improve light-trapping and photon absorption, translating into device efficiencies of 23% in 2009 [27]. Refinement in the fabrication processes, such as a-Si:H deposition and contact grid optimisation, meant an increase to 24.7% and eventually to 25.6% in 2014 [28-29], a world-record at the time.

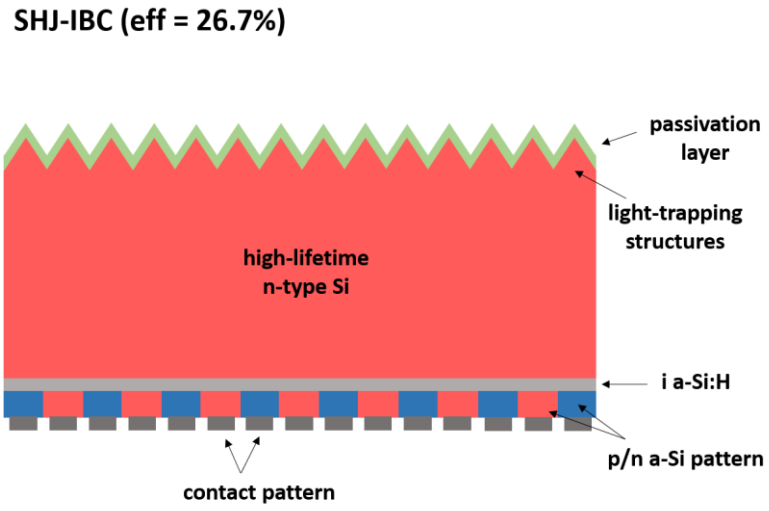

Figure 1.7: Interdigitated back-contact cell. This architecture holds the highest c-Si monojunction power conversion efficiency as of 2017.

Since 2017, a completely different solar cell architecture than previously described would hold the highest silicon cell efficiency, fabricated by Kaneka [30]. The interdigitated back contact (IBC) cell was originally developed as early as 1977 [31] and was aimed towards concentrator applications, were the light bias is higher than 1 sun. The main feature of this design is the placement of the metal contacts and the junction at the rear of the solar cell in an alternating pattern, such that the entire front surface is planar and available for texturing, as in Figure 1.7. As such, the finger to spacing ratio has to be carefully optimised and high-quality materials with excellent surface passivation are needed, whereby the minority carriers have large lifetimes. This is due to carriers generated near the top surface of the cell, which have to diffuse the entirety of the device thickness to be collected by the p-n junction at the rear. For this architecture, efficiencies as large as 29% have been predicted for bulk lifetimes in excess of 1 ms and surface recombination velocities below 20 cm/s [31]. The work by Kaneka employed a silicon heterojunction and again made use of the excellent passivating properties of a-Si:H. Careful design of this architecture led to an impressive power conversion efficiency of 26.3% in 2016, later improved to 26.7% in 2017 [30]. As such, PV silicon technology is getting close to the predicted Shockley-Queisser limit of ~30% for silicon solar cells, but innovative engineering design is needed to boost cell efficiencies further.

1.2 Prospects over the coming decade

Although laboratory silicon PV devices are closing in on the theoretical power conversion efficiency limit of just above 30%, there is still a lot of scope left in this area. Not only is there a gap of 4-5% remaining in to be filled by research advancements, but commercial silicon solar cells are much less efficient, due primarily to constraints such as costs and scalability of existing laboratory technologies. Therefore, the preoccupation of PV community is two-fold, which must be addressed concomitantly: i) advancement of various existing and new fabrication technologies and innovative device architecture design to push the current efficiencies up to the predicted value; ii) reduction of current costs

associated with manufacture of existing designs, as well as integration of current laboratory methodologies in industrial cycles.

Moving forward, it is obvious by the two highest power conversion efficiency values that silicon heterojunction devices have great potential of rapid growth, in particular a-Si/c-Si architectures. This is mainly due to the electrochemistry between the two materials, where a mismatch in the energy levels of the valence and conduction bands leads to continuous Fermi level under equilibrium, but discontinuous energy bands in either conduction or valence bands. This translates into charge accumulation in one of these bands, such that charge separation inside the device becomes more pronounced and thus an increase in the collection efficiency of the junction is immediate [32]. Moreover, chemical and physical depositions of the a-Si layers for junction formation are more beneficial as an alternative to the more pervasive high-temperature (T~900 °C) dopant-diffusion, which leads to lower quality materials and non-uniformity in the product. As such, the a-Si deposition for the HIT cells occurs at 200° C, translating into vastly reduced fabrication costs and thermal budgets, as well as less thermal degradation of c-Si substrates (especially p-type due to B-O defects [33]) that in turn affect the power conversion efficiency. However, concerns regarding the contact formation, careful control of TCO electrical and optical properties and parasitic absorption in the a-Si layers primarily remain when employing such a method.

Another strategy currently employed by researchers for significant performance increase is a multijunction (tandem) solar cell, whereby each junction operates independently and is responsible of collecting various parts of the incident irradiance. Amongst these, silicon/perovskite tandems are currently the most promising, due to the synthesis of perovskite materials with excellent optical properties that can complement those of silicon. Relatively low costs associated with demonstrated power conversion efficiencies exceeding 20% are reported for a stand-alone perovskite cell with substrate thicknesses in the order of hundreds of nanometres [34-36]. In such a tandem device, the perovskite material has an ideal bandgap of 1.5-1.6 eV for the top cell responsible for absorbing high energy photons, yielding open-circuit voltages in excess of 1.5 V [37-38]. This cell is transparent to

longer wavelength photons that are transmitted to the bottom silicon cell and absorbed here, leading to demonstrated efficiencies of up to 28% [39]. However, perovskite materials are susceptible to degradation mechanisms that affect long-term stability and hinder the integration of this technology in mass-production.

The route for single junction crystalline silicon solar cells can be expanded in a few ways. Firstly, as previously mentioned, development of methods that can epitaxially grow doped c-Si are preferable to the high temperature diffusion steps for junction formation, in order to avoid activating material defects in the bulk and incompatibility with fabrication processes that cannot be subjected to extreme temperatures. Secondly, surface passivation remains as important as ever. The highest efficiencies are achieved by use of advanced passivation schemes and materials that can overcome the passivation performance of industrial materials such as silicon nitride. To this end, materials in which a large fixed charge can be activated are starting to find their way in the PV field, such as aluminium oxide [39] or titanium oxide [40]. Alternatively, diffusion of hydrogen species in the already existing Si/SiO_2, Si/SiN_x or Si/a-Si systems yields highly improved interfaces from an electrical perspective and significant enhancements in open circuit voltages of the cells. Thirdly, passivated carrier selective contacts are a topic of interest currently for integration in high-efficiency laboratory cells. Traditionally, high recombination at the metal-silicon interfaces has been addressed by minimisation of metal-silicon contact area and locally heavily diffused materials in this region (e.g. see the PERL cell). However, this leads to high levels of Auger recombination that remain detrimental to the overall performance of the device. More recently, the idea of metal-insulator-semiconductor (MIS) junctions came back into the PV field for addressing voltage losses associated with contacts [41-42]. Ideally, the passivated contact must fulfil two requirements concomitantly: i) interface recombination must be minimised such that charge carriers do not recombine before extraction; and ii) the MIS system acts as a charge barrier, letting through one type of carrier, while repelling the other type of minority carrier. By using a metal with a suitable workfunction, one type of carrier can be depleted from the interface, thus reducing recombination. In general, for hole-selective contacts, a metal with a large

workfunction is required, while a small workfunction is required for electron-selective contacts [8]. More recently, a heterojunction passivating contact structure was reported by Feldmann et al. [43], called TOPCon (Tunneling Oxide Passivation Contact), whereby an ultra-thin chemically grown oxide is used in conjunction with thin PECVD deposited doped silicon layers to improve carrier selectivity to both the n-type and p-type contacts. High-temperature anneal of the passivating contact stack results in recrystallization of the thin Si layer and further enhances recombination. It was, however, shown that significantly poorer passivation using this method is achieved for the p-type contact with B-doped Si BSF [44]. As such, development of hole-selective contacts remains of utmost interest for pushing device efficiency closely to the Shockley-Queisser limit.

1.3 Motivation and potential improvements

Given the dominance of silicon in the current PV market, this technology is likely to maintain its status in the following decades. Even if the efficiency limit of 30% for single-junction silicon cells will be achieved in the immediate years with tandem cells, there is much scope and advantage for silicon PV to remain the primary technology in the field. This is true especially considering the existing industrial tools and fabrication flows in the field that are designed around silicon. Apart from the obvious methods of reducing manufacturing costs, such as finding and incorporating alternative materials (e.g. replacing expensive silver for contacting with a cheaper material with similar conductivity) in the fabrication process, the cost reduction of current commercial devices can be achieved by the implementation of a circular economy model, as in many other areas. As such, recyclability of various PV technologies is of primary concern, along with non-toxicity and abundance of used materials. To this end, various programmes exist across the world, that allow solar panels to be discarded and recycled by the society at the end of a module's lifetime [45].

In particular, the recent demonstration of very high conversion efficiencies achieved by interdigitated back contact (IBC) solar cell designs enables the integration and expansion of various texturing methods at the device level, which

can significantly improve light management and participate in higher current extraction. In such a back-contacted design, the top surface of the semiconductor stack is free of metallic electrodes and therefore free of contacting obstacles between the metal and the textured surface with high wettability.

Traditionally, the highest efficiency silicon solar cells were made use of a random pyramidal structure fabricated via anisotropic etching to expose various crystallographic planes of the silicon material, sometimes in conjunction with masking lithography processes for inverted pyramids. Although the optical results arising from such a strategy are highly beneficial, lower surface reflectance values can be achieved still, as well as improved light-trapping inside the silicon bulk. This is a pathway to thinner devices that can efficiently absorb low-energy photons and larger conversion efficiency, provided that the contacting scheme and other electrical parameters are unchanged [2]. Recently, efficiencies above 22% have been reported for an IBC silicon solar cell with black silicon surface, i.e. nanotextured silicon, which acts both as an antireflective coating and as a light-trapping layer [46]. While the fabrication method for the black silicon in this case was reactive ion etching (RIE), which possesses several disadvantages, such as high costs, long processing times and damaging of the semiconductor surface, alternative methods such as metal-assisted chemical etching (MACE) can be exploited, ensuring low costs and high reliability of the resulting product. In fact, as of 2014, a variation of the MACE process is widely used in the industry for the realisation of low-reflective surfaces on multicrystalline silicon solar cells, showcasing the ease of integration of such a technology in already existing process flows and feasibility from a high-throughput point of view [2].

Although highly impressive optical properties can be achieved by nanotexturing the silicon surface, increasingly so for taller nanostructures, the associated electrical losses arising from increased semiconductor surface area, and thus surface defects, hinder the beneficial gain that comes from optics. As such, excellent surface passivation is a key component in high-efficiency black silicon solar cells, irrespective of the black silicon fabrication method of choice or the morphology of the nanotexture. To this end, a resurgence of atomic layer deposition (ALD) over the

past decade has provided the means of satisfying this requirement. Materials such as aluminium oxide, which possesses high negative fixed charge, have been long known to provide excellent passivation levels for silicon surfaces [39]. The advantage of atomic layer deposition is the slow and controllable deposition rate, whereby a monolayer of material is deposited each cycle, thus providing conformal coverage even on the tallest nanosotructures and between deep crevices and trenches. Therefore, the detrimental electrical properties of such excellent antireflective surfaces can be almost completely mitigated, providing sufficiently low surface recombination velocities to remain competitive in the PV field, when compared to micron-scale random pyramidal textures, for example. For this, MACE can be employed, as a cheap, fast, straightforward and highly scalable black silicon fabrication method [47], resulting in silicon surfaces that vastly outperform optically the pyramidal surfaces, used for example in the PERL cell.

Traditionally, the figure of merit to assess the societal and economic impact of PV devices has been price/watt. This is calculated by taking into account the cost of production and installation of a unit area of PV modules and the efficiency of such modules under peak solar irradiation [48]. Given the nature and long lifetime of the PV technology when used in a household, for example, it only makes sense that a payback time would be incorporated into the price/watt figure of merit. Therefore, a more recent and comprehensive approach to assess the economic and practical usefulness of a PV device for the world is the Levelised Cost of Electricity (LCOE). LCOE refers to the revenue per unit of generated power that is needed for installation and maintenance cost amortisation, as in Equation (1.6).

$$LCOE = \frac{costs\ over\ lifetime}{power\ generation\ over\ lifetime} \tag{1.6}$$

This project aims at improving LCOE of the silicon PV technology, by tackling both the numerator and the denominator in Equation (1.6). On one hand, metal-assisted chemical etching is a wet-etching fabrication method of black silicon that is inherently cheap and thus comparable in price to the already-existing alkaline etching processes in industry. Moreover, the highest cost of silver-assisted MACE

comes from the use of silver nitrate ($AgNO_3$), which can be readily recovered and recycled from the end of the process using chemical reactions [49-50], thus providing the means of further cost reduction in the fabrication of PV devices. On the other hand, the nanotexturing of black silicon surfaces, especially in an IBC cell design, has the potential of significantly increasing the optical performance. This directly translates into larger currents through the device and eventually larger power conversion efficiencies.

In addition, the impact of various process parameters is investigated in this thesis for the metal-assisted chemical etching (MACE) of single crystal silicon substrates of various doping profiles. Although studies on MACE have been carried extensively in literature over the past decades, a few questions remain unanswered. Parameters such as etching time and solution concentrations have a strong impact on the resulting nanostructure morphology, as well as the implied fabrication cost and optoelectronic performance. However, challenges regarding effective surface passivation with the use of ultrathin dielectric layers remain in literature, especially from a morphological point of view (i.e. conformity of the dielectric layer inside deep trenches on such high aspect ratio nanostructures). To this end, this thesis aims to investigate the morphology of the atomic layer deposited layers on top of these textures with the use of high-quality helium ion microscopy (HIM) images. Furthermore, ion milling is performed horizontally through the black silicon to reveal the coating along the length of the nanowire and assess the uniformity of the dielectric deposition, which is a vital step contributing to effective surface passivation.

From an optical perspective, low surface reflectance has made black silicon into a topic of great interest for the photovoltaic community. However, no conclusive studies have been conducted yet in assessing the scattering and light-trapping properties of these textures, due to the precision and high budget required for

performing such measurements. In this thesis, a custom set-up is employed to measure the reflected scattering arising from MACE black silicon layers of various heights and the data are used to predict the portion of light trapped at various interfaces in an encapsulated solar cell, as well as calculating the photocurrent gain to be gained from such an approach. Wherever possible, direct comparisons are made to the industrial standard alkaline-etched upright random pyramids, to further confirm the superior optical capabilities of MACE black silicon textures for implementation on high-efficiency silicon solar cells.

1.4 Structure of report

The overall scope of this project is to design, fabricate and characterise black silicon layers that are strong candidates for silicon solar cell integration from both an optical and an electrical perspective. Therefore, Chapter 2 provides a review of the opto-electronic properties of crystalline silicon material, including refractive index, surface reflectance, absorption and generation, as well methods of addressing optical losses currently employed at industry level. The need for a true broadband flat optical response is shown to be currently unmet, further motivating the development of low reflectance surfaces. Chapter 3 provides a literature review of nanotextured silicon and its fabrication methods, whereby a range of morphologies can be achieved, with a special focus on one-step metal-assisted chemical etching (MACE). The electrical losses associated with increased semiconductor surface area upon texturing are also discussed, along with several dielectric materials that are commonly used for silicon surface passivation. In Chapter 4, an introduction to the various principal fabrication and characterisation methods is presented, such as electron microscopy, helium ion microscopy, reflectance measurements and deposition technologies, used throughout this project. Chapter 5 then provides an in-depth look at the MACE process, including the role of various chemical components on the morphology of black silicon, as well as its optical performance. An optimal set of parameters is identified for reproducible realisation of low-reflective surfaces. Low-reflective black silicon is also obtained on 6-inch Silicon

wafers, confirming the scalability of the process. Chapter 6 presents an investigation into the surface passivation of these antireflective layers and highlights the trade-off between electrical and optical properties. Sufficiently low surface recombination velocities for high-efficiency solar cells are obtained for black silicon surfaces with a feature height of approximately 1 μm thickness via atomic-layers deposited aluminium oxide, with very good conformal deposition of the passivating layers, analysed by means of high quality imaging using helium ion microscopy. In Chapter 7, the scattering and light trapping properties of alkaline etched pyramids and black silicon are explored, showing the scattering and angular redistribution of the reflected light arising from these textures. Implications at device level, mainly by means of total internal reflection in an encapsulated module, are discussed, as well as the potential gain in photogenerated current for such textured surfaces. Finally, Chapter 8 reviews the key findings of this work and proposes the expansion of the current work into several future directions.

Chapter 2

Theoretical Background

This chapter firstly serves as a review of the most important optical parameters of silicon, such as refractive index and absorption coefficients, which are crucial in the design of high-efficiency silicon photovoltaic devices. The role of sunlight for PV is then discussed, including the AM1.5G spectrum. Optical responses at an air-silicon stack and the subsequent large surface reflections arising at this interface motivate the development of antireflective schemes to attenuate the significant optical losses. These include single-layer and multilayer antireflective coatings comprised of dielectric low-absorption materials, as well as industry-standard micron-scale random pyramid textures, which can drastically reduce top surface reflectance. These approaches aim to compensate for the large refractive index values of silicon, as well as low absorption coefficients that prevent optimal absorption and photo-generation of low-energy photons in particular, thus affecting the electrical parameters of the photovoltaic cell.

2.1 Opto-electronic properties of crystalline silicon

2.1.1 Energy bandgap

The energy bands of a semiconductor material are complex in nature and depend on the main crystallographic orientation of the crystal. The Pauli exclusion principle states that no two electrons can occupy the same energy level states, giving rise to multiple energy levels which the electrons can occupy [51]. As such, the energy bands consist of discrete energy levels that exist in the crystalline material closely spaced together and can be sometimes thought of as continuous. In the lower energy state levels, called the valence band, valence electrons that surround each atom fully occupy these energy levels, except for the upper most energy levels. Similarly, the higher energy levels constitute the conduction band, where the lower most level may be empty or partly filled. Excitation can promote an electron from the valence band to an energy state in the conduction band. However, no energy level states are allowed in between these two levels. This energy zone is called the forbidden gap or the ***bandgap***, which is an important value for characterising the conductivity nature of various materials. In the case of semiconductor, the energy bandgap is non-zero, such that at 0 K there is no conductivity, but small enough such that electrons can overcome this energy difference when excited. Typically, semiconductor have bandgaps of below 3 eV [51]. A simplified model for the energy band diagrams of a material may include only the highest energy level of the valence band and the lowest energy level of the conduction band. In order to excite an electron with incident light, a photon of energy higher than the bandgap must be absorbed.

One important characteristic of the bandgap is the alignment of the maximum of the valence band and the minimum of the conduction band in terms of the wave vector *k*. Schematics of a ***direct*** bandgap and an ***indirect*** bandgap material and their absorption processes are shown in Figure 2.1. In the case of a direct bandgap, electrons can be excited to directly traverse the forbidden region until they reach an energy level in the conduction band, as long as a photon of required energy has been absorbed so that energy is conserved. For indirect bandgap, however, both the energy and the momentum of the electron have to change for the excitation to occur.

As photons have very low momentum, the absorption and change in momentum must occur via participation of a phonon, so that momentum is conserved. The absorbed photon energy, *hf*, is given by the following equations, to account for the conservation in momentum and energy when an electron transition occurs and a phonon is emitted [52-53]:

$$hf = E_x - E_y + E_{phonon} \tag{2.1}$$

$$k = k_x - k_y + k_{phonon} \tag{2.2}$$

- ***h*** is Planck's constant (J sec)
- ***x, y*** are the initial and final states of the electron, in the valence band and conduction band, respectively
- E_x, E_y are the energies in the initial state and final state, respectively
- ***k, f*** are the wavevector and frequency of the absorbed photon
- E_{phonon}, k_{phonon} are the energy and wavevector of the emitted phonon.

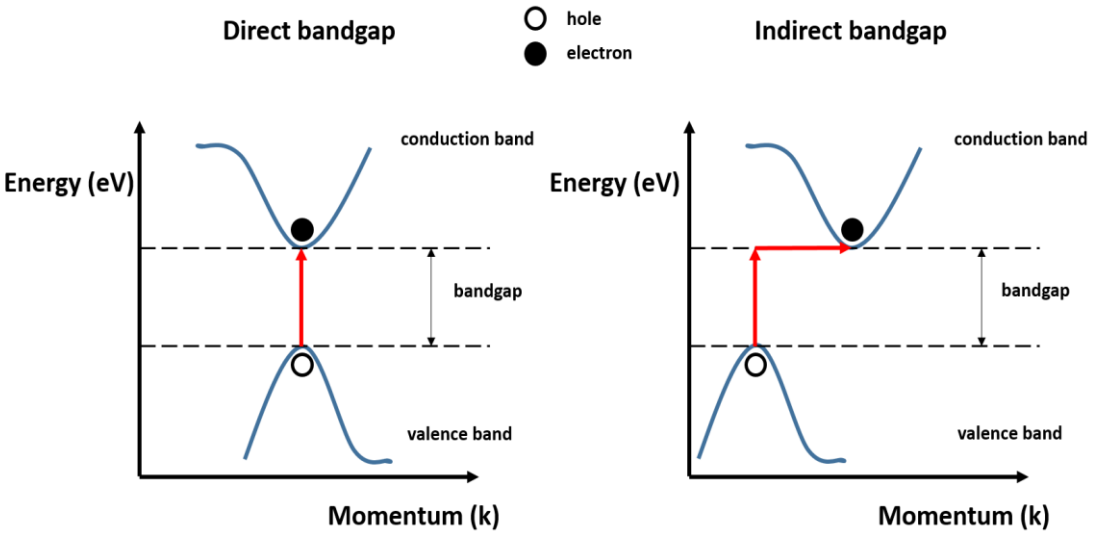

Figure 2.1: Schematics of energy band diagrams showing electron transition for direct and indirect bandgaps material.

Temperature has a significant effect on the energy bands distribution and the bandgap of the material. As the temperature increases, lower energy photons are able to participate in the excitation of electrons from the valence band to the conduction band and the absorption coefficient increases. The bandgap of crystalline silicon at 300 K is 1.1242 eV, which indicates the minimum energy of the

absorbed photons for contribution to electron-hole pair creation [8]. Considering Equation (2.3) below which relates the wavelength of the photon to its energy, the absorption edge for crystalline silicon can be calculated as 1103 nm, after which minimal or no absorption occurs. Therefore, the upper limit for the wavelength range of interest when optically characterising silicon materials is typically chosen as 1100 nm.

$$E_g = h f = \frac{h c}{\lambda} \tag{2.3}$$

- $\boldsymbol{c}$ is the speed of light in vacuum (m/sec)
- $\boldsymbol{f}$ is the frequency (Hz)
- $\boldsymbol{\lambda}$ is the incident wavelength (m)
- $\boldsymbol{E_g}$ is the bandgap (J).

2.1.2 Absorption coefficient

By considering the densities of the initial and final states of the excited electron in the valence band and in the conduction band, respectively, the ***absorption coefficient*** $\boldsymbol{\alpha}$ becomes proportional to both the product of these densities, as well as the number of phonons available with energy E_{phonon}, given by the Bose-Einstein distribution function [54]. As such, the absorption coefficient depends on the energy of the absorbed photon and can be expressed as:

$$\alpha\,(hf) = \frac{A\,(hf - E_g - E_{phonon})^2}{1 - e^{\frac{-E_{phonon}}{kT}}} \tag{2.4}$$

- $\boldsymbol{A}$ is constant ($3.2 * 10^2$ cm^{-1} eV^{-2}) [55]
- $\boldsymbol{f}$ is the frequency (Hz)
- $\boldsymbol{\alpha}$ is the absorption coefficient (cm^{-1})
- $\boldsymbol{E_g}$ is the bandgap (eV)
- $\boldsymbol{E_{phonon}}$ is the phonon energy (eV)
- $\boldsymbol{k}$ is Boltzmann's constant (J/K)
- $\boldsymbol{T}$ is the temperature (K)
- $\boldsymbol{h}$ is Planck's constant (J sec).

The absorption coefficient is the most important material parameter from an optical perspective for the design of highly efficient solar cells. The absorption coefficient of silicon at 300 K is shown in Figure 2.2. (blue trace) as a function of the

incoming wavelength. At short wavelengths (E > 3.4 eV), silicon is a very strong absorber due to the high energy of the incoming photons that are capable of exciting an electron from the valence band to the conduction band without changes in momentum and allow a direct transition. As the wavelength increases, the absorption coefficient becomes significantly smaller, manifested as a tail, due to the low energy photons that are not able to allow the direct absorption anymore. As such, one or more phonon emissions will occur in order to compensate for the required change in momentum. Furthermore, as the photon energy becomes smaller than the bandgap energy, the absorption coefficient of silicon becomes zero. The inverse of the absorption coefficient is the ***absorption depth***, which is indicative of the depth inside the material at which photons of different wavelengths are absorbed. The Beer-Lambert decay law [56], shown in Equation (2.5), describes the attenuation of light intensity with depth as it propagates inside a material. By considering a set wavelength for which the depth becomes the absorption depth and the exponential becomes e^{-1}, it follows that the absorption depth refers to the depth inside the material at which approximately 63% of the incident photons of that set wavelength are absorbed.

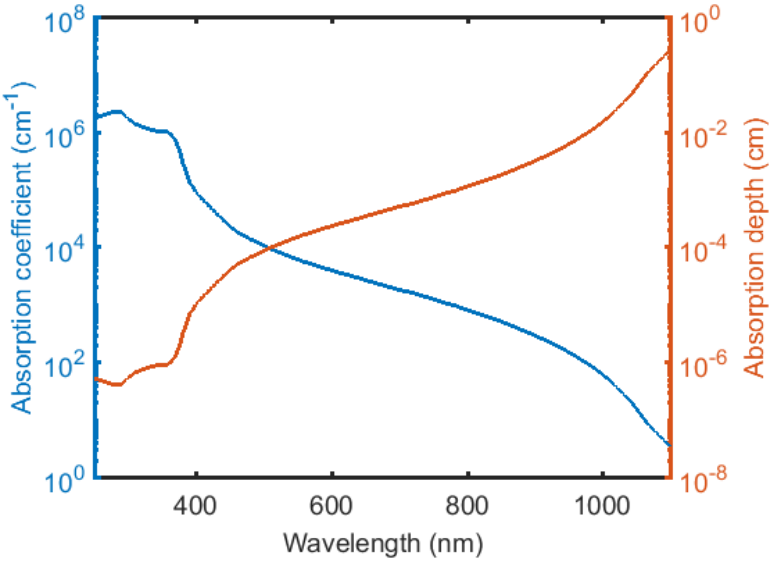

Figure 2.2: Absorption coefficient (blue trace) and absorption depth (red trace) of crystalline silicon at 300 K for wavelengths 300-1100 nm.

$$I(x, \lambda) = I_0(\lambda)\, e^{-\alpha(\lambda)\, x} \quad (2.5)$$

- ***x*** is the depth inside the material (cm)
- ***$I_0(\lambda)$*** is the initial intensity of light incident on the material
- ***λ*** is the wavelength
- ***$I(x, \lambda)$*** is the decayed intensity at depth x into the material.

Short wavelength photons are absorbed very close to the surface of the silicon substrate (within first 10 nm for wavelengths below 380 nm), while longer wavelength photons have to travel tens or even hundreds of microns in order to be absorbed. As such, silicon is a poorly absorbing material that requires large optical pathlengths for adequate broadband absorption.

2.1.3 Refractive index and surface reflectance

The refractive index is a vital optical property for the design of antireflective coatings and minimisation of optical losses at the silicon device level. It is used to describe the propagation of a wave, such as light, inside a medium or the reflectance and transmittance at a material interface. The refractive index consists of a real part *n* and an imaginary part *k*, both of which are dependent on the incoming wavelength. Figure 2.3 shows *n* and *k* for crystalline silicon at 300 K in the 300-1100 nm wavelength range [57]. The refractive index of silicon is complex and given by $\hat{n} = n - i\,k$, where *i* is $\sqrt{-1}$. *k* is called the extinction coefficient and describes the attenuation of light inside a propagating medium. As such, it is closely related to the absorption coefficient as in Equation (2.6) [54].

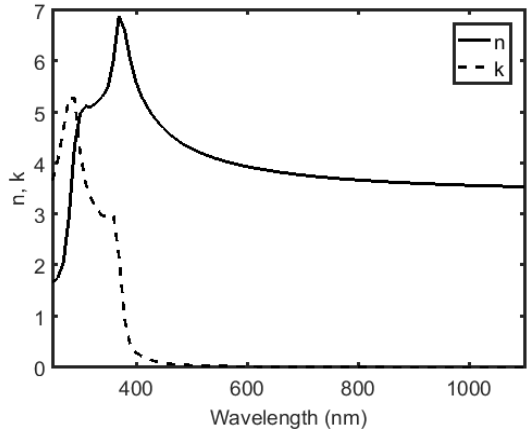

Figure 2.3: Real and imaginary parts of the crystalline silicon refractive index at 300 K.

$$\alpha(\lambda) = \frac{4\pi k(\lambda)}{\lambda} \tag{2.6}$$

- $\boldsymbol{\lambda}$ is the wavelength (cm)
- $\boldsymbol{\alpha(\lambda)}$ is the absorption coefficient (cm^{-1})
- $\boldsymbol{k(\lambda)}$ is the extinction coefficient

Fresnel's law can be used calculate the ***reflectance, R,*** of the light at an interface created by two materials, based on the refractive indices of the materials, as in Equation (2.7) [58]. Figure 2.4 shows the wavelength dependent surface reflectance of a silicon substrate surrounded by air (blue trace) and by ethylene-vinyl acetate (EVA - red trace), a typical encapsulant in PV. The surface reflectance of silicon is very large for the entire spectrum, with values above 30 % and achieving maximum values in the very short wavelength range < 400 nm, due to the peaks inherited by the *n* and *k* values in that region. The average reflectance across the wavelength range from 300 nm to 1100 nm is 35.6 % when the silicon substrate is surrounded by air and decreases to 20 % when air is replaced by EVA. This is due to the larger refractive index values of EVA when compared to air, which allows for a smaller transition between the density of silicon and that of EVA.

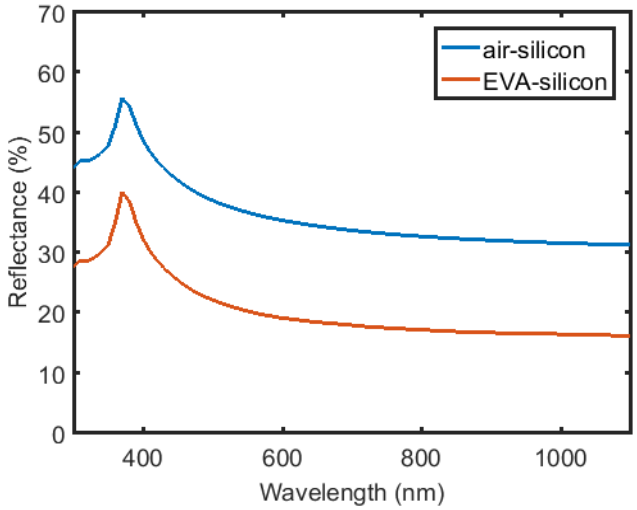

Figure 2.4: Reflectance at air-silicon interface (blue trace) and EVA-silicon interface (red trace) under normal incidence.

$$R = r^2 = \left|\frac{\hat{n}_2 - \hat{n}_1}{\hat{n}_2 + \hat{n}_1}\right|^2 \quad (2.7)$$

$\hat{n}_1$ and $\hat{n}_2$ are the complex refractive indices of the originating and destination mediums, respectively.

The refractive index is also important when studying the refraction at an interface or multiple reflections inside a thin film. As such, Snell's law in Equation (2.8) [58] is used to describe the change in direction of propagation of light from one medium into another medium as a function of the angle of incidence. Figure 2.5 is a sketch of light originating from air incident at an angle on a silicon substrate and the change in the refracted angle inside the silicon material. If the second medium has a higher refractive index, the propagating angle inside that medium will be smaller than the angle of incidence.

$$n_1 \sin\theta_1 = n_2 \sin\theta_2 \Rightarrow \theta_2 = \sin^{-1}\left(\frac{n_1}{n_2}\sin\theta_2\right) \quad (2.8)$$

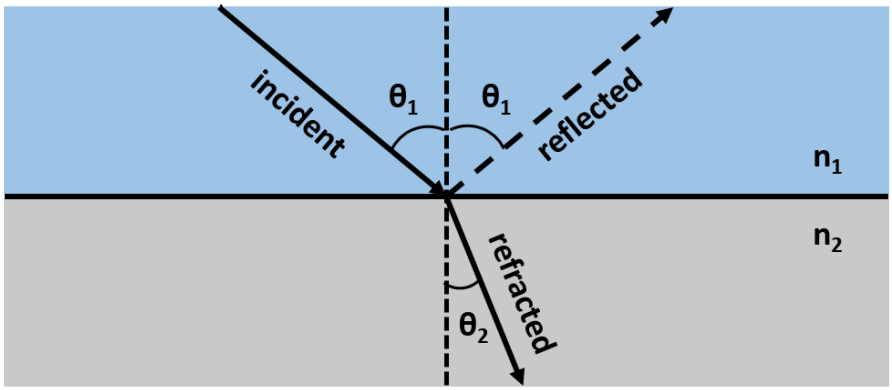

Figure 2.5: Refraction at a material interface showing change in angle of propagation.

2.1.4 Absorption and generation rate

Including all the above and considering no energy is lost upon travelling through a silicon substrate and being transmitted, the absorption for a fixed thickness of

planar silicon can be calculated under AM 1.5G photon flux, N_0, when light is normally incident on the material. Figure 2.6 a) shows the ***absorption*** of a planar silicon substrate of various thicknesses in the long wavelength region, indicating that larger amounts of material are necessary for effective absorption of low energy incoming photons. The model here includes the broadband surface reflection for an air-silicon interface, i.e. N_0 photons are incident on the semiconductor and N_0R are reflected away at the air-semiconductor interface, while transmittance is assumed to be 0. Even for silicon substrate thicknesses of above 200 μm, only a small portion of low energy photons incident on the material is absorbed compared to the middle wavelength region. As such, for a photon wavelength of 1000 nm, a 50 μm thick substrate absorbs only 19 % of the photons, while an increase to 250 μm in the silicon material thickness would yield 58 % absorption.

The ***generation rate G (λ, x)*** for a fixed thickness silicon substrate can be calculated by differentiating Eq. (2.5) with respect to depth *x* for each wavelength [54]. As such, it becomes dependent on the incident photon flux, which is the number of photons incident per area per second, which is in turn attenuated by the absorption inside the material. Equation (2.9) shows the generation rate *G (x)* as a function of depth for a 250 μm thick silicon substrate and the resulting generation rate is plotted in Figure 2.6 b). In this model, it was assumed that N_0 photons are incident on the silicon material according to AM 1.5G spectrum, $R\ N_0$ photons are reflected at the air-silicon interface and no back reflections or other losses occur. The total generation rate was calculated by integration over the wavelength spectrum in the 300-1100 nm range. The generation near the surface of the material is much larger than the generation deeper inside the bulk, due to a significant proportion of photons being absorbed in this region. Ideally, the collecting p-n junction of the device would be situated close to this surface. However, the collection efficiency of the junction and separation of charge carriers have to be carefully engineered so that the carrier collection is maximised before the pair recombines [54, 58].

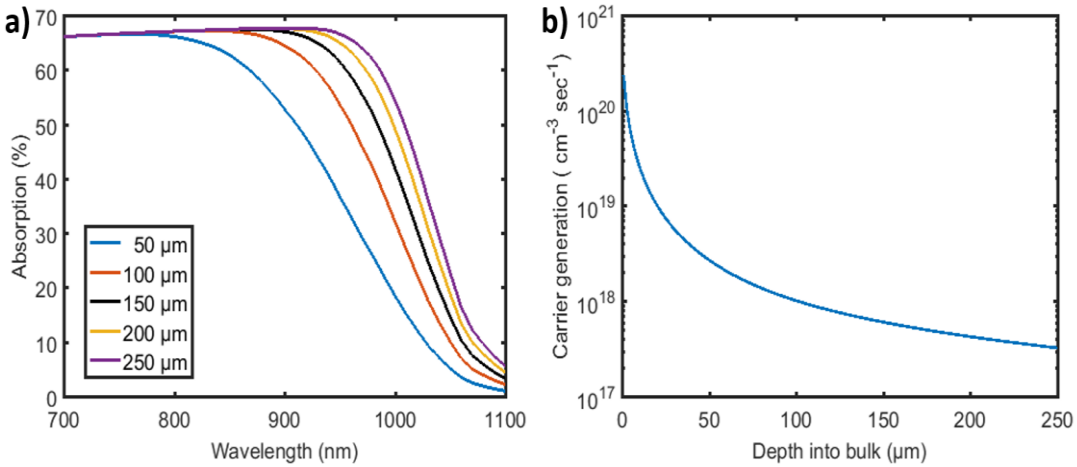

Figure 2.6: a) Absorption of light normally incident on silicon substrate of various thicknesses; b) Generation rate for a 250 µm silicon substrate in logarithmic scale.

$$G(\lambda, x) = \frac{d\,I(\lambda, x)}{d\,x} = \alpha(\lambda)\, N_0(\lambda)\, e^{-\alpha(\lambda)\, x} \tag{2.9}$$

- λ is the wavelength (m)
- N_0 is the incident photon flux (number of photons/m^2 sec)
- $G(\lambda, x)$ is the generation rate (m^{-3}/sec)
- $I(\lambda, x)$ is the intensity of the light
- $\alpha(\lambda)$ is the absorption coefficient (m^{-1})
- $N_0(\lambda)$ is the incident photon flux (number of photons/m^2 sec)
- x is the depth (m).

2.2 Sunlight

The Sun is the most important source of energy available for life on Earth. A multitude of processes and ecosystems are highly dependent on the sunlight, as well as various physical and chemical phenomena. Photovoltaics provide the means of harvesting this massive amount of energy and converting it into electrical power in a sustainable manner, as an alternative to the more polluting fossil fuels. As the Sun is a sphere of extremely hot plasma, it can be thought of as a blackbody radiator, which absorbs all incident radiation, but it is also able to emit. The surface of the Sun, called the photosphere, has a temperature of roughly 5800 K [9]. By using Planck's law and Stefan-Boltzmann's law [59], the power density H leaving Sun's

surface can be calculated as 64164532.3 W/m^2. Before reaching Earth's surface, the sunlight travels approximately 1.5 x 10^8 km or 8.5 minutes and is subjected to absorption and refraction by the atmosphere. As such, a significantly lower power density will be incident on the Earth's surface.

The irradiance spectra of sunlight used in solar cell design in known as the AM1.5G spectrum [60]. The Air Mass represents the length that sunlight travels through the Earth atmosphere as compared to the length when normally incident on Earth's surface (zenith) using a cosine factor. As such, AM1.5G measurements are taken for an incident angle of 48.2°, which represents a particular latitude on Earth that passes through countries leading development and deployment of PV [60]. The solar irradiance spectrum is shown in Figure 2.7 a), where the largest irradiance lies in the visible wavelength range 400-700 nm, fundamental for life on Earth, but also for the design of photovoltaic devices. The corresponding photon flux, which quantifies the number of photons incident per unit area every second, is derived from this spectrum as in Equation (2.10) and is shown in Figure 2.7 b).

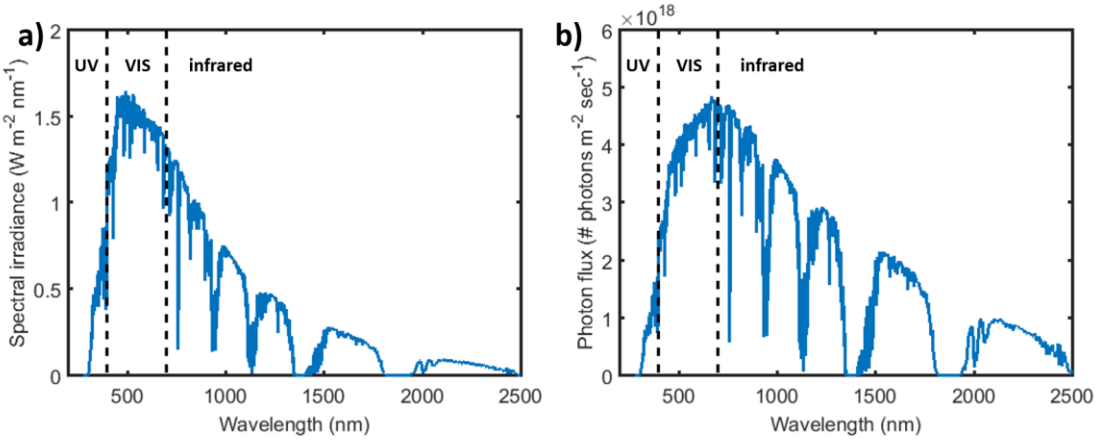

Figure 2.7: AM1.5G spectrum plotted as a) spectral irradiance and b) photon flux.

$$H(\lambda) = \Phi(\lambda)\frac{h\,c}{\lambda} \tag{2.10}$$

- $\boldsymbol{\lambda}$ is the wavelength (m)
- $\boldsymbol{H(\lambda)}$ is the incident power density (W/m^2)
- $\boldsymbol{\Phi(\lambda)}$ is the incident photon flux (number of photons/m^2 sec)
- $\boldsymbol{h}$ is Planck's constant (J sec)
- $\boldsymbol{c}$ is speed of light in vacuum (m/sec)

As such, it is clear that there is a need of broadband harvesting of solar energy and that the substrate of photovoltaics devices would ideally be an absorbing material capable of making use of the large number of incident photons on Earth's surface present in this wavelength region. Using Equation (2.3), the photon energy corresponding to the visible spectrum would lie in the range 1.8 – 3.1 eV and thus require a substrate material with a lower bandgap for optimal absorption of light and subsequent generation of electron-hole pairs. The bandgap of 1.1 eV of the Si material proves to be an excellent choice for light absorption in the wavelength range of 300 nm -1100 nm.

The AM 1.5 global spectrum helps quantify the optical performance of a photovoltaic device in relation to the photon flux in the wavelength range of interest. A more comprehensive figure of merit regarding the surface reflectance of a silicon solar cell is the weighted average reflectance, which considers the amount of photons incident on Earth's surface, distributed over then entire wavelength range [60-61]. Therefore, the design of antireflective coatings or textures can be targeted more towards the visible spectrum, where the largest power of sunlight is present, and compared using a more relevant metric for PV applications. The weighted average reflectance (WAR) is calculated as in Equation (2.11).

$$WAR = \frac{\int_{\lambda_{min}}^{\lambda_{max}} \Phi(\lambda)\, R(\lambda)\, d\lambda}{\int_{\lambda_{min}}^{\lambda_{max}} \Phi(\lambda)\, d\lambda} \tag{2.11}$$

- $\boldsymbol{\lambda_{min,max}}$ are the lower and upper limits of the wavelength range (nm)
- $\boldsymbol{R(\lambda)}$ is the surface reflectance (%)
- $\boldsymbol{\Phi(\lambda)}$ is the AM1.5G photon flux (no. of photons/ m^2 sec)

2.3 Thin antireflective coatings

Due to the large refractive index of silicon, a large fraction of incident photons are reflected at the air-silicon interface and thus are lost without being absorbed and contributing to the photocurrent of the photovoltaic device (see Figure 2.4). It is of primary concern to minimise the top surface reflectance of silicon and to minimise

these optical losses for power conversion efficiency enhancements. As such, a dielectric on top of the silicon substrate may act as an antireflective coating if it is carefully engineered and meets certain optical criteria. The presence of this dielectric material sandwiched in-between the air superstrate and the silicon substrate effectively replaces the air-silicon interface with two new interfaces, namely air-dielectric and dielectric-silicon. Therefore, the light incident on the semiconductor stack undergoes both reflections inside the thin films and refractions and optimisation of the refractive index and the thickness of the dielectric may reduce surface reflectance by means of destructive interference [61].

For this to happen, the reflected waves at the silicon-dielectric interface and dielectric-air interfaces, respectively, have to be out of phase by 180° so that they destructively interfere, cancelling each other and ideally completely supressing the overall reflectance [63]. A schematic of this mechanism is shown in Figure 2.8. There are two important material parameters that need to be optimised to ensure destructive interference at these interfaces: the thickness of the dielectric coating and its refractive index. A single layer antireflective coating is targeted to a specific wavelength, where the reflectance will be minimised. To find the optimal thickness of the coating, one has to consider the distance the photons will travel inside the material before reaching the second interface. Equation (2.12) relates the thickness of the coating with its refractive index and the condition of destructive interference.

$$2\, n_1\, d \cos\varphi = \left(m - \frac{1}{2}\right) \lambda_0 \tag{2.12}$$

- $\boldsymbol{\lambda_0}$ is the targeted wavelength (nm)
- $\boldsymbol{n_1}$ is the antireflective coating refractive index at λ_0
- $\boldsymbol{d}$ is the thickness of the coating (nm)
- $\boldsymbol{m > 0}$ is an integer
- $\boldsymbol{\varphi}$ is the angle of incidence (°).

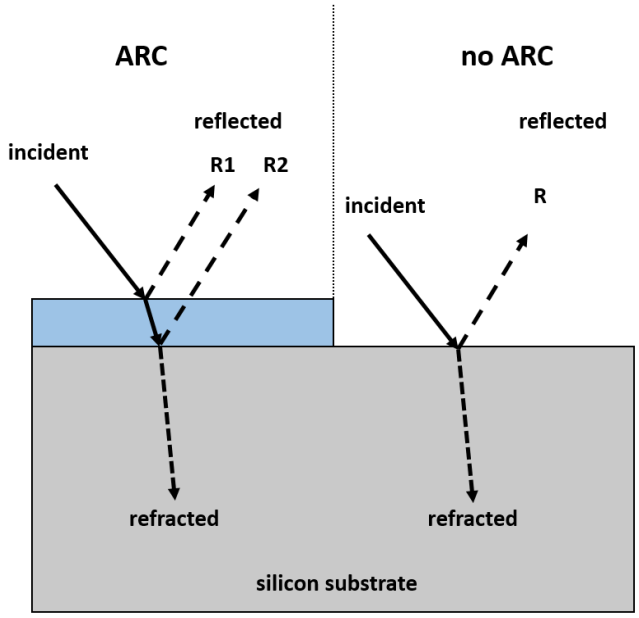

Figure 2.8: Reflection and refraction with and without an antireflective coating.

The refractive index of the material is extremely important for the optimal design of antireflective coatings and must be between the refractive index of the superstrate and that of the substrate for destructive interference to occur. Otherwise, the reflected waves will constructively interfere and create a local maximum in the spectrum. An ideal antireflective coating will have the refractive index equal to the geometric mean of those of the superstrate and the substrate, as in Equation (2.13). However, in reality, such materials are hard to come by and may further be difficult to synthesize and deposit on top of the substrate. For silicon, the material closest to the refractive index dictated by Equation (2.4) is stoichiometry-tuned silicon nitride (SiN_x), which is currently used in the PV industry for antireflective purpose, as well as the electrical passivation of the silicon surface [2]. Another advantage of this optimised material is its low extinction coefficients, which prevents large absorption inside the layer [60]. SiN_x can have a range of optical properties depending on the stoichiometry of the film [62], resulting in either silicon-rich thin films that are highly absorbing, or transparent films (nitride-rich) that are suitable for such antireflective applications.

$$n_{ideal} = \sqrt{n_0 n_2} \tag{2.13}$$

- n_{ideal} is the optimum refractive index of the coating at λ_0
- n_0 is the refractive index of the surrounding medium at λ_0
- n_2 is the refractive index of the substrate at λ_0

By considering the reflectivity at each interface, the total surface reflectance can be calculated across the entire spectrum. Figure 2.9 shows the surface reflectance for three materials commonly deposited on top of the silicon substrate for PV applications [61-62, 65-67], targeting a wavelength of 600 nm (around the peak in the AM1.5G spectrum).

In all the cases, the reflectance at this wavelength has been drastically reduced compared to the bare silicon substrate, yielding values below 10% for all of these materials with optimal thickness. In most cases, the dielectric coating has the benefit of also electrically passivating the disruptive silicon surface, which heavily promotes surface recombination and the subsequent loss of useful charge-carriers. Table 2.1 summarises the optical properties arising from the coating of the silicon substrate with the dielectric materials shown in Figure 2.9. All of the coatings were tailored so that the minimum of the reflectance spectrum is situated at λ_0 = 600 nm. It can be observed that the closer the refractive index of the coating material is to the ideal value calculated using Equation. (2.13) (for air and silicon, n_{ideal} = 2), the lower the reflectance value at λ_0.

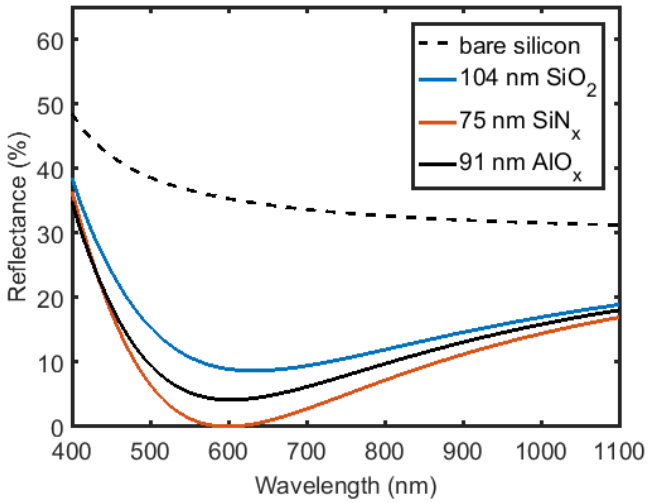

Figure 2.9: Surface reflectance for various materials employed on the silicon substrate, calculated at normal incidence and optimised for a target wavelength λ_0 = 600 nm.

Table 2.1: Summary of optical properties of silicon with various single-layer antireflective coatings optimised for a target wavelength λ_0 = 600 nm.

Material	Thickness (nm)	n at λ_0 = 600 nm	R at λ_0 = 600 nm (%)	WAR (%)
Bare Silicon	-	3.94 [65]	35.4	35.5
Silicon Nitride	75	1.99 [61-62]	0.04	8
Silicon Dioxide	104	1.45 [65]	8.95	14.3
Aluminium Oxide	91	1.64 [66]	4.17	10.7

The single layer antireflective coating has the disadvantage of minimising surface reflectance for a single wavelength [64]. As such, a stack comprising of multiple layers of various materials can be engineered to target more than one wavelength in the entire spectrum and yield lower broadband weighted average reflectance. A

gradient in the refractive index is necessary for destructive interference to occur at all stages, with gradually increasing values from the refractive index of the superstrate to that of the substrate. However, the increase in cost and deposition time arising from such an approach may outweigh the optical gain. In general, there is a trade-off between the overall deposition cost and the number of layers that are employed on top of a semiconductor substrate. Thus, antireflective stacks comprising of more than two materials are rare and instead a texturing approach can be employed for further broadband reduction of the surface reflectance.

2.4 Micron-scale random pyramids

Textured surfaces can help further reduce the optical losses associated with silicon. If the substrate is rough, incident light may undergo reflections on an inclined structure and be redirected onto an adjacent structure at an angle, rather than being normally incident on a flat surface and reflected away [68]. Multiple reflections onto a structure directly translate into reduced reflectance, due to the intensity of the light being reduced at every bounce, as some of it gets transmitted into the substrate and absorbed. Moreover, using this mechanism, light that is coupled into the substrate can be obliquely refracted by the structural array, thus travelling a longer path inside the material and having a larger probability of being absorbed [68-69], as shown in Figure 2.10. Based on this, fabrication processes have been developed over the last decades to texture the silicon surface and produce randomly distributed pyramidal arrays that can improve the optics of a solar cell [70]. Nowadays, most commercial single-crystal silicon PV devices employ such a pyramidal textured surface, that can efficiently suppress reflectance for a range of incident wavelengths when used in combination with an ARC [2].

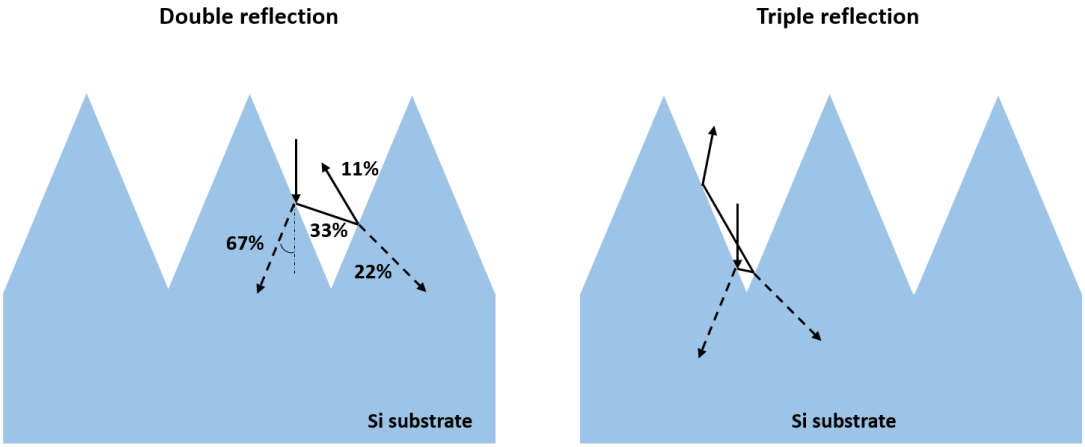

Figure 2.10: Schematic of double and triple reflections for an upright pyramidal array.

Alkaline etching processes originate from the faster etching {100} planes compared to {111} planes, resulting in a dihedral base angle of 54.7° [71]. The resulting texture is comprised of a dense array of square-based upright pyramids that have a heterogeneous distribution on the silicon surface. More details on the etching mechanism are provided in Chapter 7.2. Figure 2.11 shows the simulated surface reflectance (using PVLighthouse's OPAL 2 tool [72]) of various pyramidal textures on top of a 180 µm thick silicon substrate. The presence of these micron scale structures translates into reduced top surface reflectance of 10%-12% for the entire wavelength range (blue trace), value that can be further lowered if an ARC is used, such as 80 nm of PECVD SiNx (black trace) [71-76]. In combination with a photolithography masking step, an ordered array of inverted pyramids can be fabricated, whereby a higher proportion of incident photons experience triple reflections [24, 77]. The overall surface reflectance is reduced accordingly (orange trace). Furthermore, when a back reflection is used, a larger proportion of back-reflected light can undergo total internal reflection and be further redistributed across the bulk. The Al-BSF method provides the means of ensuring such back reflections, with R = 60%. Further advancements in the PERL cell, where a rear Aluminium material is used in conjunction with a passivating silicon dioxide layer, can increase this value to 95% [25-26].

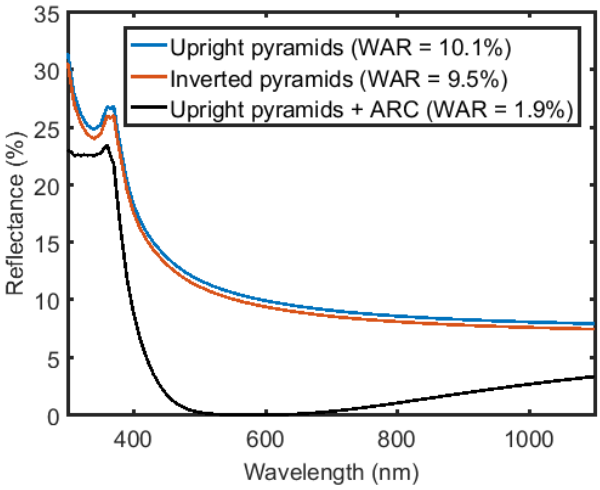

Figure 2.11: Surface reflectance of various pyramidal schemes on a silicon substrate. Simulations of data carried out using OPAL 2 quick-solver [72].

2.5 Isotextured multicrystalline silicon

A big portion of commercially available silicon solar cells with lower efficiency is comprised of devices with a multicrystalline silicon substrate [2]. This type of silicon material is of a lower quality than the single crystal silicon material, but cheaper to fabricate and process. Due to the grains in the material having orientation in all direction, not only the [100] direction, the previously mentioned alkaline etching is of limited use for such material. Instead, an acidic isotropic etching, known as isotexturing, is commonly use to take advantage of the various orientations of the grain boundaries and texture the surface with randomly oriented microstructures that can reduce surface reflectance. Usually, a solution comprising of nitric acid (HNO_3), hydrofluoric acid (HF) and acetic acid (CH_3COOH) is employed in such an etching process, resulting in 'bowl-like' spherical caps in the micron size [78]. The depth and opening of such structures is dependent on the exact etching conditions and recipe employed, with a high HNO_3:HF concentration ratio leading to deeper

etching of the silicon substrate. Figure 2.12 shows a schematic of such a microstructure on top of a silicon material and identifies the depth *d* of the structure, as well as the characteristic angle ω. In general, this angle decreases with etching depth inside the silicon material, with high characteristic angles found for flatter surfaces [79].

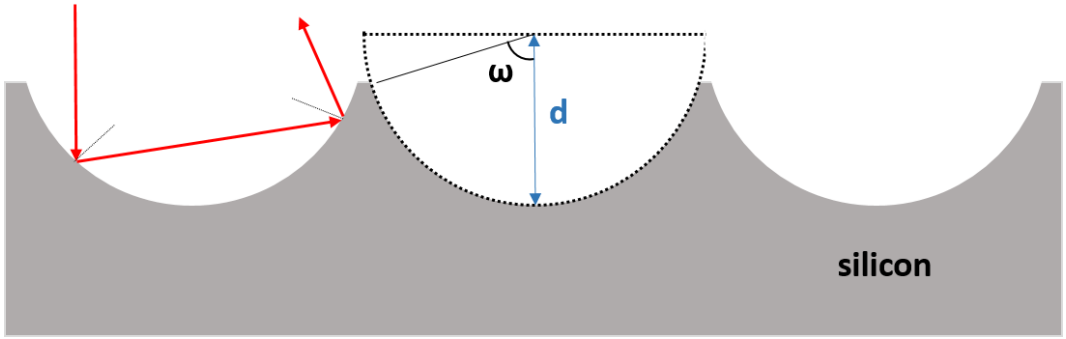

Figure 2.12: Schematic of acidic etched spherical caps on top of multicrystalline silicon substrate, showing the depth *d* and the characteristic angle ω, as well as the reflection of normally incident light.

Although the resulting textured surface rarely exhibits such perfectly spherical structures, optical ray-tracing studies reported by Li et al. (2012) [80] and Baker-finch et al. (2012) [79] confirm the validity of using this circular geometry for optical simulations. To this end, optically simulated surface reflectance is reproduced within 1% accuracy of the measured specimens for a range of angles ω. Moreover, the light-trapping properties of these isotextures can be approximated using such spherical models, with 1-2% poorer light-trapping achieved on a simulated device compared to the upright random pyramids [81]. The simulated surface reflectance of an isotextured array using PVLighthouse's OPAL 2 [72] is shown in Figure 2.13 as a blue trace, which is far greater than the surface reflectance of upright alkaline-etched random pyramids (black trace), especially without an antireflective coating

applied on the surface. Similar to the pyramids case, the presence of the spherical caps ensures multiple surface bounces of the incident light. However, the resulting surface reflectance is larger due to all of the light undergoing at most two reflections with these microstructures. In contrast, upright pyramids texture allows a significant portion of light to undergo three or more reflections on the structure's facets. As such, the surface reflectance remains larger than 20% for all of the wavelengths considered when using an acidic etched texture. Nevertheless, the acidic etching represents a cheap and scalable method of texturing multicrystalline solar cells, contributing to power conversion efficiencies as large as 22% for commercial multicrystalline devices [2].

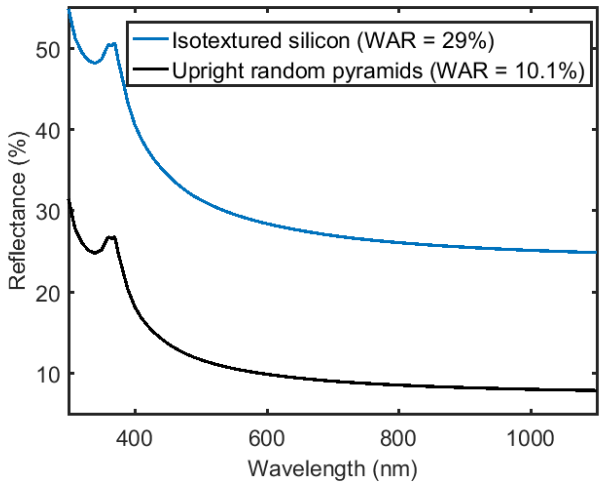

Figure 2.13: Surface reflectance of acidic etch microstructures (blue trace) and upright random pyramids (black trace) on a silicon substrate. Simulations of data carried out using OPAL 2 quick-solver [72].

2.6 Conclusions

Silicon material is an indirect bandgap semiconductor which allows excellent absorption for short wavelength (high-energy photons), but significantly poorer for

wavelengths above 400 nm and above the bandgap of the material of 1.1 eV. Large refractive index values associated with this semiconductor material lead to unreasonable large surface reflectance at air-silicon interface or encapsulant-silicon interface across the entire spectrum. As such, these optical losses have to be effectively addressed for the realisation of high-efficiency photovoltaic devices on silicon substrates. To this end, ultra-thin single and double layers antireflective coatings (ARC) can be employed on top of the substrate to supress reflectance for a target wavelength, usually chosen in the middle of the visible spectrum. However, the reflectance remains large in other parts of the spectrum and hinders photogeneration at device level. Texturing the silicon surface in alkaline solution, such as KOH, results in a randomised array of upright well-defined pyramids, which, in conjunction with thin film ARC, translates into low surface reflectance and addresses concerns related to poor absorption of longer wavelength photons via light-trapping. For multicrystalline silicon, a similar approach is employed using acidic etching to form a spherical cap texture, albeit with slightly poorer antireflective and light-trapping properties than the pyramids. However, the lack of a true broadband reduced response is still pronounced in today's commercial PV devices and alternative texturing schemes in the nanoscale, as introduced in the following chapter, are needed to overcome these limitations and further boost the conversion efficiency of the solar cell.

Chapter 3

Nanotextured Silicon

This chapter aims to serve as an up-to-date review of the most promising nano-texturing methods that prove to be strong candidates for industrial integration and realisation of record high efficiency silicon solar devices. Many fabrication methods of nanostructured silicon have been explored over the last decades, both wet and dry processing, including ordered structures using lithography patterning, all leading to impressive optical results aiming to overcome the limitation in current devices. Many different morphologies and thicknesses have been reported, possessing both advantages and disadvantages for optimum operation at device level. Whenever possible, the results are supported by reports of fabricated textured solar cells that highlight their growing potential. A special focus is given to the metal-assisted chemical etching (MACE) fabrication method that is used primarily for the realisation of low-reflective surfaces throughout this work, including details about the etching mechanism, as well as the role of various process parameters on the final product.

3.1 Biomimetic moth-eye arrays

Over the last two decades, substantial effort was dedicated to reducing top surface reflectance of silicon solar cell substrates by employing subwavelength structures. The technique of ***moth-eye arrays*** has its inspiration from the corneal nipple periodic array discovered in the 1960s [82-83] on various species of nocturnal moths and butterflies. It is assumed that the reduced glare and reflectance that the array exhibits helps the moths to camouflage during the night, while also improving transmittance of light into the eye, improving its sensitivity and thus the night vision.

Wilson (1982) [84] provided an insight into the theoretical mechanism of this structural array and fabricated corneal nipples from photoresist material on a glass substrate by interference fringes caused by the intersection of two laser beams. The superior optical properties of the subwavelength protuberances arise from the graded index effect, whereby a smooth transition from the refractive index of air to the refractive index of the substrate is created due to the tapered morphology of these features. With sufficiently small spacing between the nipples compared to the wavelength of incident light, diffractive effects can be avoided and the surface reflectance becomes virtually zero. In the study, the depth of the structures was controlled by the exposure time of the resist to the laser beam, with optimal conditions leading to measured specular reflectance below 1 % for the visible wavelength spectrum. It was reported that longer protuberances yield reduced surface reflectance and that these impressive optical properties were maintained for angles of incidence up to 40°, independent of polarisation.

Stavenga et al. (2006) [85] investigated the morphology of the corneal nipple arrays in 19 species of diurnal butterflies by means of scanning electron microscope (SEM), transmittance electron microscope (TEM) and atomic force microscope (AFM). It was reported that all these arrays present structure periodicity of approximately 200 nm, with various heights in the range 10 – 230 nm, depending on the species. By employing Bruggeman's effective medium approximation (EMA) and calculating a volume fill factor based on the volume ratio of the protuberance

and the surrounding air, using a thin film multilayer method, the group was able to replicate the measured reflectivity with good accuracy for a number of structure heights.

Later, Boden et al. (2008) [86] investigated the optical response arising from shape, height and periodicity variation in the nipple array. 1 mm^2 moth-eye samples were fabricated using electron beam lithography, with periodicities in the range 150-350 nm and heights in the range 150-500 nm. Reflectance probe measurements showed that local minima and maxima are produced in the spectrum, based on the features of the structures. It was concluded that as the periodicity increases, the local minima in the reflectance is shifted towards larger wavelengths. Rigorous coupled-wave analysis (RCWA) simulations were employed to simulate the optical effects of the moth-eye arrays, accounting for tapering with depth. This method was preferred over the effective medium approaches, because EMA does not predict variations in the optical response arising from periodicity variations.

Sun et al. (2008) [87] proposed a new scalable bottom-up fabrication method for these nanostructures consisting of spin-coated monolayer silicon colloidal crystals on the silicon substrate, which act as an etching mask for the subsequent RIE process. Due to vastly different etch rates, the exposed silicon is etched away, leaving vertical wall structures below the area covered by the silica spheres. These spheres are then removed in an *HF* solution. Using this method, the champion sample yielded measured specular reflectance below 2.5 % in the 300-800 nm wavelength range, with potential of further optimization based on the distribution and size of the silica spheres. RCWA and EMA simulations lead to good agreement between the simulated and experimental spectra in terms of absolute values, but not in terms of the peak wavelength positioning.

Boden et al. (2009) [88] extended the previous work and employed a combination of nano-imprint lithography and dry-etching RIE to fabricate moth-eye structures of 280 nm periodicity and 400 nm height. A further high temperature (> 1000° c) oxidation step for several minutes would confer a tapered profile, desirable for the refractive index transition. The best sample showed specular surface reflectance of below 10 % in the entire 400-1000 nm wavelength range, with a

predicted loss of 6.5 % in J_{sc} when simulated on top of a PERL cell, compared to an ideal zero-reflective broadband coating. Comparatively, the optimised SiN_x layer led to a predicted current loss of 8 %, while an optimised silicon dioxide ARC layer yielded a 13 % loss. Figure 3.1 shows the moth-eye array used in this work.

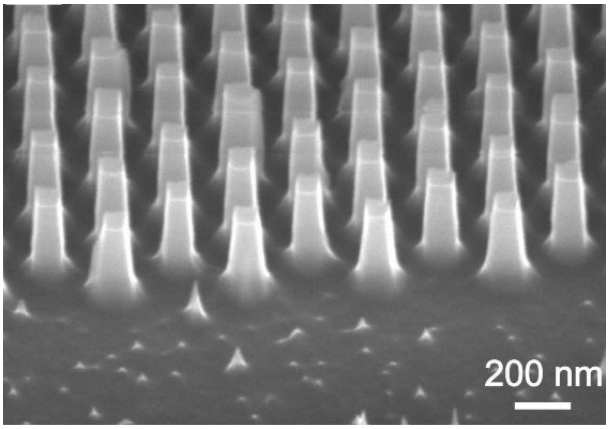

Figure 3.1: Dense silicon moth-eye arrays fabricated via nanoimprint lithography. Reproduced from [88].

Later, the optical properties of these nanostructures were thoroughly investigated by Asadollahbaik et al. (2013) [89] for a range of characterisation methods, including reflectance probe, integrating sphere and a custom-built angle-resolved reflectance setup. Two sets of moth-eye arrays were fabricated via nano-imprint lithography, one without an oxidation step, resulting in almost vertical sidewalls, and one including a 5-minute oxidation step, resulting in a tapered profile. The latter process translated into specular surface reflectance below 10 % for the entire wavelength spectrum and near-zero reflectance in the 550-650 nm range. Reflectance measurements at various angles of incidence were carried out for both p and s polarisation, showing that the good optical properties are maintained up to angles of 70° for the tapered structures. Moreover, inverse polarisation was observed for this array, where the reflectance measured under s polarisation would be lower than the reflectance of p polarisation for angles of incidence larger than 62°, unlike flat silicon. Variations in the optical profile arising from azimuth rotations were also studied, but no significant differences were reported, due to the symmetry of the structures along their long axis.

As an antireflective layer, biomimetic moth-eye arrays are a very promising technology for use in high-efficiency solar cells. However, the fabrication cost and tools involved, including RIE and lithography, remain to hinder the integration of these antireflective arrays into the PV industry and possesses concerns related to scalability.

3.2 Nanoscale inverted pyramids

Traditionally, inverted pyramids are more preferential to their upright counterparts due to the increased number of photons that experience a triple bounce at the array level, translating into reduced surface reflectance. As an example, lithography processes were employed to fabricate a periodic array of inverted pyramids for the record-high 25 % photoconversion efficiency reported by UNSW in the 1990s [24-25]. Moreover, this technique is very attractive to the PV community due to minimal increase of active surface area of just 70 % when compared to a flat semiconductor substrate, which can relax the requirements of surface passivation upon texturing and lead to higher power conversion efficiencies. As an active effort of the PV field, thinning of the semiconductor substrates is sought after for accelerating cost reduction at device level [2]. However, thin substrates of less than 70 μm are not compatible with traditional micro-scale pyramids, which can exceed heights of 10 μm. As such, smaller size pyramids are desirable as an antireflective layer on top of these devices.

Sivasubramanian et al. (2014) [90] fabricated nano-inverted pyramids (NIP) via maskless interference lithography for patterning in combination with an O_2 plasma dry etch. An optimised MgF_2/ZnS antireflective coating was deposited on top of the structure array, translating into surface reflectance below 2.5 % in the entire wavelength range for 700 nm wide nanopyramids. The group fabricated silicon solar cells with these nanostructures, showing a short-circuit current density of 16.06 mA/cm^2 and an efficiency of 6.73 %, a significant increase over the reference planar solar cells with J_{sc} = 9.43 mA/cm^2 and efficiency of 4.03 %.

Tang et al. (2017) [91] significantly advanced the understanding of NIP formation using a two-step MACE process to first create nanoporous silicon, which is then subjected to a nanostructure rebuilding high-temperature step consisting of H_2O_2 and commercial additives to create the pyramidal shape. The morphology of the NIP could be controlled by the concentration of the $AgNO_3$ used, resulting in widths ranging from 750 nm to 1100 nm for 0.25 mM – 0.75 mM molarities. The group calculated a surface area increase of 329%, 239% and 189% for silver nitrate concentrations of 0.25 mM, 0.5 mM and 0.75 mM, respectively, owing to the larger nanopores initially formed for increased molarities. Dihedral base angles of 54.7^0 were measured in all cases, corresponding to the angle formed between (100) and (111) Si planes, thus confirming the presence of pyramidal structures. The resulting hemispherical reflectance values were ranging from 8% to 10% in the entire 300-1000 nm wavelength range depending on silver ion concentration and the best texture led to similar absorption values when employed on top of a 50 μm c-Si substrate as compared to a traditional micron-textured 182 μm thick substrate.

Later [92], the group investigated the influence of MACE temperature on the morphology of the pyramidal array, showing that increased temperatures promote lateral pore formation and thus NIP with increased size. For temperatures of 25° C, the width of NIP was 768 nm, which increased to 1240 nm for 40° C and achieved a maximum of 1884 nm for 60° C. Subsequently, the hemispherical reflectance decreased with increased etching temperature, becoming as low as 8.9 % when averaged over the entire spectrum.

Zhang et al. [93] (2018) fabricated random upright pyramid solar cells, as well as NIP solar cells using a two-step MACE process, showing demonstrated power conversion efficiencies of 20.19 % for the nanotextured cell. The size of the NIP (500-1000 nm with heights of 350 nm) translated into an absolute gain of 2 mV in V_{OC} and 0.2 mA/cm^2 in J_{sc} over the micron-scale textured cell, with an average reflectivity of 9.2 %.

More recently, Huang et al. (2019) [94] fabricated NIP using a single-step MACE process to create nanopores, then a reshaping step consisting of $NaOH$ solution heated at 80° C for 2 minutes. The initial average reflectivity of 11.9 % was further

reduced to 3.94 % with the addition of an optimized SiO_2/SiN_x ARC stack and average lifetimes of 15 μs were measured on the texture. Simulations carried out on PERC cells with the nanotexture showed a short-circuit current of 10 A and open-circuit voltage of 0.669 V, translating into an efficiency of 22.1 %, which was 0.3 % larger than the simulated cell with micron-scale texturing.

As such, NIP structures are a suitable candidate to the development of ultra-thin c-Si photovoltaic devices, with MACE being a cheap and straightforward fabrication method. However, more optimisation of the final structure is required still so that higher gains can be achieved at device level.

3.3 Black silicon

3.3.1 Properties

Black silicon refers to any surface modification of the silicon substrate in the nanoscale regime, exhibiting a wide range of shapes, aspect ratios and thicknesses. The resulting nano-textured layer usually presents a very dense array of vertically aligned nanostructures that are randomly distributed onto the substrate. Over the past decades, black silicon (b-Si) has received special attention as an emerging material that can help improve various devices across a multitude of research fields, such as Li-ion batteries [95-96], Micro-Electro-Mechanical System (MEMS) [97-99], biosensors [99] and optoelectronics devices [46,100-101]. For optoelectronic applications, this is due to the optical properties this layer possesses, which makes it especially attractive for the silicon photovoltaics community, as detailed below:

- Antireflective effect, providing reduced broadband surface reflectance for the wavelength range relevant for PV applications, and thus enhanced broadband absorption
- Light-trapping material, with pronounced scattering distribution of both the reflected and refracted light incident on the b-Si layer
- Impurities gettering for silicon wafers [102]

Independent on the fabrication method, b-Si layers provide exceptionally reduced broadband reflectance when light is incident on a silicon substrate, even without the use of an antireflective coating. This is due to the multiple photons interactions that occur when light is incident on this nanotexture, such as guided modes and Fabry-Perot fringes along the length of the nanostructures [47]. Moreover, the feature size of b-Si, which is often comparable or below the incident wavelength, results in pronounced forward scattering of the light into the silicon bulk, leading to increased absorption when compared to an untextured surface. The b-Si layer can be thought of as a gradient index medium, which provides a smooth transition in refractive index, from superstrate (air) to substrate (Si) [47, 103]. The texture can effectively be replaced by a number of ultra-thin layers that provide a linear increase in refractive index as the light travels from air to the bulk material, which yields suppressed surface reflectivity for the entire wavelength range. Schematics for the refractive index variation for bare flat silicon surrounded by air (a), silicon covered with an antireflective coating (b) and the black silicon layer (c) are shown in Figure 3.2. Figure 3.2 d) shows the equivalent stack of ultrathin films that produce the same refractive index transition as b-Si and thus the same optical response.

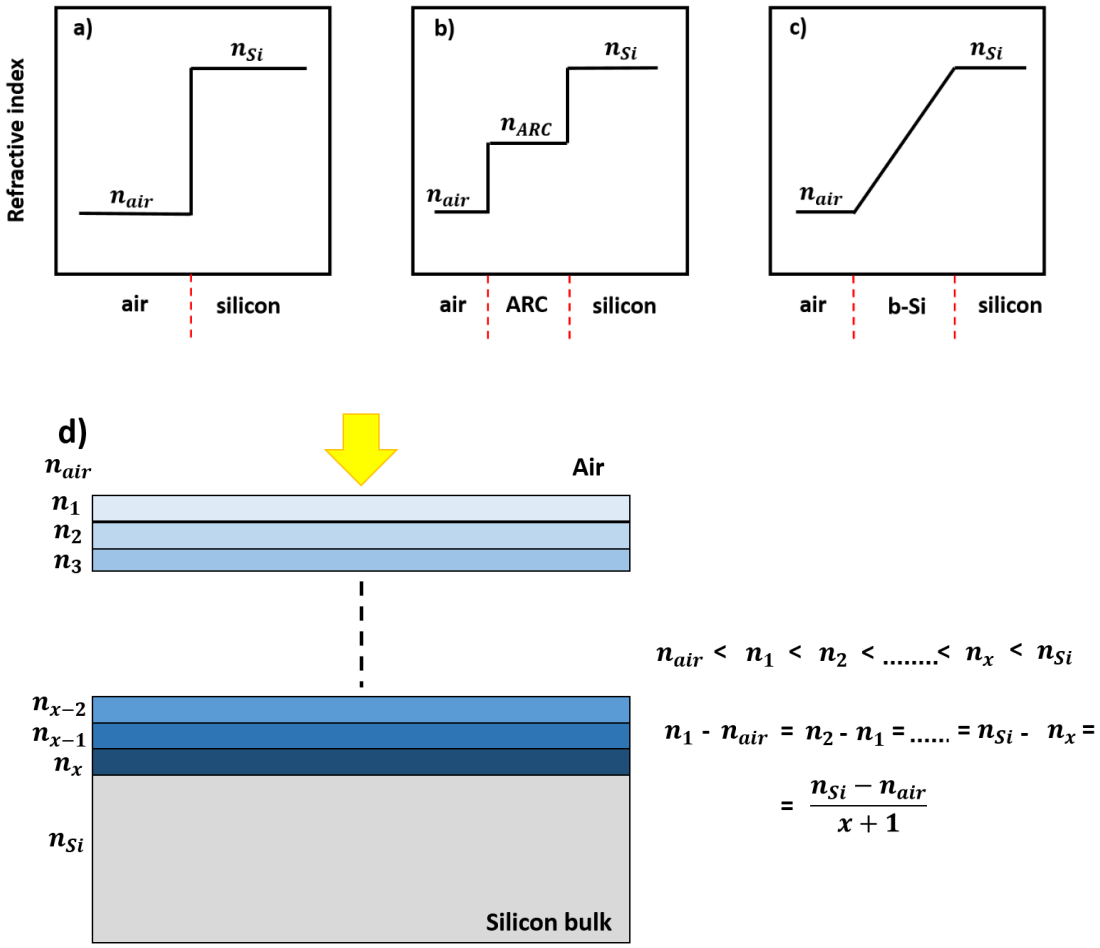

Figure 3.2: Refractive index transition for: a) bare Si; b) Si with ARC; c) b-Si; d) Equivalent stack to provide refractive index gradient. Note that the effective refractive index variation in b-Si is not necessary linear with distance, but will depend on the profile of the features.

Various studies have been conducted to optically simulate the antireflective effect of black silicon layers, mainly through means of effective medium approximations (EMA) based on Figure 3.2 d). As such, stacks of layers can replicate the effect of the black silicon texture, where each layer has an effective refractive index calculated using fill factors based on the mixture of air and silicon by employing Maxwell-Garnett theory, Bruggeman theory or Volume average theory [104-105]. Rahman et al. (2017) [105] replaced the black silicon layer with a single thin film of calculated refractive index using the above theories in an attempt to match the simulated data to the measured reflectivity of silicon nanowires. However, the degree of inaccuracy

proved to be large. The same work, along with Patchet et al. (2013) [106] employed a cut-back technique where the nanowires are first simulated using Finite-Difference Time-Domain (FDTD) that resolves Maxwell's equations to obtain transmittance and reflectance spectra at different depths into the nanotexture layer. Using Beer-Lambert's law, the absorption coefficient α, and thus the extinction coefficient k, of the nanowire array can then be calculated. Then, the refractive index n can be extracted from the simulated reflectance spectra by relation to k. These results provide a closer match to experiment than the standard effective medium techniques, but still fail to encompass the scattering response arising from neighbouring nanowires and redirection of light incident on black silicon textures. More recently, Fung et al. (2019) [107] used EMA in conjunction with FDTD to simulate the optical response from three types of texture, with various degrees of success. They identified a region where neither wave optics nor geometric optics are applicable and the simulated data using EMA becomes < 2 % accurate. However, in general, EMA fails to address the scattering effect of the nanotextures, which plays a vital role in the design and fabrication of high-efficiency silicon solar cells. FDTD and Rigorous Wave Couple Analysis (RWCA) remain as alternatives to accurately simulate light interaction with textures at the nanoscale, but at the cost of time and computational resources.

Apart from the excellent antireflective effect, black silicon layers drastically improve light-trapping inside the silicon substrate through scattering effects. This means that, unlike an ARC, normally incident light enters the silicon bulk at oblique angles and hence the optical pathlength is increased. This has important implications related to absorption of photons, as low-energy photons corresponding to large wavelengths can pass through tens of microns of silicon before being absorbed, according to Beer-Lambert decay law (see Chapter 2.1). By improving the optical pathlength of the photons travelling through the substrate, requirements for thick substrates can be relaxed, as more photons are effectively absorbed inside the device for same silicon thickness [2]. Alternatively, the bulk can be thinned down without sacrificing the output power of the solar cell, increasingly leading to cheaper photovoltaic devices and thus reduced price/watt. Garnett (2010) [108] carried out

transmission measurements on ordered silicon nanowire arrays on ultrathin silicon substrates and reported an optical pathlength enhancement factor of up to 73, depending on the nanowire geometry, effectively breaking Yablonovitch's limit of ~50 for silicon substrate when a perfect Lambertian scatterer is used in combination with a reflective back surface [109].

Moreover, reflected scattering has the potential of playing an important role when an encapsulated black silicon layer is considered, as in commercial photovoltaic cells. As such, backscattering occurring at large angles may be incident on the encapsulant layer at angles greater than the critical angles for that material. This satisfies the requirements for total internal reflection, where part of the reflected light from the nanowire array has a chance of being reflected back to the silicon bulk, effectively increasing the chances of photons to be absorbed and thus, the electrical output of the device [73]. Alternatively, new non-absorbing encapsulants can be engineered such that their refractive indices are sufficiently large to accommodate a high proportion of TIR at the Si/encapsulant interface, based on measured scattering profiles arising from black silicon layers.

In general, the main drawback of b-Si is its effect on the electrical performance of the device, mainly through means of surface recombination [47]. The nanotextured surface presents a large number of surface defects and a disruptive interface, owing to the large semiconductor surface area increase, which heavily promotes surface recombination of the generated minority carriers. While thicker b-Si layers are beneficial optically, they are detrimental electrically for this reason. Typically, there is a trade-off between the optical and electrical properties of the nanostructures, as shorter b-Si layers can be more easily passivated. The electrical passivation of the surface must be addressed properly so that, overall, the b-Si layer aids in a gain in the power conversion efficiency of the silicon solar cell compared to a planar or micro-structured silicon device.

3.3.2 Fabrication methods

3.3.2.1 Electrochemical etching of Si in HF solutions

Porous silicon (p-Si) is defined, based on the size of the pores, as microporous < 1 μm, mesoporous < 50 μm and macroporous > 50 μm. Electrochemical etching of Si substrates is based on the anodic dissolution of silicon material in HF solutions, using an applied bias such as current density or voltage. In 1958, Turner [110] successfully employed this method to electropolish a silicon wafer by producing a thin anode layer on its surface in diluted HF solution. It was reported that a sudden increase in the current density would remove this anodic layer from the Si surface, as it starts floating into the HF solutions and disintegrate as flakes, leaving behind a brown coloured surface. It was later revealed that the black and brown deposit was mostly silicon. At the time, it was thought that only p-type silicon can make use of the method, as n-type silicon would create an internal voltage barrier to prevent the process. This is due to the number of thermally generated holes being much smaller than for p-type silicon, thus requiring backside illumination to increase the flow of holes towards the front side of the wafer, typically kept in dark. Later, Lehmann (1990) [111] obtained macroporous Si on lightly-doped n-type wafers using a combination of surface patterning and backside strong illumination of 100 W from a tungsten lamp, creating high aspect ratio trenches and pores. The initial randomness of the p-Si layer can be controlled using standard lithography processes followed by alkaline etching. In this way, only selected areas can be etched by the HF solution. Later, Lehmann (1993) [112] found that the size of the pores fabricated on p-type silicon increases with doping concentration, while it decreases with doping concentration for n-type silicon. Furthermore, it was established that current densities above a critical value, J_{crit}, led to electropolishing of the Si wafer. This is due to the accumulation of holes at the electrode surface and the local depletion of *HF*, such that the dissolution becomes dependent on the mass-transfer rate and is found to be lower in the pits. In contrast, if the current density is below J_{crit}, the reverse is true: holes are locally depleted from the electrode surface and HF accumulates, resulting in pore growth due to local current density enhancement. If the current density is equal to J_{crit}, the system is under steady state conditions.

Moreover, by fluctuating the current density of the applied bias, various degrees in the porosity of the layer can be obtained, essentially introducing a porosity gradient and thus, an effective refractive index gradient, as previously discussed. From an optical point of view, this is an important result. Based on this, Striemer (2002) [113] alternated the current density in the range 0 – 100 mA/cm^2 over a short duration of 10 s, fabricating porous layers with a linearly increasing porosity gradient from 33% to 94%. The thickness of p-Si was 107 nm, resulting in reduced broadband surface reflectance of just 3.7% weighted over the solar spectrum. Similarly, Ariza-Flores et al. (2014) [114] fabricated a 243 nm thick multi-layer porous silicon ARC by varying the current density from 0.4 to 70.4 mA/cm^2, based on Bruggeman's EMA theory and simulations, which indicated an optimum thickness of 235 nm. Their specular measured reflectance, weighted over the AM1.5 spectrum, was an impressively low 1.3%. Osorio et al. (2011) [115] fabricated a three-layer, 180 nm thick porous silicon using electrochemical etching in fluorine-containing solutions to achieve measured optical transmittance of almost 96% for the entire wavelength range based on numerical simulations.

In general, this method of fabricating porous silicon is cheap, straightforward and yields reliable results. However, the need for external bias and illumination in some cases makes it difficult for industry-integration in large scale production of solar cells. The resulting morphology of porous silicon makes it challenging to effectively passivate and obtain competitive SRV. Moreover, maintaining fixed current densities over large area may prove challenging, reducing the scalability of the process.

3.3.2.2 Stain chemical etching of Si

An electroless alternative fabrication method to electrochemical etching is the so-called 'stain etching' which has the advantage of requiring no external bias. Archer (1960) [116] and Turner (1960) [117] managed to create porous silicon layers of below 100 nm thickness using a mixture of fuming nitric acid (HNO_3) as the oxidant and *HF*. The process consists of a localized electrochemical cell, as the silicon surface presents anodic and cathodic regions between which an internal electric current

flows due to free charge transfer. When nitric acid is in contact with silicon, it draws electrons from the Si valence band and creates a cathode site. The hole injected into the silicon substrate would find a silicon atom which would be etched by *HF*, creating an anode site and thus surface dissolution would occur, eventually leading to etched pits [117]. As such, this method is very similar to metal-assisted chemical etching (MACE), but lacks the metal particles that catalyse the reaction. In 1975, Watanabe et al. [118] confirmed that both electrochemical etching and stain etching produce porous silicon of similar crystallinity to the parent wafer allowing less carrier recombination and inducing a resurgence in the interest of this material, that was viewed as an unwanted process artefact until then. They concluded that the etch rate is higher for n-type silicon than for p-type silicon for the same current density. Tsuo et al. (1993) [119] fabricated porous silicon using two parts methanol to one part 48% *HF* to obtain layer thicknesses of 1.2 μm after a 3 minute etch for current densities of 1 mA/cm^2. They showed integrated reflectance values of below 10% and were first to discuss the recombination detrimental effect of this optical gain. Using photoconductance decay (PCD), they measured lifetimes of 53 μs for the porous silicon layer, owing in the most part to the H-terminated surface in the as-deposited state. In comparison, their best oxidized planar Si wafer yielded values of 230 μs. Menna and co-workers (1993) [120] expanded the work and fabricated porous silicon on polycrystalline Boron-doped 350 μm thick Si wafers using stain etching. The resulting layer had a thickness of 800 nm and an estimated porosity of 70%, yielding surface reflectance values of below 5% for specific wavelengths. They also showed the impact of the $C \times t$ parameter, where C is the concentration of the HNO_3 oxidant and t is the etching time in seconds. A $C \times t$ value of 600 yielded the lowest reflectance.

Later, Schirone et al. (1996) [121] conducted an in-depth study on the influence of the solution concentrations on the morphology of the p-Si layer using stain etching as the preferred fabrication method. They varied the concentration of the *HF* solution from 25% -50 %, while varying concentration of HNO_3 from 12 mM – 200 mM. For a 10-minute process, they obtained layer thicknesses of 300 nm which produced surface reflectance of below 3% for wavelengths below 700 nm after

rinsing in acetone. Moreover, they fabricated mC-Si cells using this antireflective layer, resulting in power conversion efficiencies of 11.8%, the highest at that time in the monojunction mc-Si solar cells category, with J_{sc} of 27.8 mA/cm^2 and V_{OC} = 579 mV. Seven years later, Lipinski et al. [122] would break the record by fabricating multicrystalline silicon solar cells with both electrochemical etching and stain etching porous silicon. They noticed a gradient in the stain etched porous layer, due to the similar rates of etching for porous silicon as for the silicon substrate. They obtained power conversion efficiencies of 13.3% and 12.6% for the mC-Si cells fabricated via electrochemical etching and stain etching respectively, showing increases of over 3% in both cases compared to planar cells. They attributed a high gain in J_{sc} to the excellent optical properties of the porous silicon layer, even though no surface passivation was employed. Figure 3.3 shows their resulting p-Si layer after electrochemical etching.

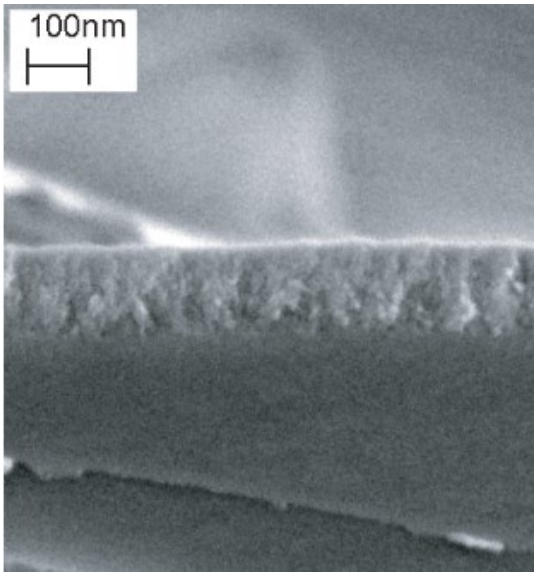

Figure 3.3: Porous silicon layer fabricated via electrochemical etching on mc-Si. Reproduced from Ref. [121].

Stain etching is low cost and easy to implement, resulting in surface reflectance < 10% for less than a minute of process time. As discussed above, it provides great results on almost all types of silicon wafers, independent of orientation and the large photoluminescence spectra arising from the p-Si layers make it a great candidate for integration with various optoelectronic devices [100-101], such as photosensors

and photodetectors. However, it has been reported that very thick films of p-Si cannot be obtained using this method and offers little control over large surface areas for industry integration.

3.3.2.3 Laser treatment of Si surfaces

In 1998, Her et al. [123] reported the fabrication of dense arrays of conical spikes on (100) n-type Si substrates without the use of a mask using femtosecond Ti:sapphire laser pulses. The group use several 500 pulses to microstructure the silicon surface both in SF_6 and Cl_2 environments, as well as in vacuum. In all the cases, high-aspect ratio silicon spikes are formed, with heights of approximately 40 μm and smooth tapered sidewalls starting from 60 μm^2 at the base to 0.64 μm^2 at the tip. The microspikes fabricated in vacuum have a more irregular shape, are bulkier and present less tapering. The group has found that lower laser fluences (energy per unit area) result in smaller and denser features that have nanostructures situated on the side of the tapered walls.

Later, Her et al. (2000) [124] fabricated such microstructures on both (100) and (111) Si wafers, confirming that higher laser fluences yield larger separations between spikes, as well as taller structures. As a rough estimate, a doubling of the laser fluence would triple the spike periodicity and increase their length by twelve times. In contrast, for low fluences of 2 kJ/m^2 only nanostructures could be observed, while a further decrease would leave the silicon surface intact. Moreover, the fabrication of the microstructures appears to be independent of the dopant concentration of the bulk materials. The work explained the tapering of the structures by increased absorption of the p-polarized light of the laser in the yz direction than s-polarized light, resulting in increased length in x direction. Figure 3.4 shows the fabricated pillars after laser treatment, where the laser fluence impact can be seen, resulting in denser and shorter structures away from the centre.

Wu et al. (2001) [125] extended the work by carrying out absorption optical measurements on the fabricated microstructures in SF_6 environment, showing large absorption > 90% for wavelengths 250 nm – 2500 nm in 50 μm long structures with a tapered side walls from 10 μm at the base to 800 nm at the tips. As expected, they

found a positive correlation between the number of laser pulses and the structure height. SIMS measurements revealed high concentrations of S and F radicals just below the surface, which decrease upon a 3 hr anneal. This in turn leads to a drastic reduction in the optical absorption for wavelengths above 1100 nm. This is due to the sulphur impurities that effectively introduce energy states into the silicon bandgap, as well as infrared absorbing states near the band edge caused by structural defects in the microstructures. Crouch et al. (2004) [126] investigated and compared the morphological and optical properties of both femtosecond and nanosecond fabricated spikes on Si substrates, where it was found that, for the same laser conditions (fluence, polarization etc), the nanosecond structures are five times larger than the femtosecond structures. Moreover, the ns-fabricated structures are smoother along the side walls with nanostructure feature diameters of 20 – 50 nm. This leads to slightly stronger absorption than the femtosecond counterparts. Structures fabricated with the same technique in vacuum or in air do not present large absorption in the sub-bandgap wavelengths of silicon, an indication that the S impurities play a vital role in this. Later, Skantzakis et al. (2006) [127] investigated picosecond laser as well with a UV laser wavelength of 280 nm, reporting similar morphology to the femtosecond produced structures. They reported that nanosecond pulses create a structural array with the largest periodicities, due to a combination of laser ablation mechanisms and excitation of the capillary waves (so-called ripples) induced by laser pulsing.

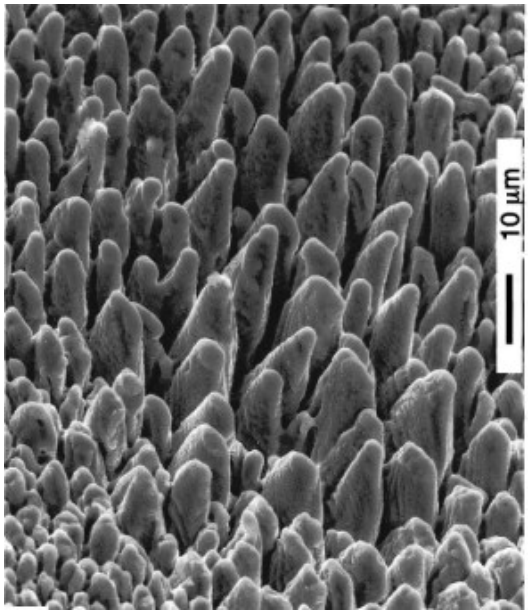

Figure 3.4: Laser-treated Si surface with b-Si layer. Reproduced from Ref. [123].

In general, despite attractive optical properties arising from enhanced absorption, the microstructures cannot be readily implemented into the PV industry, due to slow and expensive fabrication methods and high sulphur contamination. However, the sulphur contamination may lead to uses of this material as an intermediate band (IB) within the silicon bandgap that absorbs wavelengths above 1.1 µm and thus could provide a route for overcoming the well-known Shockley-Queisser limit. Sullivan et al. (2013) [128] and co-workers showed that sulphur hyperdoped silicon (Si:S) may find a use in such PV devices if the calculated figure of merit *v* is above unity, which evaluates the IB material capability to enhance the power conversion efficiency of the Si device. This is due to the implied trade-off of such architectures: thick intermediate-band layers are desirable for strong absorption, but detrimental from a carrier recombination point of view. They have calculated $v = 0.05$ for silicon doped with sulphur for concentrations of 10^{20} cm^{-3}, more than one order of magnitude lower than what would be required to enhance the efficiency of silicon devices, thus disproving the use of this material for PV applications.

3.3.2.4 Reactive ion etching

Reactive ion etching (RIE) is regarded as a stable and reliable fabrication method of black silicon needles and nanopillars on a Si substrate. The work of Jansen et al. (1995) [129] explored and significantly advanced the understanding of the surface chemistry between SF_6 based plasma processes and the silicon material. In a typical RIE process, a $SF_6/O_2/CHF_3$ plasma is used to bombard the material surface, with various flow rates resulting in different etch rates. In this system, each gas has its own specific contribution that is very well determined. SF_6 generates *F* radicals, such as F^+, SF^+, SF_3^+ or SF_5^+, that chemically etch the silicon surface, resulting in volatile radicals, such as SiF_4. *O* radicals created by the O_2 plasma react with the volatile radicals, thus creating a passivating layer on top of the silicon material that acts as an etching mask, SiO_xF_y. Next, CF_x+ and F^+ ions arising from CHF_3 bombard and remove this blocking layer etching into the surface. The cycle is repeated until the desired depth is reached. Alternatively, modern b-Si RIE processes do not use the CHF_3 plasma, relying instead on SF_x+ and F^+ ions for bombardment and subsequent removal of the passivating silicon oxyfluoride layer. Etch rates in excess of 3 μm/min are possible depending on the flow rates and RF power. Jansen and co-workers fabricated periodic trenches of up to 200 μm depth that are both positively and negatively tapered, depending on processing parameters. For b-Si needle formation, native oxide and contaminants on the wafer act as a micromask for the etching process, where spikes form in an silicon oxyfluoride layer that is usually removed. The process has generally been described as a competition between *F* and *O* radicals to etch and passivate the Si surface, respectively [129]. As such, an increase in SF_6 delivery rate leads to more isotropic etching, due to a less pronounced passivating layer being formed. In contrast, higher oxygen plasma rates make the etching less isotropic due to the etching rate decreasing and eventually leading to a positively taper in the microstructures.

In 2011, Xia et al. [130] employed Plasma immersion ion implantation (PIII) in the RIE process to fabricated b-Si pillars on p-type polycrystalline Si with 1-3 Ωcm resistivity under negative bias pulses at -500 V. The resulting structures for a 10-minute process time with SF_6/O_2 = 90/20 sccm flow rates showed weighted average

reflectance of only 1.7% and a solar cell device was fabricated with a power conversion efficiency of 15.68 %. The following year [131], the group extended the work to study the influence of the SF_6/O_2 ratio on the structure formation, showing that an increase in the ratio leads to longer structures and thus reduced reflectance from 4.8 % to 2.1 % when the ratio is changed from 1/3 to 1/4.5. The change was from porous silicon to well defined needle-like structures and the discussion established that high SF_6/O_2 ratios yield processes where the passivating layer dominates, thus creating porous silicon. The reverse is true for lower ratios, as an increase in the oxygen content leads to dominant etching.

Typically, RIE processes nowadays are carried out at temperatures below zero ^{0}C to prevent desorption of the passivation silicon oxyfluoride layer. Otto et al. (2012) [132] fabricated three types of structures with oxygen and SF_6 plasma at -120 °C with lengths of 500 nm, 600 nm and 1700 nm. Measurements showed optical absorption in excess of 90 % for all cases for wavelengths below 1000 nm. Allen et al. (2014) [133] fabricated b-Si needles on p-type (100) CZ Si wafers with an RIE time of 40 minutes with 1:1 SF_6/O_2 ratio, where the RF source has a power of 16 W. They showed a surface area enhancement factor of 14 in the fabricated layer, yielding impressive absorptions of above 98% owing to reduced broadband reflectance of 0.4 % when the structures are coated with 25 nm ALD AlO_x. Moreover, thicknesses of 20 nm – 250 nm alumina film on top of b-Si showed minimal impact of the measured reflectance response.

The record-holding IBC b-Si cell fabricated by Savin et al. (2015) [46] uses RIE as the preferred fabrication method for the ARC layer. The process was carried out at -120 °C, resulting in nanopillars of 800 nm height with base widths of about 200 nm. The measured hemispherical reflectance was below 2% for all the wavelengths under study with beneficial impact arising from alumina coating of 20 nm thickness. The measured J_{sc} was 42.2 mA/cm^2, owing to the excellent optical and electrical passivation responses. Figure 3.5 shows the b-Si RIE layer on the surface of this silicon solar cell, passivated with 20 nm AlO_x.

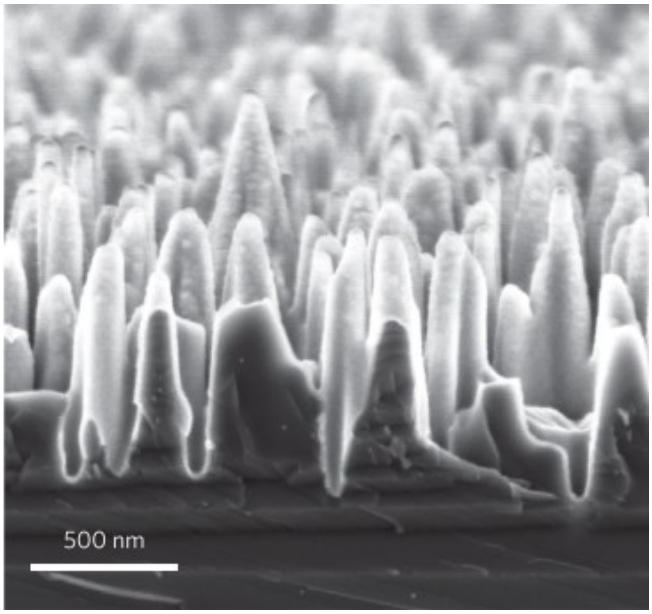

Figure 3.5: RIE b-Si surface with 20 nm ALD AlO_x. The height of the pillars is 800 nm. Reproduced from Ref. [46].

Iandolo et al. (2018) [134] performed a study of the etch time impact on the optical response of the black silicon layer. The group fabricated b-Si hillocks on p-type CZ 5 Ωcm Si wafers at a process temperature of -20 °C with a O_2/SF_6 ratio of 10:7. It was concluded that an increase in the etch time yields taller nanostructures and thus reduced surface reflectance. Under these conditions, an etch time of below 3 minutes did not result in fully-developed structures on top of the silicon wafer but showed surface reflectance of 10 %, while etch times above 4 minutes yielded pillars with lengths in excess of 150 nm. For the highest etching time of 16 minutes, the height of the b-Si features is 450 nm, showing surface reflectance of below 4-5 % for the entire wavelength range of interest.

Although RIE processes for fabrication of b-Si yield great results, the silicon surface often suffers ion bombardment damage that may require greater electrical passivation for gains in the power conversion efficiencies of silicon devices [103]. Moreover, the fabrication process is in general expensive and slow, thus proving not to be the ideal candidate for industry integration and large-scale production of black silicon.

3.4 Metal-assisted chemical etching

In recent years, much attention has been given to metal-assisted chemical etching (MACE) of silicon substrates as the principal black silicon fabrication method, due to its inherently low cost and process ease [47, 103, 135]. MACE is a top-down etching method where the semiconductor substrate is covered by a noble metal. When the semiconductor/metal stack is placed in an aqueous solution comprised of *HF* and an oxidative agent, macroscopic electrochemical cells are formed on the Si surface that facilitate the etching beneath the metal at a much higher rate through continuous redox reactions. As such, the semiconductor surface gets oxidised by the reducible species and hole injection takes place preferentially at this interface due to the localised anodes and cathodes. Therefore, MACE is very similar to the previously introduced stain etching. The first reported metal-catalysed etching process was in 1997, when Dimova-Malinskova and co-workers [136] observed enhanced etching rates of silicon surfaces that presented a 15 - 20 nm thermally evaporated *Al* film on top. Thus, porous silicon was formed in the presence of a buffered HNO_3:*HF* solution after just 20 seconds of etching. At first, it was thought that this method is just an enhanced stain etching, where normal durations for p-Si formation exceed 5 minutes, depending on the doping level of the Si substrate. p-Si films of above 100 nm were formed after just 3 minutes of MACE time, yielding top surface reflectance of about 10 % across the entire wavelength range, showing its suitability as an antireflective layers on top of silicon solar cells. After this report, many studies followed, where the oxidative agent, the metal and the deposition method of the electrodes were explored. The etching method raised interest from the photovoltaic community especially with the report of Li and Bohn [137] in 2000, that performed etching on Si substrates of various doping types and levels with various ultra-thin (<10 nm) sputtered metal films, such as *Au, Pt* and *Au/Pd* alloy in the presence of *HF* and H_2O_2. The group obtained p-Si layers as well as columnal silicon structures after a masking process with noticeable photoluminescence properties.

Typically a two-step process MACE is employed, where noble metals are deposited on the Si surface via various methods, such as sputtering [137-139], evaporation [140-141] or electroplating [142-143] and then the stack is immersed into an aqueous solution containing *HF* and an oxidative agent, such as H_2O_2 or HNO_3. This leads to very fast etching of the semiconductor surface below the metal film due to its catalytic role. The morphology of the deposited metal film dictates the morphology of the resulting silicon structures. Therefore, for high-aspect ratio formation, discontinuous metal films are desired, either using photolithography masking or by electroless deposition processes. Hydrogen peroxide (H_2O_2) is the oxidative agent of choice for most studies, due to its much more positive redox potential (1.76 V/ SHE) than for example nitric acid (0.94 V/ SHE), thus providing holes into the silicon substrate at a much higher rate according to the cathodic reaction (3.1). This is due to the Si valence band (VB) situated at 0.67 V/ SHE, thus below the redox potentials of the reducible species [142]. Here, SHE refers to the Standard Hydrogen Electrode chemical potential, which is used as a reference for redox system and has a potential of 0.0 V by definition [144].

$$H_2O_2 + 2\,H^+ \rightarrow 2\,H_2O + 2\,h^+ \qquad (3.1)$$

Due to the more positive redox potential of the HF/H_2O_2 system compared to silicon, the semiconductor is also etched without the presence of the catalytic noble metal, although at a much slower rate than the semiconductor below the metal. Thus, the metal film (or particles) sink into the silicon substrate at a depth proportional to the etching time or to the metal consumption during the process. What is left between the metal are high-aspect ratio micro-/nanostructures. Reaction (3.1) occurs much faster at the metal surface than at the silicon surface. Noble metals that have been used for the MACE process include *Ag* [145], *Au* [146-147], *Cu* [148-149], *Pt* [150-151] and *Pd* [152], with various oxidation rates and etching rates depending on the characteristic of the silicon substrate (doping, orientation etc).

Alternatively, one-step MACE process can occur with a metal salt in aqueous *HF* solution that acts both as electroless deposition means of forming metal particles and as an oxidative agent. Reports in literature suggests that there is a multitude of

salts that can be used, most notable $AgNO_3$ [135, 142-143], $HAuCl_4$ [153-154], $KAuCl_4$ [155], $PdCl_2$ [153], $Cu(NO_3)_2$ [156], H_2PtCl_6 [153,156] or K_2PtCl_6 [156]. This one-step method has the advantage of shorter processing times, as well as potentially reduced cost due to the lack of metal physical depositions in vacuum, being overall a more straightforward method of fabricating black silicon layers in a single aqueous solution. Moreover, the lack of hydrogen peroxide reduces the etch rate due to decrease hole injection into the substrate, providing more controllable means of etching high-aspect ratio structures with the desired morphology. The most widely used system in literature for MACE processing is the $AgNO_3/HF$ solution [145].

3.4.1 Mechanism

For relevancy to the fabrication process explored in this thesis, explanation of the formation mechanism of silicon nanowires will be restricted to a one-step MACE performed in aqueous $AgNO_3/HF$ solution without the presence of H_2O_2. As previously discussed, this etching process is based on a multitude of nanoelectrochemical cells present on the silicon surface that induce self-assembled selective etching in the dark, without the requirement of illumination, controlled temperature or external current bias. Nanoscopic anodes and cathodes are formed and the reduction of silver ions to elemental silver occurs at the same time as the dissolution of the silicon material, resulting in continuous galvanic displacements that propagate the metal vertically into the substrate. At first, dissolution of silver nitrate results in silver ions being formed on the Si surface, where the half-cell cathode reactions (3.2) occurs. The reduction of silver ions to elemental silver and deposition of these particles on the semiconductor surface leads to oxidation of the silicon according to the half-cell anodic reaction (3.3) that occurs concomitantly [103, 145].

$$Ag^+ + e^- \rightarrow Ag \qquad \textit{(at the cathode)} \qquad (3.2)$$

$$E_{Ag+/Ag} = 0.799\ V\ /SHE$$

$$Si\ (s) + 2\ H_2O + 4h^+ \rightarrow SiO_2 + 4\ H^+ \qquad \textit{(at the anode)} \qquad (3.3)$$

The resulting silicon dioxide pits are filled with the silver nanoparticles and they are subsequently etched by the *HF* solutions according to reaction (3.4).

$$SiO_2 + 6\,HF \rightarrow H_2SiF_6 + 2\,H_2O \tag{3.4}$$

The by-products of the reaction (H_2SiF_6) diffuse to the surface along the walls of the nanostructure. A continuous cycle as this one ensures vertical sinking of the metal particles into the silicon substrate due to the oxidation of the semiconductor material. The complete redox reaction of the system is described by reaction (3.5) [142-145].

$$Si + 4\,Ag^+ + 6\,HF \rightarrow 4\,Ag + H_2SiF_6 + 4\,H^+ \tag{3.5}$$

Understanding of the formation mechanism of black silicon and charge transfer between the semiconductor material and the $AgNO_3/HF$ solution can be addressed by studying the electrochemistry at the semiconductor/electrolyte interface. Figure 3.6 a) shows the energy band diagrams of the n-type $Si/AgNO_3/HF$ system before contact, in the dark. The electrochemical and redox potentials are calculated in absolute values (eV) with respect to the vacuum energy level and referenced to the Standard Hydrogen Electrode according to equation (3.6), where q is the electron elementary charge, E_{SHE} is the reference energy and U_{redox} is the redox potential in volts vs SHE [140-141].

$$E_{redox} = E_{SHE} - q\,U_{redox} = -4.5\,eV - q\,U_{redox} \tag{3.6}$$

In Figure 3.6 a), E_A represents the electron affinity of Si (4.05 eV), E_g is the bandgap of Si (1.12 eV), E_i is the intrinsic energy level that lies near the middle of the bandgap and E_{Fn} is the Fermi level of the moderately doped n-type Si with $n = N_D = 10^{15}$ cm^{-3}, calculated according to equation (3.7). k is Boltzmann constant (8.61 eV/K), T is the temperature in K and n_i is the intrinsic carrier concentration of Si (10^{10} cm^{-3}). Thus, at room temperature, the Fermi level, which represents the electrochemical potential of the electron in the semiconductor phase, lies about 0.23 eV above E_i.

$$E_{Fn} - E_i = k\,T\,ln\left(\frac{n}{n_i}\right) \tag{3.7}$$

The ability of the silver metal to be reduced and to inject holes into the silicon material is given by the much more positive redox potential (vs. SHE) of the species [143]. In order to calculate the redox potential of H^+/H, the concentration of H^+ ions in the *HF* solution ($[H^+]$) is calculated from its dissociation constant k_a (6.8×10^{-4}), according to equations (3.8) and (3.9). The molarity of the *HF* solution is 14 M, as used in the experimental section of the work to produce black silicon layers. The redox potentials of the electrochemical reactions are calculated using the general Nernst relationship (equation 3.10), as in equations (3.11) for H^+/H and (3.12) for Ag^+/Ag. The concentration of silver ions in the HF solution is assumed to be 0.03 M for a 0.06 M $AgNO_3$ diluted solution.

$$HF + H_2O \rightarrow H^+_{(aq)} + F^-_{(aq)} \tag{3.8}$$

$$k_a = \frac{[H^+]\,[F^-]}{[HF]} \tag{3.9}$$

$$E = E_0 + k\,T\,ln\,[Q] \tag{3.10}$$

- $\boldsymbol{E_0}$ is the standard potential
- $\boldsymbol{k}$ is Boltzmann's constant (J/K)
- $\boldsymbol{T}$ is temperature (K)
- $\boldsymbol{Q}$ is the reaction quotient.

$$E_{HF} = 0 + k\,T\,ln\,[H^+] \tag{3.11}$$

$$E_{Ag} = 0.799 + k\,T\,ln\,[Ag^+] \tag{3.12}$$

Thus, E_{Ag} is 0.0875 V/ SHE and E_{HF} = - 0.058 V/ SHE, resulting in absolute values of- 5.21 eV and – 4.45 eV, respectively.

For simplicity, Figure 3.6 b) shows the silicon substrate in contact only with the *HF* solution. When a semiconductor is submerged in an electrolyte, their Fermi levels must match at equilibrium [144]. If it does not, charge transfer will occur in the system until equilibrium is reached. In the case when the Fermi level of Si lies above the redox potential of the H^+/H, such as for n-type silicon, electrons will flow from the silicon to the solution. Thus, the semiconductor acquires a positive charge. In the moderately doped Si considered in this case, the density of states at the

surface is not enough to accommodate this excess charge, so a spatial distribution of this charge will occur away from the surface. This results in a space charge region, as shown in Figure 3.6 b) [142-144]. This implies that electrons at the interface have a different electrochemical potential that the electrons in the bulk and thus upwards band bending will occur. The potential difference $\Delta\varphi$ is called barrier height and it will experience a potential gradient towards the interface due to the formed Helmholtz layer that adsorbs ions [157].

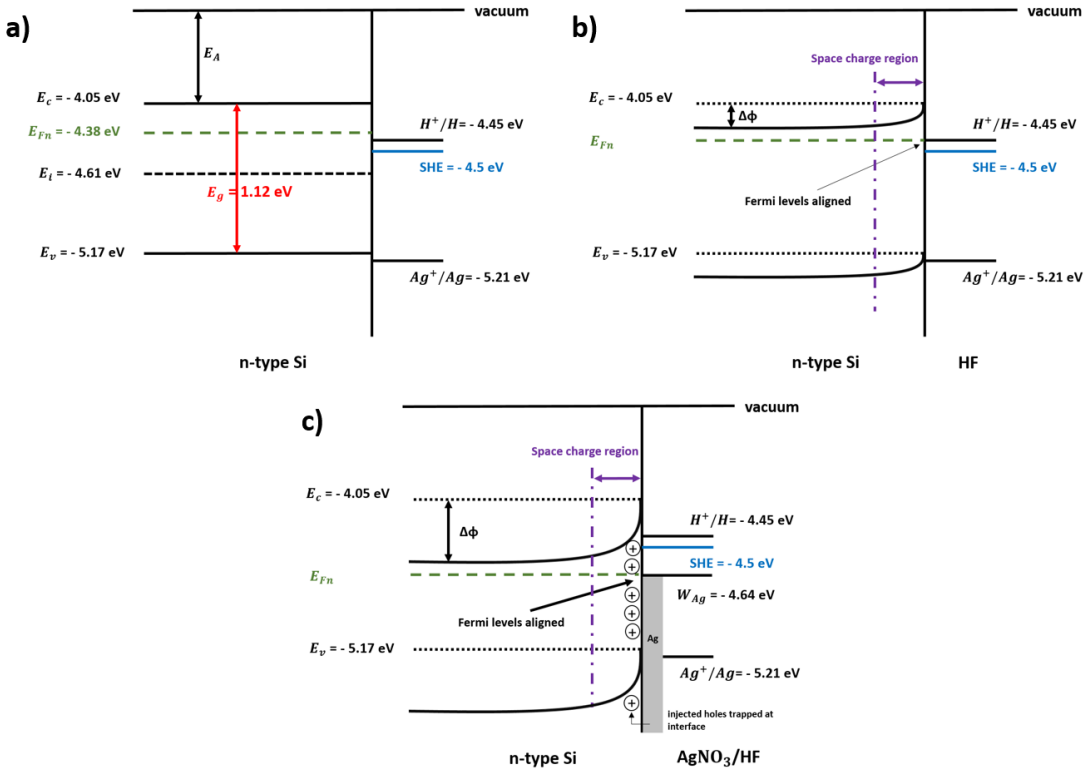

Figure 3.6: a) n-type silicon energy band-diagram at equilibrium; b) n-Si/HF system at equilibrium, here band-bending occurs; c) n-Si/$AgNO_3$/HF system at equilibrium where injected holes from Ag particles are trapped at the interface [145].

Furthermore, when silver is added to the HF solution, the band bending will become more pronounced for n-type silicon, as the Fermi level must now match the work function of the silver metal, W_{Ag} (- 4.64 eV), as in Figure 3.6 c). The electrons in the Si conductance band (CB) will go to the bulk, while the holes in the Si VB will go towards the surface. Thus, the silicon surface will now be depleted of majority

carriers, creating a positive charge at the interface [144]. Due to this, some etching is expected to occur in a *n-Si/HF* system irrespective of the presence of the metal particles. Now, the injected holes from the silver particles facilitate trapped at the surface facilitate the oxidation of silicon to silicon dioxide which is then etched by *HF*.

A similar discussion can be considered for a p-type silicon substrate, except for a couple of notable differences. First of all, the Fermi level of the semiconductor will lie 0.23 eV below the intrinsic energy level E_i for $p = N_A = 10^{15}$ cm^{-3} according to equation (3.13), as shown in Figure 3.7 a).

$$E_{Fn} - E_i = - k\,T\,ln\,(\frac{p}{n_i}) \tag{3.13}$$

In the case of a p-type silicon substrate, the band-bending will occur downwards to accommodate charge transfer when in contact with the *HF* electrolyte solution, as the Fermi levels must be aligned (Figure 3.7 b)) [158]. This time, the silicon will acquire a negative charge with respect to solution. The band bending reduces considerably when silver is added to the etching solution, due to a decrease in the barrier height $\Delta\varphi$ (Figure 3.7 c)). This is in turn caused by the alignment of the Si Fermi level to the metal work function that now lies below E_F. Similarly, as in the n-type case, to accommodate these excess charges, the spatial distribution occurs and the surface is depleted of majority carriers, which are holes this time. As such, even though the valence band of silicon lies above the redox potential of Ag^+/Ag and overlapping occurs and holes are easily injected into the silicon valence band, these holes diffuse to the silicon bulk. Therefore, the Si surface is filled with negative charges and less holes are available at the surface to facilitate the oxidation of silicon and the subsequent etching by *HF.* This results in slower etch rates for the MACE process on p-type Si than n-type Si, as previously reported [159]. Furthermore, this is also the reason why the p-type Si is only very slowly etched just in the presence of *HF*, without noble metal particles on the surface.

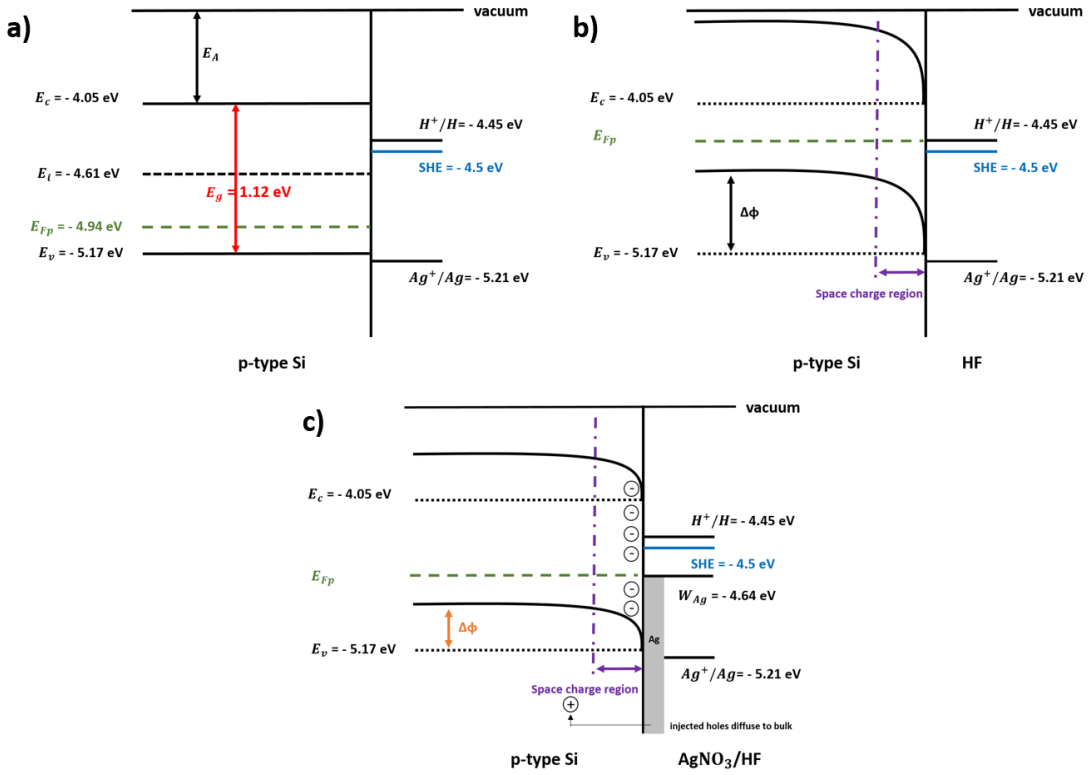

Figure 3.7: a) p-type silicon energy band-diagram at equilibrium; b) p-Si/HF system at equilibrium, ehre band-bending occurs; c) p-Si/$AgNO_3$/HF system at equilibrium where injected holes from Ag particles are trapped at the interface [145].

To summarise, Figure 3.8 shows a visual overview of the main steps involved in metal-assisted chemical etching using silver particles in *HF* solution [145]. At first, the Ag^+ ions are reduced to elemental *Ag* and are deposited on top of the silicon substrate (step 1). The silver particles start growing in size. The initial oxidation of Si atoms from the surface leaves pits that are immediately filled by *Ag* particles. This is followed by an injection of holes into the silicon valence band at the *Ag/Si* interface, which begins oxidizing the silicon (step 2). The oxides formed (SiO_2) at the silver/silicon interface are dissolved by *HF*. The by-products of the reaction (H_2SiF_6) and *HF* diffuse along the *Ag/Si* interface (step 3). As mentioned before, the silicon covered with *Ag* particles is etched much faster than the one without due to the preferential charge transfer occuring and the agglomeration of holes below the *Ag*

particles. The nanoparticles thus begin sinking vertically into the semiconductor (step 4). It has been suggested by Tsujino et al. (2007) [150] that there is indeed some hole diffusion to the side walls of the *Ag/Si* interface and that even the silicon not covered by metal particles is etched, although the etching rate is very slow (step 5). Finally, what is left between the etched region of the silicon surface represents the high-aspect ratio features that provide the antireflective and light-trapping effect for silicon solar cells.

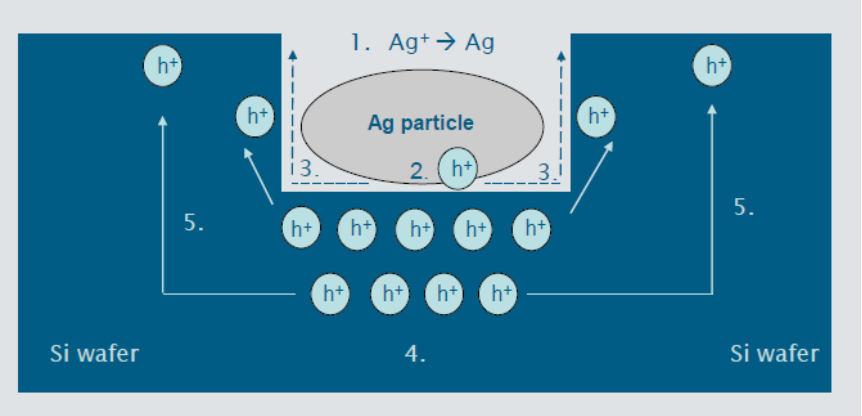

Figure 3.8: Overview of the MACE process, showing the five main steps: 1. Reduction of silver ions to elemental silver and deposition on top of substrate; 2. Injection of holes into the Si valence band and initial oxidation of Si; 3. Diffusion of by-products (H_2SiF_6) along the walls of the pit; 4. Agglomeration of holes below silver nanoparticles and vertical propagation into the silicon substrate because of the preferential charge transfer; 5. Some modest diffusion of holes to non-Ag/Si interface, which causes Si etching, but at a much slower rate.

3.4.2 Evolution of Ag particle

The evolution of the metal particle during MACE process plays an important role especially for antireflective purposes, as tapered nanowires would induce a refractive index gradient based on the silicon fill factor and more efficiently suppress surface reflectance. Tsujino et al. (2005) [150] reported the use of a metal salt solution for electroless plating of Si surfaces in *Ag* nanoparticles (NP) for a two-step MACE process, with diameters in the range 30 – 100 nm. They bored deep holes

into the substrate using H_2O_2 as an oxidant. For depths of below 40 μm, the silver particles found at the bottom of the holes were consistent in size with those observed deposited on the Si surface. However, the NPs found at the bottom of deeper holes were more spherical shape compared to the original NPs and were also smaller in diameter. Lee et al. (2007) [160] used a similar process involving micron size particles in the range 500 nm – 1500 nm. After 20 minutes of MACE processing, some of the silver particles found at the bottom of deep pores were smaller by up to a factor of 10. The presence of thinner pores indicated that bigger *Ag* particles decompose into multiple smaller pieces and re-deposit on top of the Si surface for vertical propagation. This was attributed to the smaller contact area between micron sized particles and Si than NPs, leading to decreased hole injection rate into the silicon material. Moreover, it was proposed that the electrochemical potential of the bigger silver particles shift to a sufficient level so that dissolution of silver is promoted. At the same time, Tsujino et al. [151] reported the evolution of spherical *Ag* NPs with diameters 30 -100 nm on top of (100) substrates. After MACE processing for 1 minute, it was found that in some cases, the bored deep holes etched in other directions, such as [010], [0 -1 0] and [0 0 1]. It was concluded that if the original nanoparticle is spherical, the holes are etched perpendicular to the substrate. If the nanoparticles have irregular shapes to begin with, deviations are possible due to the different catalytic activity of the metal when different facets are exposed to the semiconductor. Moreover, it was proposed that high concentrations of hydrogen peroxide promotes a higher fraction of holes diffusion to the side walls of the pores, resulting in thin porous silicon layers in the regions where no metal is deposited.

3.4.3 Effect of temperature and illumination

In some cases, the MACE process may be carried out at different temperatures compared to standard room temperature. Consequently, the effect of this parameter is of interest. Cheng et al. (2008) [161] reported MACE processes performed at temperatures of 0°, 20°, 35° and 50° C on (001) Si substrates. They found a linear relationship between the nanowire height and temperature consistent for all temperatures under study, with higher temperatures resulting in even steeper

feature height increase. For example, after 15 minutes of processing at 20° C, the nanostructure length was 3 μm, value which increased to around 12 μm when a higher temperature of 50° C was used. A similar trend was found by Ozdemir et al. (2011) [162], who studied temperatures in the range of 10° - 50° C using a one-step MACE method comprising of 0.02 M $AgNO_3$ and 4.6 M *HF*. They attributed the linear increase in nanowire height with increased processing temperature to the faster kinetics of the redox reactions. More recently, Srivastava et al. (2014) [145] performed one-step MACE for temperatures in the range 10° - 80° C and found a similar trend to the previous reports. Below 30° C, the nanowires are well-aligned. The nanostructures start experiencing bundling for temperatures between 30° C and 50° C, due to their increased height. Temperatures above 50° C yielded nanowire lengths that could not be fitted anymore to the linear relationship to the temperature. It was also noted that such high temperatures lead to uncontrolled lateral etching and eventually morphology that resembles porous silicon rather than well-defined nanowires.

Indeed, if we consider the silicon/electrolyte interface as described in Chapter 3.4.1., an increase in surrounding temperature leads to shifts in the semiconductor bandgap, electron affinity and the calculated electrochemical potentials. As such, for both p-type and n-type Si, more band bending is expected that in turn facilitates the injection of holes into the Si material, yielding longer nanostructures with increased temperature for a constant etch time. The lateral etching observed for temperatures above 50° C can be ascribed to the diffusion of holes at non-*Ag/Si* interfaces.

Illumination effects have not been systematically studied in literature so far. Huang et al. (2011) [103] reported that no noticeable difference in MACE rate is observed when the substrate is illuminated with a 20 W light bulb. However, under stronger illumination, electrons will be excited from the valence band of silicon to the conduction band, as long as the incoming photons energy is greater than the material bandgap. As such, for n-type silicon, the potential gradient at the silicon/electrolyte interface will cause the photogenerated pairs near this interface to be separated: electrons will diffuse to the bulk, while holes will be promoted to the interface. Strong illumination levels will photogenerate enough holes at the

interface that the etching rate of the semiconductor will increase as oxidation becomes prevalent.

3.4.4 Activation energy of the process

The activation energy of a chemical system is the minimum energy required for the reaction to occur. This can be calculated by studying and plotting the temperature effects on the chemical process, more specifically the etching rate. Cheng et al. (2008) [161] found the activation energy required for NW formation on (100) Si to be 0.36 eV, consistent with later studies conducted by Nassipolou et al. (2011)[162], who found the activation energy E_a = 0.37 eV and Han et al. (2014) [163] who found E_a = 0.36 eV as well. However, a number of other groups reported different results: Liu et al. (2011) reported E_a = 0.21 eV, consistent with E_a = 0.2 eV found by Kato et al. (2011) [165], while Srivastava et al. (2014) [145] found it to be about 0.5 eV. In an attempt to explain their findings, Srivastava and co-workers started experimenting on sample sizes other than the 2 × 2 cm^2. Interestingly enough, they arrived to the conclusion that the etch rate is dependent on the surface area. That is, smaller samples give longer nanowires. To support their theory, they have undertaken the same MACE process on 3 x 3 cm^2, 1 x 1 cm^2 and 0.5 x 0.5 cm^2 samples and found nanowires 4.3, 8 and 13 μm long, respectively. Moreover, they calculated the activation energy of the reaction again by using the results from the 0.5 x 0.5 cm^2 samples and concluded that the activation energy was 0.38 eV, fairly consistent with Cheng's and Han's results. Therefore, they have explained that the various values that can be found in the literature, such as 0.2 eV can be attributed to the sample size.

3.4.5 Silver dendrites removal

In general, the leftover silver nanoparticles that have not been consumed during the MACE process and are present at the bottom of the textures can act as recombination centers, thus inserting energy levels in the forbidden gap (see Chapter 3.5) and be detrimental from an electrical point of view. Usually, these particles are removed at the end of the etching process using a buffered nitric acid (HNO_3) solution for 5-10 mins [103]. The work presented in this thesis employed a

very similar procedure for silver removal, detailed in Chapter 5. Although no results are available in literature in regards to this, the leftover silver particles could potentially be completely recover at the end of the process, when submerged into a nitric acid solution, given that the volume and concentration of the solutions are fitting [49-50]. As such, the nitric acid solution in presence of silver nanoparticles can recover the silver nitrate solution, providing a means of massively reducing the cost of fabrication of such structures and improving the specimen yield by recycling the silver.

The work by Chen et al. (2019) [204] suggests that the presence of silver dendrites in the b-Si layers can drastically affect both the optical and electrical properties of such textures. The group fabricated b-Si layers that have undergone a silver removal step, as well as similar specimens from which this step has been purposefully omitted. All of the samples fabricated in the work were subjected to a chemical polishing step after the etching process. As such, it was reported that the remaining silver from the MACE process accelerates the chemical polishing in HF/HNO_3 solutions, but has a different etching mechanism than MACE itself. Therefore, the specimens that have not had the silver removed from the texture consistently showed larger measured surface reflectance of 5-7%, depending on the $AgNO_3$ concentration originally used, as opposed to the lower 2-5% surface reflectance measured in the counterparts samples, from which the silver has been removed. This is attributed to the participation of the leftover silver in the chemical polishing step, whereby the structures became shorter and shallower than a standard polishing step. Perhaps suprinsingly, the measured minority carrier lifetime upon ALD aluminium oxide passivation of the b-Si layers is larger for the specimens that have not undergone a silver removed step than for the ones that have. This suggests that the detrimental electronic activity inserted by the presence of the silver nanolayers is sufficiently small to be overcomed by the excellent surface passivation properties of the now short and shallow nanostructures, although at the expense of poorer optical properties. The work suggests that no silver contamination of the silicon bulk was found in any of the cases.

3.5 Electrical surface passivation

3.5.1 Introduction and metrics

Nowadays, the electrical performance of a silicon solar cell greatly depends on the quality of the surface passivation of the semiconductor. One must ensure that photo-generated electron-hole pairs do not recombine before contributing to the power output of the silicon device. As thinner and thinner solar cells are in demand, careful attention has to be given to any interface and surface present in such a device. Kaneka's record holding IBC solar cell [30] is a great example of effective surface passivation of their anti-reflective structures using hydrogenated amorphous silicon, achieving short-circuit current densities of above 44 mA/cm^2 . Any semiconductor exposed surface represents an abrupt discontinuity in its crystal lattice, effectively adding new energy states in the forbidden region (bandgap) due to variation in crystal structure and atom bonding angles. This can be described by Shockley-Read-Hall (SRH) or trap-assisted recombination mechanism, where energy states are present in the bandgap of the material and when the highest concentration of such energy states is assumed to be near the middle of the bandgap at a single energy level [166]. The rate of surface recombination U_s refers to the total recombinations occuring in 1 cm^2 area per second and is given by:

$$U_S = \frac{(n_s p_s - n_i)^2 \, v_{th} \, D_{it}}{\frac{n_s + n_i}{\sigma_p} + \frac{p_s + p_i}{\sigma_s}} \tag{3.14}$$

In equation (3.14), n_i is the intrinsic carrier concentration, p_s and n_s are the hole and electron density at the surface, $\sigma_{p/s}$ are the holes/electrons capture cross sections, v_{th} is the thermal velocity of the electrons and D_{it} is the density of interface states present in the midgap. The hole and electron recombination velocities, S_{p/n_0}, are related to their respective capture cross sections by:

$$S_{p/n_0} = v_{th} \, D_{it} \, \sigma_{p/s} \tag{3.15}$$

Thus, equation (3.13) can be rewritten as:

$$U_S = \frac{(n_s p_s - n_i)^2}{\frac{n_s + n_i}{S_{p0}} + \frac{p_s + p_i}{S_{n0}}} \tag{3.16}$$

Examination of equation (3.16) reveals that the recombination rate is given by the $n_s p_s - n_i^2$ parameter, which describes the change of carriers when illuminating the semiconductor surface as compared to thermal equilibrium (no bias), which cannot be directly reduced. Therefore, the surface recombination rate U_s can be decreased by a reduction of the density of interface states D_{it} introduced through defects, and thus the ratio of S_{n0} / S_{po}, affecting the denominator of U_S. This is achieved by saturating the unterminated chemical bonds, commonly refered to as dangling bonds, either by depositing a thin dielectric film at the semiconductor surface, such as silicon oxide, silicon nitride or aluminium oxide, or by diffusing hydrogen to this interface and completing these bonds. This is called the '*chemical component*' of passivation. In a silicon atom, four valence electrons are present that each require bonds to saturate the valence shell. In the bulk, the Si atoms bond with neighbouring atoms to achieve complete bond saturation. In contrast, the exposed Si surface consists of these surface defects that are electrically detrimental to the solar cell device if left unpassivated, as seen in Figure 3.9.

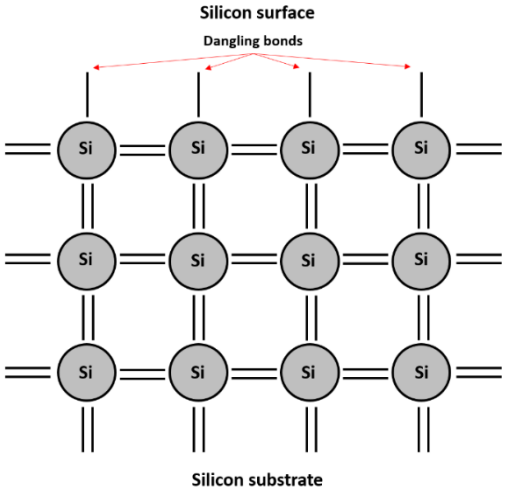

Figure 3.9: Dangling (unterminated) bonds at an exposed silicon surface.

In general, defects can trap or emit carriers based on four mechanisms and act as generation-recombination centers: 1) capture of an electron from the conduction

band to an empty defect state; 2) excitation of an electron from a defect state to the conduction band; 3) capture of hole from the valence band to empty defect state and 4) emission of hole from defect state to the valence band. These mechanisms are shown in Figure 3.10 below for silicon energy levels and bandgap.

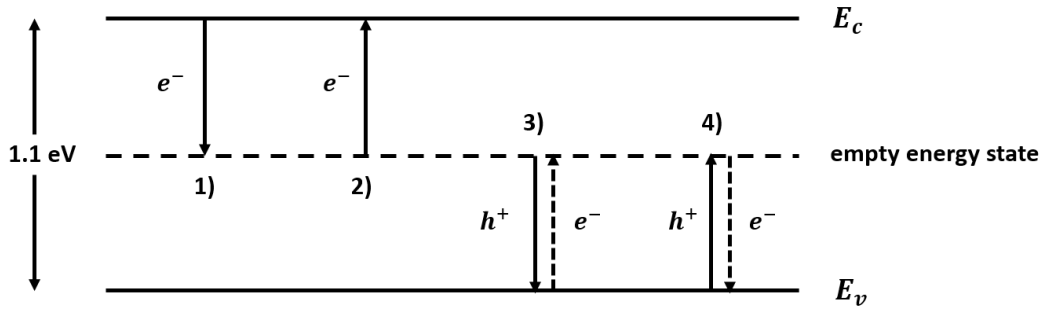

Figure 3.10: Energy band diagram of possible defect traps mechanisms.

Moreover, the surface recombination rate U_s is dictated by the number of both minority carriers at the surface, that is p_s and n_s and their ratio. For example, in n-type silicon, a low ratio of p_s/n_s yields low recombination rates at the surface due to the decrease in the number of holes in that region. This can be achieved by inducing an electric field near the surface that mirrors its charge below the interface which reduces and spatially changes the minority carrier charge concentration. The electric field induced by the charge, Q_f, can lead to either strong accumulation or inversion in the near-surface region of both p-type and n-type silicon by band-bending, depending on its polarity, as seen in Figure 3.11.

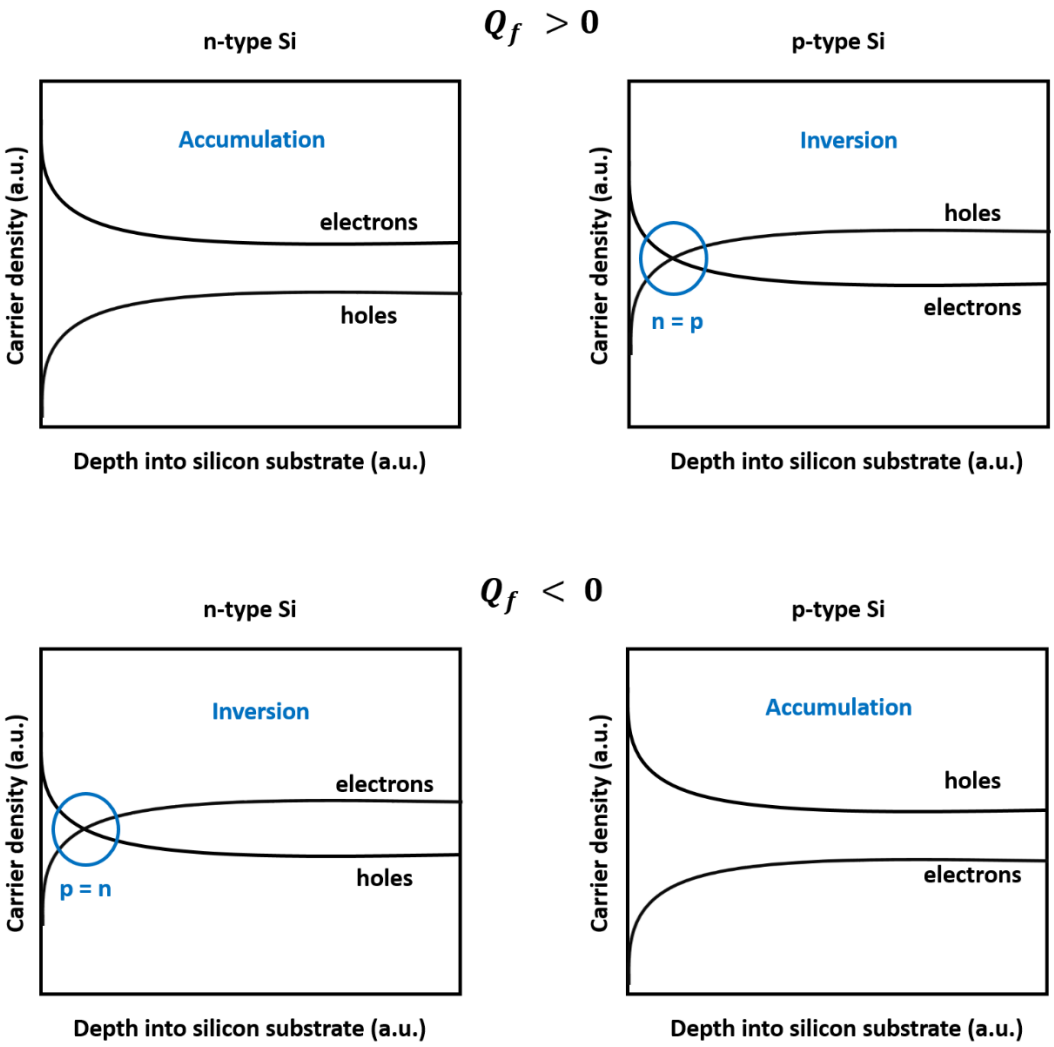

Figure 3.11: Band-bending diagrams for n-type and p-type silicon under positive and negative charges.

This is called the '*field-effect component*' of passivation (FEP). A similar method involves the heavy doping of the semiconductor surface, resulting in an emitter than creates a depletion region below the surface which again repels one type of carrier from that interface. The surface recombination velocity is given by:

$$SRV = \frac{U_s}{\Delta n} \tag{3.17}$$

where Δn is the excess minority carriers at the edge of the space charge region in cm^{-3}. Moreover, effective values for the surface recombination velocity can be extracted from the measured lifetime of the minority carriers present in the

substrate, as seen in equation 3.18. This formula shows the contributions arising from various recombination mechanisms both in the bulk and at the surface of the semiconductor. For high-efficiency silicon solar cells, both the bulk and surface lifetimes have to be maximised. The bulk lifetime includes intrinsic components such as Auger and radiative recombination, as well as SRH recombination promoted by impurities in the substrate and other lattice defects such as vacancies and interstitial atoms.

$$\frac{1}{\tau_{eff}} = \frac{1}{\tau_{bulk}} + \frac{1}{\tau_{surface}} \tag{3.17}$$

$$\frac{1}{\tau_{bulk}} = \frac{1}{\tau_{radiative}} + \frac{1}{\tau_{Auger}} + \frac{1}{\tau_{SRH}} \tag{3.18}$$

The injected minority carriers spatial distribution is crucial, as diffusion can occur from the bulk to the surface to promote recombination. Similarly, minority carriers generated near the surface can either recombine immediately or diffuse to the bulk. Based on this, Luke and Cheng (1987) [167] derived a solution to correctly calculate SRV while taking into account this carrier diffusion, as seen in Equation (3.19), where W is the thickness of the silicon sample and D is the ambipolar diffusion coefficient, typically with values of 27-30 cm^2 /s.

$$SRV = \sqrt{D\left(\frac{1}{\tau_{surface}}\right)}\, tan\left(\frac{W}{2}\sqrt{\frac{1}{D\tau_{surface}}}\right) \tag{3.20}$$

The SRV is desired to be as low as possible, indicative of good surface passivation and enhanced minority carrier lifetime. Therefore, for very low SRV and when $tan(x) \approx x$, equation (3.20) can be approximated to:

$$SRV = \left(\frac{1}{\tau_{eff}} - \frac{1}{\tau_{bulk}}\right)\frac{W}{2} \tag{3.21}$$

The accuracy of this equation is less than 4% in error, as long as the surface recombination (and therefore passivation) is similar or identical on both sides of the fabricated sample. Usually, passivation studies are carried out on float-zone (FZ) silicon wafers with sufficiently high bulk lifetime such that its contribution to equation (3.21) can be neglected. Moreover, the bulk lifetime is hard to measure.

Parametrization of Auger recombination by Kerr et al. [168] can be employed to calculate bulk lifetimes of various wafers according to their resistivity and type, but it was shown that this leads to a rather large degree of inaccuracy [168]. Instead, the bulk lifetime is assumed to be infinite for passivation schemes that yield low surface recombination velocities and thus an upper limit for the effective *SRV* can be calculated using equation (3.22).

$$SRV_{max} = SRV < \frac{W}{2\tau_{eff}} \tag{3.22}$$

Traditionally, the thin dielectric layers used for surface passivation have been tuned to provide both electrical and chemical passivation simultaneously, but also a much needed anti-reflective effect. Moreover, most of these thin dielectric films have to go through a high-temperature activation step, known as *'annealing'*, in order to further enhance both chemical and FEP passivation components. In most cases, extrinsic passivation can be provided by additional hydrogenation to enhance chemical passivation or corona discharge to enhance the FEP component temporarily. However, this has yet to be adopted by industry.

Generally speaking, the surface recombination for a textured surface is much higher than a similar size flat surface, because of the added semiconductor surface area when texturing the surface, effectively adding more defect states into the bandgap and more dangling bonds exposed on the semiconductor surface. McIntosh and Johnson (2009) [169] found that texturing a silicon surface with micron-scale pyramids fabricated via *KOH* etching adds 73% silicon surface area to the existing {100} surfaces. Moreover, they have concluded that there is a larger number of unterminated bonds for the *KOH* etched {111} surfaces than for {100}, but also a higher concentration of defect states present in the bandgap because of induced mechanical stress. The next sub-sections provide a review of the state-of-the-art passivation techniques employed in industry today, covering materials such as silicon oxide and silicon nitride, with special focus on atomic layer deposition (ALD) aluminium oxide and combinations or 'stacks' of these materials.

It is important to notice that in most cases, τ_{eff} and *SRV* are reported for a minority carrier injection level $\Delta n = 10^{15}$ cm^{-3} both in literature and in this work.

3.5.2 Silicon dioxide

The most studied dielectric in the solar cell industry is silicon dioxide, which finds a wide range of applications, including surface passivation and antireflective coatings, with a wide range of deposition tools available nowadays. The first breakthrough in the field came with the work of Aberle (1992) [170] who thoroughly investigated the *Si/SiO₂/Al* structure and its properties. It was found that after sputtering a few hundred nanometers of aluminium on top of the silicon dioxide and annealing this stack at 450° C in forming gas (in presence of H_2), the *Al* reacts with water to create aluminium oxide (AlO_x) at the *SiO₂/Al* interface. This process is called 'alnealing'. The hydrogen released from this reaction diffuses to the *Si/SiO₂* and chemically passivates the bandgap defect states, as explained by Balk (1965) [171]. Based on this principle, Kerr and Cuevas (2002) [172] obtained minority carrier lifetimes as high as 5.25 ms in FZ n-type silicon 1.5 Ωcm and 1.65 ms in FZ p-type 1 Ωcm silicon. Later, Collett et al. (2017) [173] introduced charges in the dielectric oxide film at the same time as the hydrogenation process, achieving SRV as low as 0.5 cm/s for n-type FZ 1 Ωcm silicon and showing that extrinsic methods can be applied to further enhance this passivation process.

Silicon dioxide is known to provide very good chemical passivation by producing the lowest density of interface defects at the silicon surface. Typically, an untreated silicon surface can yield D_{it} values as large as 10^{14} cm^{-2} eV^{-1}, unsuitable for high-efficiency silicon devices [54], shown in Figure 3.12 a). This is due to the presence of P_b defects at the surface, that manifest as P_{b0} and P_{b1} for (100) silicon [174]. P_{b0} represents an unpaired electron that is backbonded with three silicon atoms (≡Si●), while the P_{b1} electron is backbonded to two silicon atoms and one oxygen atom (O=Si●) [175]. Both of these defects are electrically active and introduce energy states into the bandgap, as previously discussed. Upon silicon dioxide growth or deposition, the dangling bonds at the silicon surface get saturated and D_{it} is reduced to 10^{12} cm^{-2} eV^{-1}, Figure 3.12 b). A significant decrease is observed by

introducing hydrogen species in the passivation scheme, that terminates the bonds with hydrogen, as seen in Figure 3.12 c). This is due to the fact that the now hydrogenated atom has shifted the energy level of the defect states outside the bandgap of the material, providing D_{it} as low as 10^{10} cm^{-2} eV^{-1}. [175] The P_b center is electrically passivated during annealing in a hydrogen atmosphere by the reactions below, where P_bH represents the passivated centre [176]. The *Si-H* bond energy is 2.6 eV, being much more stable than *Si-O* [177].

$$P_b + H_2 \rightarrow P_bH + H \textbf{ or } \equiv Si\bullet + H^o \rightarrow \equiv Si\text{-}H \tag{3.23}$$

For this reason, this concept is widely used in passivating stacks of different materials, where silicon dioxide is the interfacial layer and closest to the silicon surface. Bonilla et al. (2016) [178] successfully employed both extrinsic methods (i.e. corona discharge and hydrogenation) to achieve minority carrier lifetimes in excess of 5 ms for flat n-type FZ 1 Ωcm silicon, corresponding to SRV as low as 0.24 cm/s. Using the same method, the group obtained SRV of 28 cm/s for a *KOH* textured surface. Bourett-Sicotte et al. (2017) [179] expanded this work by extrinsically hydrogenating the silicon dioxide film using a shielded ammonia plasma and making use of the corona discharge to achieve minority carrier lifetimes of 6.4 ms in flat n-type FZ 1 Ωcm silicon. Even though the high quality silicon dioxide thermally grown provides satisfactory results, it is difficult to employ such a growth method for black silicon, as there is a trade-off between the optical properties and the quality of passivation. Moreover, silicon consumption during such a process can negatively impact the morphology of the nanotexture and affect the optical properties.

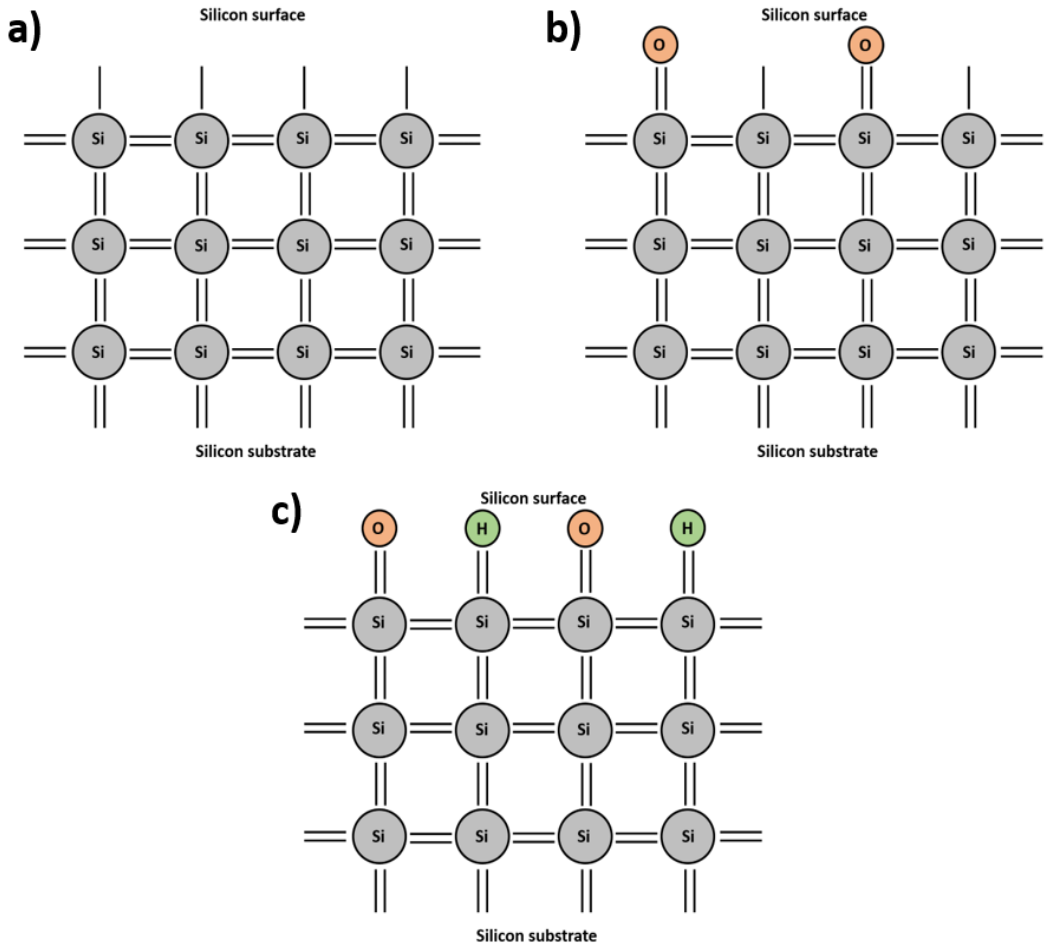

Figure 3.12: a) Unterminated silicon surface; b) Si/SiO_2 interface; c) Si/SiO_2 interface upon hydrogenation.

Therefore, one promising growth alternative for high quality SiO_2 was investigated by Grant and McIntosh (2009) [180] with moderate success. The nitric acid oxidation of silicon (NAOS) method promises to be a very cheap and reliable method of growing ultrathin silicon dioxide layers on top of the silicon surface. They used a 68% wt HNO_3 solution, boiled at 121° C for three hours to grow about 5 nm SiO_2. The group found no passivation to be present with the as-deposited film, but found an SRV of 107 cm/s after a 30 min anneal in nitrogen at 1100° C. This initial value further decreased to 42 cm/s after another 30 min forming gas anneal (FGA) in hydrogen atmosphere, but it was unfortunately found not to be stable. Therefore,

the SRV increased to 82 cm/s after a month. Others have investigated alternative deposition methods include Plasma-Enhanced Chemical Vapor Deposition (PECVD), but the passivation achieved was not comparable to that of thermally grown silicon dioxide. Duttagupta et al. (2014) [181] reports SRV of above 100 cm/s using this deposition tool, even after FGA treatment and extrinsic corona discharge.

3.5.3 Silicon nitride

Silicon nitride (SiN_x) is the most used dielectric in the photovoltaic industry because of multiple reasons. First of all, it has a suitable refractive index for anti-reflective coatings, and therefore is able to address optical losses effectively. Secondly, the deposition method of choice in industry for this material is PECVD, which releases amounts of hydrogen that diffuse to the Si/SiN_x interface and provides further chemical passivation (see above). Thirdly, silicon nitride layers are known to posses fixed positive charges, making them important candidates for passivating n-type front surfaces of commercially available solar cells. It was reported that nitride films show a high concentration of positive charge (> 10^{12} e/cm^2) that repels holes from the semiconductor surface [182]. Moreover, it has a somewhat large concentration of interface states D_{it} > 5 x 10^{11} e/Vcm^2 but slow capture rates to compensate for it. As a material and when considering the deposition method of choice, it is relatively easy to change the stoichiometry, resulting in either silicon or nitrogen-rich films. It was found that silicon-rich nitride films provide better chemical passivation, while nitrogen-rich films provide better FEP passivation because of the formation of Si-N_3 dangling bonds, a defect known as K-centre, where a silicon atom is backbonded to three nitrogen atoms [183]. However, Si-rich SiN_x layers have a larger refractive index, resulting in poorer optical respose and thus leading to a trade-off between electrics and optics inside the silicon device. Kerr and Cuevas (2002) [172] achieved SRV of 7 cm/s and 14 cm/s for n-type and p-type 1 Ωcm FZ silicon wafers, respectively, work which was later expanded by Chen et al. (2007) [184] and Richter et al. (2012) [185] to result in recombination velocities as low as 0.6 cm/s in n-type silicon.

It was found that when depositing nitride films using PECVD, a very thin interfacial SiO_2 was formed, due to a multitude of reasons, including its growth in-between wafer cleaning steps. This resulted in a dielectric stack with excellent passivation capabilities, due to the good chemical passivation provided by the dioxide and the strong FEP component of the nitride film. Bonilla et al. (2014) [186] succesfully employed such a stack to obtain SRV of 0.17 cm/s on 1 Ωcm n-type FZ wafers, using extrinsic corona discharge. With the same method, the group later [187] passivated textured surfaces, achieving SRVs of 34 cm/s for the as-deposited films, with a further reduction to 14 cm/s using corona discharge. It was reported that the silicon nitride acts as a capping layer for the silicon dioxide film, improving its chemical and thermal stability. Dingemans et al. (2011) [188] confirmed that SiO_x/SiN_x stacks posses a lower positive fixed charge than just the nitride layer, but still enough to provide effective FEP. This is most likely because the dioxide layer is preventing some charge injection from the silicon substrate into the nitride layer.

3.5.4 Aluminium oxide

The passivating properties of aluminium oxide (or alumina) have been well-known for decades, as demonstrated by Dingemans' work [189]. However, it was not until the advancements of the atomic layer deposition (ALD) method that this material became one of the first choices for electrical passivation, especially when considering the suitable refractive index and no significant absorption in the visible part of the spectrum. Hoex et al. (2006) [190] conducted an in-depth study on the electrical properties of alumina deposited via plasma-assisted atomic layer deposition (PALD), achieving lifetimes of 2-8 μs with the as-deposited film. However, after an activation step at 425° C for 30 minutes in nitrogen atmosphere, the lifetime was boosted to 6.6 ms for a thickness of 26 nm alumina layer on n-type 1 Ωcm FZ wafers, corresponding to SRV of below 2 cm/s. For p-type silicon, the effective lifetime reached a maximum of 1.2 ms, for a film thickness of 15 nm. Interestingly enough, the reported lifetime for 30 nm AlO_x on p-type is 1.2 ms as well, showing that there is a capping effect in the FEP component for thicker layers. Since oxygen was used as a precursor in his work, Hoex reported a very thin 1.5 nm SiO_2 layer being formed in-between the alumina and the silicon bulk, which again proved

to be beneficial for the passivation. It was concluded that the amount of passivation provided by aluminium oxide is comparable to that of silicon dioxide, proving satisfactory enough to raise interest.

Later, Hoex et al. (2008) [191] showed that the alumina film posseses a negative fixed charge of 10^{13} e/cm^2 and a low interface defect density D_{it} of just 10^{11} e/Vcm^2 after proper annealing and post-treatment. This is assumed to be because of the local reconstruction of the AlO_x at the interface during the annealing process. Hoex improved on his initial work to achieve lifetimes as high as 3 ms for flat n-type CZ 1 Ωcm silicon wafers. Later, Richter et al. [192] extended this work to obtain an SRV of just 0.26 cm/s for n-type silicon and of 0.95 cm/s for p-type silicon.

The composition of the alumina films varies vastly with the deposition method and temperature. Typically, hydrogenation occurs for low temperature depositions due to the presence of *OH*-group in the process, while some carbon impurities are present as well from the formed methane groups. However, it was shown that the carbon content is generally below 1% for a typical ALD process in the 150°-200° C range. It is important to specify that AlO_x films synthesized by ALD are amorphous, with lower optical bandgaps than their crystalline counterparts. This is especially important for PV applications, as parasitic absorption in the layer does not occur in the visible spectrum wavelength range, but rather for wavelengths below 200 nm.

In general, it was concluded in literature that thermal ALD (TALD) AlO_x films provide good initial chemical passivation, but poor FEP in their as-deposited state. In contrast, both PALD and PECVD AlO_x layers have poor initial chemical passivation, but better field-effect passivation [193]. This is thought to be due to an ultra-thin silicon dioxide layer grown interfacially between the silicon substrate and the alumina film. The thickness of this layer is around 1-2 nm upon deposition and proves to enhance the chemical passivation of the stack. After annealing, it has been reported that this thickness can further increase by 0.5 nm, without any detrimental effect to the passivation properties [194]. In all cases, after annealing, the parameters become similar, with a negative fixed high concentration charge of 10^{13} e/cm^2 present in the films. Dingemans et al. (2011) [194] reported that this fixed charge was found to be invariable across various depths in the alumina film.

Moreover, good surface passivation can be maintained for PALD AlO_x layers as thin as 5 nm, while TALD films would need to be at least 10 nm thick to provide comparable levels of passivation. Dingemans concluded that water-based TALD yields the lowest as-deposited D_{it} of just 10^{11} e/Vcm^2, compared to other deposition methods such as PECVD or APCVD where D_{it} exceeds 10^{13} e/Vcm^2 prior to annealing, while it also has the lowest fixed charge Q_f as deposited, 10^{11} e/cm^2 compared to 10^{13} e/cm^2 of PALD. It was reported that for high injection levels > 10^{15} cm^{-3}, the effective lifetime of alumina passivation on p-type Si decreases drastically, but with minimal change before this threshold. This is crucial for PV applications, as injection levels of 10^{12}-10^{14} cm^{-3} are typical. For n-type Si, the decrease in lifetime occurs below injection levels of 10^{14} cm^{-3}, due to increase in bulk recombination caused by the inversion layer with such a high negative charge on the surface.

Prior to the annealing of the alumina film, electron spin resonance (ESR) measurements revealed that the Si/AlO_x interface presents high density of P_b defects as in the Si/SiO_2 case with trivalently bonded Si atoms (≡Si●) [195]. This is due to the thin interfacially grown silicon dioxide layer present during ALD deposition and further increased with annealing. ESR measurements after the annealing process show that these defects do not remain at the interface. As mentioned before, some hydrogen diffusion to the interface occurs during the ALD process, yielding low D_{it} values as part of the chemical passivation.

Hoex et al. (2013) [196] later employed electron energy loss spectroscopy (EELS) to find the origin of the negative fixed charge present in the alumina layer, showing that there are electrons trapped at interstitial oxygen (I_O) and aluminium vacancies (V_{Al}). These point defects have energy levels in the bandgap. Shin et al. (2010) [197] found that both I_O and V_{Al} produce energy levels below the middle of the bandgap, closer to the valence band of silicon, thus being likely of trapping negative charges. Kimoto et al. (2003) [198] expanded the work and found that both tetrahedrally and octahedrally coordinated Al atoms are present in as-deposited alumina in an almost equal amounts, but the ratio drastically increases in favour of tetrahedrally coordinated *Al* atoms during annealing, as they start migrating towards the interface

to produce a negative charge, as opposed to the positive charge the octahedrally coordinated *Al* atoms posses.

It is clear that each of the three materials presented in here have various benefits when employed on the silicon surface, based on their electronic properties or suitability of deposition methods. Table 3.1 shows a summary of the electronic properties of these materials, where the values are reported for optimum conditions upon annealing. Few studies have succesfully reported black silicon passivation with deposition methods other than ALD, mainly due to the high deposition rates and poor conformity of oxidation processes or PECVD. As such, ALD alumina remains the main candidate for electrically passivating both p-type and n-type black silicon layers.

Table 3.1: Summary of the electronic properties of three passivating materials used in PV.

Material	Interface defect density D_{it} (cm^{-2} eV^{-1})	Fixed charge in the film Q_f (cm^{-2})	Record SRV (cm/s)
SiO_2	$>10^{12}$ (as deposited) 10^{10} (after FGA)	10^{10} – 10^{11}	0.17 [179] (n-type with extrinsic methods)
SiN_x:H	$>5 \times 10^{11}$	$>10^{12}$	0.64 [185] (n-type, PECVD)
AlO_x	3×10^{11} (as deposited) $<10^{11}$ (after annealing)	10^{11} (as deposited) 2×10^{12} – 10^{13} (after annealing)	0.26 [185] (n-type, plasma ALD)

3.5.5 Aluminium oxide for black silicon

Because ALD allows for great control over the uniformity of the film, has low deposition temperatures and low deposition rates, it quickly became the deposition method of choice for coating black silicon and other high-aspect ratio structures. Otto et al. (2012) [199] fabricated black silicon using reactive ion etching (RIE), resulting in structures of 1.7 μm height and about 180 nm period. They employed

TALD method to passivate these nanostructures with 100 nm AlO_x, achieving lifetimes of 446 μs for flat silicon and 173 μs for nanostructured silicon. Later, Otto et al. (2013) [200] fabricated three types of black silicon using the same approach, RIE with SF_6 and O_2, achieving recombination velocities of below 100 cm/s for all of the samples and SRV of below 4 cm/s for flat silicon. These deep structures presented SRV of 80 cm/s, the intermediate structures had SRV of 70 cm/s and the shallow nanostructures gave SRV of 13 cm/s, although they can be defined more as porous-silicon rather than black-silicon.

Almost at the same time, Repo et al. (2013) [201] fabricated similar nanostructures on CZ silicon, having 1 μm height and diameters of about 200 nm, showing an impressive surface reflectance of below 1% for certain wavelengths. After 23 nm alumina deposition using TALD and annealing at 430° C for 30 minutes in nitrogen atmosphere, the SRV obtained was approximately 12 cm/s, corresponding to lifetimes in excess of 2 ms. Later, the same group led by Savin successfully employed their black silicon and passivation techniques on an Interdigitated Back Contanct (IBC) solar cell to achieve efficiencies exceeding 22% [46]. Using cryogenic deep RIE, they fabricated structures of 800 nm height and diameters of 200 nm on 9 cm^2 cells. After depositing 20 nm alumina via ALD and annealing the film, they have found effective lifetimes of about 1 ms and concluded that surface recombination velocities of below 30 cm/s for such nanostructures is enough to boost the IBC power conversion efficiency to above 22%. Moreover, they have found that the alumina film plays an important anti-reflective role, further reducing surface reflectance as compared to the uncoated black silicon layer.

More recently, novel passivation schemes have emerged for black silicon, such as ALD synthesized SiO_2/AlO_x stacks. At first, van de Loo et al. (2017) [202] succesfully reported the employment of such a stack for heavily doped n^+ emitters, where passivation is more difficult. Using TALD, he deposited 5 nm of silicon dioxide followed by 30 nm of aluminium oxide on top of his nanostructures as a capping layer, such as in Figure 3.13, and annealed the stack at 400° C for 10 mins in nitrogen atmosphere. It was found that the stack provides excellent chemical passivation, showing D_{it} of below 10^{11} e/Vcm^2. Moreover, the films do not exhibit high negative

fixed Q_f, mainly because the dioxide layer is thick enough to prevent electron injection from the bulk into the alumina layer. It was reported that for low phosphorus ion implantation doses, the single alumina layer outperforms the stack, showing surface saturation current densities J_0 as low as 16 fA/cm^2. For high phosphorus ion implantation doses (10^{15} cm^{-2}), however, the implied open-circuit voltage increased from 609 mV (alumina only) to 640 mV for the stack. It is worth mentioning that the black silicon in this work received alkaline post-etching treatment, effectively reducing the nanostructures sizes down to 250 nm and thus degrading its optical properties.

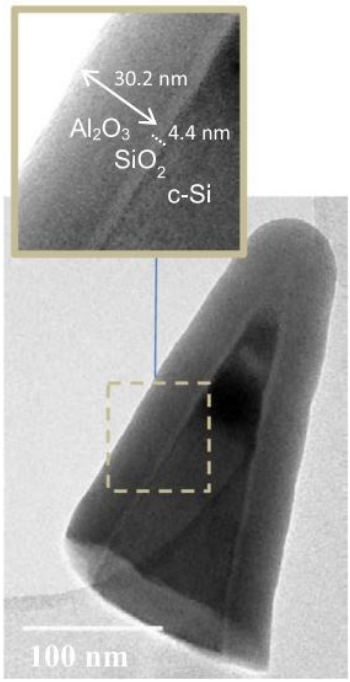

Figure 3.13: Scanning transmission electron microscope (STEM) image of a nanoneedle covered by SiO_2/Al_2O_3 ALD stack. Reproduced from Ref. [197].

Pasanen et al. (2017) [203] formed heavily doped emitters using *POCl₃* diffusion for 20 minutes for the purpose of evaluating the performance of SiO_2/AlO_x passivation stacks on black silicon. Therefore, two sets of samples were fabricated for comparison, one just with 22 nm alumina on top of the nanostructures and the other comprising of 6.5 nm SiO_2 deposited using PALD, followed by 30 nm alumina deposited via TALD. After the standard annealing process to activate the charges, it

was found that negative charge formation in the stack can be prevented by this thin dioxide layer, which acts as an electron tunneling barrier that again prevents charge injection from the bulk into the AlO_x. As such, it was reported that the stack is actually positively charged and outperforms the single alumina layer for heavily-doped n^+ emitters, because the fixed negative charge in the single alumina film is not enough to produce inversion below the surface. Moreover, it was confirmed that the stack confers a lower D_{it} because of hydrogen diffusion to the Si/SiO_2 interface. From on optical point of view, it was however reported that surface reflectance slightly increases in the 400-1000 nm wavelength range of interest. The group obtained implied open-circuit voltages comparable to those of van de Loo et al. (2017) [202]: 626 mV and 633 mV for two different $POCl_3$ recipes, respectively.

More recently, Chen et al. (2019) [204] reported lifetime values between 200 µs and 500 µs at an injection level of 10^{15} cm^{-3} for MACE fabricated structures. The results are dependent on the $AgNO_3$ solution concentration and the removal of the leftover *Ag* dendrites after the fabrication process. Surprisingly, the samples that have not undergone a silver removal step show the highest lifetimes, as RCA cleaning after the MACE process was enough to remove the leftover silver particles. Moreover, lifetimes in excess of 500 µs can be obtained upon polishing of the black silicon layer, but at the expense of sacrificing the optical properties. This is due to a reduction in the structure heights and thus silicon surface area with increased polishing duration, ensuring that the passivating layer has better conformity on the black silicon. Polishing times of 60 s can improve the effective minority carrier lifetime to above 900 µs. The group reports MACE black silicon layers with weighted average reflectance of 3.9 % and SRV below 30 cm/s upon passivation with thermal ALD and annealing at 400° C in nitrogen atmosphere.

3.6 Conclusions

In conclusion, a multitude of nanotexturing schemes have been proposed over the last decades as solutions for achievement of improved optical properties at device level, resulting in various nanostructures shapes, size and crystal orientation. Out of these, reactive ion etching (RIE) and metal-assisted chemical etching (MACE) remain the most promising black silicon (b-Si) fabrication techniques. In particular, MACE represents a straightforward wet-etching technique, that is highly scalable and provides reproducible and reliable realisation of low-reflective surfaces that aid in photongeneration. However, the improved optical properties of b-Si comes at the cost of high recombination inside the device, due to the semiconductor surface area increase that arises from such nanostructures. A range of dielectric materials can be employed as passivating films on top of a silicon substrate, to effectively reduce the density of interface defects and chemically saturate the unterminated silicon bonds. These defects have to effectively be addressed, as they essentially introduce energy levels inside the bandgap of the semiconductors, providing alternative routes of carrier recombiantion and hindering the electrical parameters of the solar cell. While materials like silicon dioxide and silicon nitride have been succesfully employed in planar or microtextured high-efficiency solar cells for decades, the deposition methods possess concerns related to the conformity on high-aspect ratio structures, such as those produced by RIE or MACE. As such, the resurgence of atomic layer deposition (ALD) promotes controllable film growth that is highly compatible with such deep nanostructures. Moreover, aluminium oxide has found great success when integrated into fabricated b-Si solar cells [46], owing to the large fixed negative charge that can be activated upon an annealing step. Table 3.2. shows a summary of the optical and electrical properties of the best-performing passivated b-Si layers with ALD aluminium oxide available in literature.

Table 3.2.: Summary of best-performing fabricated b-Si layers available in literature, indicating record SRV and average reflectance in 300-1100 nm wavelength range.

Fabrication method	Nanostructure height (nm)	Average broadband reflectance (%)	Passivating AlO_x thickness	SRV (cm/s)
RIE [201]	1000	1	23	12
RIE [46]	800	1	20	20
RIE [200]	600	6-9	100	13
MACE [204]	250	4	30	30

Chapter 4

Experimental Methods

This chapter serves as an introduction to the various fabrication and optical and electrical characterisation cleanroom and laboratory tools used throughout the thesis for the reliable realisation of low-reflective surfaces on silicon substrates. These include thermal atomic layer deposition (TALD), rapid thermal annealing (RTA), scanning electron microscopes (SEM), as well integrating sphere setups and a custom-built broadband wavelength and angle resolved spectrometer for optical measurements.

4.1 Fabrication

4.1.1Metal-assisted chemical etching (MACE)

The single-step Metal-Assisted Chemical Etching carried out in this project consists of a combination of two solutions mixed in a single beaker: aqueous $AgNO_3$ solution and a diluted *HF* solution. The substrate material used is (100) oriented double-side-polished phosphorus doped n-type c-Si wafers, with a resistivity of 1-5 Ω cm and thickness of 240 μm ± 20. Typically, cleaved samples of 4x4 cm^2 are used for fabrication and characterisation of MACE structures.

In order to remove the damage caused by the cleaving, the samples are first cleaned using a standard 3:1 Piranha etch in a Pyrex glass beaker (96% sulphuric acid and 31% hydrogen peroxide for 20 minutes). Then, they are rinsed thoroughly and dipped into a 7:1 Hydrofluoric Acid bath (50% stock *HF* for 5 minutes) for the purpose of removing any native oxides from the silicon. Another rinse for the samples is not needed, as the HF dip makes the silicon hydrophobic and does not negatively affect the MACE process itself in any way. The samples are then submerged into the etching solution consisting of 60 mM $AgNO_3$ and 14 M *HF* solution for the desired number of minutes, unless stated otherwise. These molarities correspond to 1g of $AgNO_3$ added to 150 mL of de-ionised (DI) water and topped up with 50 mL 50% *HF* to create the 200 mL MACE solution. A Fuming Nitric Acid solution (one part HNO_3 to one part DI water) is then used to remove the silver particles at the bottom of the etched nanowires for 5 minutes. A workflow diagram of the etching process is shown in Figure 4.1. Due to the *HF* in the MACE solution, the MACE step is performed in a polytetrafluoroethylene (PTFE) custom-made beaker. A fresh etching solution is prepared for each MACE process due to the silver consumption and *HF* volatility.

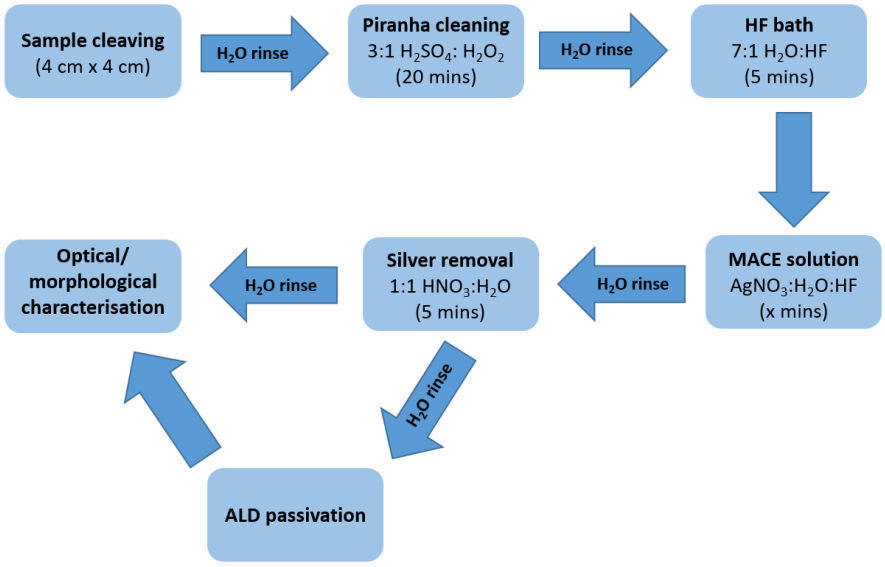

Figure 4.1: Step-by-step black silicon fabrication process diagram.

4.1.2 Thermal assisted atomic layer deposition (ALD)

Atomic Layer Deposition (ALD) is a chemical deposition method based on several sequential self-limiting reactions on top of the silicon substrate. It consists of an organometallic liquid and water precursors that are pulsed separately in order to form a monolayer of the desired material, atom by atom. The resurgence of ALD and its expansion towards new materials and mechanisms has made effective passivation of black silicon structures possible and more readily available. New materials have emerged for electrically passivating silicon surfaces using ALD, especially metal oxides such as aluminium oxide, hafnium oxide and titanium oxide, showing the flexibility and wide range of applications of the method.

In this work, the material deposited using thermal ALD is alumina, AlO_x using a Savannah ALD reactor (Cambridge Nanotech). The precursors used are water and trimethylaluminium (TMA), with the formula $Al_2(CH_3)_6$. The deposition process consists of two half-cycles and the reactions are summarised below. First, the hydroxilated surface reacts with TMA to create strong *Si-O-Al* bonds and methane (1). Then, the surface reacts with water for the creation of *Al-O-Al* bridges (2). For subsequent cycles, once *Al-O-Al* bridges are formed, reactions (3) and (4) become

valid upon TMA and water spray, respectively. Figure 4.2 below shows the chemical mechanism of the ALD growth. At first, the silicon surface is hydroxylated (*OH* terminated), either from exposure to air, oxygen or water, in order to ensure good adsorption of the precursors (a). The organometallic liquid precursor (TMA) is then sprayed onto the sample for a short period of time, to react with the hydroxyl groups (b). This removes the CH_3 groups and replaces them with *O-Al* bounds (c), while the resulting methane (CH_4) by-products and other unreacted molecules are removed from the chamber using nitrogen as inert gas (d). Water is then sprayed onto the sample (e), again removing the remaining CH_3 groups and creating *Al-O-Al* bridges to passivate the surface (f). The last step involves one more chamber purge to remove unreacted molecules and methane groups (g).

$$(1) Si\text{-}OH + Al(CH_3)_3 \rightarrow SiO\text{-}Al(CH_3)_2 + CH_4$$

$$(2) SiO\text{-}AlCH_3 + H_2O \rightarrow SiOAl\text{-}OH + CH_4$$

$$(3) Al\text{-}OH + Al(CH_3)_3 \rightarrow AlO\text{-}Al(CH_3)_2 + CH_4$$

$$(4) AlO\text{-}AlCH_3 + H_2O \rightarrow AlOAl\text{-}OH + CH_4$$

At the end of this, one monolayer of AlO_x is left on top of the silicon surface. In order to achieve the desired thickness, the number of cycles can be increased accordingly, as seen in Table 4.1, where the standard recipe used in this work is presented. In order to target thicknesses of 17 nm of alumina, 170 cycles are employed, owing to the 1 Å/cycle deposition rate at a temperature of 200° C. The recipe starts by specifying control points for the heater temperature during the process and then pre-heating of the silicon sample for 300 seconds to enhance adsorption. Lines 8 to 11 represent a basic ALD cycle (highlighted in yellow): line 8 represents the pulse time for the first precursor (TMA), then a wait period where the chamber is purged (line 9), followed again by pulsing of the second precursor (water, line 10) and eventually another chamber purge to remove by-products (line 11). Line 12 of the recipe is a loop that specifies how many cycles as those previously described are employed in the process to reach the desired thickness. It is important to notice that the pulsing of the precursors only takes milliseconds, while the purging of the chamber takes up to tens of seconds.

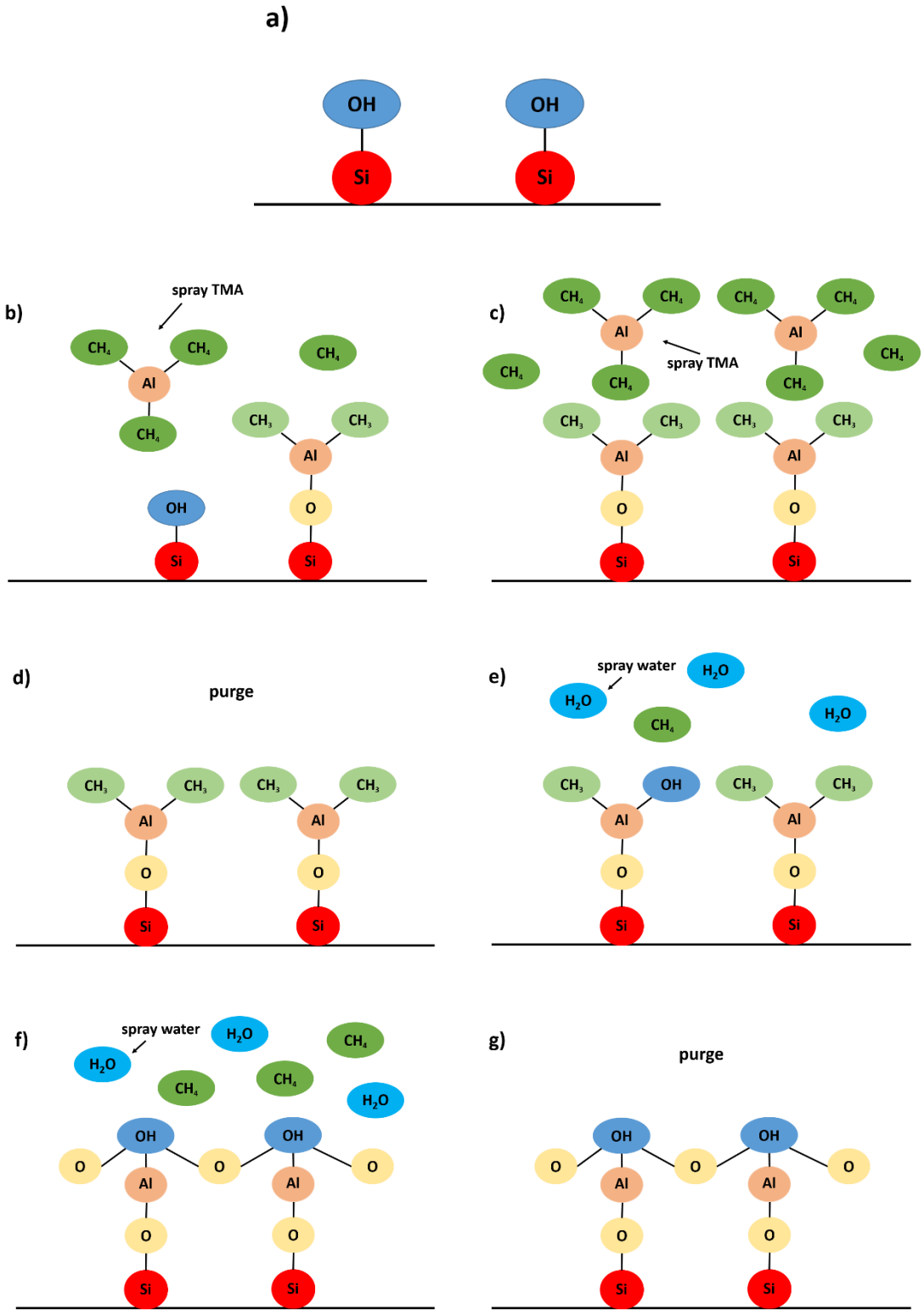

Figure 4.2: ALD growth mechanism of AlO_x showing the main steps involved. Adapted from Ref. [205].

Table 4.1: Standard recipe used for thermal ALD aluminium oxide deposition. Highlighted steps 8-12 (yellow) refer to one deposition cycle, which is repeated for a number of times in order to achieve the target thickness.

	Instruction	#	Value	Units
0	Flow	0	80	sccm
1	Heater	16	150	° C
2	Heater	15	200	° C
3	Heater	14	200	° C
4	Stabilize	16		
5	Stabilize	15		
6	Stabilize	14		
7	Wait		300	sec
8	Pulse	0	0.1	sec
9	Wait		12	sec
10	Pulse	1	0.04	sec
11	Wait		8	sec
12	Goto	8	170	cycles
13	Wait		120	sec
14	Flow	0	0	sccm

The standard recipe shown in Table 4.1 gives a flat uniform thin film of 17 nm ± 0.5 nm. However, this recipe is not suitable for high-aspect ratio structures, such as the black silicon presented in this work. For good conformal coverage, the exposure time must be extended for the precursors to penetrate in-between the nanowires and be adsorbed onto the surface of these structures. In order to achieve this, the valve that allows the inert purging gas to enter the chamber has to be specifically switched on and off in a separate line (i.e. lines 10 and 13 in Table 4.2), giving the precursors enough time to settle before chamber purging. Table 4.2 below shows an example of such an 'exposure mode' recipe, again using TMA and water as liquid precursors.

Table 4.2: 'Exposure mode' recipe for high-aspect ratio structures for ALD aluminium oxide layers. Highlighted steps 7-24 (yellow) refer to one deposition cycle, which is repeated for a number of times in order to achieve the target thickness.

	Instruction	#	Value	Units
0	Flow	0	80	sccm
1	Heater	16	150	° C
2	Heater	15	200	° C
3	Heater	14	200	° C
4	Stabilize	16		
5	Stabilize	15		
6	Stabilize	14		
7	Wait		300	sec
8	Flow	0	5	sccm
9	Wait		3	sec
10	Stopvalve		0	
11	Pulse	0	0.1	sec
12	Wait		10	sec
13	Stopvalve		1	
14	Flow	0	80	sccm
15	Wait		10	sec
16	Flow	0	5	sec
17	Wait		3	sec
18	Stopvalve		0	
19	Pulse	1	0.04	sec
20	Wait		10	sec
21	Stopvalve		1	
22	Flow	0	80	sec
23	Wait		10	sec
24	Goto	8	170	cycles
25	Wait		120	sec
26	Flow	0	0	sccm

Lines 8 to 24 represent an ALD cycle comprising of six main steps. At first, the carrier gas flow must be decreased in line 8 to ensure that the pressure inside the chamber when pulsing does not get close to atmospheric pressure. Line 10 closes the stop valve and allows the first precursor (TMA) to diffuse inside the black silicon layer for 10 seconds, after which the stop valve is opened again. This is followed by a standard chamber purge using inert gas at 80 sccm to remove by-products. The carrier gas flow is decreased once more for the second precursor pulse and the process is similar: the valve is switched off to allow a diffusion time of 10 seconds (line 20), then switched on and the chamber is cleaned. This whole cycle is repeated for 170 times in order to achieve the 17 nm thickness desired.

An 'exposure mode' ALD recipe for SiO_2 has also been developed for the purpose of passivating black silicon surfaces with a dual-stack comprised of alumina and an ultrathin dioxide layer to improve the chemical passivation component. The precursors in this case are tris(dimethylamino)silane (TDMASi) with chemical formula $((CH_3)_2N)_3SiH$ and ozone (O_3) obtained from the ozone generator of the Savannah ALD tool. Table 4.3 shows the ALD recipe of 200 cycles at 150° C that yields a silicon dioxide layer thickness of 2 nm, corresponding to a deposition rate of 0.1 Å/cycle at this temperature.

The deposition process is similar to the AlO_x case, but has some extra steps inserted for turning on the ozone valve and the external ozone generator (lines 8 and 10 respectively), connected to #4. The first cycle syntax (lines 12 to 14 highlighted in blue) is added to purge the silicon wafer inside the chamber with ozone for further cleaning of the substrate before deposition. Lines 16 to 26 (yellow) indicate a normal exposure mode ALD cycle where the precursors are pumped sequentially inside the chamber with the purging valve turned off for 28 seconds for every TDMASi spray.

Table 4.3: Exposure mode ALD recipe for SiO_2 deposition. Highlighted steps 12-14 (blue) and 16-26 (yellow) refer to one deposition cycle, which is repeated for a number of times in order to achieve the target thickness.

	Instruction	#	Value	Units
0	Flow		5	sccm
1	Heater	14	150	° C
2	Heater	15	150	° C
3	Heater	16	150	° C
4	Stabilize	14		
5	Stabilize	15		
6	Stabilize	16		
7	Wait		300	sec
8	Ozone flow		1	valve on
9	Wait		20	sec
10	Ozone power		1	O_3 on
11	Wait		120	sec
12	Pulse	4	0.2	O_3
13	Wait		10	sec
14	Go to	12	30	cycles
15	Wait		20	sec
16	Flow		5	sccm
17	Wait		1	sec
18	Stopvalve		0	
19	Pulse	2	0.05	sec
20	Wait		28	sec
21	Stopvalve		1	
22	Flow		20	sccm
23	Wait		13	sec
24	Pulse	4	0.2	sec
25	Wait		13	sec
26	Go to	16	200	cycles
27	Ozone power		0	O_3 off
28	Wait		30	sec
29	Ozone flow		0	valve off
30	Flow		5	sccm

4.1.3 Rapid thermal annealing (RTA)

Annealing refers to any modification of the properties of a material when subjected to high temperatures. In this work, a JIPLEC RTA furnace is used to anneal the as-deposited alumina passivation films to activate the negative fixed charge in this layer. The furnace can achieve temperatures as high as 1000° C for 15 minutes with a maximum step change of 25° C/second. The main advantage of using this tool as opposed to full-scale boat furnaces is given by the reduced time of the annealing process, where loading of the wafers and temperature ramping up are significantly decreased. Effective electrical passivation using this tool is reached when annealing the alumina layer at 425° C for 30 minutes in N_2 atmosphere and the recipe used is detailed in Table 4.4. A type K chromel-alumel thermocouple in contact with the substrate ensures accurate reading of the sample temperature and minimal to no fluctuations in the process.

Table 4.4: RTA recipe parameters for optimal annealing of ALD AlO_x layers.

Step number	Instruction	Duration
1	Buffer wait	3 sec
2	Chamber vacuum	30 sec
3	Chamber purge (wafer clean)	30 sec
4	Chamber vacuum	30 sec
5	Chamber purge (wafer clean)	30 sec
6	Chamber vacuum	10 sec
7	N_2 flow (500 sccm) and power setpoint (first ramp-up)	30 sec
8	N_2 flow (500 sccm) and power held at setpoint (425° C)	30 sec
9	N_2 flow (500 sccm) and temperature setpoint (second ramp-up)	1 min
10	N_2 flow (500 sccm) and temperature held at setpoint (425° C)	30 mins
11	N_2 flow (500 sccm) and power setpoint to 0 (ramp-down)	30 sec
12	Cooldown	5 mins

4.2 Standard characterisation

4.2.1 Scanning electron microscopy (SEM)

Scanning electron microscopy (SEM) is a characterisation tool that has found its place in many research fields that include material and nanomaterial characterisation. The electron microscope is capable of providing morphological and topographical detail of a specimen with good resolution < 10 nm by employing an electron beam that scans the surface of a sample in a pattern and forms an image from electrons or x-rays arising from a multitude of interactions with the atoms in the sample [206-207]. In traditional SEM, an electron gun is comprised of a thermionic emitter such as tungsten filament to provide a large and stable current in a small electron beam. The tungsten material is either heated at large temperatures or subjected to a strong electric field such that electrons escape from the material itself and high energy is transferred to the beam. These electrons, known as primary electrons (PE) are further accelerated so that they possess very high kinetic energies up to 40 keV and interact with the sample atoms in the near-surface regions.

After the electron beam is formed from the filament, electromagnetic lenses made from copper wire coils converge the beam by the application of large currents that in turn generate a magnetic field. A condenser lens reduces the beam diameter to the desired spot size for the process and enables good resolution. Scanning coils are used to scan the sample surface with the electron beam and an increase in the current flowing through the coils leads to higher possible magnification. The objective lens, which is the lowest lens in the SEM column, is used to focus the beam on the specimen according to the working distance (distance between specimen and this lens). A schematic of the SEM columns containing these components is shown in Figure 4.3.

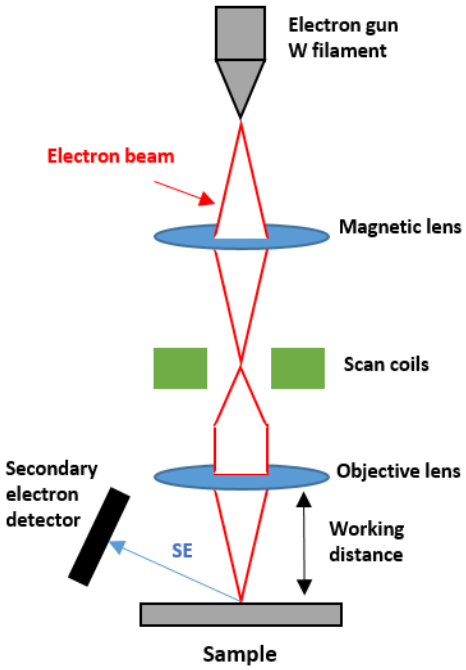

Figure 4.3: SEM column showing the main components and the travel path of the electron beam. Adapted from Ref. [206].

Primary electrons are incident on a sample surface and upon inelastic scattering, electrons that are loosely bounded to the outer shell of the atoms are emitted with very low kinetic energies < 50 eV, known as secondary electrons (SE). Due to this low energy, only SE generated within a few nanometers of the surface of the sample material have a chance of escaping the material. Usually, SEM imaging is carried out in high vacuum conditions (pressure < 10^{-6} mTorr) so as to prevent the interactions of SE with environmental gas molecules that may be present in the chamber and allow them to be safely collected by a secondary electron detector. The intensity and the position of these collected SE allow for morphological and topographical representation of the specimen, such as height, depth and orientation of the features.

Several parameters influence the operation of the SEM and the depth at which these electron-atom interactions occur within the sample, known as interaction volume. For example, if the acceleration voltage is large, the interaction volume

increases and the primary electrons are able to penetrate deeper into the material. Conversely, if the atomic number of the specimen is high, the energy loss per nanometer of the primary electrons increases and they cannot penetrate as deep into the material. Typically, backscattered electrons (BSE) are also emitted from the specimen as the primary electrons that are reflected back and are used in studying the surface composition variation of the sample materials, but not used for imaging. Large tilt angles of the specimen lead to PE being able to move larger distances in the near-surface region, resulting in many SE and thus these regions appear brighter than the region where the electron beam would be normally incident. As such, a clear distinction can be made between the different facets of a prepared specimen, leading to a quasi 3D representation.

In this work, various magnifications, accelerating voltages, emission currents, tilt angles and field of views are used to morphologically characterise textured black silicon surfaces, from both top-view and cross-sectional perspectives. The SEMS used are JEOL JSM-7500F FEG-SEM and CarlZeiss NVision40 FIB-SEM. In many cases, the high resolution and quality of the SEM images result in various parameters, such as thickness and diameters of the nanostructures, to be taken directly from the post-processed images.

4.2.2 Helium ion microscopy (HIM)

The recent development of the Helium Ion Microscopy (HIM) aims to overcome a number of limitations commonly found in traditional SEM processes and builds upon Field Ion Microscopy (FIM) introduced in the 1950s [208-209]. As such, HIM is very similar to SEM in operation, but with the use of a helium ion beam rather than an electron beam, which possesses several advantages. However, it still mainly operates on the collections of secondary electrons to provide details on surface morphology of the sample.

In FIM, a very sharp tungsten tip is subjected to a large positive voltage in cryogenic temperatures and in ultra-high vacuum in the presence of helium or neon gases, which leads to a strong electric field across the metal tip. This electric field ionizes adsorbed gas atoms onto the filament tip and thus the noble gas atoms

become positively charged and are repelled and accelerated away from the tip [209]. In HIM, the commonly obtained spherical tip of the filament is further manipulated so that a pyramid shaped bump is formed instead, leading to a set of three atoms (trimer) that share the entire helium gas supply, rather than a few hundred atoms [210].

In general, as previously discussed, the interaction volume of the electron beam inside the specimen material is desired to be as low as possible, such that information is collected of the morphology in the immediate near-surface of the material and thus resolution is not affected. For SEM, one primary electron from the electron beam generates a single secondary electron, while for HIM, a single helium ion generates 2 to 11 secondary electrons [211]. This abundance of SE leads to high contrast imaging and eases the process of differentiating between various materials in the sample. Moreover, the use of the He beam (as opposed to a heavier ion beam such as gallium) ensures that less damage in the form of in-situ chemical or physical alterations occurs to the target specimen.

Another advantage of HIM over traditional SEM is the very large brightness of 1-4 x 10^9 A/cm sr^2. In combination with a very low energy spread < 1 eV, this leads to a much smaller probe size on the sample of interest. Furthermore, the depth of field is increased by a factor of 5 over SEM when similar conditions are used. In SEM, the electrons possess small momentum that lead to pronounced diffraction effects that may affect the collected data. In contrast, the helium ion momentum is over 300 times larger and subsequently leads to de Broglie wavelengths that are 300 times smaller, thus minimising these effects. It was reported that resolutions below 0.3 nm are possible with HIM operating at a voltage of 25-30 kV [211].

More advanced HIM tools allow the user to switch between the He beam and the more aggressive neon beam, which can be used for milling silicon surfaces and textures. As such, more insight can be gained by sectioning long aspect ratio nanostructures, such as MACE black silicon, to enable morphological characterisation towards the bottom of the wires. Moreover, the conformity of the passivating layers can be further studied in the deep trenches and crevices of the textured bulk by this method, leading to an advanced understanding of optimised

deposition processes for this purpose. The tool employed in these studies is a Zeiss Orion Nanofab *He/Ne* ion microscope with in-situ milling capabilities. Unless otherwise stated, the *He* ion beam current used for imaging was 0.5 pA at an accelerating voltage of 30 kV and the *Ne* ion beam current was 3 pA.

4.2.3 Hemispherical reflectance measurements

Hemispherical reflectance measurements are important to characterise the optical response of a textured surface and to obtain a metric that can directly assess a texture's capability of reducing top surface reflectance. In this work, the measurements are carried out with a DTR6 integrating sphere as part of the PVE300 Bentham system [212] to provide a comparison between flat and textured surfaces obtained via various etching methods, such as alkaline-etching or MACE processes, with and without an anti-reflective coating.

The system makes use of a dual light source with 75 W xenon and 100 W quartz tungsten-halogen bulbs that ensure broadband emission in the range 300-2500 nm. A symmetric triple-grating monochromator allows for precise control over the wavelength of the incident light with an accuracy of ± 0.2 nm. The integrating sphere has a diameter of 150 mm and its interior is coated in a highly reflective barium sulphate (Ba_2SO_4) material with > 99 % reflectance. At the bottom of the sphere, a calibrated silicon detector is responsible for collecting data in the typical wavelength range of 300-1100 nm. The sample is mounted at 8° angle to the incoming beam so that the specular reflection does not exit out of the input port and instead is reflected onto the walls of the integrating sphere, such as in Figure 4.4 a). The presence of a baffle between the sample and the detector prevents light being collected immediately and promotes multiple bounces inside the sphere. Typically, a known calibrated reference reflection standard is used prior to the sample measurement, which consists of a near 100% reflective material $R_{standard}$, to establish a reference for the collected signal's intensity $I_{standard}$. Then, the standard is replaced by the actual sample of interest and the intensity I_{sample} is again collected when light is incident on the specimen. The ratio of the two will represent the percentage of the standard's known reflectance and be used to calculated the sample's reflectance

R_{sample}, as in Equation (4.1). As such, reflectance data is expressed in percentage and refers to the percentage of total incident light that is reflected away from the sample surface.

$$R_{sample}(\lambda) = R_{standard}(\lambda)\frac{I_{sample}(\lambda)}{I_{standard}(\lambda)} \quad (4.1)$$

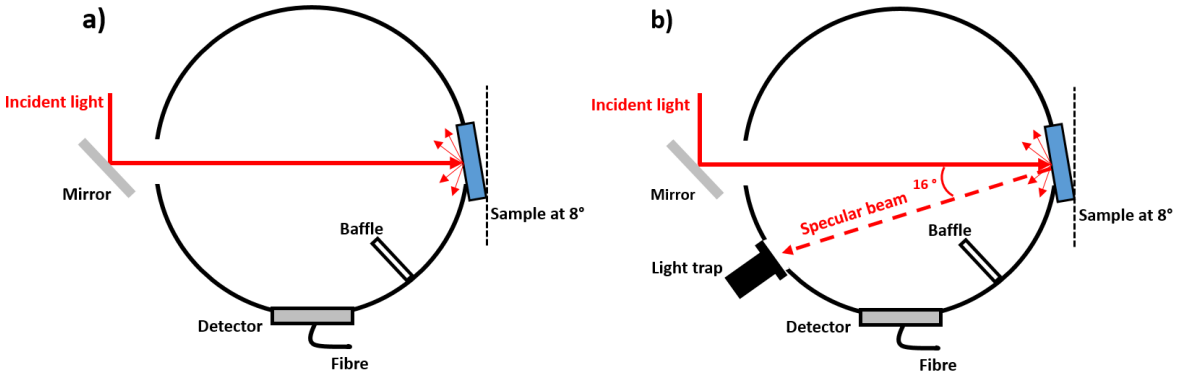

Figure 4.4: Schematic of the integrating sphere for a) total hemispherical reflectance; b) diffuse hemispherical reflectance measurements.

In general, a typical hemispherical reflectance measurement taken with the setup shown in Figure 4.4 a) involves the collection of reflected light averaged for all scattering angles and all azimuth rotations, due to multiple bounces occurring inside the sphere and some of the reflected light being incident again on the sample. The resulting data is the total hemispherical reflectance R_{total}. However, if one of the exit ports is replaced with a light trap to remove the specular beam from the integrating sphere without any bounces, only light reflected away from the specular direction will be averaged and thus collected. This is called diffuse hemispherical reflectance ($R_{diffuse}$) and a schematic of this setup is shown in Figure 4.4 b). The ratio of these introduces a metric called reflectance haze (H), which describes the percentage of light reflected and scattered away from the specular direction and thus how diffusely-reflective a textured surface is, as in equation (4.2) [213]. It is important to notice that no angular description can be inferred from these measurements, as the reflectance haze contains the contribution of the reflections arising from all angles of rotation and scattering. Moreover, the eliminated specular reflectance $R_{specular}$ can

be calculated as the difference between the total and the diffuse hemispherical reflectance, as in Equation (4.3).

$$H(\lambda) = \frac{R_{diffuse}(\lambda)}{R_{total}(\lambda)} \quad (4.2)$$

$$R_{specular}(\lambda) = R_{total}(\lambda) - R_{diffuse}(\lambda) \quad (4.3)$$

In the case of the DTR6 integrating sphere, the exit port diameter is 30 mm. As such, for diffuse reflectance measurements, light reflected in a cone of ± 6° about the specular reflectance point is eliminated from the system. For a more accurate measurement of the surface reflectance of a sample, an appropriate reflectance standard must be used. For example, if the sample consists of a highly diffuse textured surface, such as MACE black silicon, a low reflective diffuse standard is required. If a polished silicon surface is measured, then a specular, high reflectance standard is appropriate. Therefore, for b-Si measurements shown in this work, a 2 % diffuse black reflective standard was used to avoid large errors in the collected signal. Data was collected every 5 nm in the 300 nm – 1100 nm wavelength range.

4.2.4 Quasi-steady-state photo-conductance decay

Large effective minority carrier lifetimes are crucial for the design and operation of high efficiency silicon solar cell, so that photogenerated electron-hole pairs can contribute to the electrical power of the silicon device before recombining. However, measurements of such lifetimes have been traditionally difficult to carry out. In the 1990s, due to developments of Cuevas and Sinton [214-215], the quasi-steady-state photoconductance decay (QSSPCD) method was established as a straightforward and convenient method of providing carrier lifetime values without the need of electrical contacts for the target specimen. QSSPCD measurements are carried out at or near steady-state conditions in a silicon sample, such that the recombination and generation processes are assumed to be similar, as well as their respective current densities, in equations (4.4-4.5). Moreover, light absorbed by a semiconductor material gives rise to a number of free charge carriers that increase the conductivity of the material, known as photoconductance. Assuming charge

equilibrium at steady-state inside the silicon material, the photoconductance, σ, can be written as in equation (4.6).

$$J_{recombination} = J_{photogenerated} \tag{4.4}$$

$$\Delta n = \Delta p \tag{4.5}$$

$$\sigma = q\,(\mu_n \Delta n + \mu_p \Delta p) \Rightarrow \sigma = q\,\Delta n\,(\mu_n + \mu_p) \tag{4.6}$$

- $\boldsymbol{\mu_{n.p}}$ are the mobilities of electrons and holes, respectively
- $\boldsymbol{\Delta n,p}$ are the excess minority carrier concentrations
- $\boldsymbol{q}$ is the elemental charge.

The recombination rate, G, inside the material can be expressed as a function of the minority carrier effective lifetime τ_{eff} as in equation (4.7):

$$\Delta n = G\,\tau_{eff} \tag{4.7}$$

The developments of the Sinton WCT-120 lifetime tester [216] allows for measurements of excess photoconductance of a sample upon subjection to a short light pulse using an RF inductive coil. As such, if the light pulse is long and slow-decaying such that it is at least 10 times larger than the effective minority carrier of the specimen, steady-state conditions are met and the above equations are valid. The conductivity is measured, as well as the initial intensity of the light pulse using a light detector mounted on the tool, both as functions of time. Using equation (4.6) above, the conductivity values can be converted into excess minority carrier densities for any moment in time, using input parameters such as the resistivity and the thickness of the sample, as well as various look-up tables or models for charge carrier mobilities inside the silicon material available in literature as functions of resistivity and doping profiles [168]. The measured light intensity can be converted into generation rates G with various options accounting for the optical constant of the specimen, such as various antireflective coatings or textured surfaces on top of the bulk. As such, the generation rate as a function of excess minority carrier density

can be measured, and then the effective lifetime as a function of excess minority carrier density can be calculated using equation (4.7).

Transient photoconductance decay measurements are also possible for long lifetime samples, assuming carrier concentrations are not in steady-state and generation rate is zero. Equation (4.8) shows the dependency of carrier lifetime, τ_{eff}, with respect to the transient decay of the excess minority carrier concentration with time, leading to the generalized case presented in equation (4.9), where both generation and non-steady-state conditions may be present. When G=0, equation (4.9) becomes equation (4.8), and when $d\Delta n/dt$ = 0, equation (4.9) becomes equation (4.7) above.

$$\tau_{eff} = \frac{-\Delta n}{d\Delta n/dt} \tag{4.8}$$

$$\tau_{eff} = \frac{\Delta n}{G - d\Delta n/dt} \tag{4.9}$$

In the transient case, the pulse of light must be sufficiently short compared to the minority carrier lifetime of the sample so that excess carrier density is present after the flash has been turned off. This mean that only well passivated specimens can be measured using the transient method, with effective lifetimes > 100 μs. However, this method does not involve generation rate calculations, making the results independent of optics and sample shape, leading to more accurate results.

4.2.5 Wavelength and angle resolved scattering measurements

4.2.5.1 Introduction and setup description

Wavelength and angle resolved scattering (WARS) measurements can provide useful insight into the antireflective texture morphology and its optical behaviour and help tailor these responses for efficiency gain at device level. It is preferential that the textured solar cell top surface not only maintains low surface reflectance across a variety of incident wavelengths and angles, but that it also redirects the reflected and transmitted energies to wide and oblique scattering angles for the entire spectrum. The importance of these measurements comes from the lack of characterisation of these properties with commonly used tools, such as hemispherical reflectance measurements carried out with an integrating sphere. One metric used to describe how a textured surface scatters light upon incident illumination is the reflectance haze, which represents the ratio of the diffuse hemispherical reflectance and the total reflectance (see section 4.2.3) [213]. However, the reflectance haze shows only how diffusely reflective a surface is and lacks information on the angle distribution of these reflections. A textured surface that predominantly scatters light around 20° can have the same reflectance haze profile as a textured sample that scatters at much steeper angles, even though their implications and utility in a silicon solar cell device might vastly differ.

For this purpose, a previously introduced [219] home-built tool was employed in this project to capture such angle and wavelength dependencies and to further optically characterise scattering properties of textured surfaces that complement their antireflective properties. The setup consists of a collimated supercontinuum white laser that irradiates a mounted textured sample and a detector arm that sweeps in a circle around the sample to collect the reflections at various angles in plane. The optical fibre on the detector side is coupled to a spectrophotometer sensitive in the wavelength range 300-950 nm. A sketch of the system is presented

in Figure 4.5. The accurate control of the rotation stages is ensured by a custom LabVIEW interface that writes the data in Excel files for further processing.

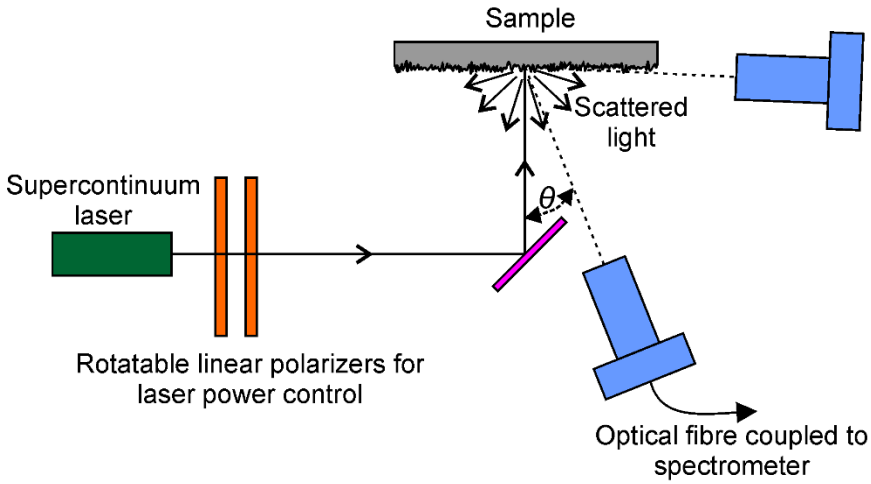

Figure 4.5: Schematic of the WARS system, showing optical components, sample illumination and detector movement.

4.2.5.2 Light source

For this type of measurements, it is important that the light source allows investigations of millimetre areas on the textured samples and be collimated to avoid diffraction artefacts during data collection. A Fianium SC-450-2 laser [220] is used as the primary source for the WARS tool, which outputs energy in the 450-2200 nm wavelength range and has an output power of 2W, powerful enough to detect signals when the measurement is carried in-plane and thus only a small portion of the total reflected out-of-plane light is sampled. When passed through the various optical components, the beam spot size that reaches the sample is ~1.5 mm in diameter, which covers a sufficient area of the textured surface to observe reflectance patterns for nanostructured specimens (i.e. black silicon). The incident laser light passes through two Glan-Taylor calcite prisms that polarise it by the means of total internal reflection, allowing either s or p polarised light to go through while eliminating the other, according to the position of the second polariser. The prisms also allow control over the intensity of the laser beam using Malus' law described in Equation (4.10) by changing the relative angle between the two prisms

using a DC motor, resulting in minimal or no changes to the laser beam profile as a function of wavelength.

$$I = I_0 cos^2\theta \tag{4.10}$$

- $\boldsymbol{I_0}$ is the intensity of the initial laser beam
- $\boldsymbol{\theta}$ is the relative angle in degrees between the two calcite polarisers

Figure 4.6 shows the laser beam distribution with wavelength that is incident on the sample, which must be taken into account when applying quantitative corrections to the collected data. As only one measurement of the direct beam proved to be noisy (blue trace), multiple measurements were taken and averaged in order to smooth the signal (red trace). For this, the detector was positioned at roughly 180° such that it is aligned to the path of the incident beam and the signal is maximised, ensuring that there is no scattering from apertures or other optical components that might affect data collection and thus the spectrum.

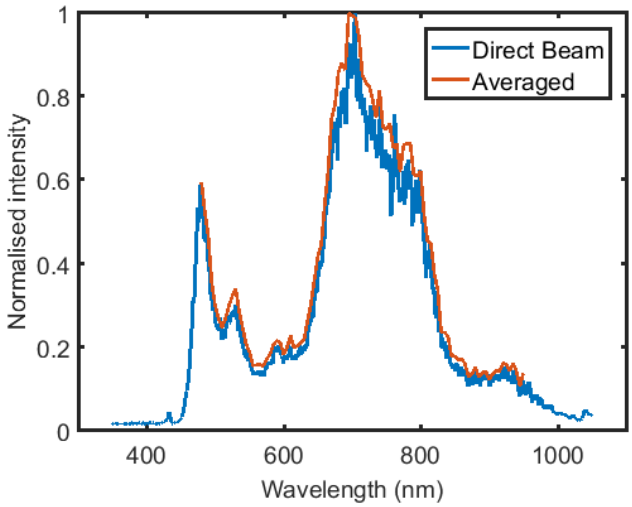

Figure 4.6: Normalised (such that the highest value is equal to 1) supercontinuum laser spectral distribution profile.

4.2.5.3 Data collection

As minimising data collection time is desirable for these measurements, as opposed to a monochromator, the system makes use of a 16-bit B&WTek Glacier X Si CCD array spectrophotometer with 25 μm wide slits for high enough throughput connected with a multimode optical fibre with 600 μm collection diameter. The spectrophotometer is sensitive in the 350-950 nm wavelength range and thus combines with the light source to reliably capture useful data in the 450-950 nm range. The ideal dynamic range of the spectrometer is 65535 counts. The LabVIEW program offers a variety of options for selecting integration time, including dynamic adjusting during measurement to maximise the captured signal without saturation. However, it is preferential that the integration time of the spectrophotometer is chosen such that the signal-to-noise ratio (SNR) of the data is maximised to filter out unwanted artefacts without saturating the signal, resulting in longer integration times and total measurement times for low reflective surfaces, such as MACE black silicon.

Figure 4.7 shows an exemplary measurement of the same sample at various integration times with the incident laser power kept fixed. Even though all of the data presents the same signal envelope and preserves its shape, it is obvious that longer integration times improve the signal-to-noise ratio, as the black trace corresponding to 13000 ms integration time is the smoothest signal and fluctuates the least. As the data is not normalised and the unit for intensity is the total number of counts, the relationship between the integration time and the intensity of the signal is therefore proportional, shown by the intensity of the peak situated at about 450 nm in Figure 4.7. For each integration time, a corresponding measurement of the dark spectrometer noise was taken, as this does not scale proportionally with the signal. Thus, the SNR values for each case can be calculated by taking the ratio of the power of the signal to the power of the noise and the results are shown in Table 4.5. It is important to notice that changing the intensity of the direct beam via the polarisers will have an impact on the optimal integration time and the SNR as well. Therefore, there is a trade-off between the intensity of the direct beam and the

integration time when carrying out measurements for a particular sample and the most optimal parameters will differ accordingly for various textures.

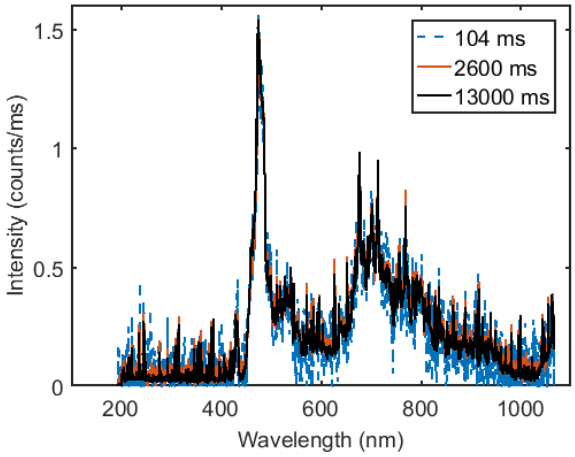

Figure 4.7: Exemplary measurement with three integration times. The highest integration time (black trace) measurement shows the best signal-to-noise ratio and is preferential for measurements on textured surfaces.

Table 4.5: Calculated SNR values for different integration times for fixed nominal laser power.

Integration time (ms)	**SNR (signal : noise)**
104	6 : 1
2600	14 : 1
13000	27 : 1

In most cases, multiple measurements are taken for the same data point to make the signal smoother when averaging in the post-processing steps and eliminate

errors, as well as multiple initial measurements to establish the optimum SNR for the target specimen.

4.2.5.4 Position control

Part of the reason why scattering measurements are scarce in literature is the complex nature of the system alignment and the precise control over the various components. For this purpose, both the DC motor-driven translational and rotational stages are controlled via a Newport XPS controller, capable of maintaining 0.01 μm and 0.02° positional and angular resolution, respectively. This enables free motion of the sample wall in the *x, y* and *z* directions for alignment, as well as polar and azimuth angle rotations for incidence. The detector arm has 180° motion and can be used for both transmittance and reflectance scattering measurements. For accurate positioning of the textured sample, certain alignment steps must be followed, such as ensuring that the specular reflected beam overlaps with the laser direct beam for normal incidence, as well as alignment of the detector arm to the centre of rotation of the sample in both polar and azimuth directions. One important consideration is the tilt of the sample and its distance from the detector, as reflections are desired to pass through the centre of the optical fibre and thus the collected signal be maximised. A variable aperture is placed in front of the optical fibre to change the angular acceptance of the data collection, as the beam spot size is greater than the diameter of the fibre and measurements are typically carried out for every 1° movement of the detector. In most cases, the angular acceptance of the system is kept to ± 0.4° to prevent overlapping of data during consecutive measurements. The LabVIEW program has a built-in delay for every angle of motion, enough to ensure that all the stages are in the desired positions before capturing the signal.

4.2.5.5 Limitations and errors

The complex process of aligning the various optical components and stages may lead to errors or unwanted artefacts during the measurement. For example, the laser beam is redirected by many mirrors and through apertures that may have their own

scattering contribution to the data collected. For this reason, the inside of the system enclosure is taped with black cloth at various points to minimise stray light and the laser origin and its intensity control are separated from the sample under study.

A 45° redirecting mirror just in front of the sample wall makes it impossible to capture the specular beam of the sample (see Figure 4.5). Therefore, the system is capable of outputting reliable data only in the 6° - 90° angular range. As part of the alignment process, the low reflectance textured sample is usually replaced with a mirror or another highly reflecting material that may not have the same thickness as the specimen under study. Therefore, this may lead to inconsistencies in the measurement if the thickness of the wafer is not accounted for when re-adjusting the translation stages or if the sample is not mounted flat on the wall due to varying tilt. In some rare cases, large azimuth rotations of the sample may trigger the need for realignment due to the resolution of the rotational stages. As such, the sample position needs to be compensated for to ensure the direct beam irradiates the same area of the specimen when the azimuth angle is changed.

4.2.5.6 Angular and geometrical corrections

As common with spectroscopy measurements, the noise level of the spectrophotometer and the dark intensity of the environment must be collected and subtracted for each measurement of a sample. As the supercontinuum laser has its own wavelength distribution profile (see Figure 4.6), the collected data is also scaled accordingly and usually standardised with the integration time in counts/ms.

Due to the movement of the detector arm, the measurements are taken in-plane, as seen in Figure 4.8 (red path). However, these results can be converted to total (i.e. including out-of-plane scattering) approximations using Equation 4.11 and the qualitative data becomes quantitative for a full description of the scattering profile of a textured sample, as at large collection angles a smaller proportion of the reflected signal is captured than at small collection angles. For this, the total signal scattered is assumed to be a curved band with the width equal to the detector diameter, due to the angular acceptance of the system of ±0.4°. If the scattered signal band is wider than the detector, the signal would be captured during the

measurement corresponding to the next polar angle. From Figure 4.8, it follows that the radius R of the scattered cone is a function of the polar angle θ as $R = a \sin \theta$, where a is the distance between the sample and the detector (15 cm). The signal is centred on the detector and its total intensity, $I_{scattered}$ can be approximated as in Equation (4.11), where r is the radius of the optical fibre (600 µm).

$$I_{scattered}(\theta,\lambda) = \frac{I_{measured}(\theta,\lambda)\ 4\ a\ sin\theta}{r} \tag{4.11}$$

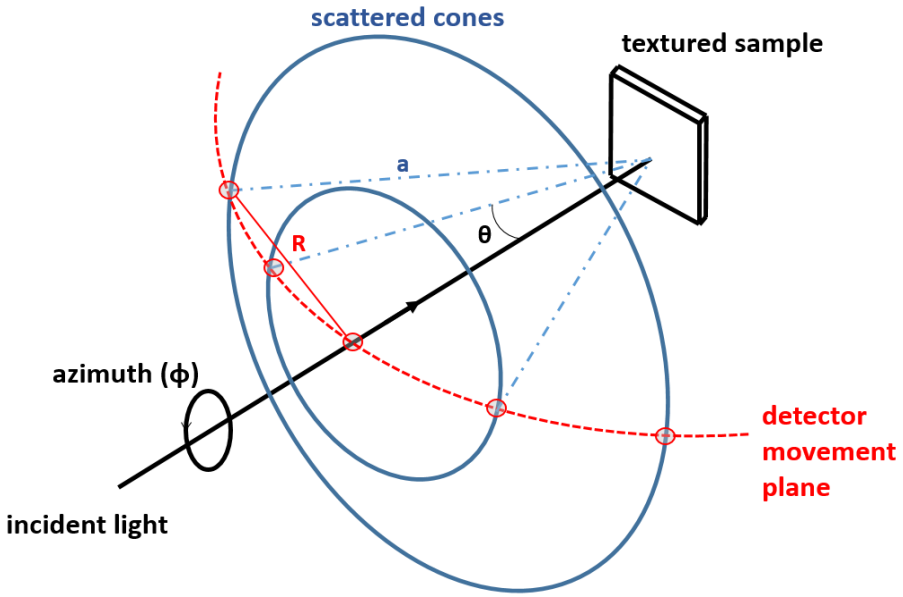

Figure 4.8: Representation of the reflected scattered cones of light from the textured sample and the detector movement plane.

For a comprehensive optical characterisation of a textured surface, the WARS measurements complement hemispherical reflectance measurements. As diffuse reflectance can be measured using an integrating sphere for scattering angles above 6°, the results can be approximated to the WARS data upon integration over the polar angular range while maintaining the wavelength dependency. This is especially important, as in some cases, the incident laser beam has to be powerful enough to provide good signal-to-noise ratio in the collected data of low-reflective surfaces and the intensity cannot be directly measured without achieving

saturation. As such, quantification of data is very difficult and a complementary method, such as hemispherical reflectance measurements, is useful in this regard.

Chapter 5

Metal-assisted Chemical Etching (MACE)

The uniformity and optical properties of the black silicon layers fabricated by MACE are highly dependent on the etching parameters of the recipe, such as the etching time and concentrations of the mixed solutions. Therefore, it is important to identify the contribution of each parameter on the nanowire morphology for the reliable and reproducible realisation of low-reflective black silicon layers that can also be electrically passivated without much difficulty. This Chapter presents a comprehensive investigation into the morphology of the MACE black silicon fabricated under different conditions, where etching times or solution molarities are changed for a fixed set of the rest of the parameters. Cross-sectional and top-view SEM images and hemispherical reflectance measurements are presented in each case and an optimum set of parameters is identified for a desirable balance between optical and electrical properties at the device level.

5.1 Effect of etching process duration

5.1.1 Morphology

Silicon wafers are cleaved into 4 cm x 4 cm pieces and cleaned using a 3:1 Piranha solution followed by an *HF* bath to remove native silicon dioxide, then submerged into a MACE aqueous solution for several minutes. In all cases, as a starting point, the $AgNO_3$ solution molarity is 60 mM, the *HF* solution molarity is 14 M and a fresh solution is prepared every time, without external temperature or illumination bias. The aim of this study is to investigate the effect of the process time on the nanowire morphology and their optical response for samples of fixed areas. To ensure reproducibility of the textures and reliability of the presented data, two samples were fabricated for each of the parameter sweep presented in this chapter. The full data can be shown in the tables in Appendix B. Figure 5.1 (a-f) shows cross-sectional SEM images of the resulting black silicon layer, for etch times of 1 minute (a), 2 minutes (b), 6 minutes (c) and 10 minutes (d). Figure 5.1 (e) and (f) show 1 minute and 2 minutes etched layers under higher magnifications. All of the SEM images are taken with a 10° stage tilt and the scale bar is indicated in the figures. Generally, the resulting surface presents vertically aligned, well defined nanowires of uniform height and random distribution. Increasing etching times yield longer nanowires, as seen directly from the images. This is due to the nucleation of the silver nanoparticles on top of the silicon surface and their vertical propagation inside the substrate catalysed by the *HF* solution. As the silicon is exposed to the MACE solution, the silver nanoparticles sink deeper into the substrate, thus yielding longer nanopillars in-between. The leftover created silver dendrites are then removed using a nitric acid solution, leaving a dense array of nanostructures. The lengths and the diameters of the black silicon layers can be extracted directly from the SEM images for various magnifications, where the 10° stage tilt is geometrically accounted for according to Figure 5.2.

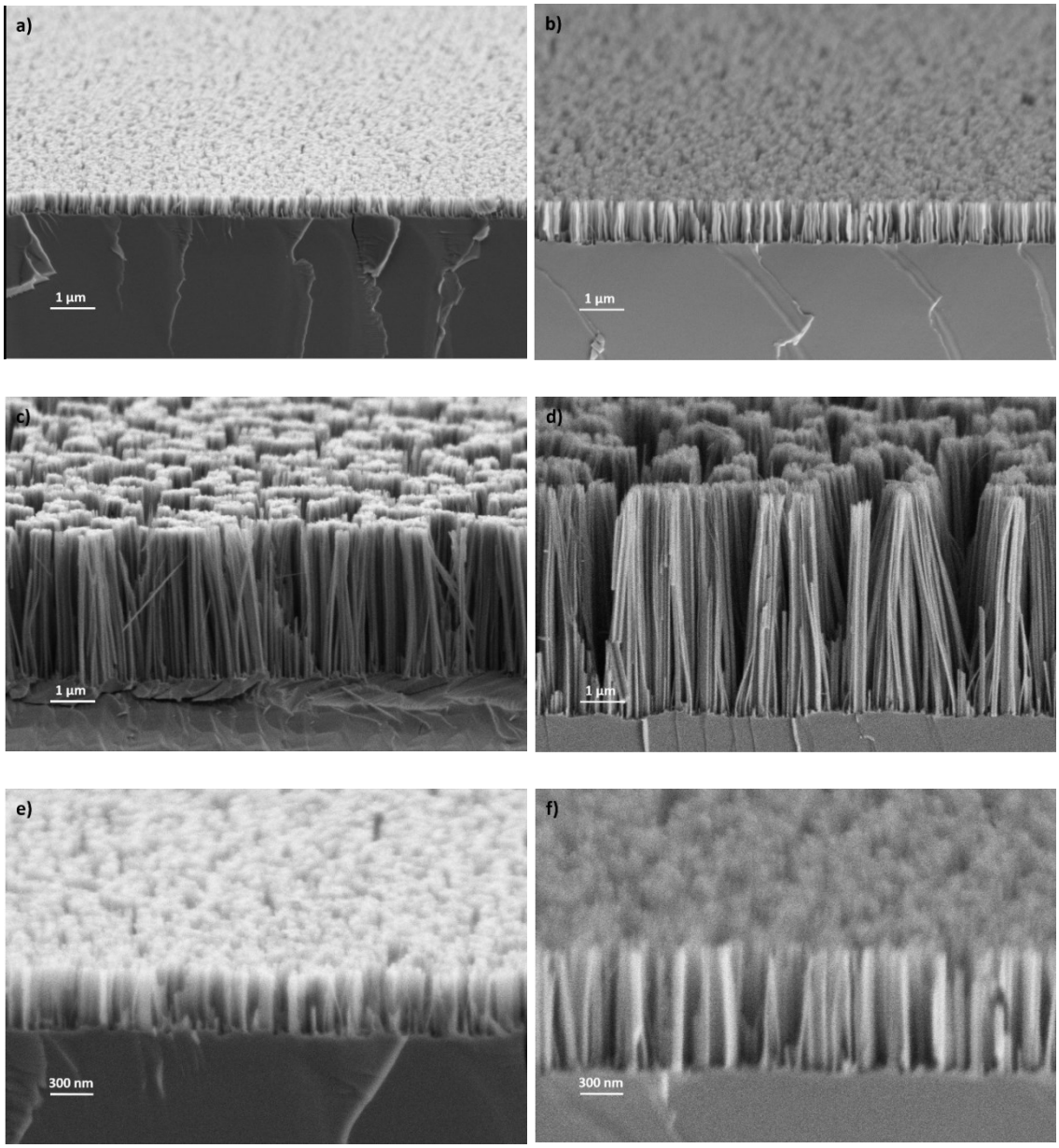

Figure 5.1: Cross-sectional SEM images under 10° stage tilt for MACE black silicon etched for: a) 1 minute; b) 2 minutes; c) 6 minutes; d) 10 minutes; e) 1 minute (higher magnification); f) 2 minutes (higher magnification);

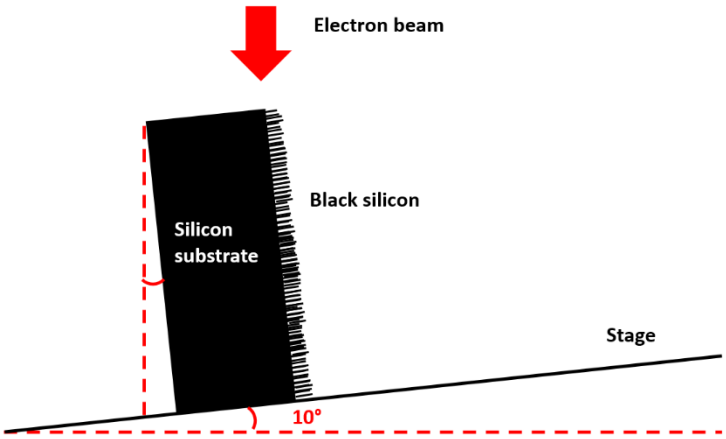

Figure 5.2: Schematic of the silicon specimen relative to the incident electron beam inside the SEM chamber.

Figure 5.3 shows the nanostructure height as a function of etching time for the four specimens under study with error bars indicated. The relationship between the two is linear and shows that great control can be achieved over the nanostructure length by adjusting only the MACE process time. These findings are in line with previous reports [140], where it has been shown that long etch of above 15 minutes times can lead to saturation in the nanowire length due to the silver particles consumption in the *HF* solution. However, for the relatively short process times in here, this has not been observed. From the measured data, a constant etch rate of R_{etch} = ~500 nm/min is calculated for all of the cases, with minimal impact on the nanowire diameter and the array distribution on the silicon surface. For etching times of 1, 2, 6 and 10 minutes, the resulting nanostructures heights are 499 nm ± 21 nm, 986 nm ± 42 nm, 3057 nm ± 56 nm and 4974 nm ± 109 nm, respectively upon measurements on multiple points in the images. Similarly, the measured nanostructure diameters are all in the range of 80-100 nm, irrespective of process duration. This is line with expectations, as the silver nitrate molarity remains constant between specimens and thus does not affect the structure diameter or the distribution on the surface.

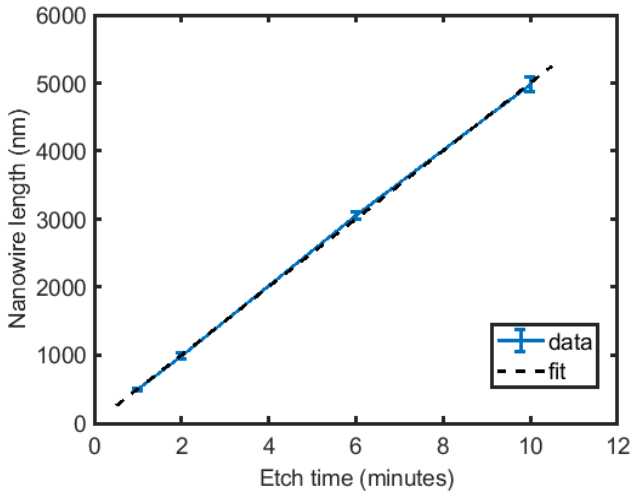

Figure 5.3: Linear relationship between black silicon height and etch time, resulting in etching rate R_{etch} = ~ 500 nm/min. Error bars indicated.

Figure 5.4 shows top-view SEM images of the four samples with different MACE process times, all for the same magnification. Nanowire bunching towards their tips that results in agglomerations are evident for longer structures. This is due to several reasons, including surface tension induced by the drying process, as well as nanoscopic van der Waals forces that have a more significant contribution for longer nanowires [221]. Also, increased aspect-ratio (defined as height/diameter) results in more flexible nanostructures that cannot sustain their own weight and that are prone to lean and touch each other and not be vertically-aligned and free-standing, visible especially in Figure 5.4 c) and d). This can potentially have implications on the optical response of the samples, as these agglomerations will interact differently with incident light compared with free-standing nanowires, as well as on the conformity of the dielectric passivation layer and the resulting electrical parameters.

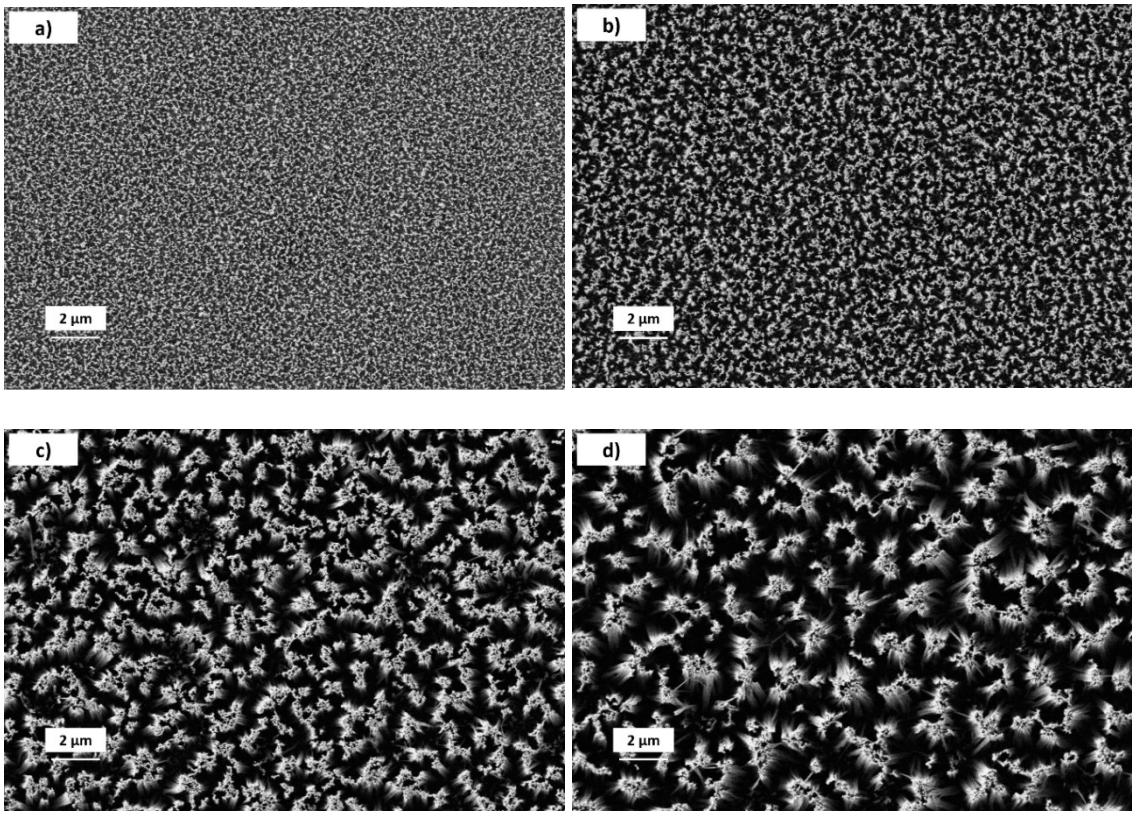

Figure 5.4: Top-view SEM images of MACE black silicon for etch times of: a) 1 minute; b) 2 minutes; c) 6 minutes; d) 10 minutes.

As the silver nitrate solution molarity was kept unchanged for the four MACE processes, it is expected that the number of nanowires in a given region is similar and independent of etching time, due to the fact that approximately the same number of silver nanoparticles nucleate the same silicon area in all cases. As all of the SEM images in Figure 5.4 a)-d) are taken under the same conditions for the secondary electron detector such that it does not impact the grayscale intensity of the images, as well as same magnification and tilt, image processing can be employed to further analyse the density of the nanowires on the silicon surface. However, forces as those mentioned above which agglomerate the nanowires towards their tips make it difficult for a direct approximation of the number of nanostructures in an image. Instead, an approach was preferred where the region covered by black silicon in the top-view SEM image is calculated and expressed as a percentage of the entire silicon area. For all of the samples, the raw images were converted to grayscale images and a unique grayscale intensity threshold was

chosen for binary conversion when creating a black and white image. This threshold was chosen not for a set intensity or grayscale pixel, but rather using a self-consistent percentage approach (i.e. for all images, same percentage of grayscale pixels out of total available pixels would be converted to white). An example of the resulting processed image is shown in Figure 5.5, where the original is on the left and the black and white processed image is on the right. Thus, the nanowire coverage area could be approximated for this field of view and assumed to remain constant for the entire area of the specimen.

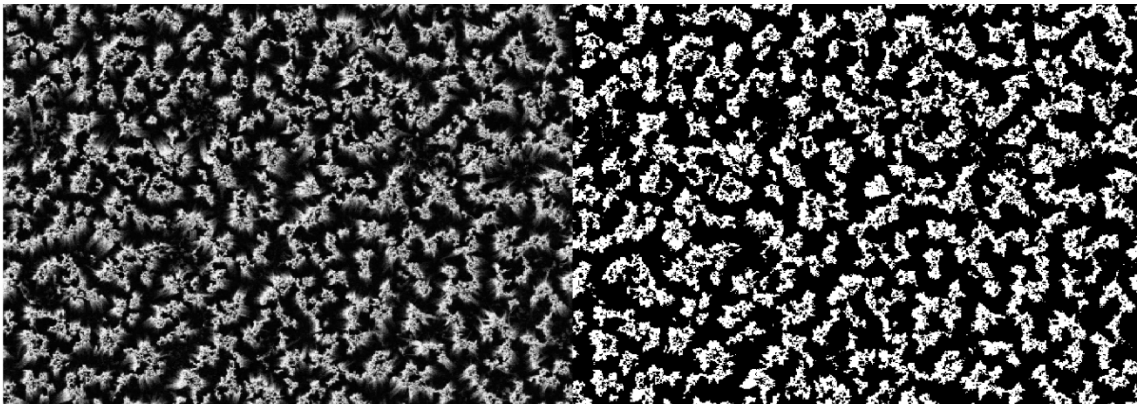

Figure 5.5: Example of original SEM image on the left and the processed black and white image on the right.

Image processing reveals that the area covered by nanowires is very similar among the four specimens, yielding values of 25.3 %, 28.9 %, 28.2 % and 27.4% covered area for the 1 minute, 2 minutes, 6 minutes and 10 minutes etched silicon surfaces respectively. This is an important result that validates the model proposed here, as no coverage variation is expected for constant silver nitrate molarity (i.e. same number of silver nanoparticles nucleate the same specimen area for all samples). Small differences and errors between the four values can originate from the fabrication method itself, where slight inaccuracies in the measured solutions can arise, such as the silver nitrate quantity.

In order to approximate the semiconductor surface area increase upon MACE texturing, each resulting nanowire can be thought of as a right cylinder of length L and an average radius r, in a square unit cell of length l. Using the results from the image analysis, the top down area of the nanowire, which is πr^2, represents on

average *x %* of the area of the square unit cell, with area $A_{cell} = l^2$. Here, *x* represents the areal coverage values obtained from the image processing above. Assuming an average radius value identical for each nanowire, the unit cell length can then be calculated as:

$$l = \sqrt{\frac{\pi r^2}{x}} \tag{5.1}$$

As such, the silicon surface area increase, *SA*, can be written as in equation (5.2), where $A_{NANOWIRE}$ represents the sum of the top down area and the area of the side walls of a nanowire.

$$SA = \frac{A_{NANOWIRE}}{A_{CELL}} = \frac{2\,\pi\,r\,L + l^2}{l^2} \tag{5.2}$$

Taking into account a mean value of x = 27% for the area covered by the nanowires based on the image-processing presented above and a radius *r* of 50 nm, the total silicon surface area increase SA is 6.4 times, 11.8 times, 33.5 times and 55.1 times for MACE durations of 1 minute, 2 minutes, 6 minutes and 10 minutes respectively. This surface area increase creates a disruptive nanowire interface, filled with unsaturated chemical bonds, which are essentially equivalent to energy levels inserted in the silicon bandgap and thus heavily promote trap-assisted recombination. A summary of the morphological characteristic of the fabricated sample is shown in Table 5.1.

Table 5.1: Morphology characteristic of MACE fabricated nanowires for varying etching times. Silver nitrate molarity 60 mM and HF molarity 14 M for all cases.

t (mins)	Nanowire length (nm)	Nanowire coverage area (%)	Increased silicon surface area (# of times)
1	499 ± 21	25.3	6.4
2	986 ± 42	28.9	11.8
6	3057 ± 56	28.2	33.5
10	4974 ± 109	27.4	55.1

5.1.2 Hemispherical reflectance

After the etching process, the samples are characterised using an integrating sphere system to extract results on the hemispherical total reflectance and hemispherical diffuse reflectance, as well as the reflectance haze, which is calculated as the ratio of the two. The fabricated black silicon is measured using a low-reflective black reflectance standard that has reflectance values of below 2% for the entire wavelength range of 300 nm – 1100 nm for higher degree of data accuracy. Figure 5.6 a) shows the measured total hemispherical reflectance for the fabricated silicon samples in the entire wavelength range and bare flat silicon measurement as dotted line, for reference. Increased nanostructure height yields lower reflectance values due to the graded refractive index effect the black silicon possesses.

It is well established that the excellent absorption properties of silicon nanowires arise from the presence of confined modes inside the nanostructures, such as leaky modes and strong Fabry-Perot resonances, which emerge as consequences of the structure geometry and size [222]. For a periodic nanowire array, the fundamental mode and the first few key modes are strongly absorbing in the short wavelength region and decay with increased incident wavelength. Upon a nanowire radius increase, these confined modes are red-shifted and more propagating modes emerge towards larger wavelengths which are better coupled to

by the incident plane waves [223]. It has been previously reported [224-225] that the Mie absorption and scattering efficiencies for nanowire diameters below 100 nm reaches its maximum at short wavelengths λ < 500 nm due to the presence of the fundamental mode. As such, in a heterogenic nanowire array fabricated via MACE, it is hypothesised that the multitude of radii distributions leads to a superposition of these associated optical responses and eventually to enhanced absorption (i.e. supressed reflectance) across the entire wavelength spectrum. Furthermore, a large silicon to air material fill factor promotes reduced reflectance in the short wavelength region, as in the case of MACE black silicon arrays that are extremely dense. As such, thicker layers result in supressed surface reflectance due to added interaction between the photons and exhibit increased absorption inside the silicon substrate. Due to the feature size of the nanowires, the reflectance is more readily reduced in the short wavelength region where the nanowire length to incident wavelength ratio is small, providing a smoother, more gradual transition from air to silicon [84]. For the same reason, longer nanostructures are also capable of enhancing the optical response in the long wavelength region, which can be indicative of the light-trapping properties of the sample, when reflections from the bottom surface are considered. By replacing one of the ports on the integrating sphere with a light trap, the specular reflection of the sample can be eliminated from the system in a cone around 6° and the diffuse hemispherical reflectance can be directly obtained. This is a measure of the reflected light that is redirected away from the surface normal when incident on the black silicon layer and is shown in Figure 5.6 b). The diffuse reflectance measurements are consistent with total reflectance measurements and decrease with increasing nanostructure height, showing that all the fabricated black silicon layer have some scattering properties.

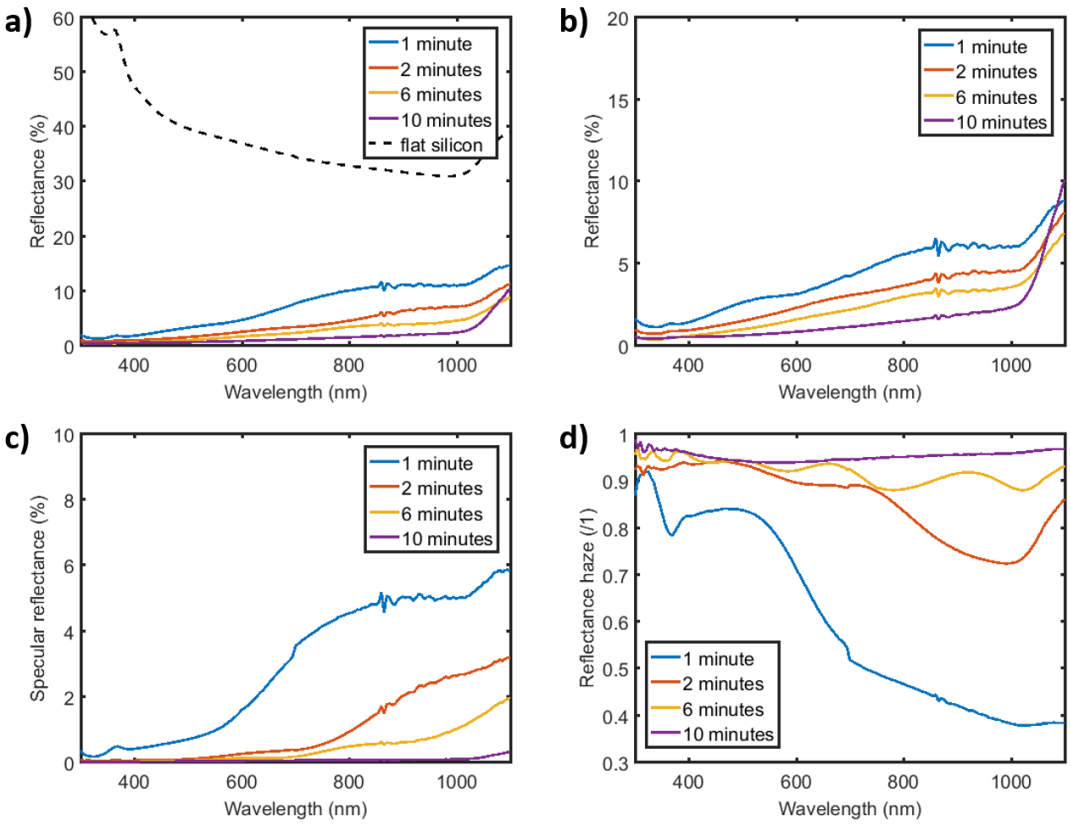

Figure 5.6: a) Measured total hemispherical reflectance; b) Measured diffuse hemispherical reflectance; c) Calculated specular reflectance; d) Calculated haze reflectance for the fabricated black silicon samples with various MACE durations.

The specular reflectance for each sample can be calculated as the difference between the measured total hemispherical reflectance and the measured diffuse hemispherical reflectance and it is shown in Figure 5.6 c). The specular reflectance drastically decreases with increased nanostructure length, especially in the long wavelength region. This confirms the light-trapping capabilities of this nanotexture, as longer nanowires redirect the reflected light away from the specular direction. In contrast, short nanowires of 500 nm have poorer scattering properties and their specular reflectance is larger for long wavelengths. The ratio of the two measurements represents the reflectance haze and it is shown in Figure 5.6 d). It is a measure of the proportion of light reflected at angles larger than 6° from the specular direction and the total light reflected. Again, long nanowires show large values for the reflectance haze, as their specular reflectance is very low. As opposed to this, the shortest nanowires yield poor haze values for long incident wavelengths,

where the reflection occurs mostly in a specular direction. However, reflectance haze calculations and measurements do not contain any information on the angle distribution of the scattered light.

A summary the optical properties of the fabricated samples is shown in Table 5.2. An important figure of merit for photovoltaics is the weighted average surface reflectance, that is calculated by taking into account the AM1.5 spectrum distribution and the weighting arising for each wavelength of incidence (see Chapter 2.2). As such, all of the data presented are weighted averages over the wavelength range for a more relevant representation for PV.

Table 5.2: Optical characteristics of the MACE fabricated silicon samples for varying etching times. Silver nitrate molarity 60 mM and HF molarity 14 M for all cases.

t (mins)	WAR total (%)	WAR diffuse (%)	WAR specular (%)	WAR haze (/1)
1	6.65	3.24	2.64	0.58
2	3.56	2.80	0.75	0.87
6	2.43	2.10	0.33	0.92
10	1.44	1.37	0.06	0.95

5.2 Effect of silver nitrate solution concentration

5.2.1Morphology

Silicon wafers are cleaved into 4 cm × 4 cm pieces and cleaned using a 3:1 Piranha solution followed by an *HF* bath to remove native silicon dioxide, then submerged into a MACE aqueous solution. In all cases, the *HF* solution molarity is 14 M, the etching process time is six minutes and a fresh solution is prepared every time, without external temperature or illumination bias. The aim of this study is to investigate the effect of the silver nitrate solution molarity (M_{Ag}) on the nanowire morphology and their optical response for samples of fixed areas. Figure 5.7 shows cross-sectional SEM images of the resulting black silicon layers, for silver nitrate molarities of a) 20 mM, b) 40 mM, c) 60 mM and d) 80 mM, all under the same magnification and 10° stage tilt. It is obvious that increased M_{Ag} yields longer nanostructures, due to the higher quantity of silver present in the MACE solution and thus the increase in the hole injection rate into the silicon valence band. The lowest molarity of the silver nitrate solution, corresponding to M_{Ag} = 20 mM does not yield vertically aligned nanowires of uniform height, as seen in Figure 5.7 e) under high magnification. Instead, the resulting layer exhibits randomly-shaped pillars of varying lengths and diameters which are much thicker than what is expected from MACE nanowires, due mainly to the scarcity of silver nanoparticles that nucleate the silicon surface. As such, the feature size of this texture is greater than for other molarities due to the distribution and density of the silver nanoparticles during the MACE process and may result in a poorer optical response with large surface reflectance. However, when M_{Ag} is increased to 40 mM, vertically aligned high aspect-ratio nanostructures are fabricated onto the silicon surface, with uniform length and random diameters. The lengths of the black silicon layers can be extracted directly from the SEM images for various magnifications, where the 10° stage tilt is geometrically accounted for from multiple data points.

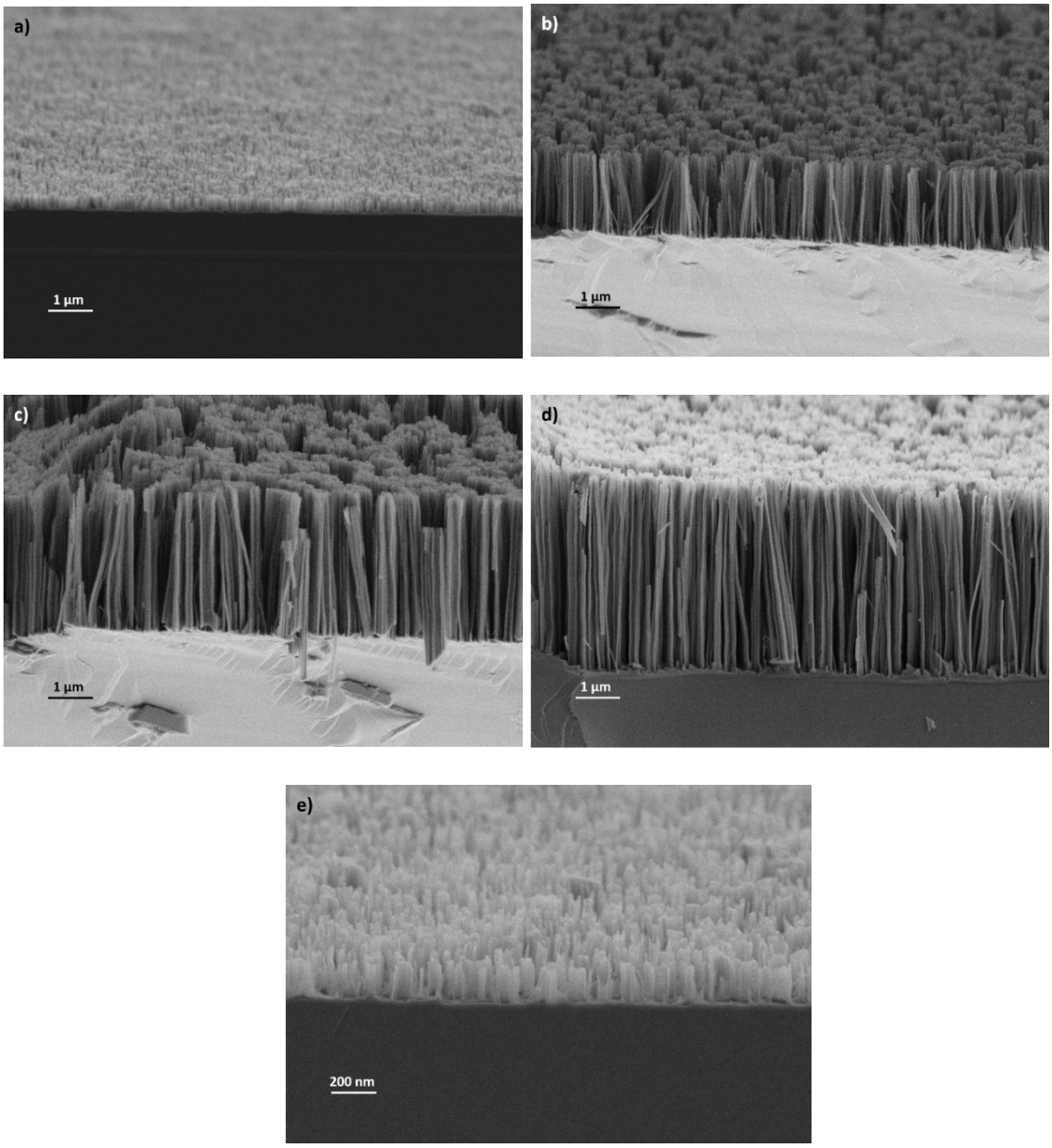

Figure 5.7: Cross-sectional SEM images of the fabricated MACE black silicon under 10° stage tilt for: a), e) M_{Ag} = 20 mM; b) M_{Ag} = 40 mM; c) M_{Ag} = 60 mM and d) M_{Ag} = 80 mM.

Figure 5.8 shows the nanostructure height as a function of silver nitrate molarity for the four specimens under study with error bars indicated. The relationship is linear at first for M_{Ag} below 60 mM and then starts saturating for higher concentrations. This is thought to be due to the silver consumption during the MACE process that eventually slows down hole injection into the silicon valence band. These results are in line with previous reports from Srivastava et al. (2014) [145].

Therefore, the length of the fabricated nanowires are 262 nm ± 20 nm, 1755 nm ± 51 nm, 3057 nm ± 56 nm and 4102 nm ± 97 nm for M_{Ag} of 20 mM, 40 mM, 60mM and 80 mM respectively. Srivastava also observed that M_{Ag} > 100 mM can promote lateral and chaotic etching due to silver particle migration to the silicon/air interface, but this was not observable in the current study. As the MACE duration was kept to six minutes for the four samples, the etch rate can be calculated and it is in direct proportion to the amount of silver available, yielding etch rates R_{etch} of 43 nm/min, 290 nm/min, 505 nm/min and 680 nm/min, respectively. These results are of great importance because the silver nitrate molarity proves to be a crucial component of fabricating low-reflectance black silicon layers with great control over the feature size.

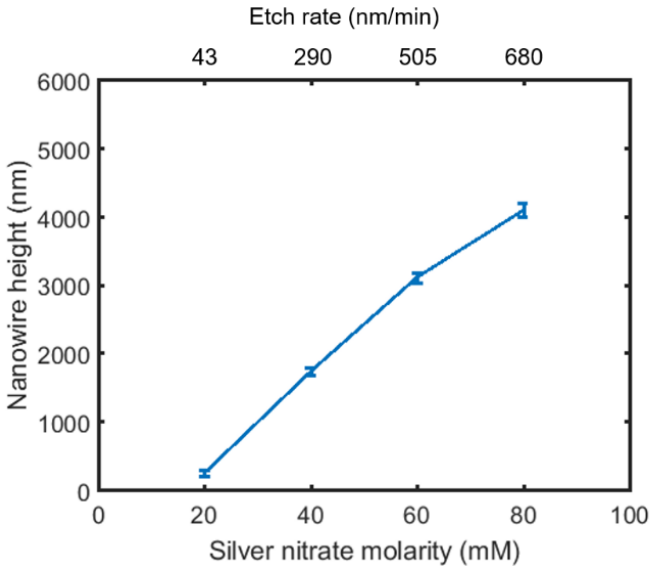

Figure 5.8: Relationship between M_{Ag} and nanowire length for six minutes etch time and 14 M HF solution. Etch rates indicated on top x-axis.

The diameters of the nanostructures can be directly measured from the SEM images and vary with silver nitrate concentration. As such, diameters of 130 nm ± 30 nm, 105 nm ± 17 nm , 100 nm ± 13 nm and 93 nm ± 16 nm are measured for M_{Ag} of 20 mM, 40 mM, 60 mM and 80 mM, respectively.

One aspect that is generally less discussed when characterising MACE black silicon is the importance of the density of the nanowire array on the optical

response, mainly due to the difficulty of evaluating the number of nanowires in a given area and how this changes with the MACE solution composition. Figure 5.9 shows top-view SEM images of the fabricated black silicon surfaces for different M_{Ag} on the left-hand side and the corresponding black and white processed images for analysis on the right-hand side, all taken for the same magnification and conditions. As before, long nanowires are bunching together towards the tips, because of their flexibility and nanoscopic forces at play. This is less visible for $M_{Ag} < 40$ mM.

Apart from the influence on the nanowire length, it is clear that increasing values of M_{Ag} affect the nanostructure distribution and density on the silicon surface, owing to the increased number of silver nanoparticles that nucleate on the substrate during the MACE process. From an antireflective perspective, the density of the nanostructures on the silicon surface and their distribution would have a large contribution. Using an effective medium approximation technique and calculating an associated silicon fill factor, the denser nanowire array would result in a smaller unit cell, out of which the nanowire would represent a larger fraction. This leads to a more graded transition of the refractive index from air to silicon and thus reduced surface reflectance. Intuitively, a higher number of silver nanoparticles nucleating the same material area should result both in thinner nanowires and in a larger number of such nanostructures. Therefore, the nanowire cover area should decrease with increasing number of nanoparticles.

Analysis of the SEM images reveals that the nanowire coverage area differs vastly indeed between specimens and, perhaps surprisingly, increases with increased silver nitrate added into the system (see Table 5.3). This trend is ascribed to the tendency of the silver particles to deposit not entirely random on top of the silicon surface, but rather at defect sites and disruptive areas on the semiconductor [226]. As such, if the silicon surface is saturated with silver nanoparticles, excess particles will deposit on top of already existing ones, creating clusters or agglomerations that increase in size. Venkatesan et al. [227] reported that increased silver nitrate solution concentrations translate into Ag island clusters of similar density, but larger size. Therefore, a saturation point will exist, whereby a number of closely-distributed but individual nanoparticles will come together and create a larger Ag

island. This phenomenon will yield a saturation in the diameter reduction of the nanostructures (i.e. off-metal silicon) without affecting their number (i.e. density) and therefore lead to larger nanowire coverage areas, in line with diameter measurements reported above. As such, the nanowire area coverage is calculated as 18.6 %, 22.1 %, 28.6 % and 31.1 % for silver nitrate molarities of 20 mM, 40 mM, 60 mM and 80 mM, respectively. The increasingly lower difference in the coverage area from 40 mM to 60 mM and 60 mM to 80 mM is thought to be because of the effect of larger solution molarities on the feature size of the nanowires (i.e. saturation in thinning).

Using Equations (5.1) and (5.2) introduced in the previous subsection, the silicon surface area is increased by 2.8 times, 16.4 times, 34.6 times and 51.8 times for the four fabricated samples respectively. A summary of the morphological characteristic of the black silicon samples is shown in Table 5.3.

Table 5.3: Morphological properties of MACE fabricated black silicon with varying M_{Ag}. Etch time is 6 minutes and HF molarity 14 M for all cases.

M_{Ag} (mM)	Nanowire length (nm)	Etch rate (nm/min)	Nanowire diameter (nm)	Nanowire coverage area (%)	Surface area increase (# of times)
20	262 ± 20	43	130 ± 31	18.6	2.45
40	1755 ± 51	290	105 ± 17	22.1	15.8
60	3057 ± 56	505	100 ± 13	28.6	35.3
80	4102 ± 97	680	93 ± 16	31.1	54

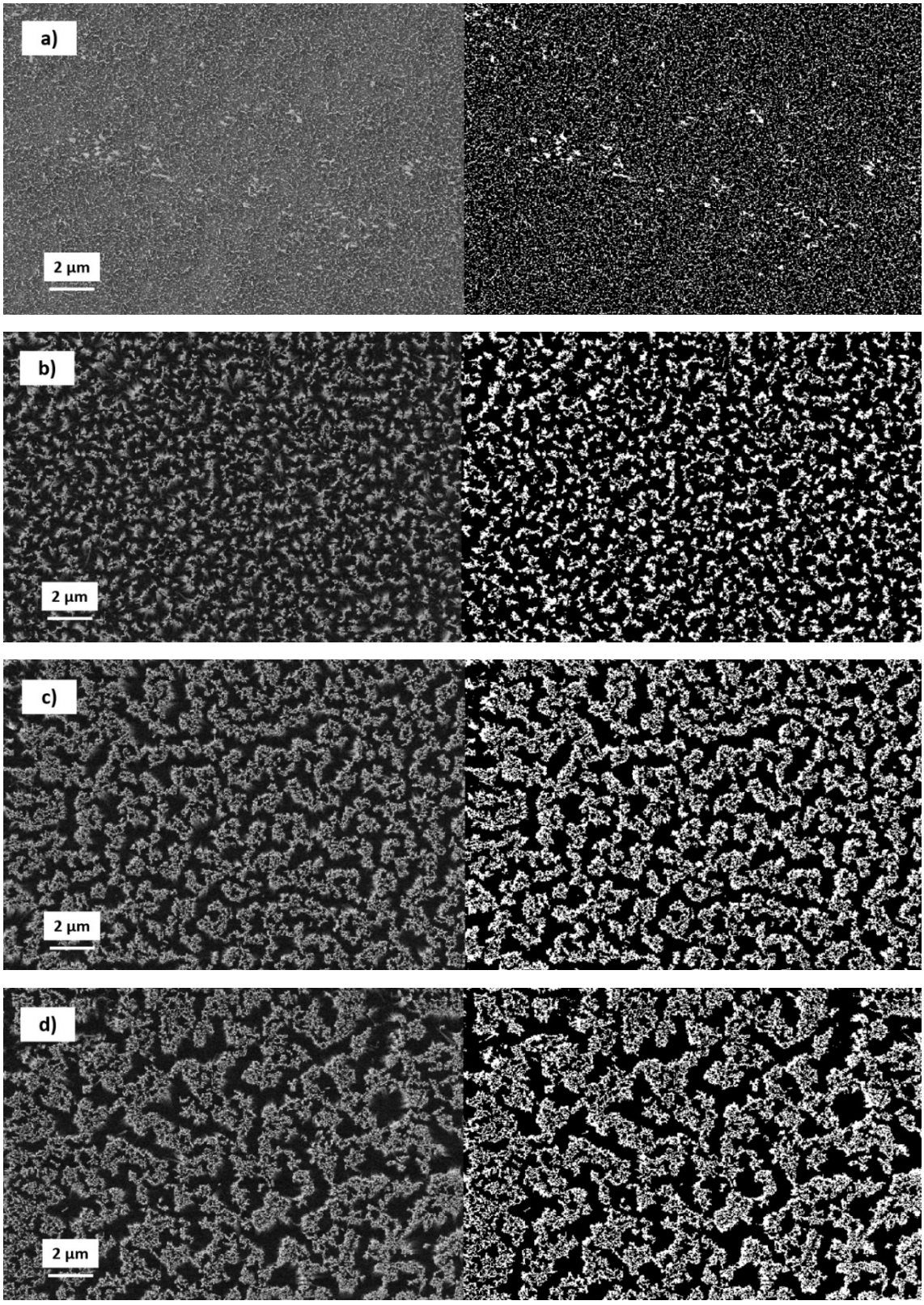

Figure 5.9: Top-view SEM images (left) and corresponding binary images (right) of MACE black silicon fabricated with: a) M_{Ag} = 20 mM; b) M_{Ag} = 40 mM; c) M_{Ag} = 60 mM; d) M_{Ag} = 80 mM.

5.2.2 Hemispherical reflectance

After the etching process, the samples are characterised using an integrating sphere system to extract results on the hemispherical total reflectance and hemispherical diffuse reflectance, as well as the reflectance haze which is calculated as the ratio of the two. The fabricated black silicon is measured using a low-reflective black reflectance standard that has reflectance values of below 2% for the entire wavelength range of 300 nm – 1100 nm for higher degree of data accuracy. Figure 5.10 a) shows the measured total hemispherical reflectance for the fabricated silicon sample in the entire wavelength range, as well as the measured data for a bare flat silicon polished piece for reference, as a dashed line. As before, increased nanostructure height yields supressed top surface reflectance, with the added benefit arising from increased density in the structural array that contributes as well to further reducing the optical response. The signal corresponding to M_{Ag} = 20 mM (blue trace) is significantly larger than what is expected from a black silicon surface, due to the morphology of the resulting surface (see Figure 5.7 a) and e)). This sample can be described more as porous silicon, where the scarcity of silver particles gave raise to randomly-shaped structures with large diameters and random distributions. As such, the optical response is much larger than desired, especially in the short wavelength range where the characteristic reflectance peak of polished silicon can be observed around 350 nm. This is indicative of feature sizes larger than the incident wavelength and similar to the surface reflectance of micron-sized random pyramids layers etched onto the silicon surface. Diffuse hemispherical reflectance measurements of the samples are shown in Figure 5.10 b), where all the fabricated black silicon layers show some scattering and redirection of reflected light at angles above 6°. The lowest molarity fabricated sample corresponding to M_{Ag} = 20 mM yields high diffuse reflectance in the short wavelength range, thus scattering a large proportion of high energy incident photons away from the specular reflection direction.

Figure 5.10 c) shows the calculated specular reflectance of each sample, as the difference between the measured total and diffuse hemispherical reflectance. As

discussed in the previous Chapter, longer nanowires exhibit lower specular reflectance and redirect most of the incoming photons towards oblique scattering angles, especially in the long wavelength region. The density of the nanostructures plays an important role in this as well, with the purple trace corresponding M_{Ag} = 80 mM yielding specular reflectance values close to 0. In contrast, the lowest concentration fabricated sample inherits the large value reflectance peak from flat polished silicon due to the lack of density in the structures array. The reflectance haze is calculated and shown in Figure 5.10 d), with increased silver nitrate concentrations resulting in increased reflectance haze values for the entirety of the wavelength range. As such, it is proposed that M_{Ag} in the range of 60 mM – 80 mM is the optimal value for a one-step MACE process, yielding a black silicon layer of sufficient height and density for photovoltaics applications and its subsequent optical requirements. However, if the silver nitrate molarity is too large, the resulting black silicon surface may prove hard to electrically passivate by industry-compliant deposition methods such as PECVD or ALD with good conformity onto the dense array of nanostructures. Table 5.4 shows a summary of optical characteristics for the fabricated MACE silicon samples with varying silver nitrate concentrations. As before, data represents weighted average calculated values that take into account the spectral irradiance of the sun for maximization of data relevance for PV applications.

Table 5.4: Summary of morphological and optical characteristics of the MACE fabricated silicon samples. HF concentration 14 M and etching time is 6 minutes for all cases.

M_{Ag} (mM)	WAR total (%)	WAR diffuse (%)	WAR specular (%)	WAR haze (/1)
20	16.12	4.01	12.11	0.24
40	6.06	3.67	2.38	0.70
60	2.43	2.10	0.33	0.92
80	1.36	1.30	0.05	0.95

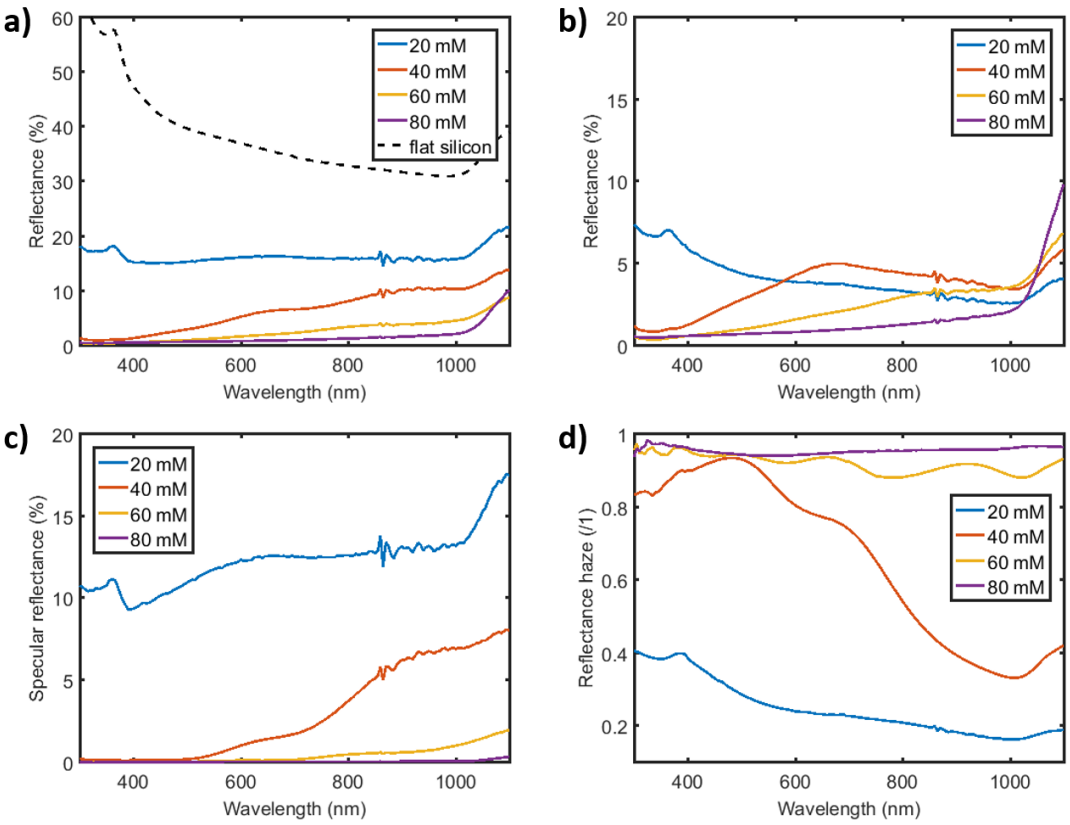

Figure 5.10: a) Measured total hemispherical reflectance; b) Measured diffuse hemispherical reflectance; c) Calculated specular reflectance; d) Calculated reflectance haze for fabricated MACE black silicon with various silver nitrate concentrations.

5.3 Effect of hydrofluoric acid solution concentration

5.3.1 Morphology

Another important parameter of the MACE process is the *HF* solution molarity, which acts as a catalyst for the MACE redox reaction and removes by-products. For investigating its effect on the MACE process itself, silicon wafers are first cleaved and cleaned using a 3:1 Piranha solution followed by an *HF* bath to remove native silicon dioxide. The substrates are then submerged into a MACE aqueous solution for six minutes. In all cases, the $AgNO_3$ solution molarity is 60 mM and a fresh solution is prepared every time, without external temperature or illumination bias.

The resulting surfaces are then cleaned in a diluted nitric acid for the purpose of removing leftover silver films from the sample. Figure 5.11 shows cross-sectional SEM images for MACE black silicon fabricated with *HF* molarities (M_{HF}) of 7 M in a), 11 M in b), 14 M in c) and 21 M in d) at the same magnification. It is evident that increasing *HF* concentrations yield longer nanowires, due to the enhanced etch rate of the formed SiO_2 [137-138] during the MACE process. Bunching of the nanostructures is experienced for high M_{HF} due to their high aspect-ratio, as in the previous cases. Generally, all of the molarities under study produced vertically aligned silicon nanowires arrays, but the structures become very thin for larger concentrations, for example when M_{HF} = 21 M (see figure 5.11 d)). It has been previously reported [145] that such large M_{HF} may lead to lateral and uncontrolled etching due to the migration of silver nanoparticles to Si/air interfaces, but when used in conjunction with lower silver nitrate molarities. The relatively larger M_{Ag} used here may prevent some of this lateral etching from occurring, but instead the nanowires appear less uniform, possess reduced diameter and have a spiky sharp aspect to them. This may have implications on the surface reflectance of the structures array.

Moreover, the black silicon corresponding to M_{HF} = 21 M appears to have similar height to the case when M_{HF} = 14 M, indicating that the hole injection rate saturates when a certain M_{HF} threshold is reached and the etching rate slows down. Figure 5.12 shows the relationship between the nanowire height, extracted directly from the SEM images, and the *HF* solution concentration, with error bars. For $M_{HF} \leq 14$ M, there is a linear increase in the nanowire height with increased *HF* concentration, in line with the findings from previous reports [145]. However, this indeed starts saturating for larger M_{HF}, potentially because some lateral etching occurs and the etching in the (100) direction is therefore slower. For a six-minute MACE process, the etch rates R_{etch} are calculated and presented in Table 5.5. Although there is not much difference in the nanowire morphology apart from height for low M_{HF}, i.e. all resulting surface exhibit well-defined free-standing nanostructures, there is a general trade-off between control of the nanostructure height and process duration

to achieve the desired morphology. Table 5.5 shows a summary of the morphological characteristic of the MACE fabricated black silicon with varying M_{HF}.

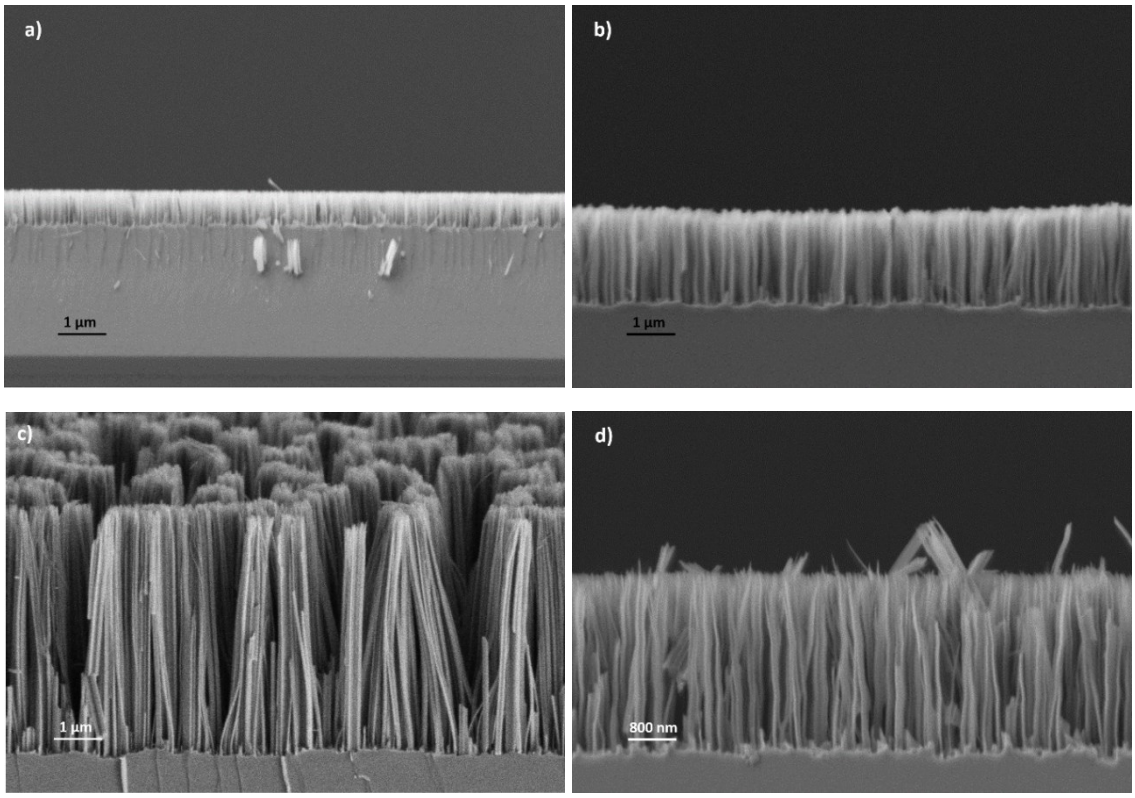

Figure 5.11: Cross-sectional SEM images of MACE fabricated black silicon with: a)M_{HF} = 7 M; b) M_{HF} = 11 M; c) M_{HF} = 14 M; d) M_{HF} = 21 M. The etching time is six minutes and the silver nitrate molarity is 60 mM for all cases.

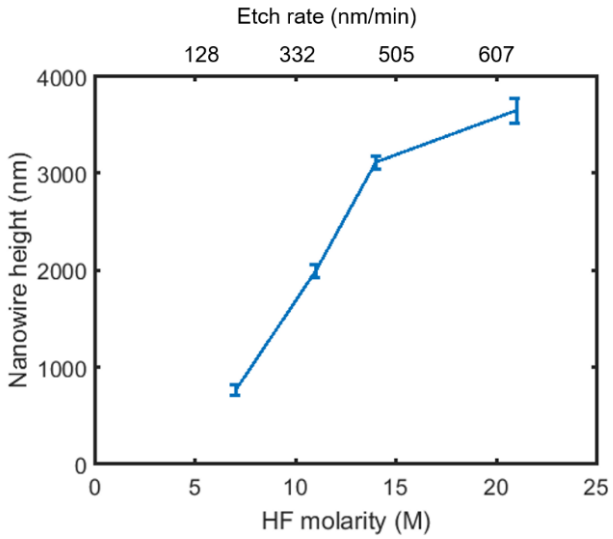

Figure 5.12: Relationship between M_{HF} and nanowire length for six minutes etch time and 60 mM $AgNO_3$ solution. Etch rates indicated on top x-axis.

Table 5.5: Morphological properties of MACE fabricated black silicon with varying M_{HF}. Etch time is 6 minutes and $AgNO_3$ molarity 60 mM for all cases.

M_{HF} (M)	Nanowire length (nm)	Etch rate (nm/min)
7	768 ± 26	128
11	1997 ± 68	332
14	3057 ± 56	505
21	3654 ± 128	607

5.3.2 Hemispherical reflectance

The fabricated samples are characterised using an integrating sphere setup in the 300 nm – 1100 nm wavelength range. Figure 5.13 a) shows the measured total hemispherical reflectance of the four silicon samples with polished silicon measurement as dashed line for reference. Increased nanostructure height yields supressed broadband surface reflectance, except for M_{HF} = 21 M, which has similar

values as for the lowest *HF* concentration. This is a confirmation of lateral etching occurring within the sample and the different nanowire morphology to the other specimens, since it should yield the lowest surface reflectance as it exhibits the longest nanostructures. Figure 5.13 b) shows the measured diffuse hemispherical reflectance, where again the sample corresponding to M_{HF} has the largest values. This time it is an indication of strong scattering of photons to large angles, based on the nanostructure heights. The other measurements are in line with expectations, where the nanowires reflect light at angles larger than 6° from the specular reflection direction, especially for the longer wavelengths.

Figure 5.13 c) shows the calculated specular reflectance for each fabricated sample, where the nanowires exhibit supressed broadband reflectance in the normal direction, increasingly so for larger heights. Most of the signal occurs for large incident wavelengths, where losses occur due to back reflections and incomplete absorption of incident photons. The calculated reflectance haze as a ratio between the total and diffuse hemispherical reflectances is shown in Figure 5.13 d). *HF* molarities below 11 M produce nanowire arrays that redirect only a small proportion of low-energy photons to large scattering angles. In contrast, the nanostructures corresponding to $M_{HF} \geq 14$ M experience excellent light trapping properties, where more than 90% of the photons are reflected away from the substrate normal. Table 5.6 shows a summary of the optical properties of the fabricated silicon samples, where reflectance values are calculated as weighted average over the wavelength spectrum according to the AM1.5G irradiance.

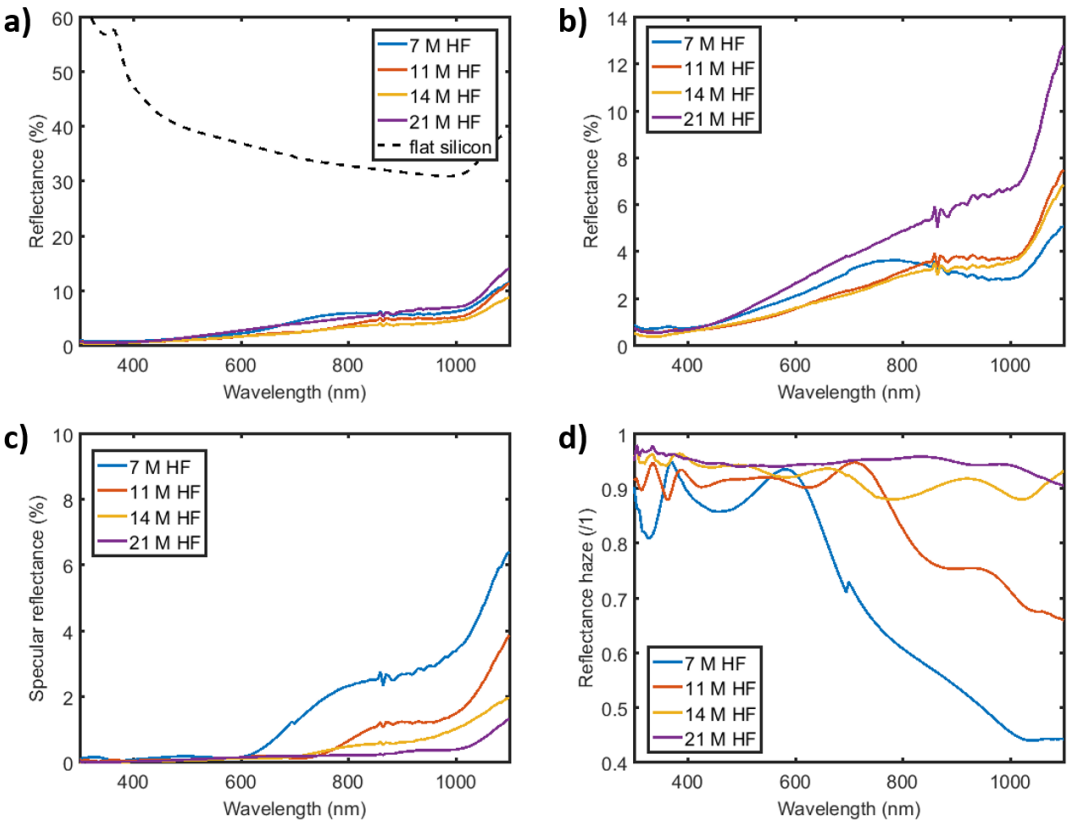

Figure 5.13: a) Measured total hemispherical reflectance; b) Measured diffuse hemispherical reflectance; c) Calculated specular reflectance; d) Calculated reflectance haze for fabricated MACE black silicon with various HF solution concentrations.

Based on these results, optimal *HF* concentration for a one-step MACE process lies in the range 11 M ≤ M_{HF} ≤ 14 M when M_{Ag} = 60 mM, such that there is no lateral etching during the fabrication process, but good control over the nanowire morphology can be achieved.

Table 5.6: Summary of morphological and optical characteristics of the MACE fabricated silicon samples. $AgNO_3$ concentration 60 mM and etching time is 6 minutes for all cases.

M_{HF} (mM)	WAR total (%)	WAR diffuse (%)	WAR specular (%)	WAR haze (/1)
7	3.68	2.38	1.29	0.74
11	2.73	2.21	0.51	0.86
14	2.43	2.10	0.33	0.92
21	3.77	3.56	0.21	0.94

5.4 Hybrid structures

5.4.1 Morphology

The potential of improved light-trapping and large broadband photon absorption into the silicon substrate can be maximised by combining nanostructures and micron-scale pyramids into hybrids. As such, the MACE process is carried out on a *KOH* etched silicon sample with randomly distributed upright micron-scale pyramids for various MACE durations. First, polished silicon wafers are cleaved into 4 cm × 4 cm pieces, then cleaned using a 3:1 Piranha solution, followed by an *HF* bath. The alkaline etching of the pyramids consists of a single solution of 0.2 M *KOH* and 5% IPA to improve wettability and produces randomly distributed and overlapping pyramidal structures with smooth walls. Then, samples are submerged into the aqueous MACE solution for 4 minutes, 8 minutes and 12 minutes respectively, resulting in a dense array of nanowires that have etched into the pyramids surfaces. The silver nitrate molarity is 60 mM and the *HF* solution concentration is 14 M, as discussed in the previous sections. Figure 5.14 shows cross-sectional images of the resulting silicon surfaces (b-d) and an alkaline etched surface that has not undergone MACE processing in a) for reference.

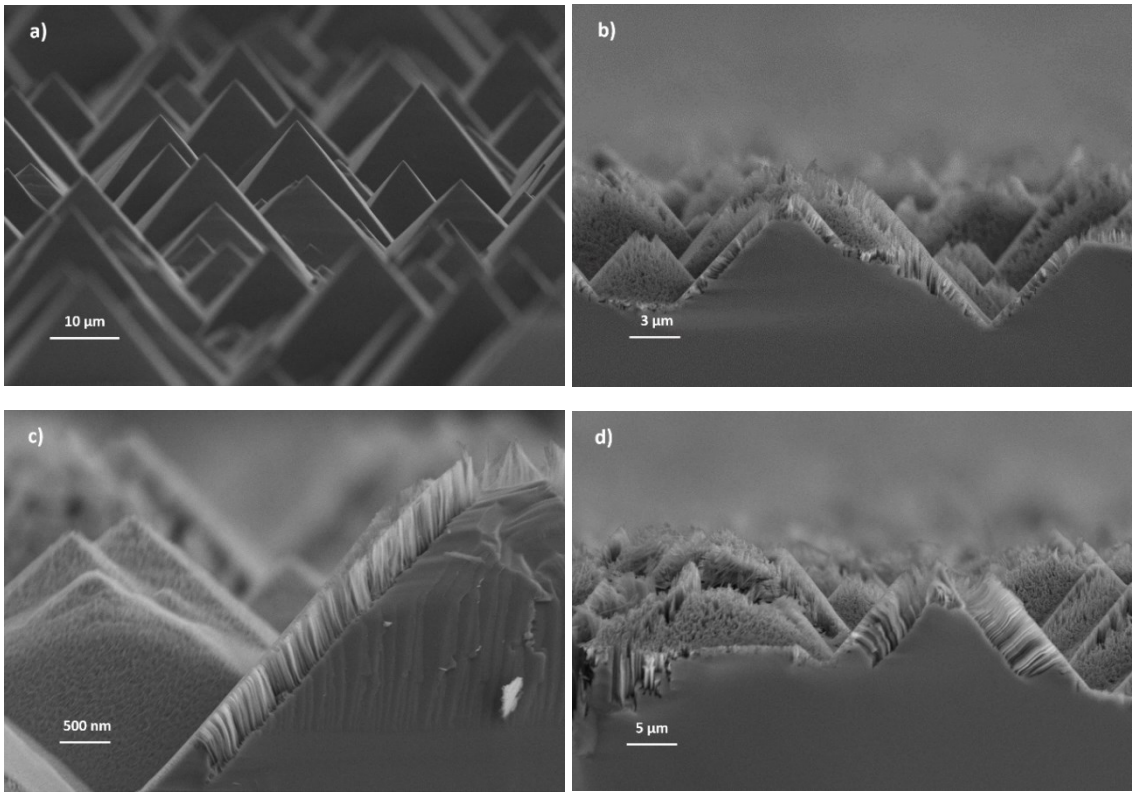

Figure 5.14: Cross-sectional SEM images of KOH etched silicon surfaces with MACE process durations of a) 0 minutes; b) 5 minutes; c) 10 minutes; d) 15 minutes.

The resulting surfaces exhibit uniform nanowires of fixed length that have etched following the crystalline orientation of the micron-scale pyramids, i.e. perpendicular to the {111} planes. In some cases, due to the geometry of the structures that limits *Ag* nanoparticles nucleation, the nanowires are very short inside deep trenches. The overall size of the hybrid structure is the same as the original bare pyramid. The height of the MACE structures can be extracted directly from the images with lengths of 1834 nm ± 49 nm, 4133 nm ± 83 nm and 6348 nm ± 117 nm respectively. Figure 5.15 shows the dependency on the nanowire height with increased MACE process duration, where a linear trend is found for all cases. The resulting etch rate is R_{etch} = 360 nm/min, which is lower than the values reported in Chapter 5.1 of ~ 500 nm/min for a similar MACE solution due to the difference in the crystallographic orientation of the initial surface and other geometric restrictions.

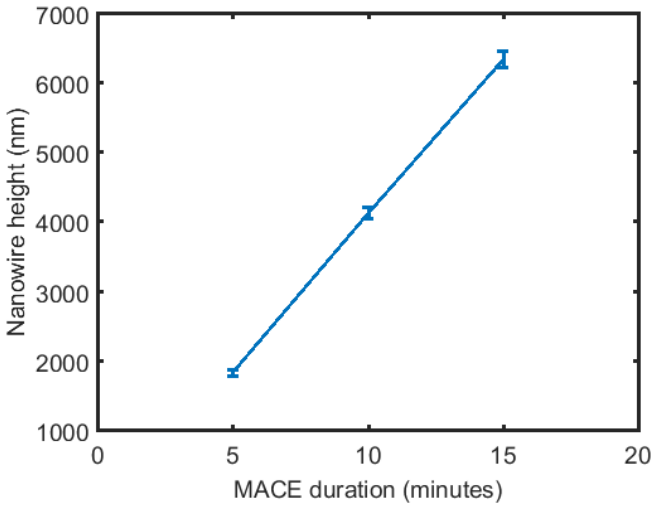

Figure 5.15: Relationship between nanostructure heights etched on pyramids and MACE process duration.

Top-view SEM images presented in Figure 5.16 reveal that the micron pyramids are fully covered by the MACE nanowires on all facets. Due to various forces, among which gravitational and van der Waals forces play an important role, the nanowires are inclined towards the base of the pyramids, following the parent material's crystallographic orientations and leaving the edges free and clearly visible as darker colours, exposing the pyramid vertices. This occurs increasingly so for longer MACE durations, as the structures become more flexible due to increased aspect-ratio. It is also clear from these images that the nanostructures inherit the crystallographic orientation of the original substrate, as they are found to etch orthogonal to the {111} pyramidal planes. This is an especially important pre-requisite for electrical passivation, as carrier recombination is heavily promoted at so-called 'grain boundaries', where the crystallographic orientation of the material changes.

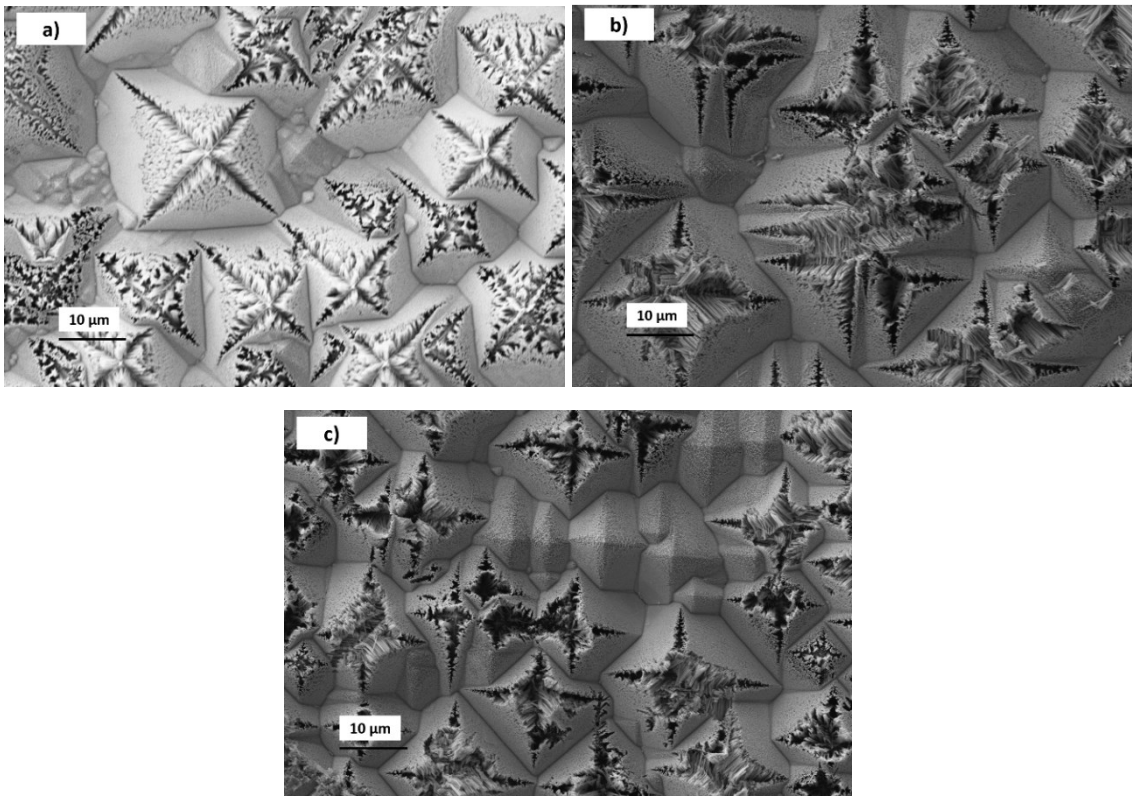

Figure 5.16: Top-view SEM of hybrid structures for MACE durations of: a) 5 minutes; b) 10 minutes; c) 15 minutes.

5.4.2 Hemispherical reflectance

The resulting surfaces are optically characterised using an integrating sphere system in the 300 nm -1100 nm wavelength range and the results are shown in Figure 5.17. As discussed in the previous section, an increase in the nanostructures length yields reduced surface reflectance, a trend that is maintained for the hybrid structures and shown in Figure 5.17 a) for measurements of the total hemispherical reflectance. The hybrid structures effectively supress reflection especially in the short wavelength range, where the peak commonly noted in bare pyramids inherited from the response of polished silicon substrates is significantly reduced and no longer visible. Diffuse hemispherical reflectance measurements presented in Figure 5.17 b) confirm the superior light-trapping capabilities of these hybrid structures when compared to bare alkaline etched micron pyramids, increasingly so for longer MACE durations. An increased in the nanowire heights beneficially impacts the long wavelength region as well.

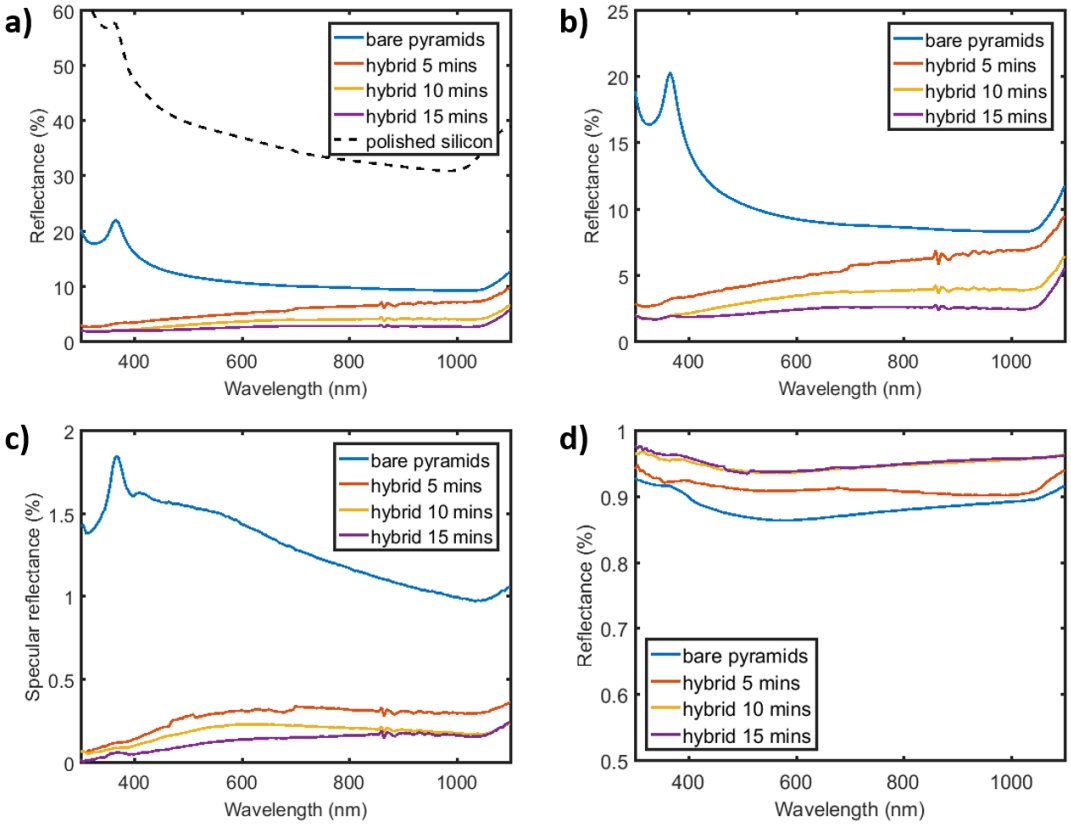

Figure 5.17: a) Measured total hemispherical reflectance; b) Measured diffuse hemispherical reflectance; c) Calculated specular reflectance; d) Calculated reflectance haze for fabricated hybrid structures with varying MACE durations.

The specular reflectance and haze can be calculated using the data shown in Figure 5.17 a) and b). These metrics are shown in Figure 5.17 c) and d), where increased MACE durations yield hybrid structures that scatter at large angles. The proportion of light redirected away from the specular reflection direction increases with the nanowire height, but with minimal difference between a 10 minute and a 15 minute MACE process. Table 5.7 shows a summary of the optical properties of the fabricated micro-nano hybrid structures, where data is calculated as a weighted average taking into account the AM1.5G spectral irradiance. Although the hemispherical total reflectance for the hybrid structures is similar to the values measured for just the black silicon layers alone of same height, there are notable differences in specular reflectance and reflected haze values between the two. As such, the hybrid structures proved to be better light-trapping candidates for the use

on top of silicon solar cells devices, given the same level of surface passivation to not be detrimental from an electrical point of view.

Table 5.7: Summary of optical characteristics for hybrid structures fabricated for various MACE durations.

t (mins)	WAR total (%)	WAR diffuse (%)	WAR specular (%)	WAR haze (/1)
0	11.35	10.04	1.34	0.88
5	5.52	5.24	0.28	0.91
10	3.63	3.43	0.19	0.94
15	2.66	2.42	0.13	0.95

5.5 MACE wafer scaling

5.5.1 Fabrication

MACE is a cheap and fast process that is attractive to industry for large-scale fabrication of high-efficiency silicon solar cells, consisting of only wet-etching silicon wafers. In terms of process ease and scalability, it is therefore similar to the existent KOH and acidic processes that result in random pyramids or isotextured multicrystalline silicon devices that have been adopted by the industry. As such, MACE processes that yield low-reflectance uniform substrates on both p and n-type silicon are desirable for industry integration, where up to 25 wafers can be textured in a single solution. For this purpose, three different MACE solutions differing in both silver nitrate and *HF* concentration were prepared for wafer texturing in a PTFE pocket in the wetbench (20 cm × 20 cm × 5 cm) (see Figure 5.18). All three solutions have a volume of 1.6 L such that a 6’ silicon wafer (15.6 mm x 15.6 mm) is fully submerged. The etching time is 30 minutes for all processes and the wafers are vertically standing such that both sides are textured. Prior to etching, all of the wafers were first cleaned using a 3:1 (H_2SO_4:H_2O_2) Piranha solution for 20 minutes, followed by thorough DI water rinse and a 7:1 H_2O:*HF* bath for 5 minutes for silicon

dioxide removal. After the MACE process, the leftover silver dendrites are removed using a 1:1 HNO_3:H_2O solution, followed by copious rinsing.

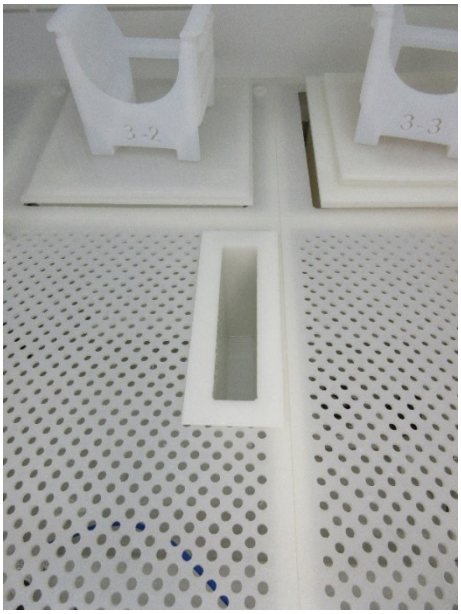

Figure 5.18: PTFE HF-resistant pocket inside the wetbench for MACE processing of Si wafers.

Wafer 1 was subjected to the same MACE solution concentration and recipe that reliably yields low-reflectance black silicon on 4 cm x 4 cm Si pieces (see Chapters 5.1-5.3) for a process time of 6 minutes. However, after etching, the silicon wafer remained polished showing only few regions that appear visually black, as pictured in Figure 5.19 a). This is thought to be due to poor dissolution of the silver nitrate inside the aqueous solution, which consequently affects silver nucleation and formation of silicon dioxide pits that can then be etched by the HF solution. As such, only a few regions of the wafer have been nucleated by the silver particles and present black silicon on the surface. Earlier literature reports [228] suggest that b-Si textures on wafer scale can be achieved for even lower solution concentrations at the expense of increased process time. As such, the recipe was changed accordingly for the next experiments in order to fabricated uniform b-Si across the entirety of the Si surface.

For wafer 2, a recipe available in literature was thus followed [228], with silver nitrate molarity of 15 mM and *HF* concetration of 4 M. The etching process duration

was 30 minutes. Wafer 2 is pictured in Figure 5.19 b) and exhibits a darker colour overall compared to wafer 1, indicative of some texture present on its surface. However, visual inspection reveals that the wafer retains a lot of specular reflectance and it is highly non-uniform. The main reason for high specular reflectance is thought to be the reduced length of the nanostructures, as well as their distribution and therefore density on the surface. This is indicative of small amounts of silver nitrate used for the increased silicon area, where not enough particles were present on the wafer to etch a dense array of nanowires. As such, a higher quantity of silver nitrate is desirable to promote nucleation on the silicon surface. The black appearance of the wafer in certain regions indicated that the *HF* concentration was sufficient to etch into the silicon, provided the nucleation of silver particles in those areas.

In line with the results obtained on wafer 2, the silver nitrate solution concentration was then increased to 30 mM, while *HF* concentration and process duration were unchanged. As such, wafer 3 exhibits fully-etched black silicon layer of sufficient length to massively supress top surface reflectance, as seen in Figure 5.19 c). Moreover, the black silicon appears to be very uniform on top of the silicon, indicating that both the silver nitrate and HF concentrations were adequate for the MACE process. Visual inspection confirms similar behaviour to the black silicon etched onto 4 cm × 4 cm silicon pieces, along with little specular reflection when the wafer is tilted at large angles, which is indicative of high aspect-ratio nanostructures. Figure 5.19 d) shows an image of the three wafers taken at an oblique angle, with decreasing degrees of specular reflectance and higher black silicon uniformity from wafer 1 to wafer 3.

Table 5.8 shows a summary of the conditions and solution concentrations used for the three wafers in Figure 5.19. The recipe created for 4 x 4 cm^2 did not yield b-Si on a full 6-inch Si wafer. This is thought to be due to poor dissolution of silver nitrate inside the deep wetbench pocket, where it was presumably sitting at the bottom of the pocket. In the later experiments (wafer 2 and 3), the solution was properly stirred so that b-Si could be fabricated. Therefore, the recipe used for wafer 1 should work for 6-inch Si wafers if certain experimental steps are carefully

followed, for shorter processing times at the expense of higher solution concentration.

Table 5.8: Summary of MACE parameters for texturing a 6'' Si wafer.

Wafer #	$AgNO_3$ concentration (mM)	HF concentration (M)	Etching time (mins)
1	60	14	6
2	15	4	30
3	30	4	30

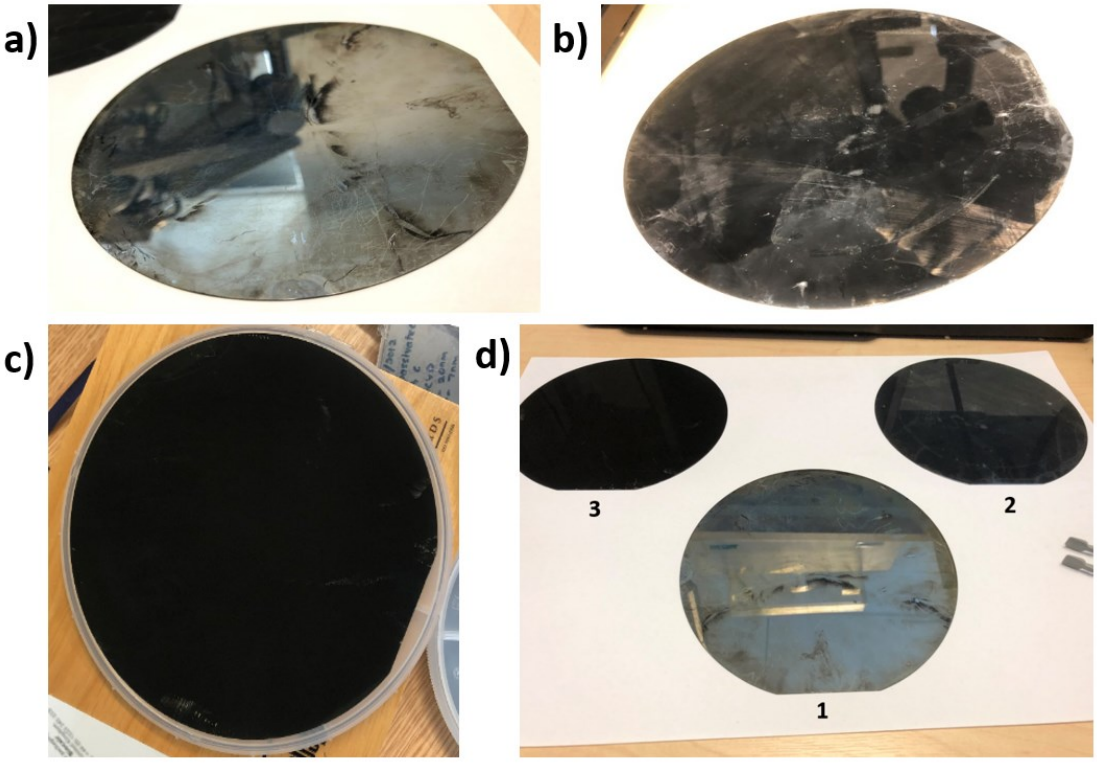

Figure 5.19: Photographs of the MACE 6' Si wafer: a) Wafer 1; b) Wafer 2; c) Wafer 3; d) All three wafers under large tilt.

5.5.2 Optical characterisation

In order to measure the optical properties of each wafer, as well as the uniformity of the black silicon layers across the surface of the wafers, a custom reflectometry setup has been used, pictured in Figure 5.20 a) to assess the specular reflectance of the fabricated structures. The light source is a tungsten-halogen source that, in combination with a spectrophotometer sensitive in the visible range, can collect data in the 340 nm – 1022 nm wavelength range, important for silicon photovoltaics. An optical fibre is mounted on top of the black silicon wafers on a fixed arm in a way that light is normally incident to the substrate. The optical fibre has six spots distributed in a circular pattern from which light shines onto the samples, and another spot in the middle of the circular pattern to collect reflected light, as pictured in Figure 5.20 b). As common with spectroscopy measurements, the noise levels of the spectrometer and environment have also been collected to correct the data.

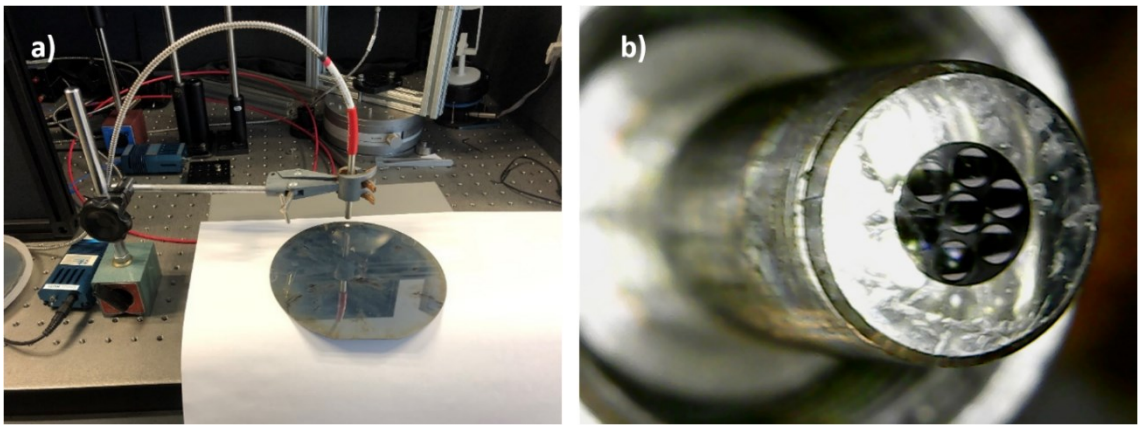

Figure 5.20: a) Reflectometry setup collecting specular reflectance in the 340 nm -1020 nm wavelength range; b) dual optical fibre used, outer spots shine light, inner spot collects data.

The three wafers have been characterised using a scanning pattern grid as shown in Figure 5.21 a), where every square is 1 cm x 1 cm, resulting in a total of 45 measurements per sample. Data is collected for every 1 cm movement of the wafer and thus allows for the creation of a uniformity heatmap associated with each etched wafer. Reflectance values can be calculated using the measurements of a

polished silicon wafer and assuming the relationship between collected intensity and integration time is proportional. As such, Figure 5.21 b)-d) show the uniformity plots of the wafers, with specular reflectance values in colour, where each data point was average over the wavelength range. As expected from visual inspection, the wafers have decreasing degrees of measured specular reflectance and increasing degrees of nanostructure uniformity across their surfaces. Table 5.9 shows a summary of the optical properties of each etched wafer, where wafer 1 yields specular reflectance R = 15.25 % ± 3.26 %, wafer 2 R = 7.41 % ± 3.51 % and wafer 3 R = 2.13 % ± 0.16 %. The larger deviation corresponding to wafer 2 is caused by the measurement near the bottom right side noticeable in Figure 5.21 c). Table 5.9 presents a summary of the optical properties measured for wafers 1-3.

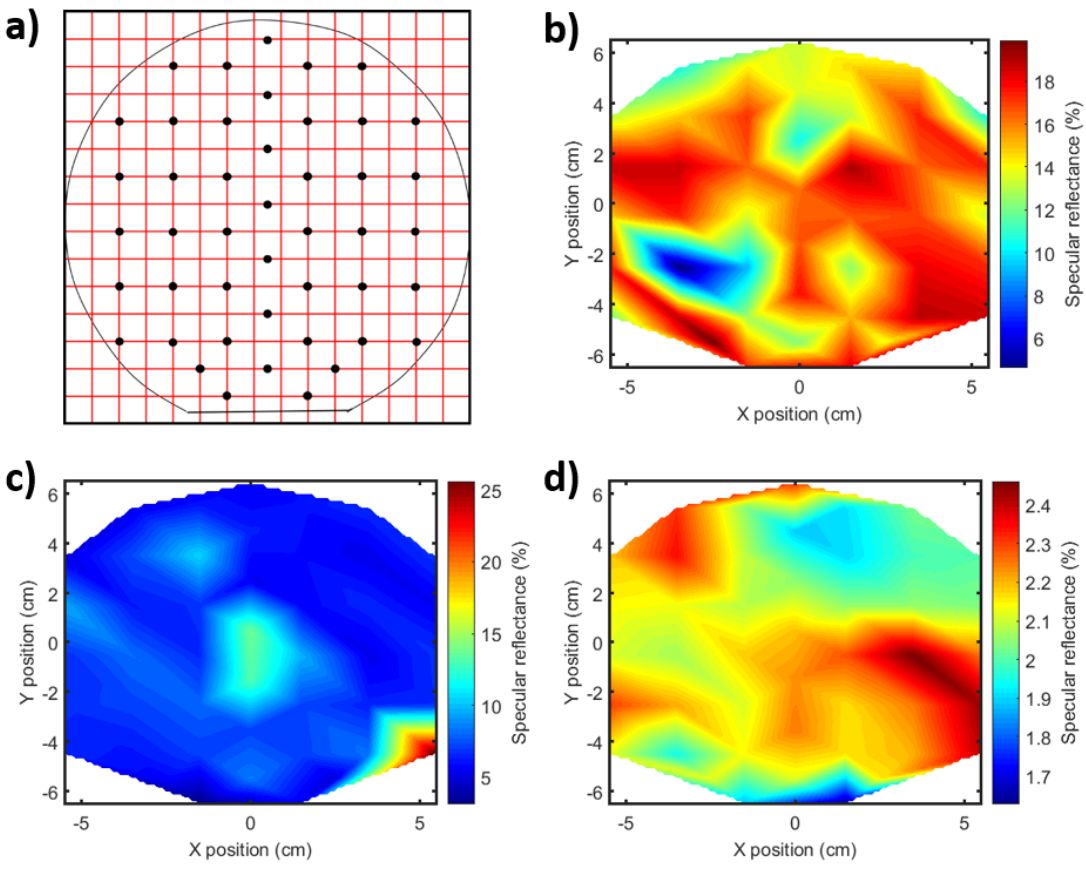

Figure 5.21: a) Grid scanning pattern used to measure black silicon wafers; b) Specular reflectance heatmap of wafer 1; c) Specular reflectance heatmap of wafer 2; d) Specular reflectance heatmap of wafer 3.

Table 5.9: Summary of optical properties of the black silicon wafers.

Wafer #	Integration time (ms)	Specular reflectance (%)	Standard deviation (%)
1	5	15.25	3.26
2	10	7.41	3.51
3	30	2.13	0.16

5.6 Conclusions

In this chapter, the role of the etching parameters onto the black silicon morphology and optical properties is studied, such as etching duration, silver nitrate solution molarity and hydrofluoric acid solution molarity. Each set of parameters is changed independently for a fixed set of the rest of the parameters. By varying the etching time, the length of the resulting nanotextures can be controlled, with longer process times yielding longer nanostructures on the silicon surface. The black silicon layer is comprised of well-defined, vertically aligned nanowires with uniform skyline. When the silver nitrate concentration is varied, the length of the nanostructures changes accordingly, as well as the diameter of the nanowires and the density on the surface. As a direct consequence of this, the nanowire top down coverage area increases with increased silver nitrate molarity. If the hydrofluoric acid solution concentration is increased, the etching of the silicon surface occurs at a higher rate, due to faster dissolution of the formed silicon dioxide pits beneath the propagating metal particles. However, large *HF* concentrations lead to chaotic etching in the lateral direction and to less control over the desired nanowire morphology. Considering the impact of these parameters on both the morphology of the texture and its optical response, an ideal silver nitrate molarity is chosen as 60 mM, while the *HF* concentration is chosen in the range of 7-11 M. Although b-Si textures can be

achieved for other solution molarities, there is a definitive trade-off between the etching process duration and the aspect of the nanostructures that this chosen parameters satisfy. Moreover, hybrid micro-nano textures are fabricated (i.e. alkaline etching to form random pyramids, then MACE) with excellent optical properties and the MACE process was applied to a 6-inch standard silicon wafer, with measured specular surface reflectance of below 2%. This demonstrates the scalability of the etching process and its suitability for high-throughput integration at industry level for the reliable and reproducible realisation of antireflective surfaces for high-efficiency silicon photovoltaics.

Figure 5.22 shows the best (blue trace) and worst (red trace) performing uncoated b-Si layers fabricated in this work from a measured hemispherical reflectance perspective, suggesting the broad range of resulting optical and electrical properties that this method can yield. Upon altering the etching recipe and conditions, any optical result between these two can be achieved. As such, these properties can be tailored for various applications, so that both optical and electrical performance of the device are satisfying.

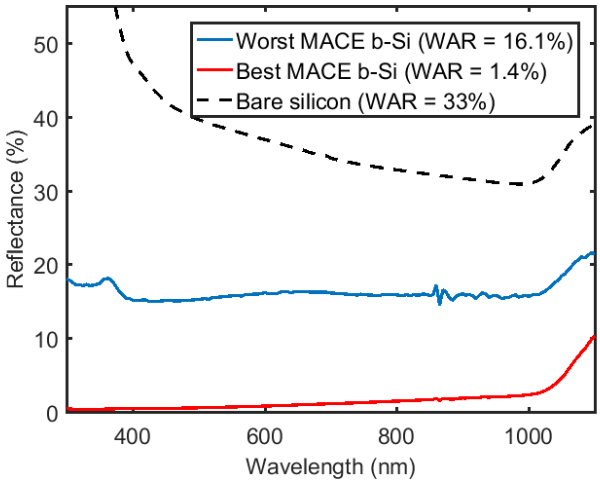

Fig. 5.22: Comparison between the worst performing MACE b-Si texture (blue trace) and best performing (red trace) measured surface reflectance. Bare silicon reflectance shown as dashed black trace for reference.

Chapter 6

Electrical passivation of black silicon

For an effective gain in the power conversion efficiency of a silicon solar cell that employs MACE black silicon as an antireflective layer, sufficient surface passivation is required to mitigate the associated electrical losses. The increase in the semiconductor surface area by tens of times upon surface texturing introduces a very large density of traps in the bandgap of the material which must be effectively addressed. Therefore, the surface recombination velocity of MACE b-Si must be minimised significantly to values comparable to alkaline-etched surfaces currently available in industry for the superior optical capabilities to enhance the photocurrent of the device. In this chapter, an investigation into the passivating properties of ALD aluminium oxide is presented, for both flat and nanotextured surfaces. Sufficiently low surface recombination velocities are obtained in both cases and for a range of nanowire lengths. Moreover, it is found that an extra diffusion step in the ALD cycle can further contribute to the increase of minority carrier lifetimes.

6.1 Thermal ALD aluminium oxide

Owing to its fixed negative charged that can be activated in the layer, aluminium oxide has become an excellent candidate for electrical passivation of both p-type and n-type silicon substrates. This negative charge is activated upon a moderate temperature annealing step in nitrogen atmosphere and it has been reported that the duration of this step is highly important for the performance of the passivating layer. For thermal ALD, the optimum annealing conditions of the Al_2O_3 layer are reported to be 400 ° - 425° C for 10 to 30 minutes.

6.1.1 Annealing duration

As such, an in-depth study has been conducted on the effect of annealing duration of a 15 nm ALD alumina layer both on n-type and p-type polished silicon for lengths of 0 - 60 minutes. The n-type wafers are CZ 1-5 Ωcm with thickness of 240 µm ± 20 µm, while the p-type wafers are CZ 1-10 Ωcm with thickness of 280 µm ± 20 µm. The thermal ALD process uses TMA and H_2O as precursors and is described in detail in Chapter 4.1.2. QSSPC measurements for n-type silicon substrates are shown in Figure 6.1 a). It is clear that an increase in the annealing duration yields higher effective lifetimes up to 30 minutes, after which the effective lifetime drastically decreases to values comparable to the as-deposited state. This is due to the negative fixed charge, Q_f, activated in the layer that increases in magnitude with increased annealing durations, owing to the migration of tetrahedrally and octohedrally coordinated Al atoms and their ratio at the silicon-alumina interface [198]. The alumina layer improves the effective lifetime of the carriers for low injection levels < 10^{15} cm^{-3}, but significantly reduces the lifetimes above this threshold. This is a direct consequence of increased Auger recombination in the annealed layers for such minority carrier densities [195]. In contrast, the shape of the trace of the as-deposited state (blue, no annealing) does not show this decrease for large minority carrier densities. In almost all cases, the highest effective lifetime is measured at an injection level of 10^{15} cm^{-3} and below, where data in literature is typically reported. This is an important result for PV, as solar cells operate under low-illumination

[190]. Therefore, by extracting effective lifetimes at this value, the relationship between lifetime and annealing time is shown in Figure 6.2 a). Interestingly, an almost linear proportion is found for durations up to 30 minutes, where the maximum surface recombination velocity SRV is calculated to be 13 cm/s in the 240 µm thick silicon wafer by assuming infinite bulk lifetime, corresponding to an effective lifetime of 920 µs.

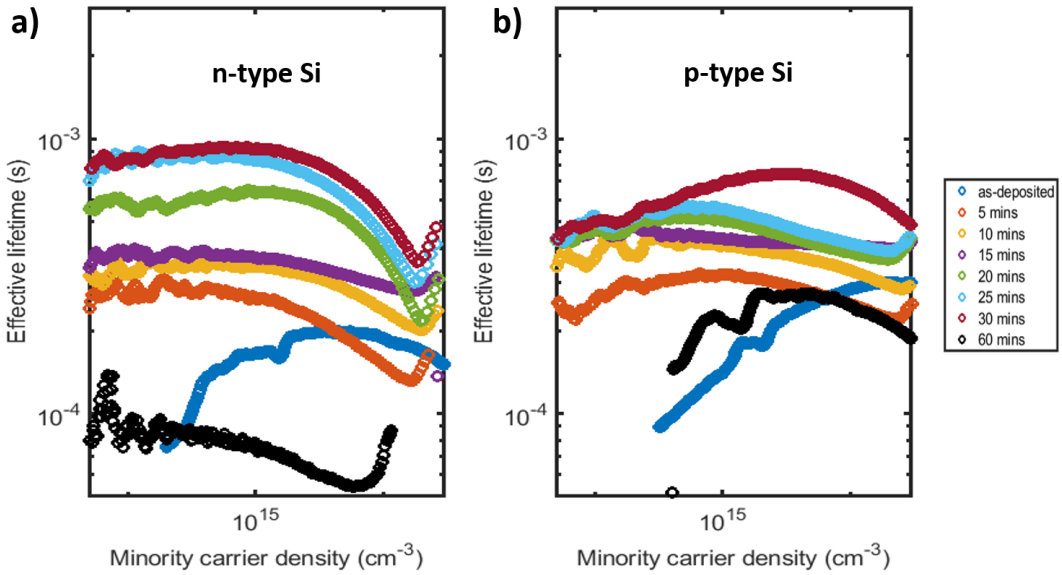

Figure 6.1: QSSPC measurements as function of injection level for a 15 nm ALD Al_2O_3 with various annealing durations on: a) n-type silicon; b) p-type silicon.

Similarly, Figure 6.1 b) shows the annealing duration impact on the alumina layer for polished p-type wafers, where the trend is maintained: longer anneals give rise to larger negative charge in the passivating layer and thus to enhanced field-effect passivation [190-191]. This in turn leads to increased effective lifetimes, as large as 684 µs for 30 minutes anneal. A 60 minutes anneal yields reduced lifetimes, comparable to the as-deposited state, due to a decrease in the fixed negative charge, Q_f. It is unclear what is the source of this reduction, but it appears the chemical component of the passivation is reduced as well. Figure 6.2 b) shows the effective lifetime at injection levels of 10^{15} cm^{-3} for each annealing duration and again an almost linear relationship is calculated, shown by the red trace. The highest SRV is

calculated as 20 cm/s for 30 minutes annealing length, corresponding to an effective lifetime of 684 µs. Overall, the passivation level for n-type silicon is more effective than for p-type silicon, suggesting the strong inversion caused by the negative fixed charge in the alumina layer. This is in line with previous reports [190] and can be further explained in this study by the activation of B-O defects commonly observed in the CZ p-type material upon high-temperature annealing, which act as recombination traps [229].

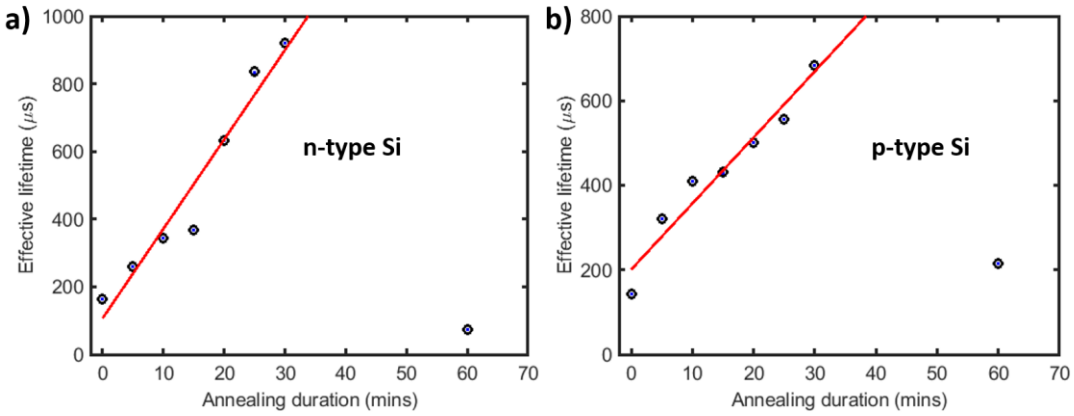

Figure 6.2: Effective lifetime as a function of annealing time for 15 nm alumina layer deposited on polished silicon: a) n-type; b) p-type. All values quoted at $\Delta n = 10^{15}$ cm^{-3}.

Table 6.1 shows a summary of the effective lifetimes and corresponding maximum surface recombination velocities calculated by SRV < $\frac{W}{2\tau_{eff}}$, when the bulk lifetime is assumed to be infinite. It can be observed that annealing times below 15 mins yield comparable results for both p-type and n-type silicon, mainly due to the inversion in n-type silicon being characterised as weak up to this annealing duration. However, upon annealing durations of more than 15 mins, the passivation quality of the AlO_x layers on n-type Si exceeds that of p-type Si, as the inversion of the carriers becomes more pronounced and more defects are activated in the p-type material.

Table 6.1: Summary of effective lifetimes and maximum SRV corresponding to increased annealing times. All values quoted at Δn = 10^{15} cm^{-3}.

Annealing time (mins)	Effective lifetime τ_{eff} (µs)		SRV (cm/s)	
	n-type	p-type	n-type	p-type
0	165	143	72.7	97.9
5	261	321	45.9	43.6
10	344	409	34.8	34.2
15	369	430	32.5	32.5
20	633	501	18.9	27.9
25	833	557	14.4	25.1
30	920	684	13	20
60	74	216	162.1	64.8

6.1.2 Film thickness

Another important parameter for optimizing the passivating layer is the film thickness. This can have various implications, from deposition time and therefore the cost, to conformity and uniformity on top of black silicon layers and other high-aspect ratio structures. Figure 6.3 a) shows the QSSPC measurements for various alumina layer thicknesses deposited on polished n-type silicon wafers after the moderate-temperature annealing step at 425 °C for 30 minutes. It is obvious that thicker layers yield higher effective lifetimes due to the field-effect passivation component, where more negative charge can be activated in the film. Figure 6.3 b) shows the relationship between effective lifetimes and alumina layer thickness, where a saturation starts to occur for thicknesses above 20 nm. This agrees well with previous reports from Dingemans [189, 193], who found that AlO_x layers of 15-20 nm are enough to provide most of the field-effect passivation and increases past

this threshold are minimal. This is thought to be due to a deterioration in the chemical passivation component for very small thicknesses below 15 nm arising from the interfacial silicon dioxide grown during ALD process. However, an increase in the ratio of tetahedrally and octahedrally coordinated Al atoms is expected to occur in thicker layers close to the SiO_2/AlO_x interface, which leads to an increase in Q_f mirrored charge in the silicon material. Table 6.2 shows a summary of the electrical characteristics for increasing ALD AlO_x films in thickness.

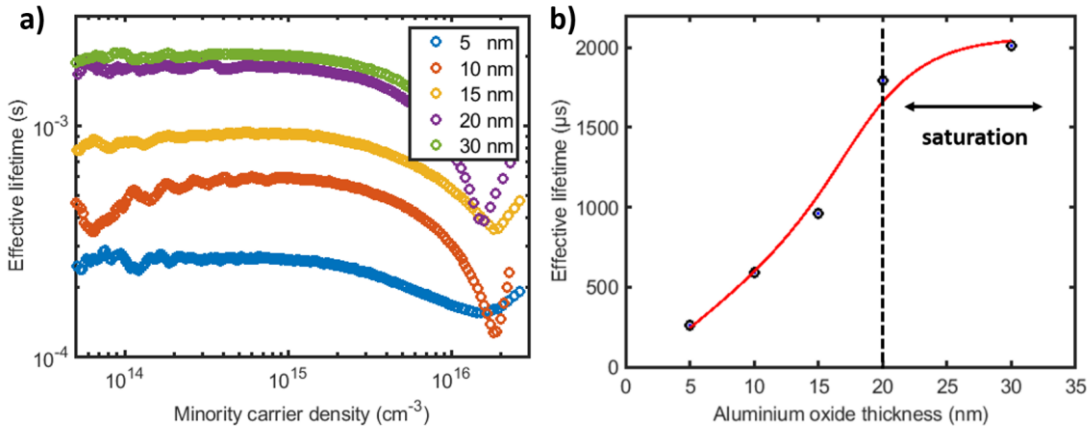

Figure 6.3: a) QSSPC measurements for various alumina thicknesses on n-type silicon; b) Effective lifetimes at $\Delta n = 10^{15}$ cm^{-3} for increasing thicknesses, saturation region indicated.

Table 6.2: Summary of electrical characteristics with increased alumina film thickness. All values quoted at $\Delta n = 10^{15}$ cm^{-3}.

Al_2O_3 thickness (nm)	Effective lifetime τ_{eff} (µs)	SRV (cm/s)
5	263	45.6
10	593	20.2
15	963	12.4
20	1791	6.7
30	2011	5.9

6.1.3 Passivation of black silicon

Atomic layer deposition is the preferred deposition method for ultra-thin passivating layers on textured surfaces, especially those with nanostructured black silicon on top. This is because the slow deposition rate at low temperatures allows for precise control and conformal coverage of the high-aspect ratio structures. As discussed in Chapter 5, texturing a silicon substrate increases the semiconductor surface area and thus the density of the dangling bonds at the surface, which in turn adds energy states into the bandgap of the material, effectively increasing D_{it}. This is especially crucial for MACE black silicon, as the semiconductor surface area is increased by tens of times, depending on the length of the nanowires. The excellent optical properties black silicon provides in reduced broadband reflectance and increased broadband absorption can all be lost if the resulting surface is not effectively electrically passivated, hindering the development of high-efficiency silicon solar cells.

6.1.3.1 Exposure vs. non-exposure mode

As previously explained in Chapter 4, 'exposure mode' atomic layer deposition refers to a modification of the standard deposition recipe, such that the precursors (i.e. TMA and water for AlO_x) are given more time to settle on the target surface. This is achieved by introducing a particular step within the ALD cycle, essentially delaying the purging of the chamber by a number of seconds, and is especially useful for coating high-aspect ratio structures such as MACE b-Si.

Figure 6.4 a) shows the decrease in effective lifetimes with increased MACE duration in the bare (uncoated) specimens. At first, the polished silicon n-type substrate has effective lifetime of 5-6 µs, which is significantly reduced to 3 µs and 1.7 µs for MACE durations of 4 minutes and 10 minutes, respectively, when the black silicon layers remain uncovered. By deposition of a 15 – 17 nm alumina layer on top of the nanostructures via non-exposure mode (standard) ALD and optimal annealing, the resulting effective lifetimes can be boosted by at least two orders of magnitude, as seen in Figure 6.4 b). Here, lifetimes of 672 µs and 236 µs can be

measured for the same etching conditions, visible in the dashed traces. Moreover, if the purge valve is closed during the ALD process such that the precursors are given increased time (10 s) to properly settle inside deep trenches and saturate the black silicon surface, better deposition conformity and uniformity is achieved for these high-aspect ratio structures. This is called 'exposure mode' ALD process. The measured effective lifetimes after this ALD process for the two black silicon layers that have undergone the same MACE duration is also shown in Figure 6.4 b), as denoted by 'o' symbol. As such, a relative increase of 20-40% in the effective lifetimes is possible for identically fabricated nanostructures, with values of 892 µs and 402 µs, respectively. Therefore, for the 4-minute MACE sample, the SRV has decreased from 18 cm/s to 13.4 cm/s utilising an exposure mode ALD process which consists in the insertion of a diffusion step for the precursors. More importantly, this increase has been achieved without sacrificing any of the morphology and the optical properties of the black silicon layer, whereas the common practice is for the MACE layers to undergo a polishing step to achieve better electrical passivation and lose their impressive broadband absorption effect and aspect ratio [204].

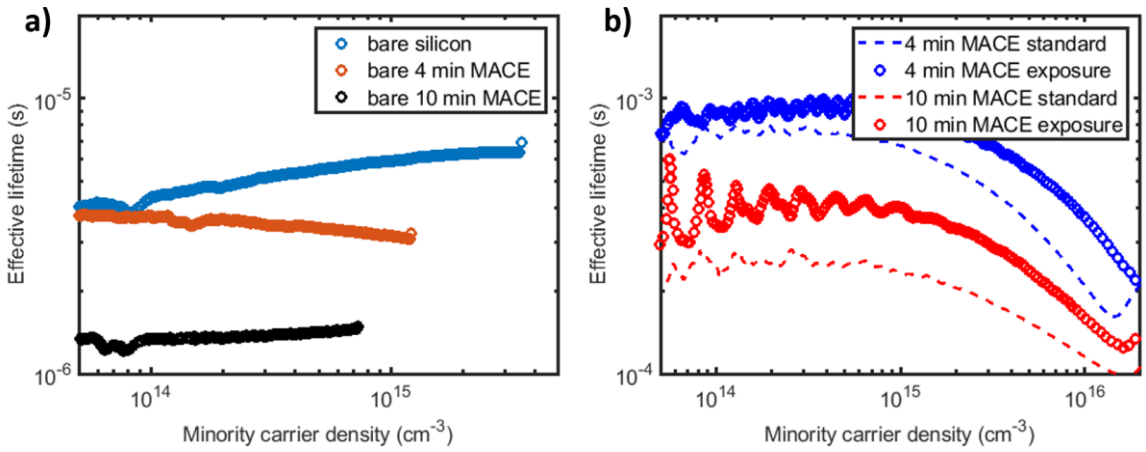

Figure 6.4: a) QSSPC measurements for unpassivated MACE layers; b) QSSPC measurements for passivated MACE layers, showing gain by using exposure mode ALD process.

As such, this is a very important result for effectively passivating black silicon and nanostructured silicon surfaces, where the only downside is the slight increase in the deposition time, as each ALD cycle is now 10 s longer. Depending on the desired

thickness of the alumina layer, this can prolong the ALD process by 20-30 minutes for a 20-40% relative gain in the passivation level.

6.1.3.2 Impact of black silicon length

An investigation for various MACE process durations has been conducted to observe the level of passivation on top of the resulting black silicon layers covered with double-sided 17 nm of 'exposure-mode' ALD alumina. As such, different MACE b-Si has been etched for process time of 4 minutes, 6 minutes, 8 minutes, 10 minutes and 12 minutes, respectively, on n-type CZ wafers. QSSPC measurements for various MACE lengths are shown in Figure 6.5 a), where a decrease in effective lifetimes with increased MACE duration is noticeable, even for this exposure mode ALD process. Moreover, the passivation levels of the shorter etching times are comparable to the polished silicon values (see Figure 6.3 a)), showing the suitability of the process and the black silicon layers as a whole for high-efficiency silicon devices. For example, the 4 min MACE b-Si sample yields a minority carriers lifetime of 842 µs, which is very similar to the 963 µs obtained on the polished surface of the same wafer type. Figure 6.5 b) shows the linear relationship between the effective lifetimes and the MACE duration process. This can be explained by the linear increase in the nanostructure height with etching time as the etch rates are constant (see Chapter 5.1.). Due to the fact that the same silver nitrate molarity solution has been used, the distribution of the nanowires on the silicon surface is similar among these samples and the dominant parameter dictating the surface area increase is their height, which increases linearly with MACE durations (see Figure 5.2). Table 6.3 summarises the electrical characteristics of black silicon layers, fabricated using various MACE durations, then passivated with a 15 nm alumina layer that has underwent optimal annealing.

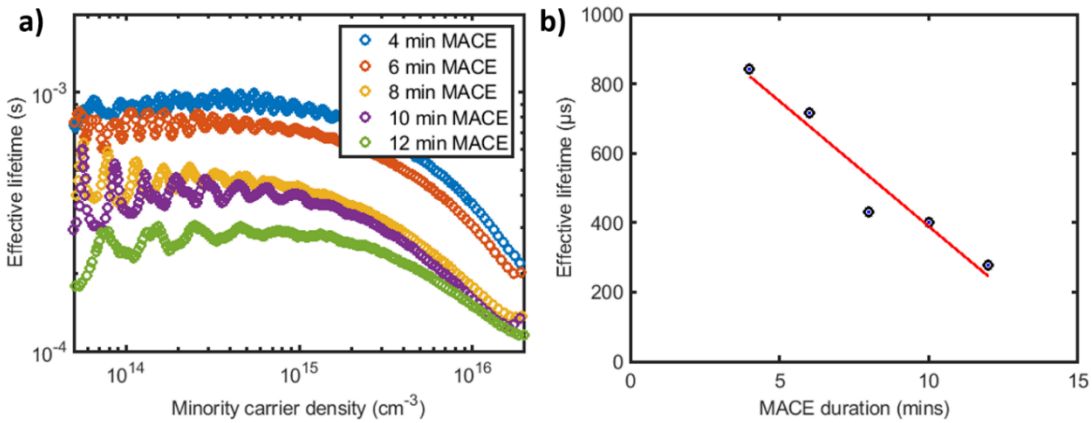

Figure 6.5: a) QSSPC measurements for ALD alumina layers on black silicon layers with various MACE durations; b) Effective lifetimes as function of MACE duration. All values quoted at $\Delta n = 10^{15}$ cm^{-3}.

Table 6.3: Electrical characteristics of black silicon layers, fabricated using various MACE durations, then passivated with a 15 nm alumina layer. All values quoted at $\Delta n = 10^{15}$ cm^{-3}.

MACE duration (mins)	Effective lifetime τ_{eff} (µs)	SRV (cm/s)
4	842	14.2
6	715	16.7
8	432	27.7
10	400	30
12	279	43

One of the main advantages of the ALD amorphous AlO_x thin layers is that they provide parasitic absorption only for wavelengths below 200 nm, which is outside the wavelength range of interest for silicon photovoltaics. This is due to the extinction coefficient, *k*, being zero for photon energies up to 6 eV [66-67]. As such, the alumina layer not only electrically passivates the black silicon nanostructures, but it has the potential to provide some antireflective effect to improve the optical

response of the stack. It has been previously reported [46] that thin layers of 20 nm of alumina on top of black silicon improve the surface reflectance in the near UV region. Figure 6.6 shows total hemispherical reflectance measurements of a black silicon sample fabricated for MACE duration of 5 minutes, before and after the dielectric deposition. It can be seen that the 17 nm alumina film has a beneficial impact on the short wavelength response and the resulting weighted average reflectance of the sample is 2.9%. In contrast, the uncoated nanowires yield a weighted average reflectance of 3.4%. The difference between the two values is attributed to the alumina layer acting as an antireflective coating due to photon interference, even for such a small thickness.

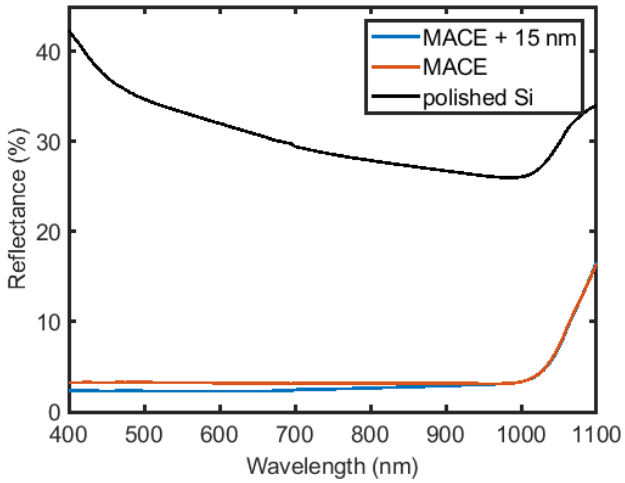

Figure 6.6: Optical impact of a black silicon texture with (blue) and without (red) 15 nm ALD AlO_x.

Although no systematic study has been reported in literature so far concerning the effect of b-Si doping upon the passivation quality of the ALD layers, the trend found for polished wafers is expected to persist upon texturing. As such, ALD aluminium oxide should prove more effective surface passivation for n-type b-Si layers than for p-type. The work by Pasanen et al (2017) [203] has investigated the passivation properties of various dielectric stacks upon lightly-doped emitters with a random pyramidal texture. It was found that a 10 nm Al_2O_3 layer deposited via ALD could confer a surface

recombination current on n^+ emitters as low as $J_{0,n}$ = 45 fA/cm^2 in comparison to $J_{o,p}$ = 500 fA/cm^2 for p^+ emitters.

6.1.4 Conformity of ALD layers on black silicon

An important prerequisite for the electrical passivation of black silicon nanostructures is the conformity of the ALD deposited dielectric on the surface. This impacts both the chemical passivation, as the dangling bonds are saturated only by a layer that is in contact with the silicon surface, and the field effect passivation, as the negative charges activated in the alumina film have to be as close to the *Si/AlO$_x$* interface as possible. The geometry of the nanowires may prove difficult for good conformal coverage, as the nanostructure array is very dense and presents high-aspect ratio features. Therefore, some precursor penetration might be limited in the very deep trenches and crevices between black silicon structures. Furthermore, the bunching of nanowires previously reported in MACE structures [216] may prevent coating in-between and result in unreasonable levels of passivation due to lack of dielectric at the base of the nanostructures. For this reason, helium ion microscopy (HIM) has been employed to assess the conformity of the ultra-thin passivating layer on two black silicon morphologies, that have undergone MACE process for 5 and 10 minutes, respectively. HIM has appealing advantages over traditional SEM for imaging of these thin films, such as higher resolution and larger depths of field.

Figure 6.7 shows tilted top-view images of the nanowires formed by a 10 minute MACE process before (a) and after (b) the ALD alumina deposition. Both arrays indeed experience significant bunching towards the tips of the nanostructures because of the various nanoscopic forces at play. The as-fabricated MACE layers exhibit very thin nanowires that are sharp towards their tips, as seen in the inset of Figure 6.7 a). After ALD deposition (Figure 6.7 b), these structures appear thicker and the tips appear rounded, due to the alumina coating layer. The images in the inset suggests that during the exposure mode ALD process, conformal coverage towards the bases of the nanowires comes at the cost of some precursor saturation towards the tips of the nanostructures.

Figure 6.8 shows cross-sectional images of the black silicon layers with and without ALD coating. The sample has been cleaved and mounted so that the nanowires are perpendicular to the incoming He beam. The nanostructures present a uniform skyline and diameters in the range 20 nm - 50 nm across the entirety of the sample. The bright thin layer in Figure 6.8 b) is the alumina coating that surrounds the darker silicon material with good conformal coverage down to the bottom of the nanopillars and on top of the smallest intricate features. Once coated, the diameters of the nanowires visibly increase and become morphologically more robust.

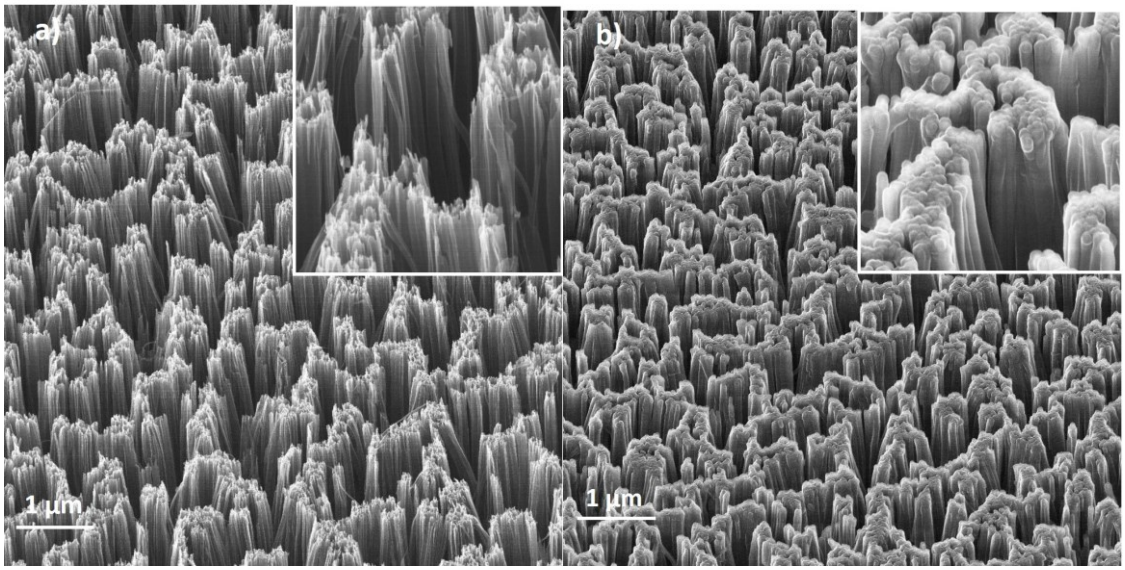

Figure 6.7: 10-minute processed MACE black silicon a) before and b) after the ALD deposition process. The tilt angle of the sample in both images is 45°.

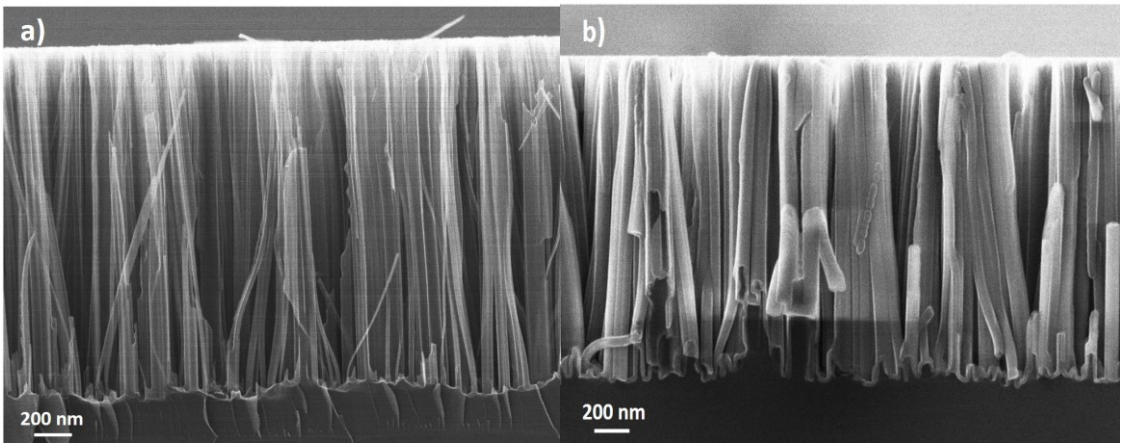

Figure 6.8: Cross-sectional HIM images of MACE fabricated black silicon layers a) before and b) after ALD deposition.

In some cases, the cleaving of the nanostructures exposed individual nanowires that have been sectioned along their short axis, revealing an inner silicon dark core uniformly cladded by a brighter aluminium oxide layer, as in Figure 6.9 a). Similarly, some nanostructures were cleaved along their long axis, where it can be seen that the dielectric film covers the black silicon layer all the way to the bottom of the pillars, including deep trenches and crevices, as shown in Figure 6.9 b). The thickness of the ALD deposition can be extracted directly from the high-resolution images for two sets of MACE nanowires with different lengths of ~414 nm and ~1508 nm, respectively. The alumina thickness is measured across multiple data points and yields values of 17.9 nm ± 1.3 nm and 18.4 nm ± 1 nm for the two nanowire morphologies, respectively. This is in good agreement with expectations from the ALD recipe and reference polished silicon samples where ellipsometry was employed. Slight thickness increase over the standard ALD recipe (i.e. non-exposure mode) is due to some underside deposition during the ALD process on the sample face sitting on the chamber stage, as alumina deposition is performed twice, on both sides. This is an especially important result, as the silicon surface area is significantly increased from the flat silicon deposition by tens of times. The similar thickness among these samples indicates that the precursor delivery is sufficient during the ALD process to not limit growth and no change in the coating thickness is observed when deposited on top of such different high aspect-ratio structures.

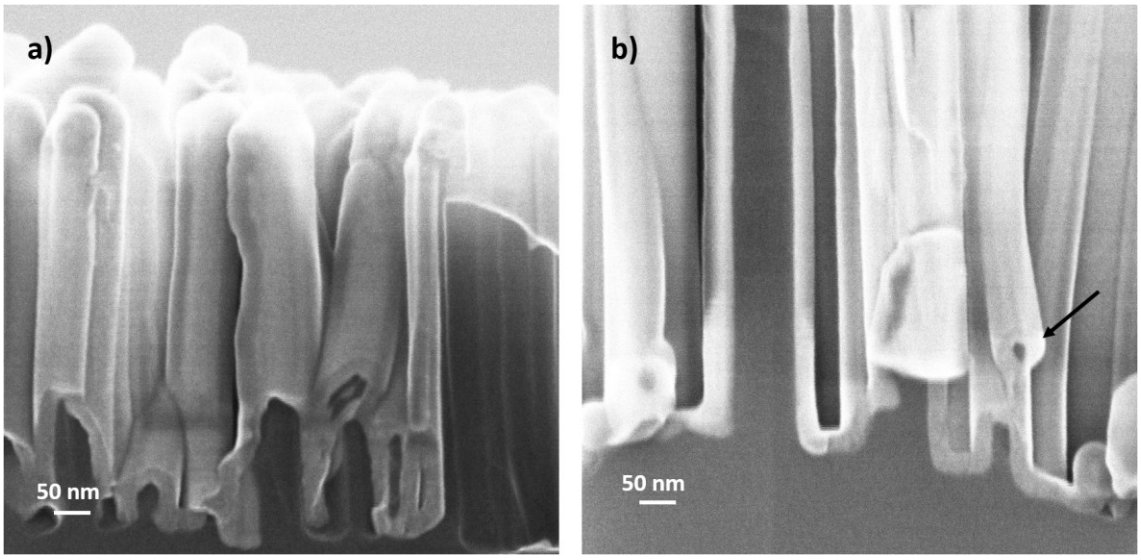

Figure 6.9: Magnified cross-sectional HIM images of black silicon layers for a) 5 minute and b) 10 minutes MACE durations.

As previously discussed, there is a possibility that nanowire agglomeration and bunching prevents ALD precursor penetration in-between the nanostructures, resulting in no coating at the bases of these black silicon layers. However, this is not visible from either the top-view or cross-sectional HIM images presented above. As such, a more novel method has been preferred, where the nanostructures are milled with the *Ne* ion beam perpendicular to their long axis couple of hundred of nanometres below their joined tips. This novel technique involves precise milling, which is possible at this scale due to the 1 nm *Ne* ion beam spot size capability of the Orion tool. Various dosages and dwell times were tried to obtain the best results, with optimal conditions being a single scan with a dose of 2 nC/μm^2 and a dwell time of 2 ms. While some of the images were captured with the *Ne* beam resulting in lower quality, where possible, the source was changed to *He* beam. Figure 6.10 shows a diagram of the sample loading and milling inside the chamber.

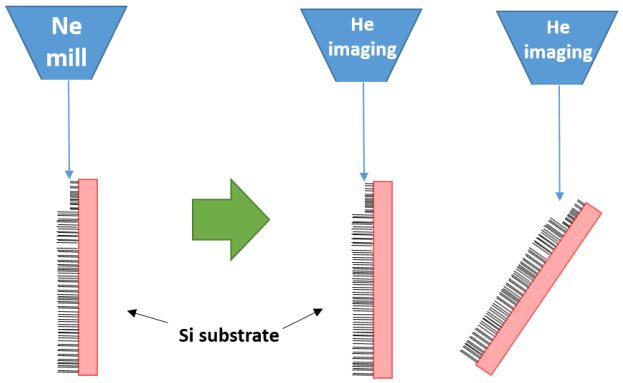

Figure 6.10: Schematic of milling and imaging process on b-Si sample.

Figure 6.11 shows the MACE black silicon layer before (a) and after (b) the milling process, where the same nanostructure region has been imaged. The images reveal that about 270 nm were removed from the tips of the nanowires, sufficient to assess the conformity of the ALD deposition inside the agglomerations. An image taken with the Ne beam midway through the milling process is shown in Figure 6.10 c), along with the milling box of 300 nm × 500 nm. A tilted top-view image of the milled region is visible in Figure 10 d), where the bright alumina coating is seen to surround the darker silicon cores of the nanowires. This confirms that the ALD process is highly conformal on top of high-aspect ratio, as the Al_2O_3 has penetrated below the nanowire agglomerations and coated the surfaces from within. Rather than individual nanowires, the agglomerations are still visible, indicating that such large surface area structures become very flexible for heights even below 1 µm. The morphological details presented in these images can potentially be useful when MACE black silicon layers are modelled optoelectronically on top of silicon devices.

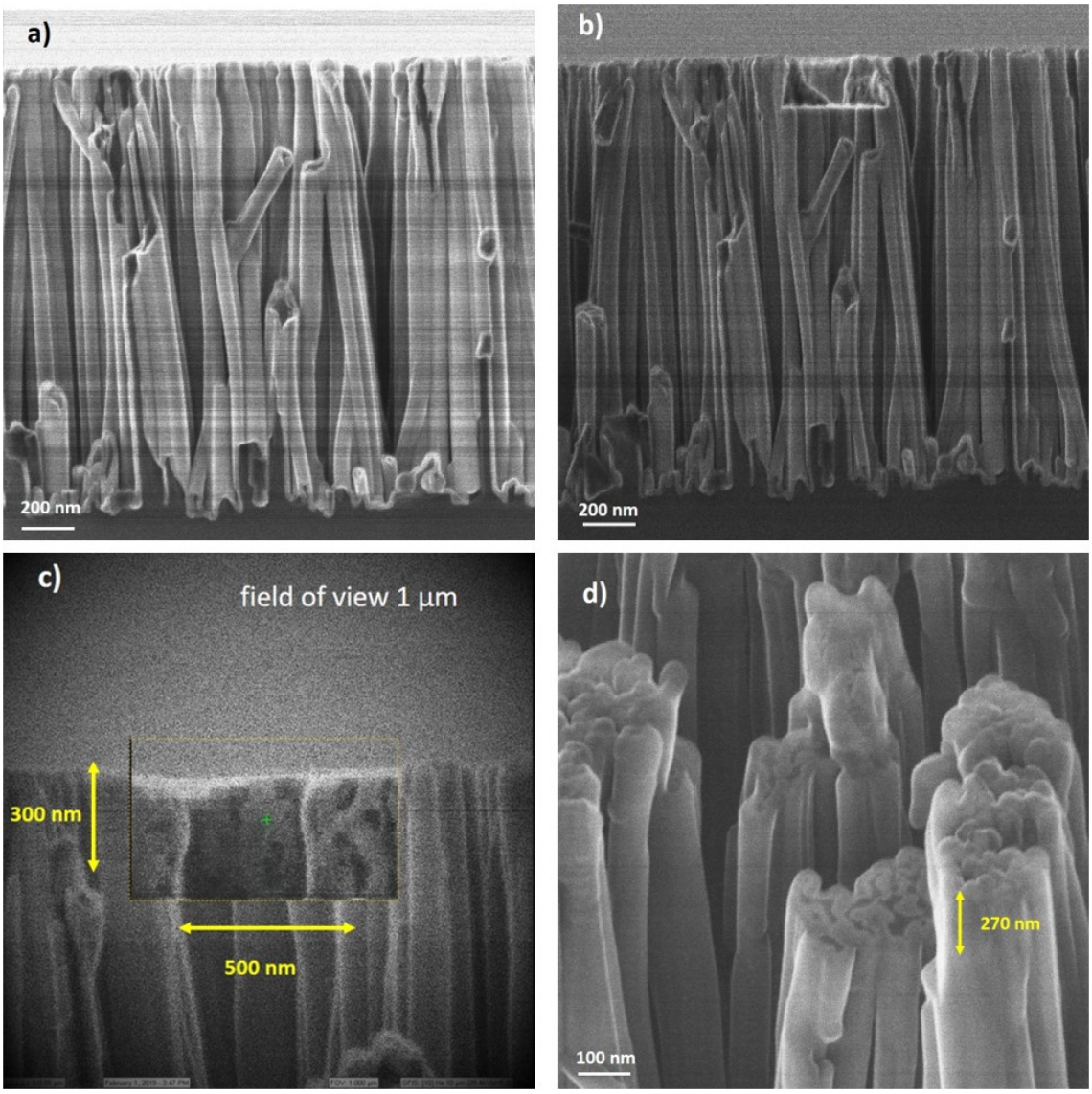

Figure 6.11: a) Ne beam image of nanowire region before milling; b) He beam image of nanowire region after milling; c) Ne beam image during the milling process, milling box defined; d) HIM image of milled area taken with a stage tilt of 45°.

6.2 Conclusions

Black silicon textures provide excellent antireflective effects for photovoltaic applications. However, the large increase in semiconductor surface area translates into unacceptable levels of carrier recombination and hinders the electrical

performance of the solar cell. To this end, surface passivation of the nanostructures is a crucial step for implementation into high-efficiency photovoltaics. Atomic layer deposition (ALD) is a low-temperatue controllable deposition method which is applicable for such high-aspect ratio structures. Aluminium oxide can provide sufficient chemical passivation on the silicon surface, as well as field-effect passivation owing to the negative fixed charged that can be activated inside the layer upon high-temperature annealing. This is demonstrated on both n-type and p-type polished silicon wafers for various alumina thicknesses and annealing durations, as well on MACE black silicon of increasing lengths. Moreover, a diffusion step can be inserted into the ALD process recipe, effectively delaying the purging of the deposition chamber and giving the precursors more time to settle within the deep trenches and crevices created by the nanostructures. As such, an overall increase of 20-40% in the passivation level is achieved with this method compared to the standard recipe, without sacrificing the optical properties of the nanotextures. The conformity of the alumina thin layers was analysed by means of high-quality imaging using helium ion microscopy with a He ion beam on sample cross-sections. Using the built-in milling capabilities of such a tool, an entirely novel approach was employed to assess the layer deposition along the length of the b-Si nanowires using the Ne ion beam. As such, the nanowires were horizontally milled using this technique, revealing their cross-sectional morphology and confirming the presence of alumina material below the agglomerations, down to the base of the nanostructures. This is an important step towards effective surface passivation, and surface recombination velocities below 30 cm/s are obtained for a range of nanostructure heights. This demonstrates the fabrication of b-Si textures with excellent optical responses that are not detrimental from an electrical point of view when integrated at device level

Chapter 7

Wavelength and angle resolved scattering measurements

Wavelength and angle resolved (WARS) reflectance measurements can provide useful insight into the morphology of a textured surface, as well as its light-trapping capabilities that complement the antireflective properties. This can have important implications at various levels of device operation, such as in an encapsulated PV module, where encapsulant materials and glass are present on top of the textured surface. The fraction of light trapped by total internal reflection of the scattered light can be calculated and used as a metric of comparing and assessing various texturing methods and surfaces. Moreover, photocurrent can be approximated by a more comprehensive model that takes into account the angular distribution of the surface reflectance and the fraction of light trapped at various PV interfaces, rather than just considering the hemispherical surface reflectance of the texture. In this Chapter, WARS measurements are presented for three types of textures: periodic inverted pyramids, random upright pyramids and MACE b-Si. For the nanotextured surfaces, the impact of the black silicon height on the surface scattering is investigated and it is shown that larger angle scattering favourably promotes an increase in fraction of light trapped at encapsulated stack interfaces and photocurrent gains compared to the pyramids texture.

7.1 Regular inverted micron-scale pyramids

Initial measurements with the WARS tool are performed on a silicon sample with a surface consisting of regular inverted micron-scale pyramids coated with an ~85 nm silicon nitride antireflection layer. The sample was obtained from a previous project, where it was produced by KOH etching silicon through photolithographically-defined holes in a mask. A top-view SEM image of the microstructures is shown in Figure 7.1, where the etching process results in an uniform pattern of square-based inverted pyramids with ~10 μm base length and 9650 nm ± 100 nm periodicity.

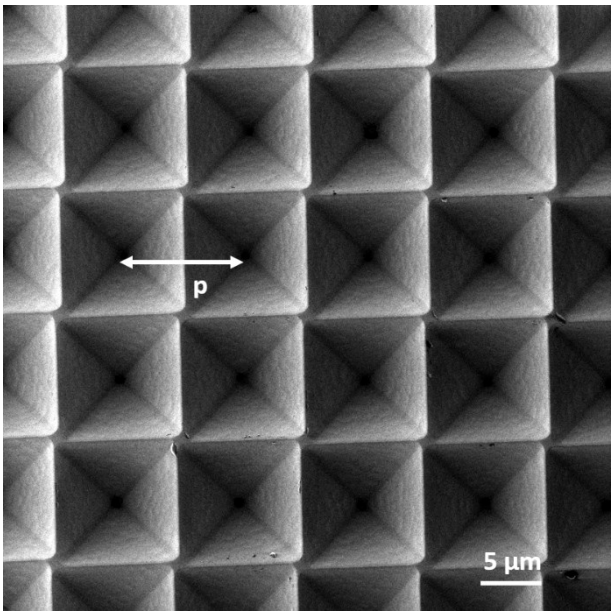

Figure 7.1: Top-view SEM image of the inverted pyramidal layer with 10 μm periodicity (p) indicated.

The specimen is chosen as its scattering reflectance response can be calculated from the 2D reflective grating equation (Equation 7.1) due to the periodicity of its features. It can thus be matched to the measured spectra obtained from WARS, where p is the structure period, θ is the scattering angle, λ is the incident wavelength and m is the mode number (order). It is important to notice that the intensity of the resulting modes cannot be calculated using this equation, but rather the angular and wavelength positioning. Figure 7.2 a) shows calculated diffraction modes reflected

from the inverted pyramid pattern up to the twentieth order in the 6°-80° scattering angular range and for wavelengths from 480 nm to 950 nm. However, as the modes differ vastly in intensity and require various integration times for data collection in practice, the WARS measurement of this pattern is challenging. Ideally, data for each scattering angle is collected for its own spectrometer integration time so that the signal is close to saturation and all of the modes can be detected. It is expected, according to Equation (7.1), that the higher order modes are less intense due to their position further away from the normal, where the reflected signal is the highest.

$$p \sin \theta = m \lambda \tag{7.1}$$

Figure 7.2 b) shows the WARS spectra of the pyramidal surface for every 1° movement of the detector in the 6°-80° angle range and 480 nm -950 nm wavelength range. The data is obtained from three different measurements with integration times in various angle ranges stitched together, such that it allows the less intense modes to be made visible without saturating the others. Even so, most of the modes are only partially visible as they are masked by the dark noise of the spectrophotometer. In the 6°-30° angle range, the integration time is 1000 ms, increasing to 10 000 ms in the 31°-51° angle range and to 20 000 ms in the 52°-80° angle range. Due to the discrete nature of data collection every 1°, the diffraction modes are not continuous and appear dashed. The strong signal centred around 20° all across the wavelength range is attributed to photons emerging from the pyramidal array after a double bounce onto two opposite facets of the same microstructure, commonly referred to as “path A” [73]. This photon path emerges on-axis and is thus detected when measuring the pyramidal pattern under no azimuth rotations.

Figure 7.2 c) shows the superimposed diffraction modes onto the WARS data to verify for angular and wavelength positioning. In general, there is excellent agreement between the two, but slight variations can be noticed for higher collection angles in the 70°-80° range potentially arising from the angular resolution of the rotation stage, which has an increased positional error at large detector angles. Another error-contributing factor might be the tilt of the wall-mounted

sample, which is typically adjusted such that the specular reflection overlaps with the incoming laser beam. However, it can be slightly misaligned in rare cases and thus introduces errors in data collection at large angles. Also, variations in the periodicity of the inverted pyramids on the surface of the specimen can lead to a mismatch between the calculated and the measured data. From the data available, at 80° scattering angle, the maximum wavelength error was 4 nm for fifteenth through seventeenth order modes.

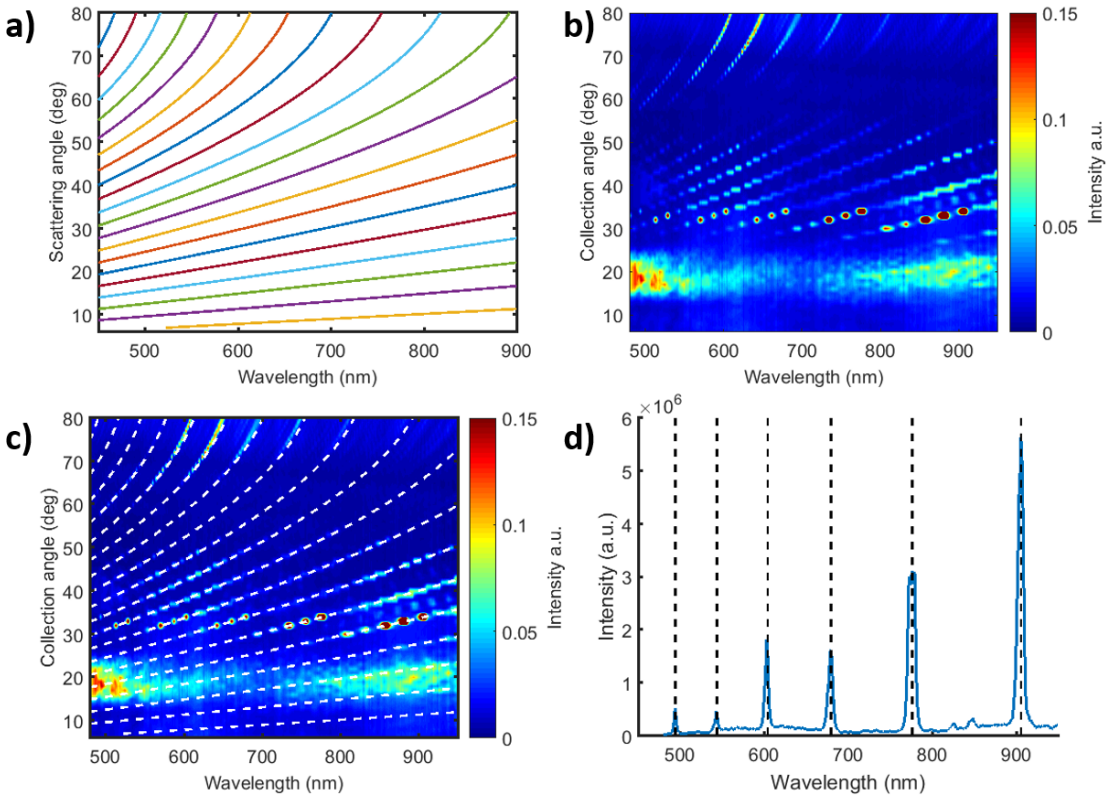

Figure 7.2: a) Twenty diffraction modes calculated from 2D diffraction equation (7.1) for 9.7 µm periodicity; b) WARS measurement of the inverted pyramidal pattern, intensity shown in colour; c) Calculated diffraction modes superimposed onto the WARS measurement; d) Exemplary WARS data at a set scattering angle of 35° to show intensity variation between modes. Vertical dashed lines calculated from equation (7.1) as guides for eye.

A slice through the measured WARS data for a fixed detector angle of 35° is presented in Figure 7.2 d), where six diffraction modes are visible with various intensities. Vertical dashed lines are traces as guide to the eye through calculated wavelengths according to equation (7.1). A pyramidal array periodicity of 9700 nm

leads to excellent results, where all of the six measured modes overlap with very good accuracy over the calculated modes, proving the correct calibration of the spectrometer with great angular and wavelength resolution.

7.2 Random upright micron-scale pyramids

The industry standard of addressing optical losses at silicon solar cell device level is the anisotropic wet etching of the silicon surface to obtain a structured layer comprised of upright square-based pyramids of random height and placement. This texture helps reducing top surface reflectance by a multiple bounce mechanism, where photons lose intensity upon each interaction with a pyramid facet due to absorption. Moreover, the pyramidal array has important light-trapping properties due to it redirecting light at oblique angles, both in the reflected and transmitted waves, thus ensuring multiple bounces or increased optical path length through the silicon substrate.

7.2.1 Theoretical background

In order to obtain such a texture, various KOH or TMAH processes are used, in combination with IPA as an additive, to etch the silicon crystallographic planes. As KOH preferential etches (100) Si planes about 5-200 times faster than (111) planes at a rate of 1-1.3 μm/min [230-231], maskless processes result in a dense array of randomly distributed square-based pyramids with slopes comprising of {111} planes. Many parameters affect the etch rate and the formation of the microstructured surface, among which temperature, *KOH* concentration and IPA concentration are the most important [230]. In general, temperature affects the etch rate of the (100) Si planes, *KOH* concentration affects the density and height of the pyramids and IPA used as an additive helps smooth out the pyramid surfaces and slopes for light-reflecting purposes. Typically, for photovoltaics applications, a 0.2 M aqueous *KOH* solution is used with 5% IPA heated at 80° C to obtain a pyramidal texture that reduces top surface reflectance to about 10% in the 300 nm-1100 nm wavelength range. The resulting structures have heights and base lengths in the range 3 μm-10 μm and full heterogeneity is desired, where the pyramids are not

base-aligned and may be overlapping, i.e. smaller underdeveloped pyramids on top and in-between other bigger pyramids. Thus, the planar area is almost non-existent and photons are guaranteed to be incident on one of the structures facets. Moreover, due to the anisotropic wet-etching mechanism, the {111} faces of the pyramids have a slope of α relative to the (100) planes of the Si according to Equation (7.2). This result is typical for an aspect ratio of 0.707 (i.e. $\frac{1}{\sqrt{2}}$), where the aspect ratio is defined as the ratio between the height *h* and the width *w* of the pyramid [230]. For a square-based pyramid fabricated via alkaline etching, $w = h\sqrt{2}$.

$$\alpha = \arctan\left(2\frac{h}{w}\right) = \arctan\sqrt{2} = 54.74° \quad (7.2)$$

This calculation of α is extremely important as this large dihedral base angle allows photons multiple bounces from the pyramids facets and reduces the overall intensity of the light reflected away from the pyramidal surface. As the size of the structures is larger than the wavelength of the incident irradiation, the paths that the photons experience can be analytically described using ray-tracing implemented via Monte Carlo simulations to obtain angular information on the surface reflections. Various literature reports [232-233] show that light undergoes up to seven distinct paths when incident on such a pyramidal texture, each with its own polar and azimuth exit angle from the array, if certain conditions are met: i.e. enough number of rays traced, high degree of randomness in structure height and positioning, as well as overlapping pyramids that are not base aligned.

By defining the incident light and the facet planes normal as vectors, a custom MatLab script was written to calculate the exit angles for the seven distinct paths that photons undergo, assuming a dihedral base angle α of 54.74° and normal incidence to the sample plane. These results are summarised in Table 7.1, along with the angles of incidence relative to the normal of the pyramidal facets and are in excellent agreement with previous reports [232]. Figure 7.3 shows a schematic of the two paths, A and B, that exit in-plane (i.e. 0° azimuth angle) and undergo two and three reflections, respectively. For path A to occur, the initial reflection on the first pyramid has to be close to the middle of the facet to redirect photons onto the opposite facet of a neighbouring pyramid. Thus, the exit angle of the light from the

structured array is 4 α - 180°, which corresponds to 38.96° when α = 54.74°. According to literature [232], path B occurs when the light falls on a pyramid and the neighbouring pyramid is at least twice taller than the initial pyramid (but preserving its aspect ratio), or when the first reflection on the first pyramid occurs very close to the base of the structure, as in Figure 7.3. Then, the photon is incident on an opposite facet, followed by a bounce on the original facet of the first pyramid close to its vertex. The exit angle of the light is 360° – 6 α, which corresponds to 31.56° when α = 54.74°; this path is not possible for all dihedral base angles. Similarly, as path C exits at a non-zero azimuth angle (i.e. out of plane) due to reflections on three different pyramid facets, the initial reflection on the first pyramid has to occur very close to the edge of the facet to ensure next incidence on a neighbouring facet of a near pyramid that is not base-aligned, as in Figure 7.4 b).

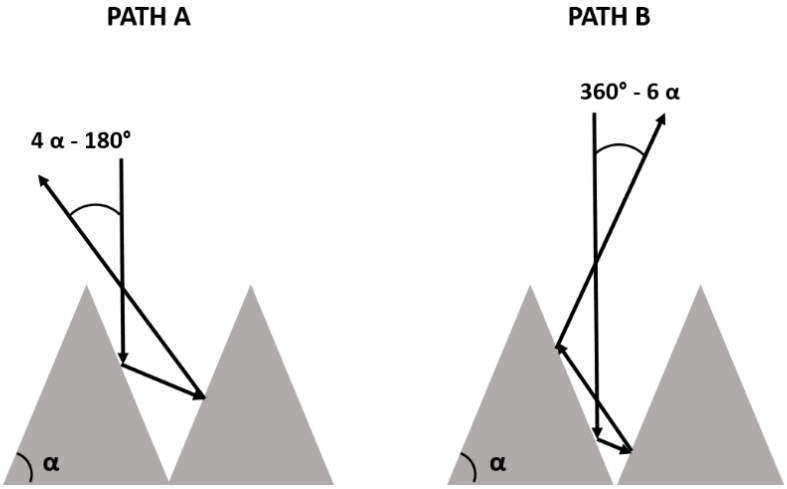

Figure 7.3: Schematic diagram of photon paths A and B when incident on a pyramidal texture with dihedral base angle α. Both reflections exit in-plane.

Results from Table 7.1 reveal that paths C through G exit out of plane from the pyramidal array at angles that can be calculated from the fixed known geometry of the structures. The right-most column indicates the number of the planes on which each reflection is incident, according to Figure 7.4 a), where square-based pyramids are sketched as viewed from above. As such, light can undergo up to five different

reflections onto the pyramids facets if certain geometrical conditions are met. In general, paths D through to G are special cases of the out of plane path C. Figure 7.4 b) shows the pyramid facet regions on which photons have to be incident to undergo exit paths A, B or C. Although no reflectance weightings can be calculated using this approach, it is expected that a larger number of bounces onto pyramids results in lower surface reflectance due to the increased transmittance inside the silicon substrate upon each impact. Therefore, path A, which consists of two reflections, would have a much higher weighting than the rest of the paths, while path G, which consists of five reflections, will, for the same reason, have the smallest reflectance weighting out of all paths. Literature based on Monte Carlo simulations reports reflectance weightings for each path and the results are summarised in Table 7.2, conformal with assumptions [232-233].

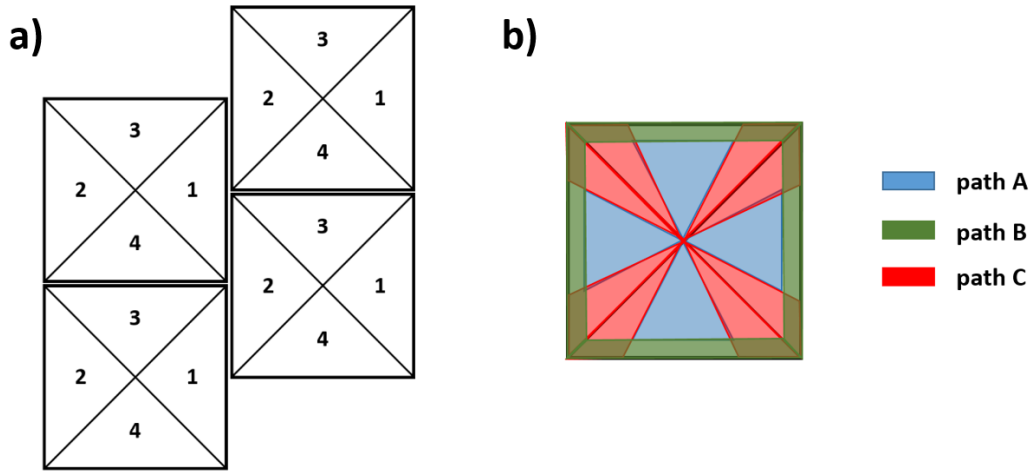

Figure 7.4: a) Neighbouring pyramids seen from above with plane numbers indicated; b) Incidence region of the photons to undergo paths A (blue), B (green) and C (red) respectively.

Table 7.1: Scattering and azimuth exit angles of paths A-G from the pyramidal surface. Reflections incident on planes numbered according to Figure 7.4.

Path	Polar Scattering angle θ (°)	Azimuth angle φ (°)	R1 (°)	R2 (°)	R3 (°)	R4 (°)	R5 (°)	Plane number (See Fig 7.4)
A	38.96	0	54.74	15.78				1 2 3 4
B	31.56	0	54.74	15.78	86.3			1 2 3 4
C	31.6	36.86	54.74	78.9	33.48			1 2 3 4
D	74.97	12.53	54.74	78.9	71.28			1 2 3 4
E	73.49	10.48	54.74	78.9	71.28	88.76		1 2 3 4
F	12.76	18.44	54.74	78.9	71.28	51.67		1 2 3 4
G	10.4	14.91	54.74	78.9	71.28	88.76	52.71	1 2 3 4

Even though path B consists of the same number of reflections as path C, its reflectance weighting is much smaller, due to the added requirements that the initial reflection has to be incident very close to the pyramid base to experience a third bounce that barely glances the neighbouring pyramid near the tip. Paths E and G suffer from the same requirements with the added fact that, being special cases of path C, the photons have to be incident both near the base of the pyramid and close

to the edge of the facet, resulting in very low reflectance weighting due to the low probability of this happening.

Table 7.2: Reflectance weightings of paths A-G, data taken from [232-233].

Path #	Number of reflections	Reflectance weighting (%)
A	2	68.3
B	3	3.2
C	3	18.6
D	3	3.7
E	4	0.1
F	4	5.8
G	5	0.1

7.2.2 Morphology and surface reflectance

An upright random pyramidal texture is fabricated and optically characterised with the WARS system and the integrating sphere in order to detect the individual photon paths. N-type CZ <100> 1-5 Ωcm c-Si wafer is first cleaved into 4 × 4 cm^2 and cleaned using a concentrated Piranha solution for 30 minutes to remove organic residues and diluted *HF* solution for native oxide removal. The alkaline etching of the texture is performed in a 0.2 M *KOH* solution with 5% IPA as additive in a heated environment at 80° C for 60 minutes. Top-view and cross-sectional SEMs of the textured surface are presented in Figure 7.5. The etched square-based pyramids have base widths of 5-25 μm and are randomly distributed on the silicon surface, as in Figure 7.5 a). The image shows that there is no planar fraction on the sample surface, which is crucial for PV and optical applications. The images in Figure 7.5 also show that some of the pyramids have etched on top of others, thus not having their base at the same level and that the array is extremely dense. Smaller features are also visible, which can lead to additional scattering and reduced surface reflectance in the measured optical response.

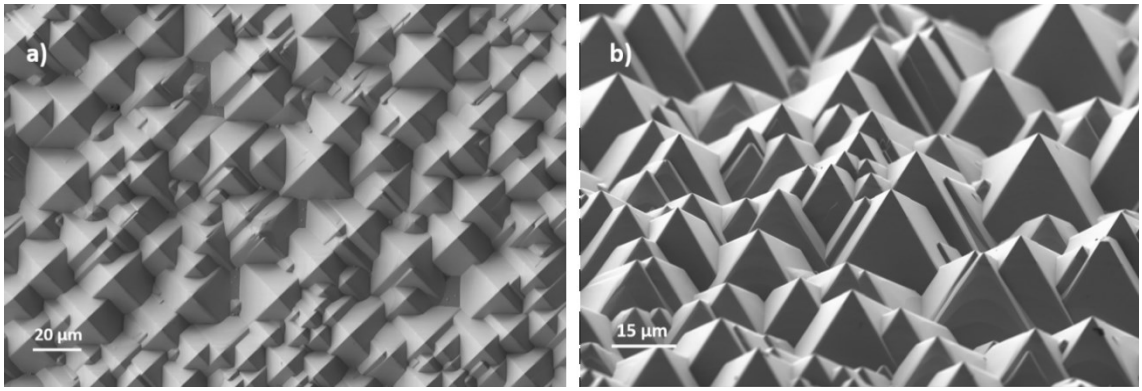

Figure 7.5: SEM images of the fabricated pyramidal texture: a) top-view; b) stage tilted at 54° so that electron beam is perpendicular on one of the facets..

Hemispherical reflectance measurements taken with an integrating sphere complement WARS measurements and provide information on the total and diffuse reflectance of a textured surface (see Chapter 4.2.3). Figure 7.6 shows total measured reflectance for the pyramidal array in the 450 nm- 950 nm wavelength range. The AM1.5G weighted average total reflectance of the sample is 11.3%. The specular reflectance of the sample can be calculated as the difference between the two measured signals, which is important considering the WARS system can only collect data for detector angles greater than 6°. The reflectance haze, defined as the ratio between the diffuse and total hemispherical reflectance, is thus calculated and presented in Figure 7.6 as a red line corresponding to the right-hand y-axis. The weighted average reflectance haze value of the pyramid texture is 0.94, indicating strong scattering to angles larger than 6^0 for the entire spectrum. However, no information on the angular distribution of these reflections is available from such measurements, which is key when characterising light-trapping through total internal reflection in an encapsulated module.

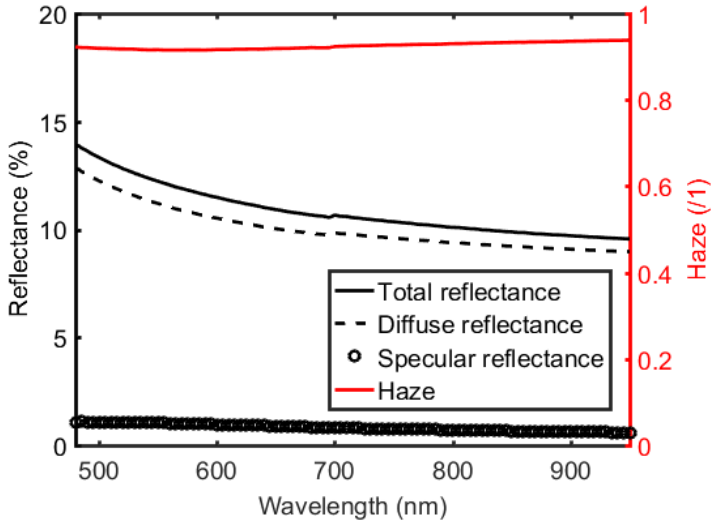

Figure 7.6: Total (solid) and diffuse (dashed) hemispherical reflectance measurements of the pyramidal texture. Reflectance haze (red) is also calculated.

7.2.3 WARS measurement

Due to the geometry of the pyramids, for a 0° azimuth positioning of the sample under normal incidence, only paths A and B should be detected in a WARS measurement, as per Table 7.1, at 39° and 31° scattering angles respectively. No other distinct features should be noticeable across the entire wavelength range. Figure 7.7 shows the WARS measurement of a random upright pyramidal surface in the 6°-90° angular range and for wavelengths ranging from 480 nm to 950 nm. A strong broad scattering peak is noticeable for detector angles below 30°, which is in agreement with previous work on the topic [234] for wavelengths of 270 nm and 532 nm, but contrary to the results calculated from ray tracing. As the scattering peak is dictated by the base angle α as 4 α - 180°, these results are indicative of different pyramid morphology than that assumed when deriving the results in Table 7.1 and base angles below the assumed value. Indeed, earlier reports show that pyramidal textures can be fabricated via alkaline etching with a base angle of arctan ($\sqrt{2}$) – arctan (r), where r is the etching rate ratio between (111) and (100) planes and has values between 0.05-0.2 [226,230]. This means that the base angle α can take values below 54° and as low as 49°, thus decreasing the angle at which path A

exits from the pyramidal array. A scattering peak centred around 28° as the one in Figure 7.7 would correspond, according to path A calculations, to a dihedral base angle of α = 52°. The data shows no strong wavelength dependency, but the signal is slightly stronger at shorter wavelengths, which is in line with hemispherical reflectance measurements (see Figure 7.6) and characteristic of this texture.

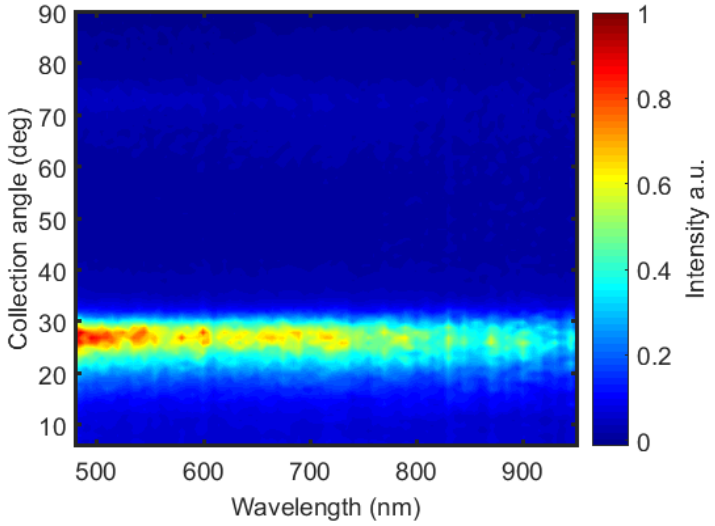

Figure 7.7: Wavelength and angle resolved reflectance measurements of the pyramid texture, with normalised intensity shown in colour.

7.2.4 Reassessment of pyramid morphology

Direct measurements of the base angle are impossible from the SEM images presented in Figure 7.5, due to the slope of the facet perpendicular to the electron beam, which would lead to incorrect values. Therefore, the pyramidal textured surface under study was subjected to a milling process using a *Ga* focused ion beam (FIB) perpendicular to the silicon substrate and near the apex of the structures, to reveal a cross-section through the pyramid. The milled facet is shown in Figure 7.8 a) from a top perspective. Transversally cutting through the structures allows for correct measurements of the base angle α directly from the SEM image presented in Figure 7.8 b), where the sample is tilted to 54° and tilt correction of 36° is applied to the image. As such, all of the angles measured are indeed well below the assumed 54.74°, with an average value of 52.1° ± 1.1°.

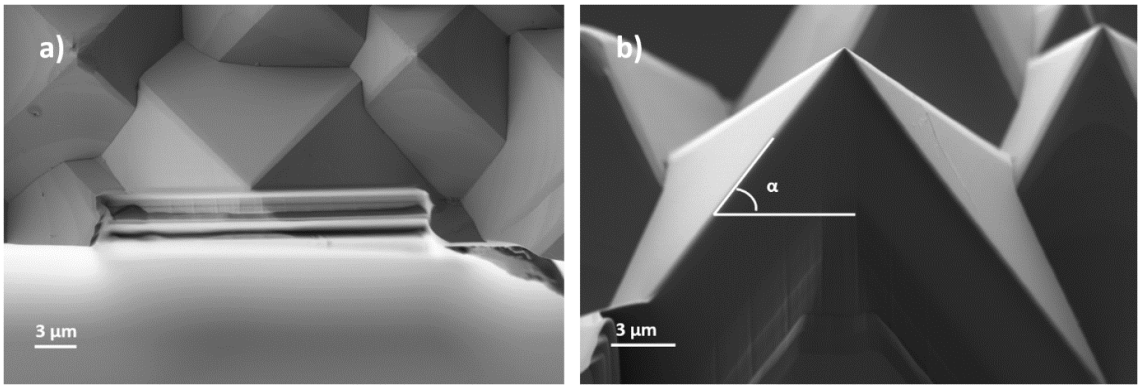

Figure 7.8: SEM image after Ga FIB milling on the pyramid: a) top-view, showing milled facet; b) correct base angle measurement, stage tilted to 54° and tilt correction to 36°.

As measurements reveal base angles in the range 51°-53.2°, new calculations for path A can be carried out, thus positioning the peaks in the 24°-32.8° scattering range, which is in line with the WARS measurement. The variation of α explains why the measured peak in Figure 7.7 is broad, rather than a single sharp peak at the expected angle. Integration of the data over the wavelength range allows for more precise analysis of the scattering peaks and their distribution. Thus, Figure 7.9 a) shows the measured peak formed from the WARS data integrated over the wavelength range, as a function of scattering angle with the calculated upper and lower limits assuming a dihedral base angle in the range 51°-53.2°. Similarly, Figure 7.9 b) shows the corresponding base angles of the measured signal, based on $\alpha = \frac{path\ A + 180°}{4}$, where the grey area indicates base angles in the measured range from Figure 7.8 b). Although the upper limit is in line with calculations, it seems that the textured surface exhibits pyramid base angles below the expected lower limit based on the SEM analysis, corresponding to dihedral base angles as low as 49°. The SEM analysis here was limited to measurements on a cross-section of a single pyramid and it is entirely possible that there exists a wider range of dihedral base angles, extending down to 49°, on the sample, which would explain the scattering angle distribution in the WARS measurement. Indeed, reports in the literature show AFM

measurements on similar samples that reveal lower base angles in the range 49°-52° [74, 235].

The decrease in base angle compared to theory of the alkaline etched fabricated surface shows that a re-evaluation of the pyramid morphology is necessary for more accurate simulation inputs when performing Monte Carlo simulations and photon path descriptions. This update implies changes in the simulation parameters, as well as the results, such as antireflective and light-trapping response, leading to changes in the electrical output of the simulated device and at module level. The polar and azimuth exit angles of paths A-G from the pyramidal array with an average base slope of 52.1° ± 1.1° are presented in Table 7.3.

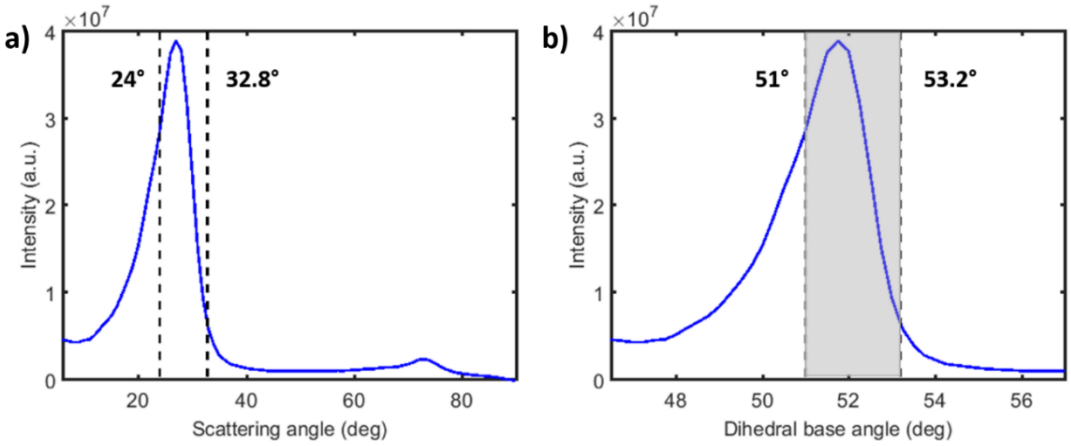

Figure 7.9: WARS measurement integration over wavelength range: a) path A signal versus scattering angle, limits indicated; b) corresponding calculated dihedral base angle α , grey area shows measured base angles from milling process.

Table 7.3: Calculated angle ranges for photon paths A-G for pyramids with experimentally measured base angle in the 51°-53.2° range. Grey-out rows are for paths that are no longer allowed in this new morphology due to geometric restrictions. Total reflected power data approximated from [232-233].

Path	Scattering angle θ (°)	Azimuth angle φ (°)	R1 (°)	R2 (°)	R3 (°)	R4 (°)	Approximate proportion of total reflected power (%)	Plane number (see Fig 1)
A	24-32.8	0	51-53.2	27-20.4			71.2	1 2 3 4
B	-	-						1 2 3 4
C	18.5-26.1	39.6-37.9	51-53.2	82.4-80.2	38-35.3		18.6	1 2 3 4
D	79-76.2	4.9-9	51-53.2	82.4-80.2	79.3-74.6		4.4	1 2 3 4
E	-	-						1 2 3 4
F	4.9-9.1	11.7-15.7	51-53.2	82.4-80.2	79.3-74.6	50.1-51.2	5.8	1 2 3 4
G	-	-						1 2 3 4

Interestingly, the decrease in base angle to values below 54° leads to the disappearance of paths B, E and G (greyed out), due to geometric restrictions. Previously, paths B, E and G were special cases of paths A and D, respectively, where the photons had a chance of hitting the pyramids close to the base and thus the next reflection would be incident on an opposing facet at very large angles (i.e. 86°-88°) close to the apex of the structures. Now, there is no region close to the base of the structures that photons may hit to undergo these paths, as calculations show incidence angles of above 90° (i.e. photons missing the facet) and the number of the available photon paths is reduced to four. As such, the reflectance weightings of the disappeared paths are redistributed to the remaining paths A, C, D and F. As previously mentioned, path B becomes path A as it was an extension case of it and its reflectance weighting is transferred accordingly. Similarly, paths D and G without their last reflections become path C. Their reflectance weightings can also be approximated in this manner. Therefore, Table 7.3 also shows the calculated reflectance weighting for the remaining paths, according to data from Table 7.2 [232, 233]. As a whole, these findings aim to give a more precise description of the scattering profile of light normally incident on a *KOH* fabricated pyramid texture than the results calculated considering only a dihedral base angle of 54.7^0 (Tables 7. 1 and 7.2)

7.2.5 Impact of azimuth rotations

As higher photon paths (C-G) exit out-of-plane from the pyramidal pattern, WARS measurement for various azimuth rotations of the textured surfaces are relevant for detecting these paths that travel away from the horizontal plane. Therefore, WARS measurements are performed for every 5° azimuth movement of the sample in the 0°-90° azimuth range. Exemplary full data is presented in the colourmaps in Figure 7.10 for azimuth rotations of 15°, 30° and 45°. The general response is similar to the measurement in Figure 7.7 for no azimuth rotation of the sample, where a strong scattering peak is observed for detector angles below 30°. However, for larger azimuth rotations, this scattering centre moves to lower angles and appears to

become broader but less intense. Also, other signals are emerging at very large scattering angles > 70°, possibly attributed to path D.

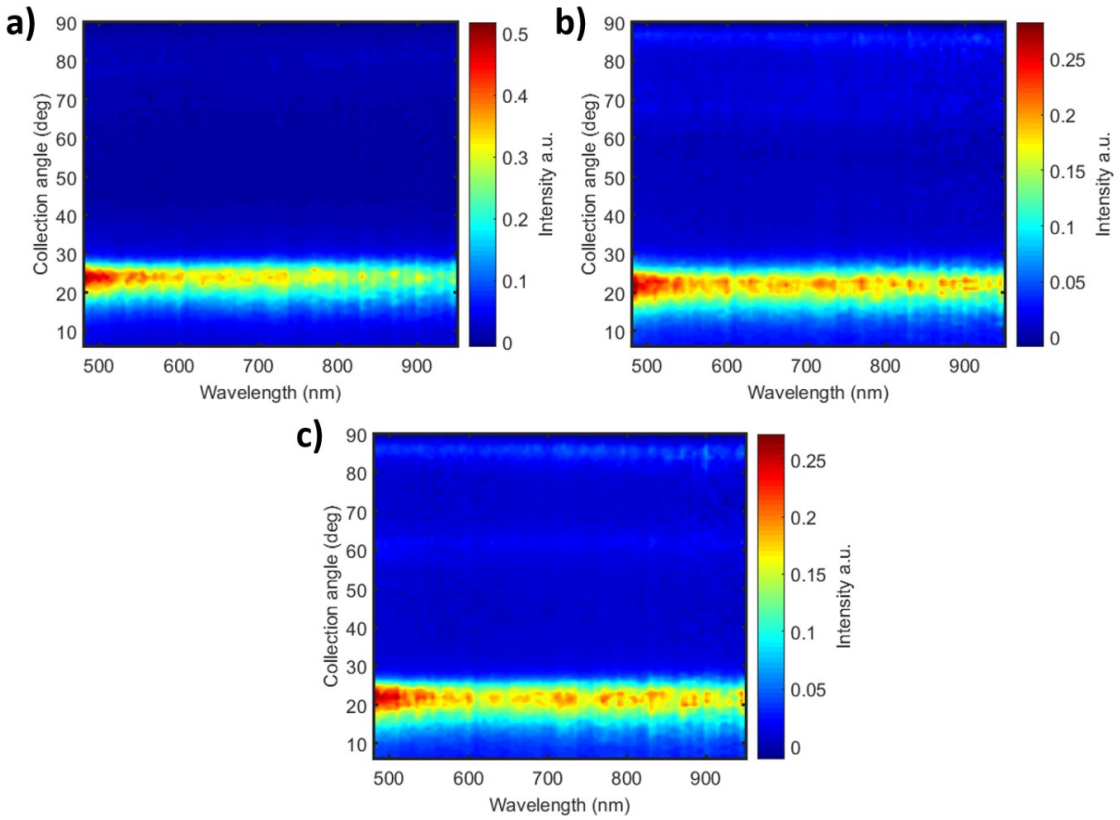

Figure 7.10: Wavelength and angle resolved reflectance measurements for pyramidal textured surface for: a) 15° azimuth rotation; b) 30° azimuth rotation; c) 45° azimuth rotation. Intensity shown in colour.

Integration over the wavelength range leads to more in-depth analysis of the collected signals, as shown in Figure 7.11 a) for four different azimuth rotations. Indeed, the maximum of scattering moves to lower collection angles and decreases in intensity with increasing azimuth angle. Even though no peaks should be seen for azimuth angles between 0° (path A) and 40° (path C) for angles below 30° according to Table 7.3, the intensity of the signals suggest a transition with azimuth angle as the stronger path A exits the detector plane and the less intense path C enters the horizontal plane. Vertical dashed lines are traced through the position of the peaks of the signals corresponding to azimuth angles of 0° (blue) and 40° (black). These

are in line with the average scattering angles calculated for Path A and C, respectively (see Table 7.3). Smaller peaks can be observed for very large scattering angles that are close to the predicted scattering range of path D (76°-79°), although not for the predicted azimuth range. These can be attributed to additional scattering from smaller features present in the pyramidal array, such as underdeveloped pyramids, as well as other photon paths that may have not been taken into consideration in the ray tracing simulations. One such path may consist of one of the reflections being incident close to the apex of the structures, where the silicon thickness is in the orders of hundreds of nanometers and may not be absorbing photons of all energies, and is transmitted partially onto the opposite side of the structure. A similar path was previously reported in the work of Fung et al [237], where Monte Carlo ray-tracing simulations were improved by the addition of a Phong scatterer, which mimics the base angle distribution normally observed in fabricated pyramidal arrays.

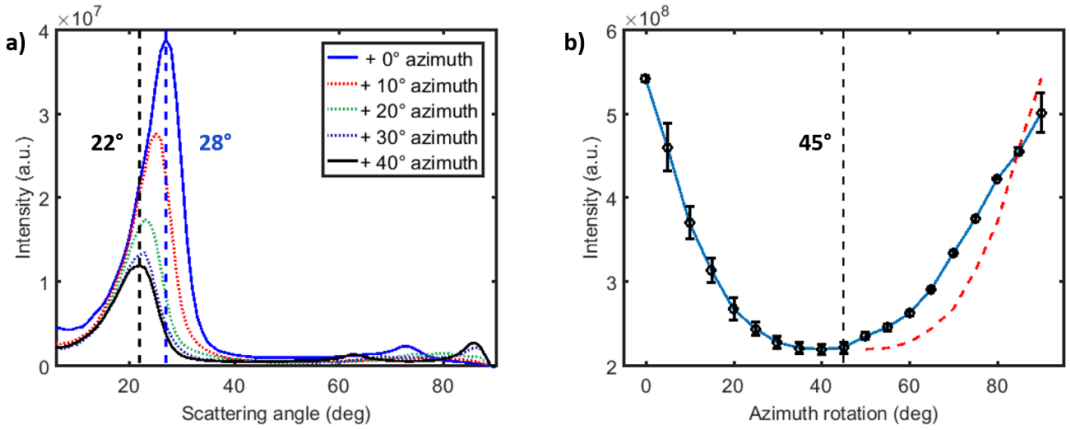

Figure 7.11: a) Collected data integrated over wavelength range for five increasing azimuth rotations, path A in blue, path C in black and their respective scattering angle peaks, in good agreement with the results in Table 7.3; b) Total reflected power for azimuth rotations in the 0°-90° range, showing symmetry around 45°.

As right-angle square-based pyramids present four-fold symmetry over their long axis, it is expected that measurements show symmetry around 45° azimuthal rotations. Figure 7.11 b) shows total power (integration over wavelength and scattering angle) as a function of azimuth rotations from 0°-90°. This plot exhibits

maxima at 0 and 90 due to the dominant presence of path A which accounts for most of the reflected power from the sample and a minimum at 45° azimuth, thus confirming the presence of square-based symmetric pyramids. The red dashed line mirrors the signal from the first half of the plot into the second half and small differences can be observed between the two. This is mainly due to the fact that measurements in the 0°-45° azimuth range are carried out on adjacent facets to the measurements in the 45°-90° range which can be morphologically different (i.e. base angle, see Figure 7.8 b)). Moreover, the neighbouring pyramids onto which the photons are incident next can also differ in morphology and give rise to other photon paths that have various contributions to the total signal. There are no peaks visible in the 35°-40° (or 50°-55°) azimuth range to indicate the presence of path C. This is thought to be due to the much stronger path A masking these smaller signals that should be present according to Table 7.3.

A complete set of WARS measurements and data for polar scattering angles and various azimuth rotations of any textured surface reflections can be represented using polar coordinates. Experimental measured data for the random pyramidal array in polar coordinates is shown in Figure 7.12 a) for azimuth rotations in the 0°-90° range. The colorbar represents the percentage of the total reflected power for each data point and was calculated using diffuse hemispherical reflectance measurements of the same texture. Figure 7.12 b) shows the collected signal in polar coordinates for polar angles of up to 40°, where the majority of the reflections occur. It should be noted that in both plots, lines for scattering angles of 28° and 22° are traced in the quadrant, identifying the peaks of reflections arising from photon paths A and C. Figure 7.12 c) shows a complete representation of the scattering measurements, where quadrants 2-4 (greyed out) are copied and mirroring the measured signal from the first quadrant. The shape of the overall reflected strong signal corresponding to paths A and C confirms the presence of square-based pyramids and are similar to images captured on photographic paper from earlier work [229, 233]. The tips of the reflected square are corresponding to path A.

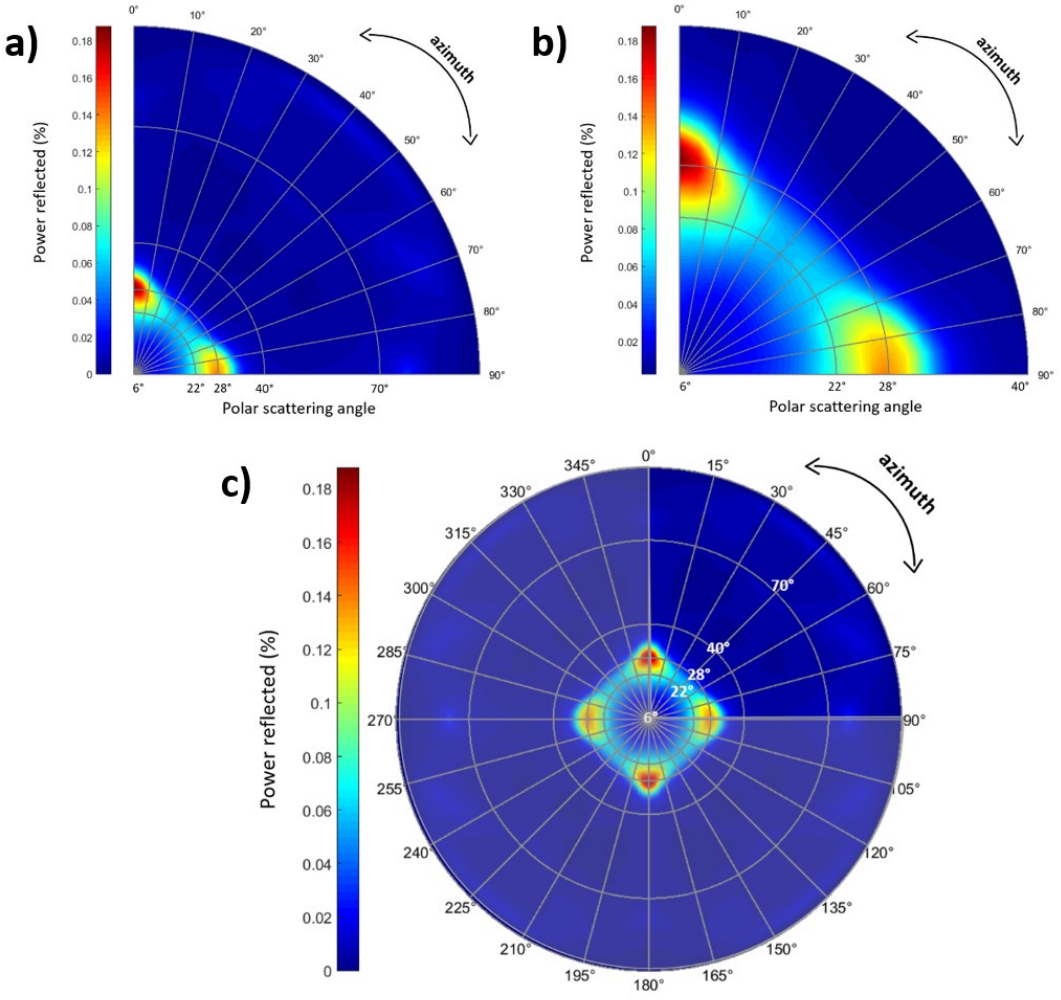

Figure 7.12: Measured reflections from a random pyramid texture in polar coordinates: a) 0°-90° azimuth range; b) 0°-90° azimuth range and polar angles below 40°; c) complete representation in the 0°-360° azimuth angle range where the other three quadrants are mirrored copies of the measured signal from first quadrant. Colorbar represents percentage of total power reflected.

Therefore, wavelength and angle resolved scattering measurements have the potential of revealing useful information about the textured surface morphology. In the case of random pyramidal textures, the position and the width of the strongest signal corresponding to path A can be used to determine the characteristic base angle α and its distribution. Moreover, it is evident that such texture provides reflections at angles considerably lower than what ray-tracing simulations indicate

and a re-evaluation of these photon paths in necessary for a more actual description. The decrease in base angle can have paramount implications when considering the optical pathlength increase of the photons travelling inside the silicon substrate or when considering the fraction of reflected light trapped at encapsulant-air interface in an encapsulated module that makes use of this texture.

7.2.6 Total internal reflection (TIR)

When assembled in a PV module, silicon solar cells are encapsulated for moisture and mechanical damage protection that can arise from environmental conditions. As such, some of the reflected light from the textured surface can be trapped by total internal reflection (TIR) at these newly added interfaces if certain criteria are met and be redirected back onto the silicon surface, further contributing to the electrical response of the PV device. TIR occurs in cases when the reflected light is incident on a material at an angle larger than the critical angle of that material, which is based on its refractive index and the refractive index of the medium from which the light originates (see Equation 7.2). Figure 7.13 shows a sketch of the TIR mechanism for a random pyramid texture, where reflected light outside the escape cone (grey triangle) is redirected back to the pyramidal array and gains a second chance of being absorbed.

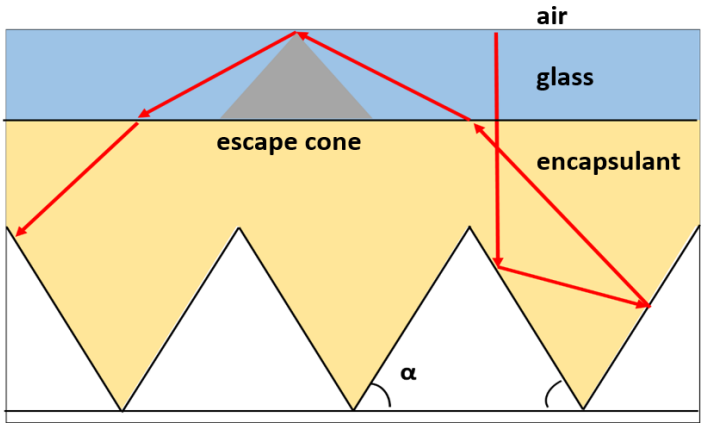

Figure 7.13: Diagram of light undergoing total internal reflection at the glass-air interface. Layers not to scale.

If light is travelling from medium 1 with refractive index n_1 and is incident on a medium 2 with refractive index n_2, and $n_1 > n_2$, the critical angle can be calculated according to equation (7.2), derived from Snell's law. Therefore, if the light originating from medium 1 is incident on medium 2 at an angle greater than θ_{crit}, the light will be totally internally reflected and redirected back to medium 1, rather than being transmitted to medium 2.

$$\Theta_{crit} = arcsin\left(\frac{n_2}{n_1}\right) \tag{7.2}$$

When light is travelling from encapsulant to glass, according to equation (7.2) and Snell's law:

$$n_{enc}\, sin\, \theta_{enc} = n_{glass}\, sin\, \theta_{glass} \Rightarrow \theta_{enccritical} = arcsin\left(\frac{n_{glass}}{n_{enc}}\right) \tag{7.3}$$

where n_{enc} and n_{glass} are the refractive indices of encapsulant and glass respectively, and $\theta_{enccritical}$ is the critical angle at this interface. Similarly, when light is travelling from glass to air:

$$n_{glass}\, sin\, \theta_{glass} = n_{air}\, sin\, \theta_{air} \Rightarrow \theta_{glasscritical} = arcsin\left(\frac{n_{air}}{n_{glass}}\right) \tag{7.4}$$

where n_{glass} and n_{air} are the refractive indices of glass and air respectively, and $\theta_{glasscritical}$ is the critical angle at this interface. If TIR occurs at the glass-air interface, then $\theta_{glass} = \theta_{glasscritical}$, as the angle would be maintained for the first interface as well. Applying Snell's law at the encapsulant-glass interface with the new angle when there is no TIR becomes:

$$n_{enc}\, sin\, \theta_{enc2} = n_{glass}\, sin\, \theta_{glasscritical} \Rightarrow sin\, \theta_{enc2} = \frac{n_{glass}}{n_{enc}}\, sin\left(arcsin\left(\frac{n_{air}}{n_{glass}}\right)\right) \Rightarrow$$

$$\theta_{enc2} = arcsin\left(\frac{n_{air}}{n_{enc}}\right). \tag{7.5}$$

This creates a virtual encapsulant-air interface where the critical angle is lower than at the encapsulant-glass interface, because $n_{glass} > n_{air}$. As such, the requirement for total internal reflection is dictated by θ_{enc2}, thus by the refractive index of the surrounding encapsulant. However, it is interesting to notice that for incident angles θ, where $\theta_{enc2} < \theta < \theta_{enccritical}$, total internal reflection occurs at the encapsulant-glass

interface rather than the glass-air interface as light is incident on this interface first. This can have implications if a model would take into account parasitic absorption of the glass layer.

Considering the above, the fraction of light trapped by total internal reflections when incident on this stack, f_T, can be calculated as a function of the encapsulant refractive index by using the WARS results, according to Equation (7.6). This equation calculates the ratio between the reflected power scattered outside the escape cone, which is thus undergoing TIR, and the total reflected power from the textured surface in the 6°-90° angular range, as shown in Yang et al. [234]. Here, $\overline{I_{scattered}}$ is the circularly averaged intensity of the reflections which includes contributions from measurements at all azimuth rotations, so all of the paths exiting out of plane as well, λ is the incident wavelength and θ_{crit} is the critical angle based on the encapsulant refractive index. As WARS measured data is a function of both incident wavelength and collection angle, it has to be integrated over the two to obtain the reflected power. $\overline{I_{scattered}}$ is calculated from the quantitative intensities obtained after detector movement adjustments (see Chapter 4.7.2). In the model presented here, absorptions and reflections within/ from the encapsulant and glass layers are ignored.

$$f_T = \frac{\int_{\theta_{crit}}^{90^\circ} \int_{\lambda=480}^{950} \overline{I_{scattered}}(\theta_{crit},\lambda)\, d\lambda\, d\theta_{crit}}{\int_{6^\circ}^{90^\circ} \int_{\lambda=480}^{950} \overline{I_{scattered}}(\theta_{crit},\lambda)\, d\lambda\, d\theta_{crit}} \tag{7.6}$$

Figure 7.14 shows the calculated fraction trapped, f_T, as a function of increasing surrounding encapsulant refractive index from 1 to 4 (corresponding to critical angles from 90° to 14.5°) for the measured data (in blue). The fraction trapped for the 'ideal' random pyramidal texture, described in Table 7.1 with a base angle α = 54.74°, is shown as a black trace, using the reflective weightings for each path from Table 7.2. This trace presents sharp steps at the calculated critical angles corresponding to the discreet photon paths (indicated) due to the fixed geometry of the pyramids, as well as the lack of the base angle distribution. In contrast, the measured texture presents a much more continuous function and has significant differences to the ideal case, due to the shift of some of the photon paths to lower

scattering angles triggered by lower base angles, as well a distribution in α from 51°-53.2°. For instance, for an encapsulant refractive index of 2, the ideal texture yields a value of f_T = 0.94, while the measured texture has a value of f_T = 0.21, a significant difference. The measured data shows that for an encapsulant refractive index of 3, the fabricated texture traps about 75% of the reflected light. However, such an encapsulant is not feasible for photovoltaic applications, as it would reflect too much light incident on the PV module to begin with. The ideal texture fraction trapped has values approaching unity when the refractive index of the encapsulant is set to 4. However, occurrence of paths F and G at scattering angles below 14° makes the fraction trapped yield only a value of 0.94.

In an attempt to better match the experimental data, a fraction of scattered light trapped has been calculated for a texture as the one described in Table 7.3, that accounts for a base angle decrease and distribution from 51°-53.2°. The reflectance weightings are changed according to the disappearance of paths B, E and G and calculated as in Table 7.2. Moreover, the data was modelled after the measurement, where path A response ranges from 24°-32.8°, but has a peak at 28°, thus taking into account each scattering angle weighting on the amount of power reflected. The resulting trace represents a much better approximation of the measured data than the step-function (black trace), but still has some differences, especially in the lower region of the encapsulant refractive index, where the critical angle for TIR is very large. This is due to the presence of data in the WARS measurement at very large scattering angles, that can arise from additional scattering from smaller features and other paths unaccounted for, as well as an underestimation of path D, occurring in that angular region.

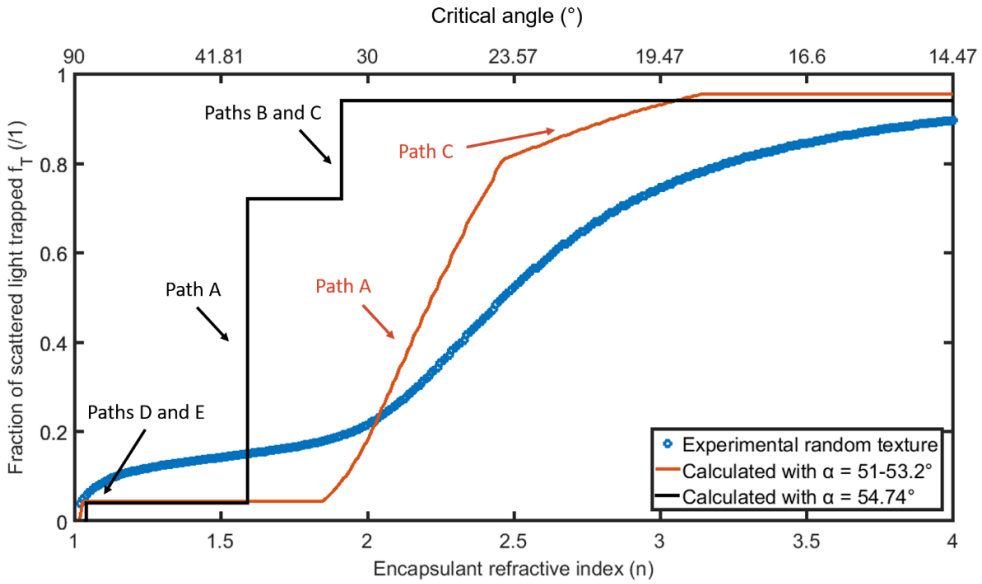

Figure 7.14: Calculated fraction trapped as a function of surrounding encapsulant refractive index from 1 to 4 for measured experimental textured (blue), ideal texture based on Table 7.1 (black) and the texture described in Table 7.3 with base angle distribution (red).

The presence of large signals at very large scatterings is important for PV applications, as the fraction of light trapped by the fabricated texture for low encapsulant refractive indices below 1.6 exceeds the simulated one. This region corresponds to PV-compliant encapsulants, such as the widely used ethylene-vinyl acetate (EVA), with a refractive index of 1.5 [239]. In this case, both of the predicted fractions yield a value of only 3.8%, due to the presence of only paths D (and E for the ideal case). In contrast, the measured data shows that 14.5% of the reflected light from the fabricated texture will be trapped at the virtual encapsulant-air interface when surrounded by EVA, an important result for the PV field, that can relax requirements when designing and engineering new materials and encapsulants on the top of the textured bulk without sacrificing the optical properties arising from TIR.

In conclusion, when simulating these textures on top of a silicon device, a more accurate approximation would consist of a base angle distribution in the range 48°-54° with a peak at 52° to better match the experimental data presented in here,

compared to a single fixed angle at 54.74° for the entirety of the structural array. Moreover, data presented in here is supported by a previous study from Fung et al [237], who were able to replicate the results of Yang et al. [234] for an experimental alkaline-etched structure. The work relies on the insertion of a Phong scattering element that mimics the now-observed base angle distribution and yields an impressive match to the experimental measurements presented in this study.

7.3 MACE black silicon

7.3.1 Introduction

Nanoscale textured silicon (black silicon) has been widely investigated over the past decades as a promising candidate for silicon solar cells front texturing scheme. Hemispherical reflectance measurements have proved that this type of texturing is vastly superior to the more traditional alkaline etched surfaces that result in random upright or inverted pyramids from an optics perspective (see Chapter 5). Moreover, it has long been postulated that the light-trapping capabilities of these layers can significantly increase the photocurrent output of a silicon device, due to the redirection of the incoming light towards oblique angles, similar to the micron-scale pyramids case. As such, b-Si more readily mimics the behaviour of an ideal Lambertian scatterer, which redirects the light equally to all scattering angles, thus yielding large fractions of light trapped at encapsulant-glass interfaces and improved optical pathlengths of low energy photons inside the substrate in particular. Unfortunately, direct measurements of this light-trapping property is no easy task and therefore scarce in literature. As b-Si yields surface reflectance of below 3%, the nominal power of the light source must be accordingly sufficient to observe these reflections at various angles. Moreover, light reflected at steep angles has very low intensity if it is collected in plane, resulting in the need for expensive and precise equipment to carry out these measurements. Kurokawa et al. [243] have presented angle resolved reflectance data for MACE b-Si layers of various thicknesses collected with a similar setup as in this study, for a variety of incident wavelengths. The MACE structures were embedded into a thin and transparent PDMS substrate and the measurements were carried out in transmittance mode,

such as to observe just the response arising from the silicon nanoneedles without being affected by the substrate. The group concluded that the highest intensity of the reflected signal occurs near-normal angles, due to the measurements being carried out in plane. In this work, we aim to overcome the limitation of the system by applying a geometric angular correction to the collected signal (see Chapter 4.2.6) to more reliably represent the entire scattered profile in 3D and account for the lower intensity of the reflected signal at large scattering angles. As such, the role of the integration time of the spectrometer becomes more important than ever and more attention must be given to the signal-to-noise ratio of the detected signal in order to maximize the quality of the collected data.

It is important to notice that, unlike the micro-scale pyramids case, where the feature size of the structures is much greater than the wavelength of the incident photons and the scattering profile can be deduced through geometric ray tracing, the diameters of the b-Si structures makes it considerably more difficult to do so. As such, computational simulations for these geometries are expensive and time consuming, due to the randomness of the nanoscale array and the wide variety of structure sizes obtained via an experimental etching process. In particular, EMA approximations discussed earlier cannot readily resolve the scattering effects arising from neighbouring nanostructures and different phenomena inside them.

The implications of wavelength and angle resolved reflectance scattering measurements at the device level are, as previously mentioned, two-fold. Firstly, the transmitted light into the substrate upon interaction with the b-Si layer undergoes an angle modification, thus entering and travelling inside the substrate at a larger angle and leading to increased optical pathlength. Figure 7.15 a) shows a schematic of this mechanism in an encapsulated stack, where the optical pathlength of the transmitted light is increased by a factor of $1/\cos\theta$ compared to normally travelling light, where θ is the angle at which the photons are transmitted inside the substrate. This can lead to either reduced substrate thicknesses without sacrificing photogeneration or to an increase in the output power of the device if the same amount of semiconductor material is used due to increased absorption of long wavelength photons. Second, the reflected light at large angles can undergo total

internal reflection (TIR) when an encapsulant and glass stack is added on top. If certain geometrical criteria are met such that the angle of incidence of light travelling from the substrate onto these newly added interfaces is greater than the materials escape cone, light will be once again redirected towards the substrate and thus given more chances of being absorbed rather than being lost in the reflected power. A schematic of this mechanism is shown in Figure 7.15 b). The analysis carried out in this work focuses on the second of this phenomena, mainly the reflected scattering arising from b-Si textures.

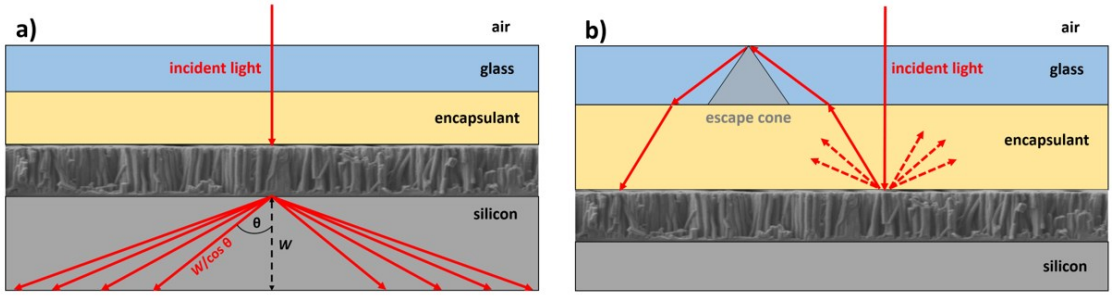

Figure 7.15: Schematic of light interaction with a black silicon layer showing: a) transmitted light into the substrate and potential optical pathlength increase; b) total internal reflection at the glass-air interface of the reflected scattered light by the b-Si layer.

7.3.2 Optical and morphological characterisation

In this work, three MACE b-Si structures are fabricated for etching times of 6, 8 and 12 minutes, according to the process flow described in Chapter 4.1. A cross-sectional scanning electron microscope (SEM) image of the 8 minutes etched specimen is shown in Figure 7.16, exhibiting well-defined vertical standing nanowires of uniform height across the entire field of view. The height of the nanostructures can be obtained directly from multiple measurements on the cross-sectional SEM images. As such, nanowire lengths of 1180 nm ± 30 nm, 1790 nm ± 40 nm and 3580 nm ± 50 nm are measured after MACE process times of 6 minutes, 8 minutes and 12 minutes, respectively.

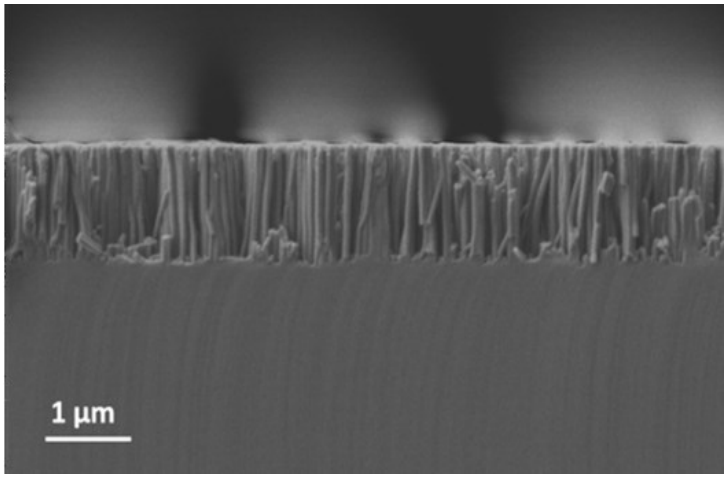

Figure 7.16: Cross-sectional SEM image of the 8 minutes MACE b-Si sample; height 1.8 µm.

For the optical characterisation of the specimens, an integrating sphere system was used to measure the total hemispherical reflectance, as well as the diffuse hemispherical reflectance of each sample. The diffuse hemispherical reflectance is measured by replacing one of the exit ports of the sphere with a light trap to remove the light in an angle of ± 6° about the specular reflection point of the sample (see Chapter 4.2.3). Figure 7.17 a) shows the measured total hemispherical reflectance (solid trace), the measured diffuse hemispherical reflectance (dashed trace) and the calculated specular reflectance (dotted trace) of the three samples. The data is consistent with the expectations of the optical response arising from b-Si layers of different heights [140] and yields weighted average total reflectance (R_{AW}) of 2.2 %, 1.6 % and 1.3 % for MACE times of 6 minutes, 8 minutes and 12 minutes respectively. Figure 7.17 b) shows the calculated reflectance haze of each sample, defined as the ratio between the diffuse hemispherical reflectance and the total hemispherical reflectance measurements. The reflectance haze is above 0.9 for all samples across the wavelength range and increases with nanowire height. This describes the proportion of light that is scattered away from the specular reflection direction (i.e. angles larger than 6°) which is a direct indication of the light-trapping potential of these nanostructures. The weighted average haze (H_{AW}) values are 0.9, 0.94 and 0.97 for MACE process times of 6 minutes, 8 minutes and 12 minutes respectively. However, no angular information is available from these calculations

and more complex systems are therefore needed to describe the reflected signal via angular means and further calculate metrics that beneficially impact the solar cell operation.

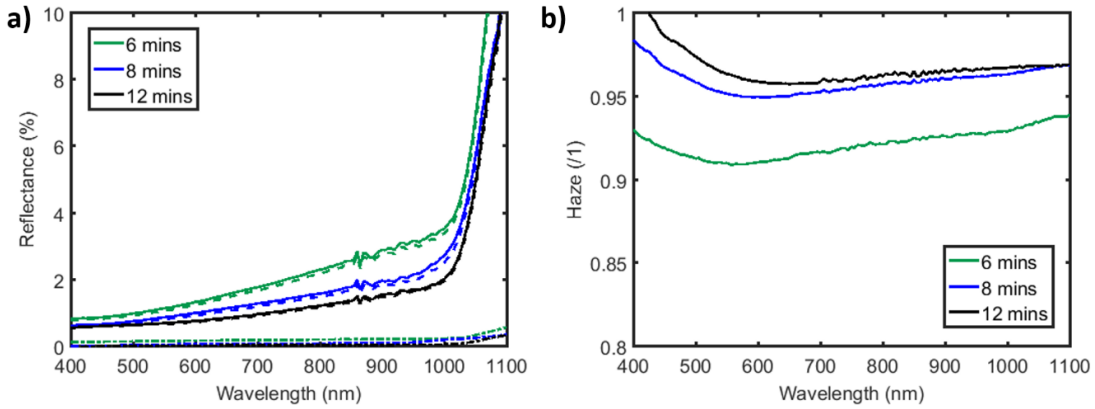

Figure 7.17: a) Measured total hemispherical reflectance (solid trace), measured diffuse hemispherical reflectance (dashed trace) and calculated specular reflectance (dotted trace) of the b-Si samples; b) Calculated reflectance haze for the three b-Si samples.

7.3.3 WARS measurement

The wavelength and angle resolved reflectance measurements of the MACE b-Si samples are shown in Figure 7.18, with p-polarized light normally incident on the surface, for wavelengths between 480 nm and 950 nm and angles in the range 6°-80°. The intensity of the reflections is normalised and shown in colour. Due to the sensitive nature of these measurements and data collection, the data was smoothed using a moving average method with a window size of 25 nm. All of the three b-Si layers exhibit a broad angular distribution of the reflected signal across multiple scattering angles for all of the wavelengths. The scattering maxima for each of the data sets lies at angles above 30° and increases with nanowire height. A strong wavelength dependency can be observed for the three plots, where the intensity of the signal is maximum for larger wavelengths, in line with hemispherical reflectance measurements. This arises from the capability of b-Si to more readily absorb short incoming wavelengths due to the feature size of the nanostructures. Moreover, the scattering angle of the reflected light is larger for short wavelengths due to increased

scattering effects in this region. The overall behaviour is very different from that of alkaline-etched micropyramids shown in the previous section, where specific photon paths are observed due to the fixed geometry of the structures, along with minimal wavelength dependency due to the size of the pyramids compared to the wavelength of the incident photons. Even the shorter 1.2 µm nanowires corresponding to Figure 7.18 a) redirect the majority of the light to angles larger than 28°, where the dominant path A occurs in the pyramids case. This confirms the superior scattering capabilities of such nanostructures compared to the industrial standard textures in the PV field.

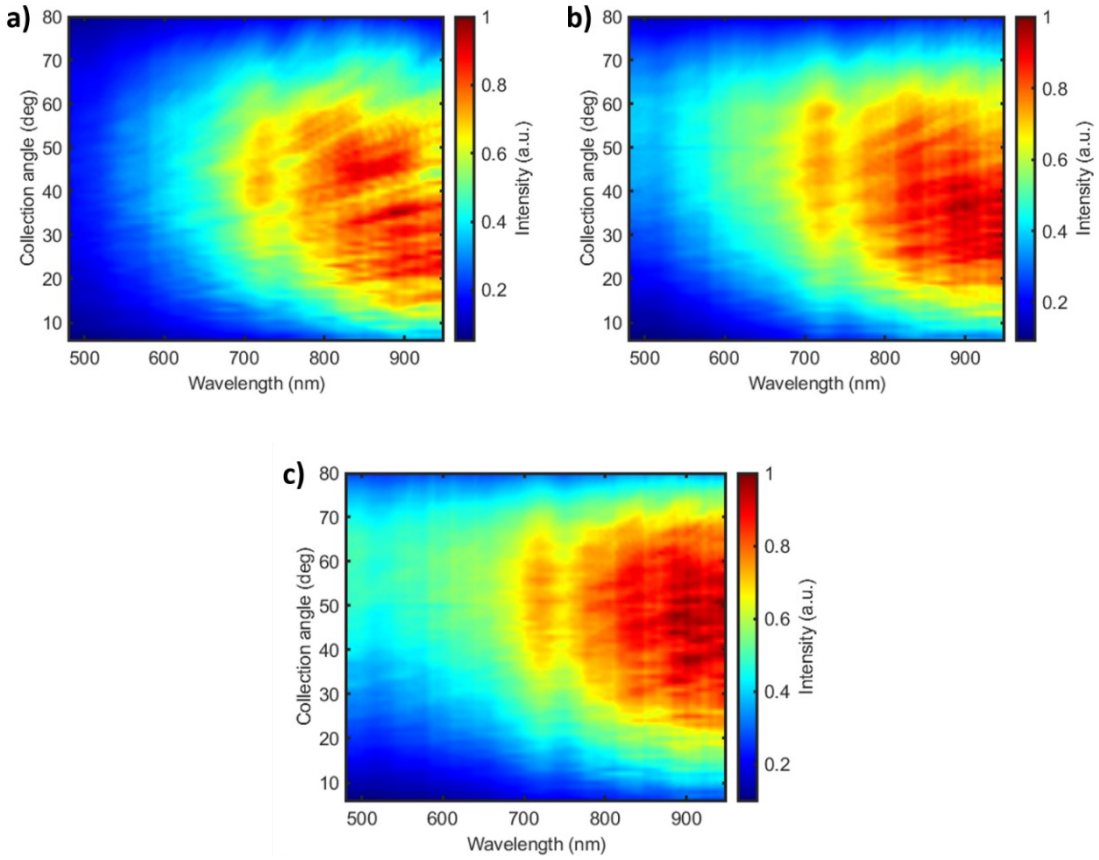

Figure 7.18: Wavelength and angle resolved (WAR) measurements of b-Si textures of different height: a) 1.2 µm; b) 1.8 µm; c) 3.6 µm.

More detailed analysis is enabled for specific wavelengths by slicing through the above data and studying the shape of the collected signal. As such, Figure 7.19 shows the collected signal for wavelengths of 500 nm, 600 nm, 700 nm, 800 nm and 900 nm for all three samples. It is evident that the intensity of the reflected light

increases with increased incident wavelength and that these signal are also shifted to smaller scattering angles

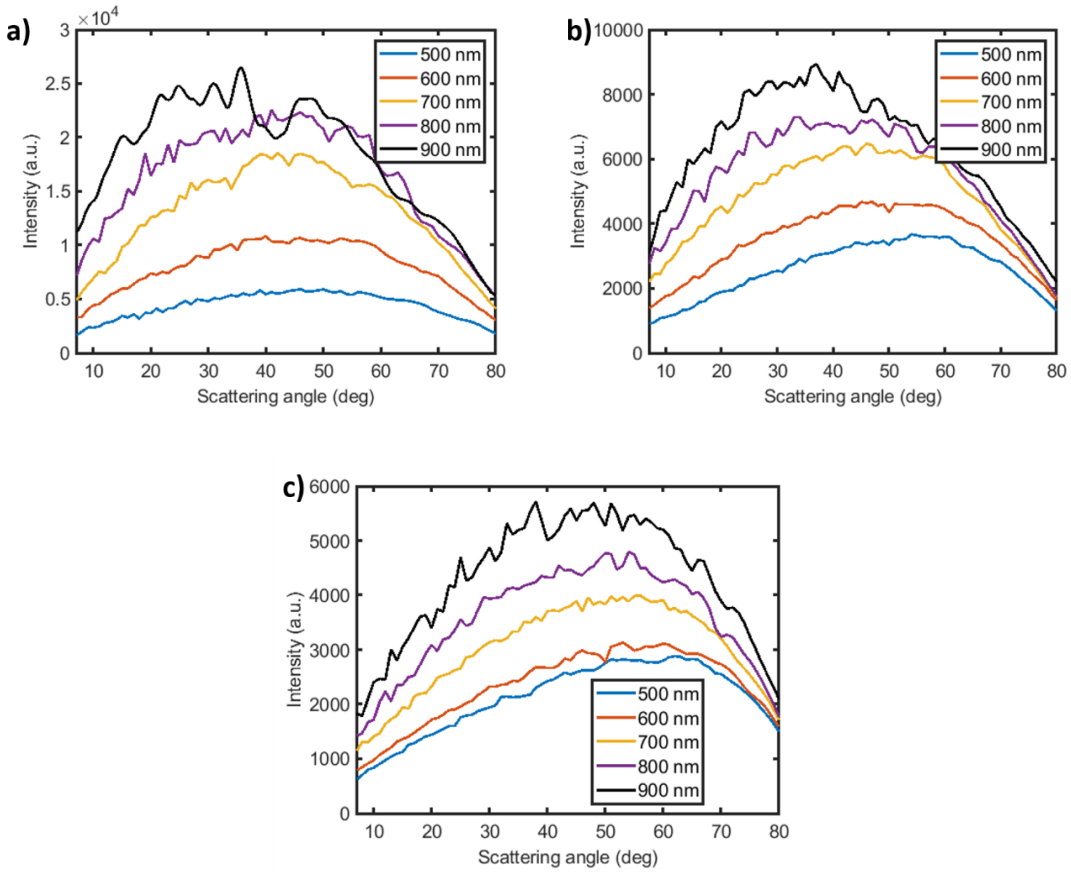

Figure 7.19: Collected (dashed trace) and polynomial fit (solid trace) signals at set wavelengths for MACE b-Si lengths of: a) 1.2 µm; b) 1.8 µm; c) 3.6 µm.

7.3.4 Impact of height

On top of yielding reduced surface reflectance, an increase in the nanostructure height translates into light scattering at larger angles, attributed to the increased number of modes into the longer nanowires and additional interference effects leading to additional scattering. While the peak in the scattering of 500 nm photons incident on the 1.8 µm b-Si texture is at ~54°, there is a gradual decrease down to angles of 34° for wavelengths of 900 nm. By comparison, the 3.6 µm long nanowires show a scattering maxima of 57° at 500 nm, while the 1.2 µm long nanowires give an angle of 47° for the same wavelength.

This trend is further illustrated in Figure 7.20 a), where the maximum scattering angle for each incident wavelength is shown for the three samples. Not only are the longer nanowires redirecting light to larger scattering angles, they also more readily maintain this scattering behaviour over the entire wavelength spectrum compared to the shorter nanowires. For example, there is 11° difference between the maximum scattering angles at 500 nm and 900 nm for the 3.6 μm long nanostructures, while the difference becomes 20° for the same wavelengths for the shorter 1.8 μm sample and 25° for 1.2 μm sample. Figure 7.20 b) shows the maximum scattering angle as a function of nanowire height and summarises this key point for a number of selected wavelengths. The error bars are calculated from multiple measurements of the same sample. Even though the measurements are carried out with various integration times for each of the b-Si textures and the data is presented as normalised in relation to the highest intensity point in the colormap, the standardization of the signals to counts/ms should agree well with the reflectance values obtained from the integrating sphere setup. Figure 7.20 c) shows that, indeed, the reflected power increases with decreasing nanostructure length. Moreover, the ratio between the intensities of the different samples at the same wavelength is very similar to the ratio between the measured diffuse hemispherical reflectances at those wavelengths, further confirming the validity of the data collected by the WARS setup. Slight differences are attributed to the fact that integrating sphere measurements are carried out at 8° angle of incidence, while the WARS measurements are performed under normal incidence, as well as reflectance below unity for the material that is coating the inside of the sphere.

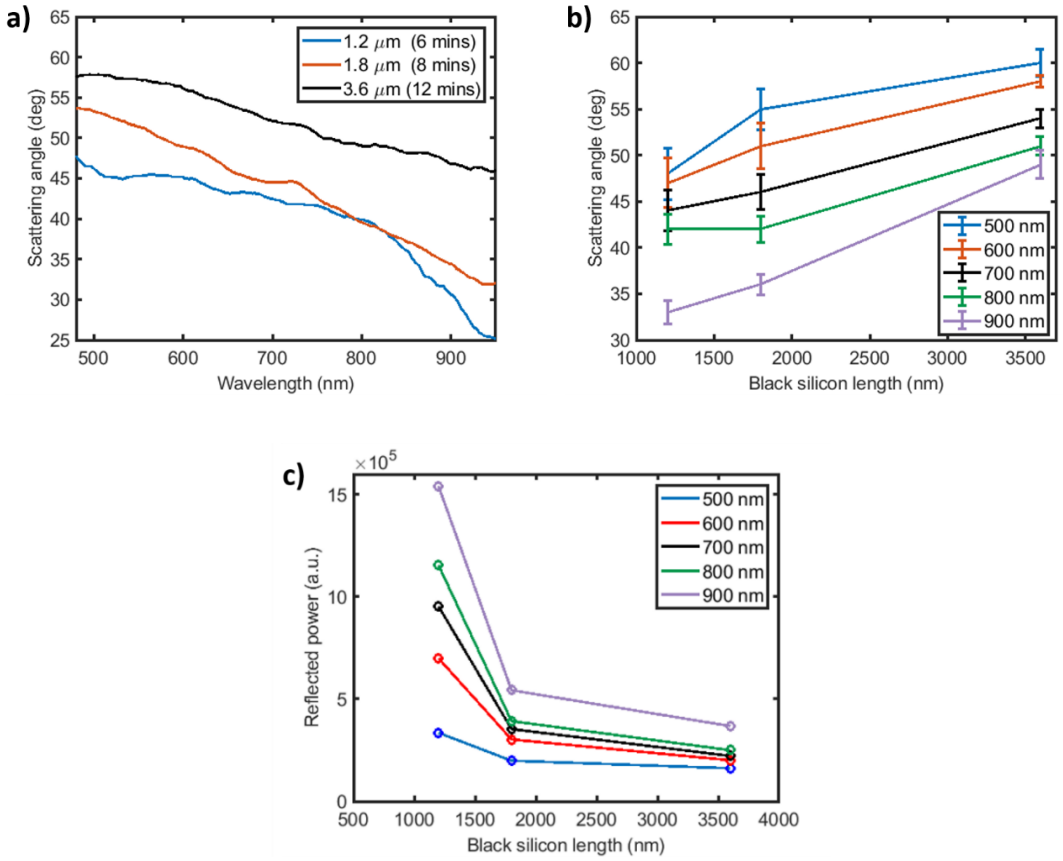

Figure 7.20: a) Maximum scattering angle for the entire wavelength range; b) Maximum scattering angle as a function of nanowire height for selected wavelengths; c) Total reflected power as a function of nanowire height for selected wavelengths.

It is of interest to assess the reflected light under various azimuth rotations to obtain a full picture of the hemispherical scattering profile. This is especially important when considering, for example, the alkaline etched micropyramids, which exhibit 4-fold symmetry and thus a different optical response under each azimuth rotation. However, the symmetry of the nanowires along their long axis should not result in significant changes when the azimuth angle of the texture is changed. Figure 7.21 shows reflectance data of the 1.8 µm thick b-Si layer for various azimuth rotations of the sample. Indeed, no significant changes are observed, as the total reflected power yields similar results independent of orientation. Slight differences arise from the morphology of the bunched nanowires, due to van der Waals forces and other nanoscopic forces at play [221] (see Chapter 5). As such,

these agglomerations may be slanted at an angle and not be perpendicular on the surface normal, leading to a modification in the nanowire geometry and shape under azimuth rotations. However, for all of the cases, differences smaller than 3.5 % are calculated (red right-hand axis, as relative to the measurement at 0° azimuth).

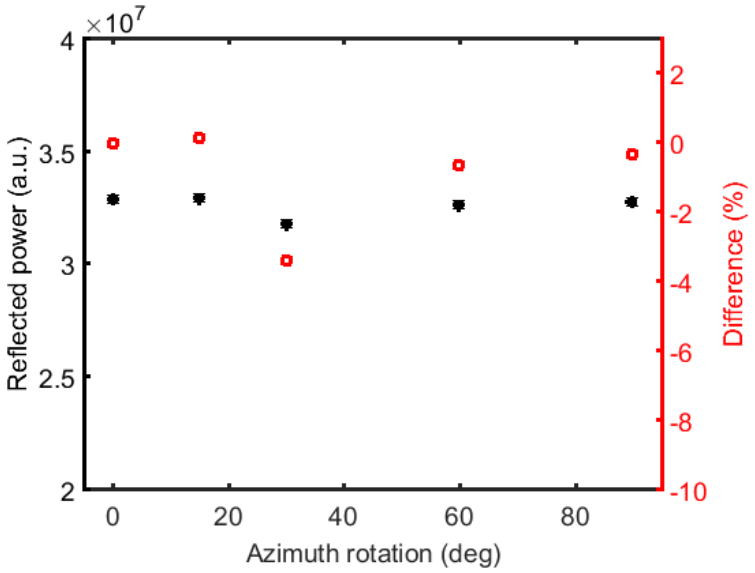

Figure 7.21: Integrated total reflected power for the 1.8 µm b-Si sample under various azimuth rotations.

Based on this, a more comprehensive description of the scattering profiles arising from these textures can be represented when considering both the polar scattering angles and the azimuth angles. Figure 7.22 below shows the angular dependent reflections in polar coordinates for the three samples, using measurements taken at 0^0 azimuth and assuming no variation in scattered light with azimuthal angle. The data was integrated over the entire wavelength range. The centre of each plot is 6° polar angle and concentric circles are traced at 30° and 60°. The reflected signal is shifted towards larger polar scattering angles with increased nanowire height and no noticeable differences are present for azimuth rotations. In all of the figures, only the first quadrant (i.e. polar angles from 0° to 90°) shows measured data. The greyed out quadrant are copied across for a complete representation.

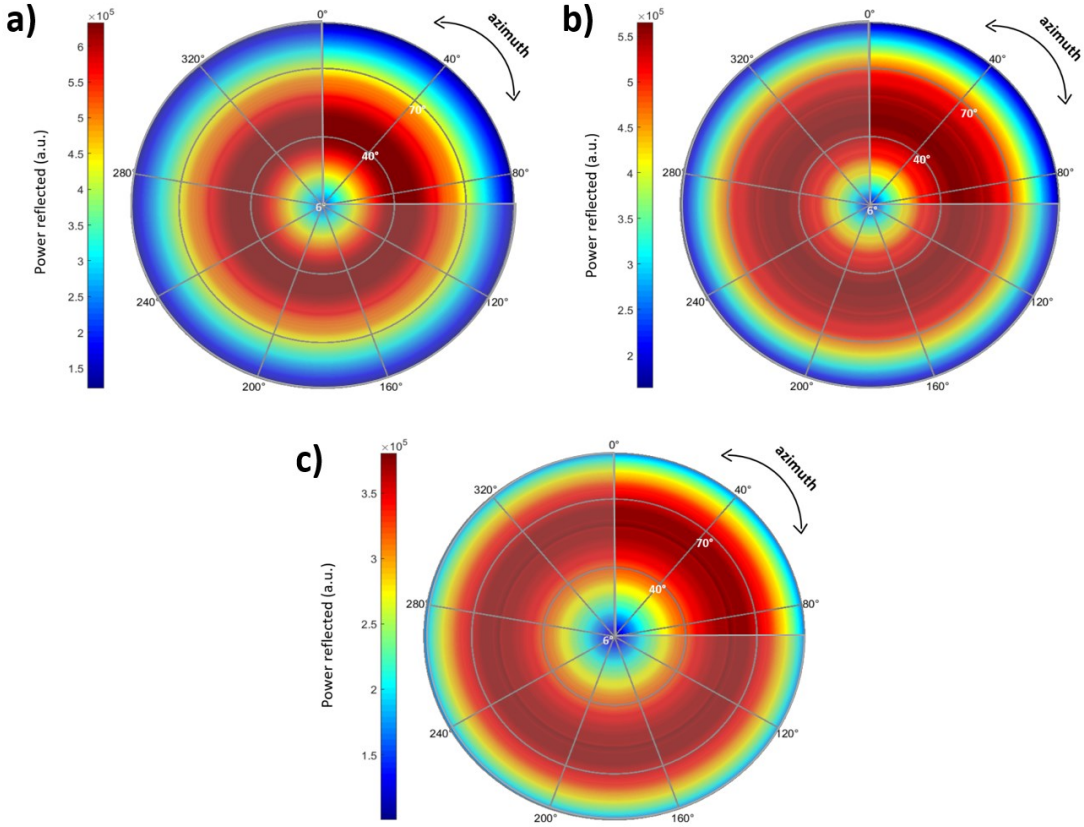

Figure 7.22: Reflected scattering profile description in polar coordinates for: a) 1.2 µm; b) 1.8 µm; c) 3.6 µm long b-Si layers.

7.3.5 Total internal reflection

As commercial solar cells are encapsulated and protected with a glass layer to avoid damage, the measurements presented here may be of interest when analysing the fraction of light trapped by total internal reflection at various interfaces in the stack. As previously discussed, the virtual glass-air interface can redirect light back towards the substrate if it is incident at an angle greater than the critical angle for that interface, which is dictated by the refractive index of the encapsulant material (see Chapter 7.2). Therefore, this fraction of light trapped by TIR can be calculated as the ratio between the reflected power outside the escape cone at the glass-air interface and the total reflected power by the b-Si texture, as in the previous section (equation 7.6).

Figure 7.23 shows the calculated fraction of light trapped by TIR, f_{TIR}, as a function of encapsulant refractive index in the range of 1-4 for the three MACE b-Si textures. The corresponding critical angle is indicated in the upper x-axis and is calculated from the encapsulant refractive index. Thus, the refractive index range 1-4 corresponds to a critical angle range 90°-14.47°. Due to the broad angular distribution of the reflected signal arising from the textures, all of the traces are continuous functions over the entire refractive index range. For a fixed refractive index, the longer nanowires yield higher f_{TIR}, due to the preferential scattering of light towards larger angles, as well as the higher amount of photons scattered compared with shorter nanowires. For refractive indices above 3, all of the textures yield similar f_T of above 80% corresponding to critical angles below 20°, as most light is scattered beyond the escape cone. An encapsulant refractive index of 3 would ensure that more than 80% of the reflected light would be trapped by total internal reflection at the glass-air interface for all of the b-Si textures and redirected back onto the semiconductor surface. However, such a high index material is not feasible for PV applications.

From a PV perspective, low refractive indices in the range of 1.4-1.6 are common in order to avoid large initial reflections when light is incident on the solar cell surface. For a typical encapsulant refractive index of around 1.5, such as EVA [239], PVB [240] or polyolefins [241], the fraction of light trapped, f_{TIR}, is 49%, 51% and 58% for b-Si textures etched for 6 minutes, 8 minutes and 12 minutes, respectively. For comparison, f_{TIR} is plotted for the experimental alkaline-etched pyramid texture introduced and calculated in section 7.2 (purple dashed trace). At a refractive index of 1.5, the f_T for pyramids is only 14.5%, due to light being scattered preferentially towards lower angles, such as the dominant path A occurring at 28°, in contrast with the scattering profile of the b-Si textures. As such, these textures vastly outperform the micron-scale pyramids from an optics perspective, not only by providing reduced top surface reflectance, but also due to their impressive scattering capabilities that provide multiple uses at the device level. Given similar levels of surface passivation such that the electrical losses are comparable between the two textures, the b-Si layers prove to be an excellent candidate to replace the alkaline-

etched textures as an industrial standard, especially when considering the similar ease of processing in both cases. Table 7.4 shows the values of f_T calculated for a number of emerging encapsulants for the three b-Si textures as well as the micron-scale upright pyramids.

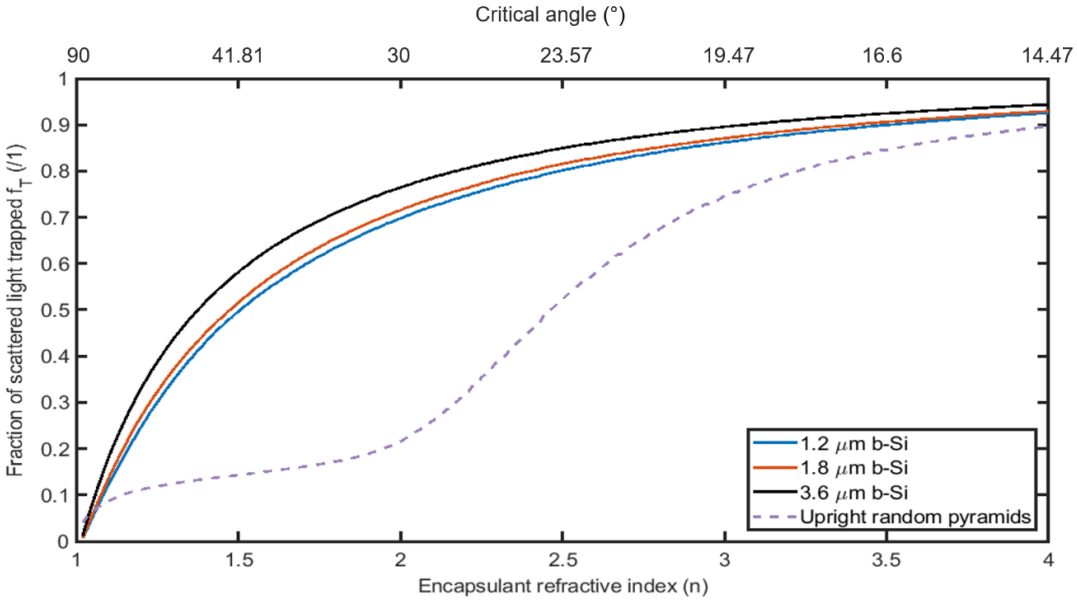

Figure 7.23: Calculated fraction of reflected light trapped at the glass-air interface as a function of surrounding encapsulant refractive index for the three b-Si textures and the alkaline-etched random pyramids (dashed purple trace).

Table 7.4: Fraction trapped of alkaline-etched and MACE textures for various PV compliant emerging encapsulants.

Texture	Fraction trapped (%)			
	PDMS	**PVB**	**EVA**	**polyolefin**
	n = 1.42 [242]	**n = 1.485 [240]**	**n = 1.5 [239]**	**n = 1.53 [241]**
Random pyramids	13.6	14.1	14.5	14.7
1.2 µm b-Si	44.5	48.3	49.5	51.2
1.8 µm b-Si	46.4	50.2	51.5	53.2
3.6 µm b-Si	53.1	56.9	58.1	59.7

7.3.6 Photocurrent gain

Information on the fraction of light-trapped at glass-air interface and on the angular distribution of the reflected light for different textures is vital and can participate in the creation of a more comprehensive and accurate model for calculating the photocurrent density (J_{PH}), than just from a surface reflectance point of view. As such, Eq. (7.4) is a derivation of the well-established J_{PH} calculation method [63-64] that takes into account the impact of the reflections at different material interfaces in the stack on the incident AM1.5G photon flux density (F_{PH}). For consistency with previously presented WARS data, F_{PH} was standardised to 100 mW/cm^2 across the whole wavelength range, but only the spectrum in the 480-950 nm range was considered in the calculations. Thus, lower values for J_{PH} are obtained than what is currently routinely achieved in real modules, where the full spectrum is available. In Eq. (7.4), q is the elementary charge (1.602 * 10^{-19} C), $R_{GLASS}(\lambda)$ is the reflectance at air-glass interface (assumed to be independent of wavelength), IQE (λ) is the internal quantum efficiency of a silicon solar cell (assumed to be 100% in all cases) and $R_{ESCAPED}(\lambda, n)$ is the reflection arising from the texture where the fraction of light trapped has been accounted for as in Eq. (7.5). The glass and encapsulant materials are assumed to be index-matched (i.e. n=1.5).

$$J_{PH} = q \int_{480\,nm}^{950\,nm} (1-R_{GLASS}(\lambda)) F_{PH}(\lambda)\ (1-R_{ESCAPED}(\lambda))\ IQE(\lambda) \qquad (7.4)$$

$$R_{ESCAPED}(\lambda, n) = R_{TEXTURE}(\lambda)\ (1 - f_{TIR}(n))\ (1-R_{GLASS}(\lambda)) \qquad (7.5)$$

In Eq. (7.5), $R_{TEXTURE}$ is the measured hemispherical reflectance of the textured surface and f_{TIR} is the fraction of scattered light trapped by TIR at the glass-air interface for the respective texture (see previous subchapter). This accounts for the reduction in the reflection due to TIR at glass-air interface, indicating a smaller value for the reflection exiting the PV module stack than the reflection exiting only the textured surface. The second reflection at the air-glass interface when reflections are travelling upwards is accounted for as well, but it was calculated using Fresnel's equations at normal incidence. In reality, a proportion of the photons that are incident onto this interface outside the escape cone will be incident at an angle

larger than 0°. For this reason, the reflectance at the glass-air interface will be lower in these cases and overestimated. The presented model will therefore lead to an underestimation of the photogenerated current.

Upon initial incidence of the photon flux on the glass layer, a J_{PH} loss of 1.2 mA/cm^2 is calculated in all cases, compared to the maximum value of 31 mA/cm^2 available in the 480-950 nm wavelength range. For a typical encapsulant refractive index of 1.5, the J_{PH} data is summarised in Tabile 7.5. The optimised ARC coated random pyramids sample yields lower photocurrent values than all of the b-Si samples under study, regardless of the nanowire length. A modest gain of only 0.24 % in J_{PH} for pyramids when the fraction trapped by TIR is considered is attributed to low f_{TIR} values at this encapsulant refractive index (14.5 %). In contrast, the gains for the b-Si samples are more substantial and a significant 0.84% gain is obtained for the 1.2 μm nanowires, owing to reduced broadband surface reflectance and f_{TIR} approaching 50%. An increase in b-Si length leads to slightly reduced gains, due to the more important role that reduced broadband surface reflectance plays when compared to small increases in f_{TIR}. However, due to large-angle scattering promoted by b-Si, the photocurrent gain remains in all cases in excess of 0.5%, suggesting the importance of these scattering profiles in an industry-standard encapsulating stack.

Table 7.5: J_{PH} calculated with and without consideration of f_{TIR} at glass-air interface for various textures.

Texture	J_{PH} (mA/cm^2)		Gain (%)
	without f_{TIR}	with f_{TIR}	
Random pyramids	28.57	28.64	0.24
1.2 μm b-Si	28.74	28.98	0.84
1.8 μm b-Si	28.89	29.08	0.65
3.6 μm b-Si	28.97	29.14	0.58

Moreover, this scattering is expected to play an even more significant role in the transmitted photons, that can be coupled obliquely into the substrate semiconductor material and lead to vastly improved optical pathlengths and increase absorption, particularly for low-energy photons. On an IBC c-Si solar cell, the short-circuit current loss due to transmittance (i.e. incomplete absorption) of long wavelength photons is as high as 0.5 mA/cm^2 for a pyramidally textured surface [244]. This figure is expected to go down substantially if black silicon is employed as a front texturing scheme, which would represent a relative gain of almost 1.5% in photogenerated current compared to a pyramid texture.

7.4 Conclusion

In conclusion, wavelength and angle-resolved scattering (WARS) measurements on reflected light have been presented for alkaline-etched upright random pyramids and MACE b-Si. The accuracy and reproducibility of such measurements were first demonstrated on a periodic pyramidal sample, where the diffractive grating equation could be employed to calculate the various modes as a function of wavelength and polar angle. Next, a KOH etched silicon sample presenting upright random pyramids on the surface was analysed in conjunction with ray-tracing reports available in literature. Due to the fixed geometry of the microstructures, discrete photon exit paths are expected at specific polar and azimuth angles. Initial poor agreement between theoretical studies and WARS measurements triggered a more in-depth analysis of the morphology of the pyramidal array. As such, lower dihedral base angles than what is expected from the etching process and the intersection between (100) and (111) planes were measured using scanning electron microscopy on a FIB-prepared cross-section of a pyramid. This result has been previously reported in several studies in the literature and allowed for a reassessment of the photon exit paths arising from such a texture. Measurements at various azimuthal rotations of the specimen confirmed the validity of the proposed model and allowed for identification of several photon paths across a wide range of polar angles, suggesting that the pyramid morphology presents a range of dihedral base angles, dependent on the exact etching recipe conditions.

Three MACE b-Si samples of various process durations, resulting in different nanostructures lengths, were then measured for a range of azimuth rotations. It was found that the b-Si scattering profile is highly dependent on incident photon wavelength and redirects the reflected light towards larger polar angles than the random pyramids, increasingly so for longer nanowires. The measured data was used to assess the amount of light trapped at various stack interfaces in an encapsulated stack. The b-Si textures vastly outperform the industry-standard alkaline-etched random pyramids textures, not only by providing reduced broadband surface reflectance, but also by redirecting these photons into more oblique angles. This directly translates into a higher fraction of light trapped at the glass-air interface by means of total internal reflection, which would lead to larger photocurrents. Provided similar levels of surface electrical passivation between these textures, MACE b-Si has the potential to become a preferable choice in the implementation of antireflection and light trapping through surface texture in high-efficiency silicon solar cells.

Chapter 8

Conclusions and outlook

8.1 Key findings

In this thesis, the design, fabrication and characterisation of metal-assisted chemically etched black silicon surfaces is presented. Firstly, a literature review of the existing antireflective schemes is provided, including planar surfaces with antireflective coatings and industry-standard alkaline-etched random pyramidal silicon arrays. It is shown that, while these schemes provide satisfactorily optical results, reduced broadband surface reflectance and improved light-trapping can be further achieved by nanoscale texturing of the silicon substrate. Then, an investigation into the metal-assisted chemical etching (MACE) process is presented, which results in a dense array of vertically-aligned and uniform nanowires, randomly distributed on the silicon surface. The influence of various etching process parameters on the morphology and the optics on the nanostructures is discussed, including process time, the molarity of the silver nitrate solution and the molarity of the hydrofluoric acid solution. Scanning electron microscope and hemispherical reflectance measurements are shown for each case. Longer and denser arrays of nanowires translate into reduced total surface reflectance and larger reflectance haze values for all of the wavelengths considered, with champion samples yielding weighted average surface reflectance below 1.5% pictured in Figure 8.1. The findings suggest an optimal set of etching parameters and conditions, for reproducible realisation of low-reflective black silicon with uniform height and well-defined features. Furthermore, the scalability of the MACE process is demonstrated on 6-inch silicon wafers, resulting in specular reflectance values below 2%. If enough throughput can be realised using this wet-etching process, then MACE can be easily and cheaply integrated into the industrial fabrication flow to manufacture low reflectance silicon solar cells.

Nanotexturing the silicon surface results in large increases of the semiconductor exposed surface area by tens of times. As such, excellent surface passivation is required so that, overall, a gain arising from the improved optical properties is obtained at the device level. To this end, atomic layer deposition (ALD) aluminium oxide is investigated as a passivating layer on both flat surfaces and on top of the

black-silicon surfaces, resulting in excellent minority carrier lifetimes due to the negative fixed charge that can be activated upon a high-temperature annealing step. Subsequently, sufficiently low surface recombination velocities are calculated for use in high-efficiency silicon devices, especially in a back contacted architecture. The influence on film thickness, annealing time and conformity of the passivating layer on these high-aspect ratio structures is also reported. Surface recombination velocities below 20 cm/s are demonstrated in this work for nanostructures of 1 µm height and for an aluminium oxide thickness of 17 nm. This value is comparable with what is traditionally obtained on the industrial random pyramids array with a thicker layer of silicon nitride and to the state-of-the-art black silicon IBC solar cell fabricated by Savin et al. [46] with an efficiency exceeding 22%. These findings indicate that surface recombination is not a limiting factor for the black silicon surfaces anymore when ALD is employed, and that these nanostructures are excellent candidates for replacement of the microstructures currently in use on commercial silicon solar cells.

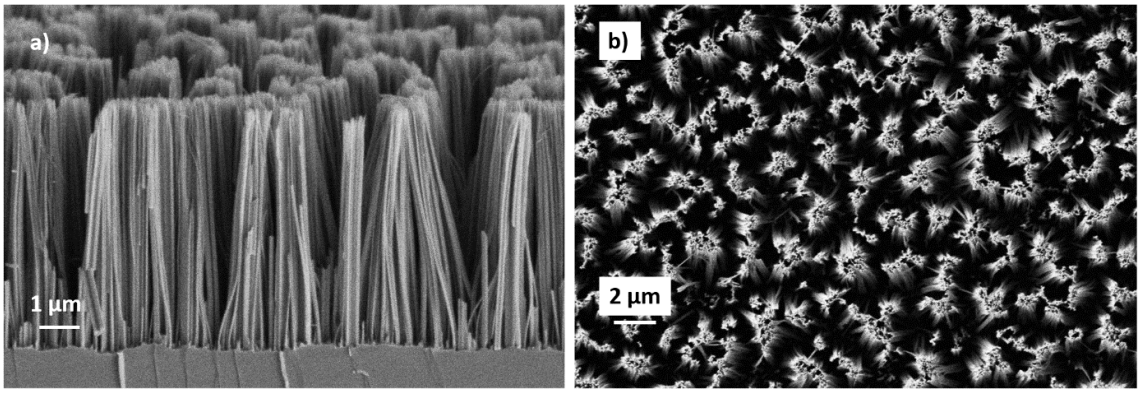

Figure 8.1: Scanning electron microscope images of metal-assisted chemically etched black silicon: a) cross-section; b) top view.

In order to analyse the conformity of the ALD AlO_x passivating layers on top of the high aspect ratio nanostructures, a novel approach was employed whereby a Ne ion beam was used to horizontally mill a couple hundred of nanometers from the tip of the black silicon layers. As such, the alumina material was found to be present below the nanowire clusters and agglomerations, all along the length of the structures. This is a direct consequence of the modified ALD recipe with the insertion of a diffusion

step, which delays the purging of the deposition chamber to allow precursor to settle inside the trenches and deep crevices at the base of the black silicon layers. The target aluminium oxide thickness was measured in multiple locations for two very different nanowire lengths, indicating that precursor delivery during the ALD process is sufficient for the associated increased silicon surface area.

Wavelength and angle resolved reflectance (WARS) measurements are carried out to provide a more in-depth look at the light-trapping capabilities of both alkaline-etched pyramids and MACE black silicon layers. It has been found that the pyramidal structures reflect the light at scattering angles that can be geometrically calculated, considering the feature size of these structures compared to the incident wavelength. Therefore, a discrete number of reflected photon paths is expected due to the fixed geometry of the pyramids. However, it was found that anisotropic etching of silicon surfaces often result in lower dihedral base angles than those expected from the intersection of {100} and {111} crystallographic planes. As a consequence, several of the ray-traced photon paths disappear upon such base angle decrease, which triggers a redistribution of power across the remaining photon paths. Moreover, a base angle distribution, confirmed by high-quality scanning electron microscope images after milling through the pyramids, leads to a continuous nature of the reflections, rather than the sharp discrete reflection peaks at known scattering angles. The scattering profile arising from the pyramidal structures is shown in Figure 8.2 a).

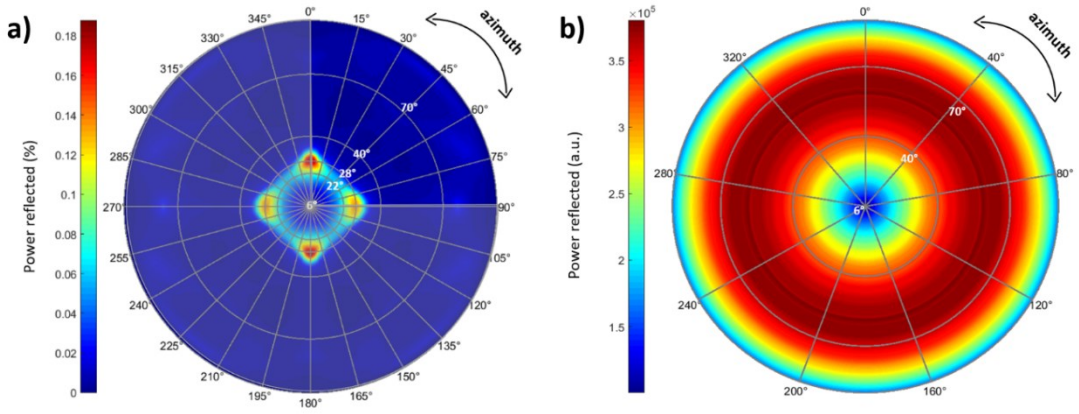

Figure 8.2: Polar plots for integrated reflected scattering arising from: a) alkaline-etched pyramidal textures; b) MACE black silicon. Measured data from 0°-90° azimuth angle (first quadrant); the rest of the quadrants are copied and mirrored across for a complete visual representation.

In contrast, the WARS profile of the black silicon surfaces shows a more Lambertian-like distribution of the reflections, across a larger range of scattering angles, as in Figure 8.2 b). The reflections have a strong dependence with wavelength, where high-energy photons are redistributed towards larger scattering angles compared to low-energy photons. Black silicon layers scatter incident light over a wider angular range than the micron-scale pyramids, which has important consequences at the device level. In particular, when an encapsulated photovoltaic module is considered and new interfaces are created, such as encapsulant-glass and glass-air, large-angle reflections may undergo total internal reflection at these interfaces. The fraction of scattered light trapped at these interfaces and redirected back onto the cell for various textures can then be calculated from their WARS profile. It was found that, due to their large-angle scattering, black silicon layers promote a higher fraction of light trapped at the glass-air interface than the random pyramid surfaces, increasingly so for taller nanowires. A comprehensive model which takes into account the reflections at various stack interfaces, as well as the fraction trapped via total internal reflection by the textures, was presented for photogenerated current density calculations. Photocurrent densities in excess of 29

mA/cm^2 are obtained for the black silicon surfaces and relative gains of more than 0.5% in photocurrent are possible for a range of black silicon lengths with the inclusion of fraction of light trapped via TIR at glass-air interface in the model. In comparison, gains of only 0.2% are possible for alkaline-etched silicon surfaces that present random upright pyramids, due to preferential scattering of the reflected light towards much lower polar angles. This demonstrates the superior antireflective and light-trapping capabilities of the nanostructures, and indicates their suitability as replacements for conventional micron-scale pyramidal textures on the surfaces of commercial monocrystalline silicon solar cells for high power conversion efficiencies.

In general, nanoscale texturing the surface of a silicon solar cell has the potential to boost the efficiencies of existing silicon solar cell deigns, given that a good balance is engineered between optics and electrics. IBC solar cells represent an excellent platform for these textures to be employed. In this cell design, the contacting scheme is moved to the back of the device, leaving the top surface free for incorporating black silicon without the complications of having to form contacts and a junction in this region of the cell.

8.2 Future work

The work presented in this thesis can be expanded in several ways. Firstly, the combination of nanoscale and microscale textures has the potential to optically outperform the alkaline-etched pyramidal surfaces or the black silicon surfaces alone. This was briefly introduced in section 5.4 as so called 'hybrid' structures: micronscale pyramids decorated with MACE nanowires. As such, near-zero broadband reflectance can be obtained, along with improved light-trapping properties, where the reflections are distributed across even larger scattering angles. Cross-sectional imaging studies can be expanded to study the crystallinity dependence of the MACE process on the facets of the pyramids, which can have direct implication on the surface passivation of these hybrid structures. Due to the combination of micro and nanoscale, WARS measurements can provide useful insights into the scattering mechanisms of such arrays, which can prove to be more

effective at device level than b-Si or pyramids alone. In addition, other antireflective textures can be evaluated with the use of such measurements, such as isotextured multicrystalline silicon that is so widely used in industry today.

Secondly, there is still much scope to the passivation of the black silicon layers via novel materials and deposition methods with good conformity. Surface recombination is one of the more detrimental losses at the silicon solar device level, increasingly so for nanotextured surfaces. While aluminium oxide is an excellent passivating material for these surfaces, the passivation level is still lower than the industry-standard PECVD silicon nitride on top of random pyramidal arrays. To this end, passivating stacks can be used, such as an ultra-thin silicon dioxide layer sandwiched between the substrate and the aluminium oxide materials. Owing to its excellent chemical passivation and suppression of surface dangling bonds, the performance of the stack should be better than just the aluminium oxide alone. Alternatively, hydrogenation of the silicon-dielectric interface is an excellent option for reducing interface state defects. Over the past decade, the resurgence of the atomic layer deposition contributed to the development of novel passivating layers, mostly metal oxides. As such, materials such as tantalum oxide [245], hafnium oxide [246] or gallium oxide [247] are promising, if the deposition is sufficiently controlled.

Wavelength and angle resolved reflectance measurements can be expanded by varying the angle of incidence, so that more complete scattering profiles are obtained from textured surfaces. This is especially important when considering the movement of the Sun throughout the day and its incidence on a practical silicon solar cell. Furthermore, transmittance measurements of these textures can be performed, if the silicon substrate is thin enough (below 30 μm). Although this might prove to be challenging, the nanostructural array can alternatively be embedded into transparent polymers (such as PDMS [242, 243]), such that the measured data becomes a contribution arising only from the nanostructures, not the substrate as well. A complete set of measurements, both in reflectance and transmittance and for a variety of incidence angles, can then be used on fast simulation software such as OPTOS [249-250] to quickly design an optimal solar cell and investigate the

influence of various materials at the device level. Furthermore, by isolating the contribution of the nanostructures on the reflected signal, various effective medium approximation techniques can be employed with a higher degree of accuracy to reproduce the optical characteristics of such surfaces. This can become very useful as a quick modelling tool at device level, where an optimum black silicon length can be found, which is beneficial both optically and electrically.

The integration of black silicon layers at the device level must also be considered. Therefore, the silicon substrate can be textured as a first step, as in the alkaline-etching case, due to the high stability of the black silicon layers upon subsequent high-temperature fabrication steps. The work of Oh et al. (2012) [251] employed a front and back metal contact solar cell structure, where the nanotexturing of the silicon surface occurred before the diffusion of dopants to form the emitter, with a photoresist on the back of the silicon to prevent etching on the underside. It has been suggested in the study that most of electrical losses from passivation arise from a consequence of significant Auger recombination due to in-diffusion through the nanostructures, rather than the surface passivation itself. As such, attention has to be given to light and shallow doping of the emitter in combination with controlled surface area increase arising from nanostructures, such that electrical losses are balanced and do not hinder the performance of the solar cell. Alternatively, the texturing of the cell can be left for the last step, if sufficient protection to the acidic solutions is given to the rear of the cell, where the contacts might be situated. To this end, preliminary work has been carried out using a 2 × 2 cm^2 PTFE holder in combination with Parylene deposition, with modest success. Figure 8.3 a) shows the rear side of a standard back-contacted IBC silicon cell with a 2 µm thick Parylene layer for metal protection. Figure 8.3 b) shows a custom designed PTFE holder that is HF and MACE solution resistant, which is submerged in the solution in Figure 8.3 c). However, the yield of such an approach was not optimal and in many cases, the MACE solution was able to reach the backside of the IBC cell and corrode the metallic contacts, thus affecting carrier extraction and the performance of the device. Therefore, improvements in the design of the sample holder are required to provide adequate protection to the rear of the cell during MACE processing. This

development must also consider how this can be scaled up to be compatible with industrial manufacturing processes. As an advantage, etching the silicon surface as a last step promotes a more straightforward device fabrication process as a whole. As such, the photolithography steps and the dopant diffusions can be carried out without worrying about deteriorating the black silicon layers due to sample handling or scratching of the surface. However, if a doped emitter is formed that is different than the doping of the parent wafer, the etching conditions and rates will change accordingly, thus potentially leading to unoptimised nanostructures. Another disadvantage, as previously mentioned, is the susceptibility of the fabricated device during the MACE process: the contacts can corrode during the etching, such that the performance of the device will be drastically affected.

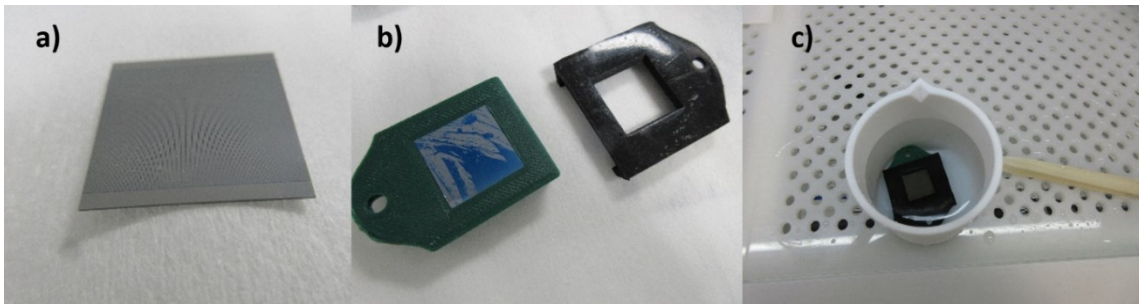

Figure 8.3: a) Rear side of a standard IBC cell coated with Parylene for contact protection; b) IBC cell inside of a custom PTFE holder; c) IBC cell and PTFE holder inside the MACE solution.

Appendix A - Lumerical FDTD simulations

In order to understand the impact of the heterogeneous black silicon surface from an optical point of view, similar nanostructures can be simulated and evaluated. Even though it is challenging to randomise the surface sufficiently to replicate the heterogeneous black silicon layer, it is still very useful to monitor the optical response of a single nanostructure modelled on top of the silicon bulk, as well as the effect of parameter variations, such as length, diameter and periodicity.

FDTD stands for finite-difference time domain and this method can cover a wide frequency range and solve Maxwell's equations by exploiting Fourier transforms. This is based on Yee's algorithm [208], which divides both time and space into small steps and considers these finite differences as approximations. Yee proposed putting the electrical field and the magnetic field vector components in cubic unit cells, so that each E-field component is situated in between two H-field components and vice-versa, as shown in Figure A.1 below. Time is also quantized into small steps and E and H are offset temporally, as E-field updates are done halfway through each H-field update. The software used in this project is FDTD solutions by Lumerical. It allows broadband simulation of nanoscale textures on top of a semiconducting material. The definition and set up of the elements provided in this Chapter have been used throughout the work. The software's website provides in-depth information on using Lumerical [214], including the usage of boundary conditions, sources, mesh types etc. and the FDTD method.

The main advantage of the FDTD method over other methods, such as transfer matrix method (TMM) or finite elements method (FEM) is the fact that FDTD works in the time domain rather than the frequency domain. This means that the equations are solved by time stepping, leading to broadband spectra and not for just a single frequency, like in FEM. It is especially helpful for the wide wavelength spectrum of interest for the silicon material. This directly translates to a shorter simulation time, being more precise and more memory efficient than its counterparts, but at the expense of additional hardware requirements.

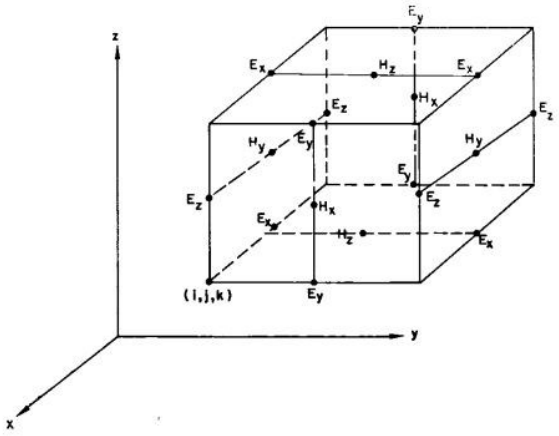

Figure A.1: Yee cell showing electric and magnetic fields distribution. Reproduced from Ref. [213].

Boundary conditions play a crucial role in FDTD, as they provide the accuracy needed along the edges of the domain. There are many types, including perfectly matched layer (PML), perfectly electric conductor (PEC), Bloch boundary conditions and symmetric/asymmetric boundary conditions. For this project, on the z-axis, there is a perfectly matched layer (PML), which absorbs any electromagnetic wave incident upon it and does not reflect at the interface. Therefore, the incoming wave is strongly absorbed in the interior of the domain. For the x and y-axes, the boundary conditions are periodic. This means that the domain is infinitely replicated to the left and to the right, so that the actual simulation uses only one nanostructure of a fixed size, rather than a multitude of wires. This shortens the simulation time drastically, but is a less accurate representation of fabricated black silicon nanostructures which are heterogenous and lack any periodicity. Reflection and transmission monitors are used to capture information about various spectra that are of interest.

For this project, the simulation domain was defined as a 3D rectangular parallelepiped, having dimensions of 100 nm along the x and y axes and a height of 2 μm along the z-axis. The origin point is halfway through this axis, making the bottom of the parallelepiped be at -1 microns and the top of it at 1 micron. The mesh type has been defined as auto non-uniform with a mesh accuracy of 3, meaning it takes into account 14 ppw (points-per-wavelength). The software uses a

rectangular Cartesian style meshing. The electric and magnetic fields are calculated at each mesh point. The higher the mesh accuracy, the smaller the mesh becomes and the greater the accuracy of the simulation, as in Figure A.2. Even though the results are more accurate for the smaller mesh sizes, the simulation time roughly doubles for each increment of the accuracy. Therefore, mesh accuracies of 3 and 4 have been used throughout this project in order to minimize the simulation time, but still provide reliable relevant results.

Next, the light source has been defined as a 2D planar wave, because the interest in these first simulations is only along the z-axis at normal incidence. It was positioned in the upper half of the parallelepiped at 0.75 μm and it was set to cover wavelengths from 300-1100 nm. Two monitors are used, for measuring reflectance and transmission. The reflectance monitor is positioned at the top of the simulation domain, just above the source of the electromagnetic wave, while the transmission monitor was placed at the very bottom. A graphical representation can be seen in Figure A.3 a) below, as well as the actual Lumerical representation in Figure A.3 b). In this image, the red rectangle is the silicon substrate, while the bright yellow squares at the top and the bottom are the reflectance and transmission monitors respectively.

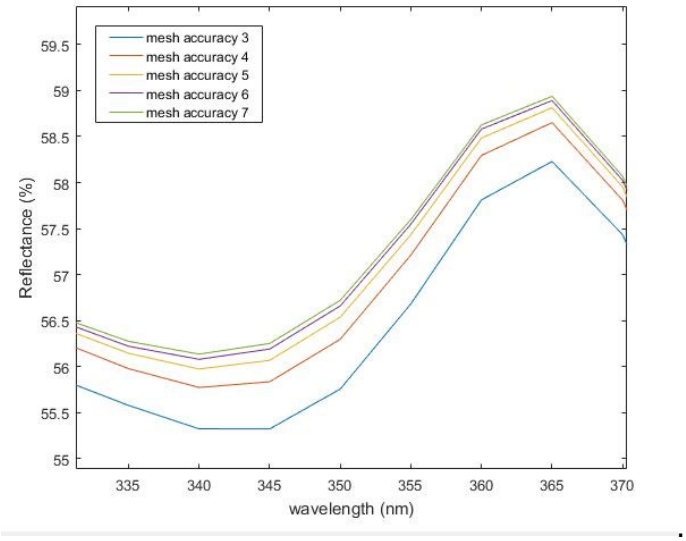

Figure A.2: Difference in reflectance spectra for various mesh accuracies.

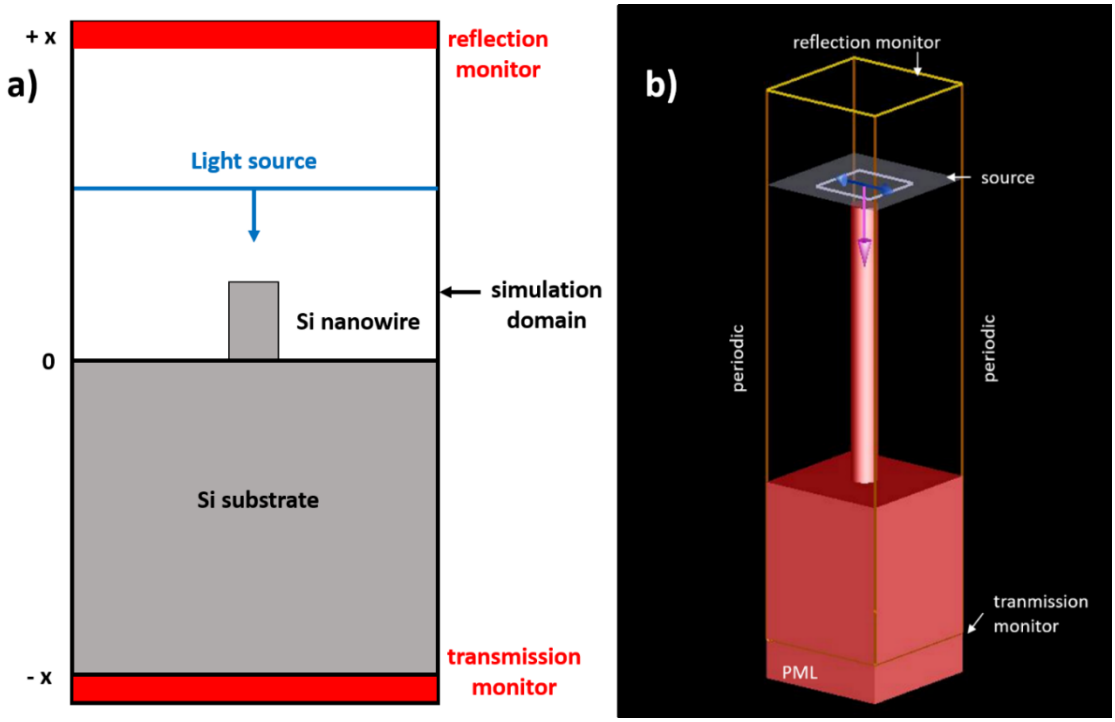

Figure A.3: a) Schematic of the FDTD simulation domain; b) Actual representation of the simulation domain, with boundary conditions included.

Appendix B – MACE parameters

Table B.1: Morphological and optical properties of MACE fabricated nanowires for varying etching times. Silver nitrate molarity 60 mM and HF molarity 14 M for all cases. Two samples for each varying duration time to show reproducibility of process.

t (mins)	Nanowire length (nm)	Weighted average reflectance (%)
1	499 ± 21	6.65
	521 ± 30	6.34
2	986 ± 42	3.56
	1033 ± 47	3.77
6	3057 ± 56	2.43
	3185 ± 71	2.22
10	4974 ± 109	1.44
	5146 ± 98	1.67

Table B.2: Morphological and optical properties of MACE fabricated nanowires for varying silver nitrate solutions. Etch time 6 mins and HF molarity 14 M for all cases. Two samples for each silver nitrate concentration.

M_{Ag} (mM)	Nanowire length (nm)	Weighted average reflectance (%)
20	262 ± 20	16.12
	315 ± 44	15.33
40	1755 ± 51	6.06
	1625 ± 72	6.52
60	3057 ± 56	2.43
	2983 ± 48	2.71
80	4102 ± 97	1.44
	4009 ± 122	1.87

Table B.3: Morphological and optical properties of MACE fabricated nanowires for varying hydrofluoric acid solutions. Etch time 6 mins and $AgNO_3$ molarity 60 mM for all cases. Two samples for each hydrofluoric acid concentration.

M_{HF} (M)	Nanowire length (nm)	Weighted average reflectance (%)
7	768 ± 26	3.68
	692 ± 49	4.12
11	1997 ± 68	2.73
	2085 ± 36	2.55
14	3057 ± 56	2.43
	3102 ± 79	2.24
21	3654 ± 128	3.77
	3735 ± 78	4.26

Bibliography

[1] Perera, F. (2018). Pollution from fossil-fuel combustion is the leading environmental threat to global pediatric health and equity: Solutions exist. International Journal of Environmental Research and Public Health, 15(1). https://doi.org/10.3390/ijerph15010016

[2] International Technology Roadmap for Photovoltaics (ITRPV), April 2020

[3] International Energy Agency. (2020). Snapshot of Global PV Markets 2020. 1–16. Retrieved from http://www.iea-pvps.org/fileadmin/dam/public/ report/technical/PVPS_report_-_A_Snapshot_of_Global_PV_-_1992-2014.pdf

[4] International Energy Agency: Technology Roadmap for Solar Photovoltaic Energy, 2014

[5] Green, M. A., Dunlop, E. D., Hohl-Ebinger, J., Yoshita, M., Kopidakis, N., & Ho-Baillie, A. W. Y. (2020). Solar cell efficiency tables (Version 55). Progress in Photovoltaics: Research and Applications, 28(1), 3–15. https://doi.org/10.1002/pip.3228

[6] Angele Reinders, Photovoltaic Solar Energy: From fundamentals to applications, First Edition, 2017

[7] Green M.A. (1991) Recent Advances in Silicon Solar Cell Performance. In: Luque A., Sala G., Palz W., Dos Santos G., Helm P. (eds) Tenth E.C. Photovoltaic Solar Energy Conference. Springer, Dordrecht

[8] 61851, I. (2006). International Standard International Standard. 61010-1 © Iec: 2001, 2006, 13.

[9] Shockley, W., & Queisser, H. J. (1961). Detailed balance limit of efficiency of p-n junction solar cells. Journal of Applied Physics, 32(3), 510–519. https://doi.org/10.1063/1.1736034

[10] Tiedje, T., Yablonovitch, E., Cody, G. D., & Brooks, B. G. (1984). Limiting Efficiency of Silicon Solar Cells. IEEE Transactions on Electron Devices, 31(5), 711–716. https://doi.org/10.1109/T-ED.1984.21594

[11] Guillemoles, J.-F., Kirchartz, T., Cahen, D., & Rau, U. (2019). Solar Energy Conversion and the Shockley-Queisser Model, a Guide for the Perplexed, (Table 1), 1–16. Retrieved from http://arxiv.org/abs/1903.11954

[12] A. E. Becquerel, Mémoire sur le rayonnement chimique qui accompagne la lumière solaire et la lumière électrique, Paris, 1842

[13] A. E. Becquerel, “Memoire sur les Effects d’Electriques Produits Sous l’Influence des Rayons Solaires,” Comptes Rendus de l’Academie des Sciences, Vol. 9, 1839, pp. 561-567

[14] Chu, E., Tarazano, D. L. (22nd A2019), A brief history of solar panels, URL https://www.smithsonianmag.com/sponsored/brief-history-solar-panels-180972006/, last accessed January 2021.

[15] Ohl, R. S. (1941). Light-sensitive electric device. United States Patent Office 2402662, 1–14.

[16] Kingsbury, E.F. and Ohl, R.S. (1952), Photoelectric Properties of Ionically Bombarded Silicon. Bell System Technical Journal, 31: 802-815. doi:10.1002/j.1538-7305.1952.tb01407.x

[17] Chapin, D. M., Fuller, C. S., & Pearson, G. L. (1954). A new silicon p-n junction photocell for converting solar radiation into electrical power . Journal of Applied Physics, 25(5), 676–677. https://doi.org/10.1063/1.1721711

[18] Mandelkorn, J., McAfee, C., Kesperis, J., Schwartz, L., & Pharo, W. (1962). Fabrication and Characteristics of Phosphorous-Diffused Silicon Solar Cells. Journal of The Electrochemical Society, 109(4), 313. https://doi.org/10.1149/1.2425407

[19] Lindmayer, J., & Allison, J. F. (1990). The violet cell: An improved silicon solar cell. Solar Cells, 29(2–3), 151–166. https://doi.org/10.1016/0379-6787(90)90023-X

[20] Rittner, E. S., & Arndt, R. A. (1976). Comparison of silicon solar cell efficiency for space and terrestrial use. Journal of Applied Physics, 47(7), 2999–3002. https://doi.org/10.1063/1.323042

[21] Green, M. A., Blakers, A. W., Shi, J., Keller, E. M., & Wenham, S. R. (1984). 19.1% Efficient Silicon Solar Cell. Applied Physics Letters, 44(12), 1163–1164. https://doi.org/10.1063/1.94678

[22] Green, M.A. (1986). Improvements in silicon solar cell efficiency. Solar Energy, 17, 75–83.

[23] Blakers, A. W., Wang, A., Milne, A. M., Zhao, J., & Green, M. A. (1989). 22.8% Efficient Silicon Solar Cell. Applied Physics Letters, 55(13), 1363–1365. https://doi.org/10.1063/1.101596

[24] Green, M. A. (1993). Silicon solar cells: Evolution, high-efficiency design and efficiency enhancements. Semiconductor Science and Technology, 8(1), 1–12. https://doi.org/10.1088/0268-1242/8/1/001

[25] Zhao J., Wang A., Green M.A. , 19.8% efficient “honeycomb” textured multicrystalline and 24.4% monocrystalline silicon solar cells, Appl. Phys. Lett. 73, 1991; https://doi.org/10.1063/1.122345

[26] Zhao, J., Wang, A., Altermatt, P. P., Wenham, S. R., & Green, M. A. (1996). 24% Efficient perl silicon solar cell: Recent improvements in high efficiency silicon cell research. Solar Energy Materials and Solar Cells, 41–42, 87–99. https://doi.org/10.1016/0927-0248(95)00117-4

[27] M. Taguchi, Y. Tsunomura, H. Inoue, S. Taira, T. Nakashima, T. Baba, H. Sakata, and E. Maruyama, “High-efficiency HIT solar cell on thin (<100 μm) silicon wafer,” in Proc. 24th Eur. Photovoltaic Sol. Energy Conf., 2009, pp. 1690–1693

[28] Taguchi, M., Yano, A., Tohoda, S., Matsuyama, K., Nakamura, Y., Nishiwaki, T., … Maruyama, E. (2014). 24.7% Record efficiency HIT solar cell on thin silicon wafer. IEEE Journal of Photovoltaics, 4(1), 96–99. https://doi.org/10.1109/JPHOTOV.2013.2282737

[29] Masuko, K., Shigematsu, M., Hashiguchi, T., Fujishima, D., Kai, M., Yoshimura, N., … Okamoto, S. (2014). Achievement of more than 25% conversion efficiency with

crystalline silicon heterojunction solar cell. IEEE Journal of Photovoltaics, 4(6), 1433–1435. https://doi.org/10.1109/JPHOTOV.2014.2352151

[30] Yamamoto, K., Yoshikawa, K., Uzu, H., & Adachi, D. (2018). High-efficiency heterojunction crystalline Si solar cells. Japanese Journal of Applied Physics, 57(8), 0–8. https://doi.org/10.7567/JJAP.57.08RB20

[31] Lammert M., Schwartz R., The Interdigitated Back Contact Solar Cell: A Silicon Solar Cell for Use in Concentrated Sunlight, , IEEE TRANSACTIONS ON ELECTRON DEVICES, VOL. ED-24, NO. 4, APRIL 1977

[32] DeWolf, S., Descoeudres, A., Holman, Z. C., & Ballif, C. (2012). High-efficiency silicon heterojunction solar cells: A review. Green, 2(1), 7–24. https://doi.org/10.1515/green-2011-0018

[33] Niewelt, T., Schon, J., Warta, W., Glunz, S. W., & Schubert, M. C. (2017). Degradation of Crystalline Silicon Due to Boron-Oxygen Defects. IEEE Journal of Photovoltaics, 7(1), 383–398. https://doi.org/10.1109/JPHOTOV.2016.2614119

[34] Jung, E. H., Jeon, N. J., Park, E. Y., Moon, C. S., Shin, T. J., Yang, T. Y., Seo, J. (2019). Efficient, stable and scalable perovskite solar cells using poly(3-hexylthiophene). Nature, 567(7749), 511–515. https://doi.org/10.1038/s41586-019-1036-3

[35] Australian National University, 29 August 2019, ANU researchers set solar record with next-gen cells, URL https://www.anu.edu.au/news/all-news/anu-researchers-set-solar-record-with-next-gen-cells, last accessed January 2021

[36] Oxford PV, 15th June 2018, Perovskite-silicon solar cell research collaboration hits 25.2% efficiency, URL https://www.oxfordpv.com/news/perovskite-silicon-solar-cell-research-collaboration-hits-252-efficiency, last accessed January 2021

[37] Oxford PV, 25th June 2018, Oxford PV sets world record for perovskite solar cell, URL https://www.oxfordpv.com/news/oxford-pv-sets-world-record-perovskite-solar-cell, last accessed January 2021

[38] Oxford PV, 20th December 2018, Oxford PV perovskite solar cell achieves 28% efficiency, URL https://www.oxfordpv.com/news/oxford-pv-perovskite-solar-cell-achieves-28-efficiency, last accessed January 2021

[39] Hoex, B., Schmidt, J., Bock, R., Altermatt, P. P., van de Sanden, M. C. M., & Kessels, W. M. M. (2007). Excellent passivation of highly doped p-type Si surfaces by the negative-charge-dielectric Al2O3. Applied Physics Letters, 91(11), 112107. https://doi.org/10.1063/1.2784168

[40] Liao, B., Hoex, B., Aberle, A. G., Chi, D., & Bhatia, C. S. (2014). Excellent c-Si surface passivation by low-temperature atomic layer deposited titanium oxide. Applied Physics Letters, 104(25), 253903. https://doi.org/10.1063/1.4885096

[41] Young, D. L., Nemeth, W., Grover, S., Norman, A., Yuan, H. C., Lee, B. G., … Stradins, P. (2014). Carrier selective, passivated contacts for high efficiency silicon solar cells based on transparent conducting oxides. Energy Procedia, 55, 733–740. https://doi.org/10.1016/j.egypro.2014.08.053

[42] Hermle, M., Feldmann, F., Bivour, M., Goldschmidt, J. C., & Glunz, S. W. (2020). Passivating contacts and tandem concepts: Approaches for the highest silicon-based

solar cell efficiencies. Applied Physics Reviews, 7(2), 021305. https://doi.org/10.1063/1.5139202

[43] Feldmann, F., Bivour, M., Reichel, C., Hermle, M., & Glunz, S. W. (2014). Passivated rear contacts for high-efficiency n-type Si solar cells providing high interface passivation quality and excellent transport characteristics. Solar Energy Materials and Solar Cells, 120(PART A), 270–274. https://doi.org/10.1016/j.solmat.2013.09.017

[44] Feldmann, F., Simon, M., Bivour, M., Reichel, C., Hermle, M., & Glunz, S. W. (2014). Efficient carrier-selective p- and n-contacts for Si solar cells. Solar Energy Materials and Solar Cells, 131, 100–104. https://doi.org/10.1016/j.solmat.2014.05.039

[45] Veolia Group, 26th March 2019, The first recycling plant in Europe for solar panels!, URL https://www.livingcircular.veolia.com/en/industry/first-recycling-plant-europe-solar-panels, last accessed January 2021

[46] Savin, H., Repo, P., von Gastrow, G., Ortega, P., Calle, E., Garín, M., & Alcubilla, R. (2015). Black silicon solar cells with interdigitated back-contacts achieve 22.1% efficiency. Nature Nanotechnology, 10(7), 624–628. https://doi.org/10.1038/nnano.2015.89

[47] Toor, F., Davidson, L. M., Duan, W., Jura, M. P., Yim, J., Forziati, J., & Black, M. R. (2016). Metal assisted catalyzed etched (MACE) black Si: optics and device physics, 15448–15466. https://doi.org/10.1039/c6nr04506e

[48] G. P. Smestad, "The Basic Economics of Photovoltaics," in Solar Energy: New Materials and Nanostructured Devices for High Efficiency, (Optical Society of America, 2008), paper STuC8.

[49] Venkatesan, R., Arivalagan, M. K., Venkatachalapathy, V., Pearce, J. M., & Mayandi, J. (2018). Effects of silver catalyst concentration in metal assisted chemical etching of silicon. Materials Letters, 221, 206–210. https://doi.org/10.1016/j.matlet.2018.03.053

[50] Harris B., Method for recovering nitric acid and purifying silver nitrate electrolyte, US patent 8282903, 2012

[51] Basu P. K., Theory of optical processes in semiconductors bulk and microstructures, Oxford Science Publication, 1997

[52] Burrell G.J., Ellis B., Semiconductor Opto-Electronics, London Butterworths, 1973

[53] Green M. A., High efficiency silicon solar cells, Trans Tech Publications, 1987

[54] Jenny Nelson, The physics of solar cell, Imperial College Press, 2003

[55] Rajkanan K., Singh R., Shewchun J. (1979), Absorption coefficient of silicon for solar cell calculations. Solid state electronics, vol. 22, pp 793-795

[56] Lambert, J. H., Photometria, sive de Mensura et Gradibus Luminis, Colorum et Umbrae, Augsburg, 1760

[57] Green, M. A. (2008). Self-consistent optical parameters of intrinsic silicon at 300 K including temperature coefficients. Solar Energy Materials and Solar Cells, 92(11), 1305–1310. https://doi.org/10.1016/j.solmat.2008.06.009

[58] Alan Billings, Optics, Optoelectronics and Photonics: Engineering Principles and Applications, Prentice Hall, 1993

[59] Boltzmann, L. (1884), Ableitung des Stefan'schen Gesetzes, betreffend die Abhängigkeit der Wärmestrahlung von der Temperatur aus der electromagnetischen Lichttheorie. Ann. Phys., 258: 291-294. doi:10.1002/andp.18842580616

[60] National Renewable Energy Laboratory, URL https://www.nrel.gov/grid/solar-resource/spectra-am1.5.html, last accessed January 2021

[61] Duttagupta, S., Ma, F., Hoex, B., Mueller, T., & Aberle, A. G. (2012). Optimised antireflection coatings using silicon nitride on textured silicon surfaces based on measurements and multidimensional modelling. Energy Procedia, 15(2011), 78–83. https://doi.org/10.1016/j.egypro.2012.02.009

[62] Nagel, H., Aberle, A., Hezel, R., (1999). Coatings for Planar Silicon Solar Cells using Remote. *Solar Cells*, *260*(November 1998), 245–260.

[63] Boden S. A. (2009), Biomimetic nanostructured surfaces for antireflection in photovoltaics, University of Southampton, PhD Thesis

[64] Zhao, J., & Green, M. A. (1991). Optimized Antireflection Coatings for High-Efficiency Silicon Solar Cells. IEEE Transactions on Electron Devices, 38(8), 1925–1934. https://doi.org/10.1109/16.119035

[65] Palik E., Handbook of Optical Constant of Solids, Volume 2, 1991

[66] Kumar, P., Wiedmann, M. K., Winter, C. H., & Avrutsky, I. (2009). Optical properties of Al2O3 thin films grown by atomic layer deposition. Applied Optics, 48(28), 5407–5412. https://doi.org/10.1364/AO.48.005407

[67] Kim, Y., Lee, S. M., Park, C. S., Lee, S. I., & Lee, M. Y. (1997). Substrate dependence on the optical properties of Al2O3 films grown by atomic layer deposition. Applied Physics Letters, 71(25), 3604–3606. https://doi.org/10.1063/1.120454

[68] Redfield, D. (1974). Multiple-pass thin-film silicon solar cell. Applied Physics Letters, 25(11), 647–648. https://doi.org/10.1063/1.1655344

[69] Goetzberger A. Optical confinement in thin Si solar cells by diffuse back reflectors. Proceedings of the 15th IEEE Photovoltaic Specialists Conference, Orlando, 1981: 867–870.

[70] King DL, Buck ME, Experimental optimization of anisotropic etching process for random texturization of silicon solar cells, 22nd IEEE Photovoltaics Specialist Conference, vol. 1, 1991, p. 303-308

[71] Merlos, A., Acero, M., Bao, M. H., Bausells, J., & Esteve, J. (1993). TMAH/IPA anisotropic etching characteristics. Sensors and Actuators: A. Physical, 37–38(C), 737–743. https://doi.org/10.1016/0924-4247(93)80125-Z

[72] PVLighthouse, OPAL 2 version 2.0.0, 1st June 2012, URL https://www2.pvlighthouse.com.au/calculators/OPAL%202/OPAL%202.aspx, last accessed January 2021

[73] Baker-finch, S. C., & Mcintosh, K. R. (2011). Reflection of normally incident light from silicon solar cells with pyramidal texture, (October 2010), 406–416. https://doi.org/10.1002/pip

[74] Manzoor, S., Filipič, M., Topič, M., & Holman, Z. (2016). Revisiting Light Trapping in Silicon Solar Cells with Random Pyramids, 2952–2954. https://doi.org/10.1109/PVSC.2016.7750201

[75] Campbell, P., & Green, M. A. (1987). Light trapping properties of pyramidally textured surfaces. Journal of Applied Physics, 62(1), 243–249. https://doi.org/10.1063/1.339189

[76] Campbell, P. R., & Green, M. A. (1986). On Intensity Enhancement in Textured Optical Sheets for Solar Cells IEEE Transactions on Electron Devices, 33(11), 1834–1835. https://doi.org/10.1109/T-ED.1986.22753

[77] Smith, A. W., & Rohatgi, A. (1993). Ray tracing analysis of the inverted pyramid texturing geometry for high efficiency silicon solar cells. Solar Energy Materials and Solar Cells, 29(1), 37–49. https://doi.org/10.1016/0927-0248(93)90090-P

[78] Schultz O., Emanuel G., Glunz S.W., Willeke G. P. (2003), Texturing of multicrystalline silicon with acidic wet chemical etching and plasma etching, 3rd World Conference on Photovoltaic Energy Conversion, Osaka, Japan.

[79] Baker-Finch, S. C., McIntosh, K. R., & Terry, M. L. (2012). Isotextured silicon solar cell analysis and modeling 1: Optics. IEEE Journal of Photovoltaics, 2(4), 457–464. https://doi.org/10.1109/JPHOTOV.2012.2206569

[80] Li Y, Li Z, Zhao Y, Lennon A. Modelling of light trapping in acidic-textured multicrystalline silicon wafers. International Journal of Photoenergy 2012; 369101.

[81] McIntosh, K. R., Abbott, M. D., & Sudbury, B. A. (2016). Ray Tracing Isotextured Solar Cells. *Energy Procedia*, *92*, 122–129. https://doi.org/10.1016/j.egypro.2016.07.041

[82] Bernhard, C. G. & Miller, W. H. 1962 A corneal nipple pattern in insect compound eyes. Acta Physiol. Scand. 56, 385–386.

[83] Bernhard, C. G., Miller, W. H. & Møller, A. R. 1965 The insect corneal nipple array. Acta Physiol. Scand. 63(Suppl. 243), 1-25.

[84] Wilson, S. J., & Hutley, M. C. (1982). The Optical Properties of "Moth Eye" Antireflection Surfaces. Optica Acta: International Journal of Optics, 29(7), 993–1009. https://doi.org/10.1080/713820946

[85] Stavenga, D. ., Foletti, S., Palasantzas, G., & Arikawa, K. (2006). Light on the moth-eye corneal nipple array of butterflies. Proceedings of the Royal Society B: Biological Sciences, 273(1587), 661–667. https://doi.org/10.1098/rspb.2005.3369

[86] Boden, S. A., & Bagnall, D. M. (2008). Tunable reflection minima of nanostructured antireflective surfaces. Applied Physics Letters, 93(13), 2008–2010. https://doi.org/10.1063/1.2993231

[87] Sun, C. H., Jiang, P., & Jiang, B. (2008). Broadband moth-eye antireflection coatings on silicon. Applied Physics Letters, 92(6). https://doi.org/10.1063/1.2870080

[88] Boden, S. A., & Bagnall, D. M. (2009). Nanostructured biomimetic moth-eye arrays in silicon by nanoimprint lithography. Biomimetics and Bioinspiration, 7401, 74010J. https://doi.org/10.1117/12.826201

[89] Asadollahbaik, A., Boden, S. A., Charlton, M. D. B., Payne, D. N. R., Cox, S., & Bagnall, D. M. (2014). Reflectance properties of silicon moth-eyes in response to variations in angle of incidence, polarisation and azimuth orientation. Optics Express, 22(S2), A402. https://doi.org/10.1364/oe.22.00a402

[90] Sivasubramaniam, S., & Alkaisi, M. M. (2014). Inverted nanopyramid texturing for silicon solar cells using interference lithography. Microelectronic Engineering, 119, 146–150. https://doi.org/10.1016/j.mee.2014.04.004

[91] Tang, Q., Shen, H., Yao, H., Gao, K., Jiang, Y., Zheng, C., … Zhang, L. (2017). Solar Energy Materials and Solar Cells Potential of quasi-inverted pyramid with both e ffi cient light trapping and su ffi cient wettability for ultrathin c -Si / PEDOT : PSS hybrid solar cells. Solar Energy Materials and Solar Cells, 169(November 2016), 226–235. https://doi.org/10.1016/j.solmat.2017.05.025

[92] Tang, Q., Shen, H., Yao, H., Jiang, Y., Li, Y., Zhang, L., & Ni, Z. (2018). Applied Surface Science Formation mechanism of inverted pyramid from sub-micro to micro scale on c -Si surface by metal assisted chemical etching temperature. Applied Surface Science, 455, 283–294. https://doi.org/10.1016/j.apsusc.2018.05.023

[93] Zhang, C., Chen, L., Zhu, Y., & Guan, Z. (2018). Fabrication of 20.19% Efficient Single-Crystalline Silicon Solar Cell with Inverted Pyramid Microstructure. Nanoscale Research Letters, 13, 4–11. https://doi.org/10.1186/s11671-018-2502-9

[94] Shen, W. Z., Gao, K., Wang, X. G., Xu, C., Song, X. M., Shi, L. X., Hoex, B. (2019). Large-area MACE Si nano-inverted-pyramids for PERC solar cell application, 188(June), 300–304. https://doi.org/10.1016/j.solener.2019.06.015

[95] Szczech, J. R., & Jin, S., Nanostructured Silicon for High Capacity Lithium Battery Anodes, Energy Environ. Sci., 2011, 4, 56

[96] Kim, H., Seo, M., Park, M. H., & Cho, J. (2010). A critical size of silicon nano-anodes for lithium rechargeable batteries. Angewandte Chemie - International Edition, 49(12), 2146–2149. https://doi.org/10.1002/anie.200906287

[97] Jansen, H. V. (2012). Guidelines for etching silicon MEMS structures using fluorine high-density plasmas at cryogenic Guidelines for Etching Silicon MEMS Structures Using Fluorine High-Density Plasmas at Cryogenic Temperatures, 11(December), 385–401. https://doi.org/10.1109/JMEMS.2002.800928

[98] Lilienthal, K., Fischer, M., Stubenrauch, M., & Schober, A. (2010). Self-organized nanostructures in silicon and glass for MEMS, MOEMS and BioMEMS. Materials Science and Engineering B: Solid-State Materials for Advanced Technology, 169(1–3), 78–84. https://doi.org/10.1016/j.mseb.2009.11.020

[99] Zheng, G., Gao, X. P. A., & Lieber, C. M. (2010). Frequency domain detection of biomolecules using silicon nanowire biosensors. Nano Letters, 10(8), 3179–3183. https://doi.org/10.1021/nl1020975

[100] Huang, Z., Carey, J. E., Liu, M., Guo, X., Mazur, E., & Campbell, J. C. (2006). Microstructured silicon photodetector. Applied Physics Letters, 89(3), 14–17. https://doi.org/10.1063/1.2227629

[101] Huang, S., Wu, Q., Jia, Z., Jin, X., Fu, X., Huang, H., … Xu, J. (2020). Black Silicon Photodetector with Excellent Comprehensive Properties by Rapid Thermal Annealing and Hydrogenated Surface Passivation. Advanced Optical Materials, 8(7), 1–7. https://doi.org/10.1002/adom.201901808

[102] Pasanen, T. P., Laine, H. S., Vähänissi, V., Schön, J., & Savin, H. (2049). Black silicon significantly enhances phosphorus diffusion gettering. Scientific Reports, 8, 1–6. https://doi.org/10.1038/s41598-018-20494-y

[103] Huang, Z., Geyer, N., Werner, P., De Boor, J., & Gösele, U. (2011). Metal-assisted chemical etching of silicon: A review. Advanced Materials, 23(2), 285–308. https://doi.org/10.1002/adma.201001784

[104] Bruggeman, D.A.G. (1935), Berechnung verschiedener physikalischer Konstanten von heterogenen Substanzen. I. Dielektrizitätskonstanten und Leitfähigkeiten der Mischkörper aus isotropen Substanzen. Ann. Phys., 416: 636-664. doi:10.1002/andp.19354160705

[105] Rahman, T., & Boden, S. (2017). Optical Modeling of Black Silicon for Solar Cells Using Effective Index Techniques. IEEE Journal of Photovoltaics, 7(6), 1556–1562. https://doi.org/10.1109/JPHOTOV.2017.2748900

[106] Patchett, S., Khorasaninejad, M., Nixon, O., & Saini, S. S. (2013). Effective index approximation for ordered silicon nanowire arrays. Journal of the Optical Society of America B-Optical Physics, 30(2), 306–313. https://doi.org/10.1364/JOSAB.30.000306

[107] Fung, T. H., Khan, M. U., Zhang, Y., Western, N. J., Payne, D. N. R., Mclntosh, K. R., & Abbott, M. D. (2019). Improved Ray Tracing on Random Pyramid Texture via Application of Phong Scattering. IEEE Journal of Photovoltaics, 9(3), 591–600. https://doi.org/10.1109/JPHOTOV.2019.2894688

[108] Garnett, E., & Yang, P. (2010). Light trapping in silicon nanowire solar cells. Nano Letters, 10(3), 1082–1087. https://doi.org/10.1021/nl100161z

[109] Yablonovitch, E. (1982). Statistical ray optics. Journal of the Optical Society of America, 72(7), 899. https://doi.org/10.1364/JOSA.72.000899

[110] Dennis R. Turner 1958, Electropolishing Silicon in Hydrofluoric Acid Solutions, J. Electrochem. Soc. 105 402

[111] Lehmann, V. (2002). Electrochemistry of Silicon (Vol. 3).

[112] Lehmann, V. (1993). The Physics of Macropore Formation in Low Doped n-Type Silicon. Journal of The Electrochemical Society, 140(10), 2836. https://doi.org/10.1149/1.2220919

[113] Striemer, C. C., & Fauchet, P. M. (2002). Dynamic etching of silicon for broadband antireflection applications. Applied Physics Letters, 81(16), 2980–2982. https://doi.org/10.1063/1.1514832

[114] Ariza-Flores, D., Pérez-Huerta, J. S., Kumar, Y., Encinas, A., & Agarwal, V. (2014). Design and optimization of antireflecting coatings from nanostructured porous silicon dielectric multilayers. Solar Energy Materials and Solar Cells, 123, 144–149. https://doi.org/10.1016/j.solmat.2014.01.019

[115] Osorio, E., Urteaga, R., Acquaroli, L. N., García-Salgado, G., Juaréz, H., & Koropecki, R. R. (2011). Optimization of porous silicon multilayer as antireflection coatings for solar cells. Solar Energy Materials and Solar Cells, 95(11), 3069–3073. https://doi.org/10.1016/j.solmat.2011.06.036

[116] R.J. Archer, *Stain films on silicon,* Journal of Physics and Chemistry of Solids, Volume 14, 1960, Pages 104-110

[117] Turner D.R., On the mechanism of chemically etching germanium and silicon, Journal of the electrochemical society, vol. 107, 10, 1060, p. 810-816

[118] Watanabe, Y. (1975). Formation and Properties of Porous Silicon and Its Application. Journal of The Electrochemical Society, 122(10), 1351. https://doi.org/10.1149/1.2134015

[119] Tsuo, Y. S., Xiao, Y., Heben, M. J., Wu, X., Pern, F. J., & Deb, S. K. (1993). Potential applications of porous silicon in photovoltaics. Conference Record of the IEEE Photovoltaic Specialists Conference, (4), 287–293. https://doi.org/10.1109/pvsc.1993.347169

[120] Menna, P., Di Francia, G., & La Ferrara, V. (1995). Porous silicon in solar cells: A review and a description of its application as an AR coating. Solar Energy Materials and Solar Cells, 37(1), 13–24. https://doi.org/10.1016/0927-0248(94)00193-6

[121] Schirone, L., Sotgiu, G., Rallo, F., & Califano, F. P. (1996). Porous-silicon coatings for photovoltaic devices. Nuovo Cimento Della Societa Italiana Di Fisica D - Condensed Matter, Atomic, Molecular and Chemical Physics, Biophysics, 18(10), 1225–1232. https://doi.org/10.1007/BF02464700

[122] Lipiński, M., Bastide, S., Panek, P., & Lévy-Clément, C. (2003). Porous silicon antireflection coating by electrochemical and chemical etching for silicon solar cell manufacturing. Physica Status Solidi (A) Applied Research, 197(2), 512–517. https://doi.org/10.1002/pssa.200306555

[123] Her, T. H., Finlay, R. J., Wu, C., Deliwala, S., & Mazur, E. (1998). Microstructuring of silicon with femtosecond laser pulses. Applied Physics Letters, 73(12), 1673–1675. https://doi.org/10.1063/1.122241

[124] Her, T. H., Finlay, R. J., Wu, C., & Mazur, E. (2000). Femtosecond laser-induced formation of spikes on silicon. Applied Physics A: Materials Science and Processing, 70(4), 383–385. https://doi.org/10.1007/s003390051052

[125] Wu, C., Crouch, C. H., Zhao, L., Carey, J. E., Younkin, R., Levinson, J. A., … Karger, A. (2001). Near-unity below-band-gap absorption by microstructured silicon. Applied Physics Letters, 78(13), 1850–1852. https://doi.org/10.1063/1.1358846

[126] Crouch, C. H., Carey, J. E., Warrender, J. M., Aziz, M. J., Mazur, E., & Génin, F. Y. (2004). Comparison of structure and properties of femtosecond and nanosecond laser-structured silicon. Applied Physics Letters, 84(11), 1850–1852. https://doi.org/10.1063/1.1667004

[127] Skantzakis, E., Zorba, V., Papazoglou, D. G., Zergioti, I., & Fotakis, C. (2006). Ultraviolet laser microstructuring of silicon and the effect of laser pulse duration on the surface morphology. Applied Surface Science, 252(13 SPEC. ISS.), 4462–4466. https://doi.org/10.1016/j.apsusc.2005.07.120

[128] Sullivan, J. T., Simmons, C. B., Krich, J. J., Akey, A. J., Recht, D., Aziz, M. J., & Buonassisi, T. (2013). Methodology for vetting heavily doped semiconductors for intermediate band photovoltaics: A case study in sulfur-hyperdoped silicon. Journal of Applied Physics, 114(10). https://doi.org/10.1063/1.4820454

[129] Jansen, H., Boer, M. de, Legtenberg, R., & Elwenspoek, M. (1995). The black silicon method: a universal method for determining the parameter setting of a fluorine-based

reactive ion etcher in deep silicon trench etching with profile control. Journal of Micromechanics and Microengineering, 5(2), 115. https://doi.org/10.1088/0960-1317/5/2/015

[130] Xia, Y., Liu, B., Liu, J., Shen, Z., & Li, C. (2011). A novel method to produce black silicon for solar cells. Solar Energy, 85(7), 1574–1578. https://doi.org/10.1016/j.solener.2011.03.012

[131] Xia, Y., Liu, B., Zhong, S., & Li, C. (2012). X-ray photoelectron spectroscopic studies of black silicon for solar cell. Journal of Electron Spectroscopy and Related Phenomena, 184(11–12), 589–592. https://doi.org/10.1016/j.elspec.2011.10.004

[132] Otto, M., Kroll, M., Käsebier, T., Ziegler, J., Sprafke, A. N., & Wehrspohn, R. B. (2013). Passivation of optically black silicon by atomic layer deposited Al 2O3. Energy Procedia, 38, 862–865. https://doi.org/10.1016/j.egypro.2013.07.357

[133] Allen, T., Bullock, J., Cuevas, A., Baker-Finch, S., & Karouta, F. (2014). Reactive ion etched black silicon texturing: A comparative study. 2014 IEEE 40th Photovoltaic Specialist Conference, PVSC 2014, 562–566. https://doi.org/10.1109/PVSC.2014.6924983

[134] Iandolo, B., Davidsen, R. S., & Hansen, O. (2018). Avoiding blistering in Al2O3deposited on planar and black Si. Solar Energy Materials and Solar Cells, 187(July), 23–29. https://doi.org/10.1016/j.solmat.2018.07.014

[135] Li, X. (2012). Metal assisted chemical etching for high aspect ratio nanostructures: A review of characteristics and applications in photovoltaics. Current Opinion in Solid State and Materials Science, 16(2), 71–81. https://doi.org/10.1016/j.cossms.2011.11.002

[136] Dimova-Malinovska, D., Sendova-Vassileva, M., Tzenov, N., & Kamenova, M. (1997). Preparation of thin porous silicon layers by stain etching. Thin Solid Films, 297(1–2), 9–12. https://doi.org/10.1016/S0040-6090(96)09434-5

[137] Li, X., & Bohn, W. (2000). Metal-assisted chemical etching in HF/H2O2 produces porous silicon. Applied Physics Letters, 77(16), 2572.

[138] Huang, Z., Zhang, X., Reiche, M., Ltu, L., Lee, W., Shimizu, T., Gösele, U. (2008). Extended arrays of vertically aligned Sub-10 nm diameter [100] Si nanowires by metal-assisted chemical etching. Nano Letters, 8(9), 3046–3051. https://doi.org/10.1021/nl802324y

[139] Huang, Z., Shimizu, T., Senz, S., Zhang, Z., Zhang, X., Lee, W., Gösele, U. (2009). Ordered arrays of vertically aligned [110] silicon nanowires by suppressing the crystallographically preferred <100> etching directions. Nano Letters, 9(7), 2519–2525. https://doi.org/10.1021/nl803558n

[140] Fang, H., Wu, Y., Zhao, J., & Zhu, J. (2006). Silver catalysis in the fabrication of silicon nanowire arrays. Nanotechnology, 17(15), 3768–3774. https://doi.org/10.1088/0957-4484/17/15/026

[141] Huang, Z., Fang, H., & Zhu, J. (2007). Fabrication of silicon nanowire arrays with controlled diameter, length, and density. Advanced Materials, 19(5), 744–748. https://doi.org/10.1002/adma.200600892

[142] Peng, K., Lu, A., Zhang, R., & Lee, S. T. (2008). Motility of metal nanoparticles in silicon and induced anisotropic silicon etching. Advanced Functional Materials, 18(19), 3026–3035. https://doi.org/10.1002/adfm.200800371

[143] Peng, K., Fang, H., Hu, J., Wu, Y., Zhu, J., Yan, Y., & Lee, S. T. (2006). Metal-particle-induced, highly localized site-specific etching of Si and formation of single-crystalline Si nanowires in aqueous fluoride solution. Chemistry - A European Journal, 12(30), 7942–7947. https://doi.org/10.1002/chem.200600032

[144] Zoski C. G., Handbook of Electrochemistry, Elsevier, First Edition, 2007.

[145] Srivastava, S. K., Kumar, D., Schmitt, S. W., Sood, K. N., Christiansen, S. H., & Singh, P. K. (2014). Large area fabrication of vertical silicon nanowire arrays by silver-assisted single-step chemical etching and their formation kinetics. Nanotechnology, 25(17), 175601. https://doi.org/10.1088/0957-4484/25/17/175601

[146] Kheyraddini Mousavi, B., Behzadirad, M., Silani, Y., Karbasian, F., Kheyraddini Mousavi, A., & Mohajerzadeh, S. (2019). Metal-assisted chemical etching of silicon and achieving pore sizes as small as 30 nm by altering gold thickness. Journal of Vacuum Science & Technology A, 37(6), 061402. https://doi.org/10.1116/1.5112776

[147] Kurek, A., & Barry, S. T. (2011). Metal-assisted chemical etching using sputtered gold: A simple route to black silicon. Science and Technology of Advanced Materials, 12(4), 6–10. https://doi.org/10.1088/1468-6996/12/4/045001

[148] Kuo, K.-H., Ku, W.-H., & Lee, B. T.-H. (2020). Photoluminescent or Blackened Silicon Surfaces Synthesized with Copper-assisted Chemical Etching: For Energy Applications. ECS Journal of Solid State Science and Technology, 9(2), 024006. https://doi.org/10.1149/2162-8777/ab682f

[149] Omer, A. A. A., Yang, Y., Sheng, G., Li, S., Yu, J., Ma, W., … Kolaly, W. El. (2020). Nano-Texturing of Silicon Wafers Via One-Step Copper-Assisted Chemical Etching. Silicon, 12(1), 231–238. https://doi.org/10.1007/s12633-019-00117-5

[150] Tsujino, K., & Matsumura, M. (2005). Boring deep cylindrical nanoholes in silicon using silver nanoparticles as a catalyst. Advanced Materials, 17(8), 1045–1047. https://doi.org/10.1002/adma.200401681

[151] Tsujino, K., & Matsumura, M. (2007). Morphology of nanoholes formed in silicon by wet etching in solutions containing HF and H2O2 at different concentrations using silver nanoparticles as catalysts. Electrochimica Acta, 53(1), 28–34. https://doi.org/10.1016/j.electacta.2007.01.035

[152] Yae, S., Tashiro, M., Abe, M., Fukumuro, N., & Matsuda, H. (2010). High Catalytic Activity of Palladium for Metal-Enhanced HF Etching of Silicon. Journal of The Electrochemical Society, 157(2), D90. https://doi.org/10.1149/1.3264643

[153] Yae, S., Tanaka, H., Kobayashi, T., Fukumuro, N., & Matsuda, H. (2005). Porous silicon formation by HF chemical etching for antireflection of solar cells. Physica Status Solidi C: Conferences, 2(9), 3476–3480. https://doi.org/10.1002/pssc.200461225

[154] Yae, S., Nasu, N., Matsumoto, K., Hagihara, T., Fukumuro, N., & Matsuda, H. (2007). Nucleation behavior in electroless displacement deposition of metals on silicon from hydrofluoric acid solutions. Electrochimica Acta, 53(1), 35–41. https://doi.org/10.1016/j.electacta.2007.04.058

[155] Peng, K., & Zhu, J. (2004). Morphological selection of electroless metal deposits on silicon in aqueous fluoride solution. Electrochimica Acta, 49(16), 2563–2568. https://doi.org/10.1016/j.electacta.2004.02.009

[156] Peng, K., Yan, Y., Gao, S., & Zhu, J. (2003). Dendrite-assisted growth of silicon nanowires in electroless metal deposition. Advanced Functional Materials, 13(2), 127–132. https://doi.org/10.1002/adfm.200390018

[157] Helmholtz H., "Ueber einige Gesetze der Vertheilung elektrischer Ströme in körperlichen Leitern mit Anwendung auf die thierisch-elektrischen Versuche", Annalen der Physik und Chemie, 165 (6), p. 211-233.

[158] Gellings P. J., Bouwmeester H. J. M., The CRC Handbook of Solid State Electrochemistry, CRC Press, 1997

[159] Lai, R. A., Hymel, T. M., Narasimhan, V. K., & Cui, Y. (2016). Schottky Barrier Catalysis Mechanism in Metal-Assisted Chemical Etching of Silicon. ACS Applied Materials and Interfaces, 8(14), 8875–8879. https://doi.org/10.1021/acsami.6b01020

[160] Lee, C.-L., Tsujino, K., Kanda, Y., Ikeda, S., & Matsumura, M. (2008). Pore formation in silicon by wet etching using micrometre-sized metal particles as catalysts. Journal of Materials Chemistry, 18(9), 1015. https://doi.org/10.1039/b715639a

[161] Cheng, S. L., Chung, C. H., & Lee, H. C. (2008). A Study of the Synthesis, Characterization, and Kinetics of Vertical Silicon Nanowire Arrays on (001)Si Substrates. Journal of The Electrochemical Society, 155(001), D711. https://doi.org/10.1149/1.2977548

[162] Ozdemir, B., Kulakci, M., Turan, R., & Unalan, H. E. (2011). Effect of electroless etching parameters on the growth and reflection properties of silicon nanowires. Nanotechnology, 22(15). https://doi.org/10.1088/0957-4484/22/15/155606

[163] Nassiopoulou, A., Gianneta, V., & Katsogridakis, C. (2011). Si nanowires by a single-step metal-assisted chemical etching process on lithographically defined areas: formation kinetics. Nanoscale Research Letters, 6(1), 597. https://doi.org/10.1186/1556-276X-6-597

[164] Han, H., Huang, Z., & Lee, W. (2014). Metal-assisted chemical etching of silicon and nanotechnology applications. Nano Today, 9(3), 271–304. https://doi.org/10.1016/j.nantod.2014.04.013

[165] Kato, Y., & Adachi, S. (2011). Synthesis of Si Nanowire Arrays in AgO/HF Solution and Their Optical and Wettability Properties. Journal of The Electrochemical Society, 158(7), K157. https://doi.org/10.1149/1.3583598

[166] Bonilla, R. S., Hoex, B., Hamer, P., & Wilshaw, P. R. (2017). Dielectric surface passivation for silicon solar cells: A review. Physica Status Solidi (A), 214(7), 1700293. https://doi.org/10.1002/pssa.201700293

[167] Luke, K. L., & Cheng, L. J. (1987). Analysis of the interaction of a laser pulse with a silicon wafer: Determination of bulk lifetime and surface recombination velocity. Journal of Applied Physics, 61(6), 2282–2293. https://doi.org/10.1063/1.337938

[168] Kerr, M. J., & Cuevas, A. (2002). General parameterization of Auger recombination in crystalline silicon. Journal of Applied Physics, 91(3), 2473–2480. https://doi.org/10.1063/1.1432476

[169] McIntosh, K. R., & Johnson, L. P. (2009). Recombination at textured silicon surfaces passivated with silicon dioxide. Journal of Applied Physics, 105(12). https://doi.org/10.1063/1.3153979

[170] Aberle, A. G., Glunz, S., & Warta, W. (1992). Impact of illumination level and oxide parameters on Shockley-Read-Hall recombination at the Si-SiO2interface. Journal of Applied Physics, 71(9), 4422–4431. https://doi.org/10.1063/1.350782

[171] Balk, P., & Klein, N. (1982). Generation of interface states in MOS systems. Thin Solid Films. https://doi.org/10.1016/0040-6090(82)90305-4

[172] Kerr, M. J., & Cuevas, A. (2002). Very low bulk and surface recombination in oxidized silicon wafers. Semiconductor Science and Technology, 17(1), 35–38. https://doi.org/10.1088/0268-1242/17/1/306

[173] Collett K. A., Bonilla R. S., Hamer P., Bourret-Sicotte G., Lobo R., Kho T., Wilshaw P. R., An enhanced alneal process to produce SRV<1 cm/s in 1 Ωcm n-type Si, Solar Energy Materials and Solar Cells 173 (2017), 50-58.

[174] Nishi, Y. (1971). Study of silicon-silicon dioxide structure by electron spin resonance I. Japanese Journal of Applied Physics, 10(1), 52–62. https://doi.org/10.1143/JJAP.10.52

[175] Helms, C. R., & Poindexter, E. H. (1994). The silicon-silicon dioxide system: Its microstructure and imperfections. Reports on Progress in Physics, 57(8), 791–852. https://doi.org/10.1088/0034-4885/57/8/002

[176] Nickel, N. H. (2000). Hydrogen diffusion through silicon/silicon dioxide interfaces. Journal of Vacuum Science and Technology B: Microelectronics and Nanometer Structures, 18(3), 1770–1772. https://doi.org/10.1116/1.591469

[177] Ho, P., & Melius, C. F. (1995). Theoretical study of the thermochemistry of molecules in the Si-O-H-C system. Journal of Physical Chemistry, 99(7), 2166–2176. https://doi.org/10.1021/j100007a056

[178] Bonilla, R. S., Jennison, N., Clayton-Warwick, D., Collett, K. A., Rands, L., & Wilshaw, P. R. (2016). Corona Charge in SiO2: Kinetics and Surface Passivation for High Efficiency Silicon Solar Cells. Energy Procedia, 92, 326–335. https://doi.org/10.1016/j.egypro.2016.07.090

[179] Bourret-Sicotte, G., Hamer, P., Bonilla, R. S., Collett, K., & Wilshaw, P. R. (2017). Shielded hydrogen passivation - A novel method for introducing hydrogen into silicon. Energy Procedia, 124, 267–274. https://doi.org/10.1016/j.egypro.2017.09.298

[180] Grant, N. E., & McIntosh, K. R. (2009). Surface Passivation Attained by Silicon Dioxide Grown at Low Temperature in Nitric Acid. 24th European Photovoltaic Solar Energy Conference, 30(9), 1676–1679. https://doi.org/10.1109/LED.2009.2025898

[181] Duttagupta, S. (2014). Advanced Surface Passivation of Crystalline Silicon for Solar Cell Applications. PhD Thesis. https://doi.org/10.1063/1.4749572

[182] Duttagupta, S., Lin, F., Wilson, M., Boreland, M.B., Hoex, B. and Aberle, A.G. (2014), Extremely low surface recombination velocities on low-resistivity n-type and p-type crystalline silicon using dynamically deposited remote plasma silicon nitride films. Prog. Photovolt: Res. Appl., 22: 641-647. doi:10.1002/pip.2320

[183] Sharma, V., Tracy, C., Schroder, D., Herasimenka, S., Dauksher, W., & Bowden, S. (2014). Manipulation of K center charge states in silicon nitride films to achieve excellent

surface passivation for silicon solar cells. Applied Physics Letters, 104(5). https://doi.org/10.1063/1.4863829

[184] Chen, F., Li, T., & Cotter, J. (2006). PECVD Silicon Nitride Surface Passivation for High-Efficiency N-Type Silicon Solar Cells. IEEE 4th World Conference on Photovoltaic Energy Conversion, 1020–1023. https://doi.org/10.1109/WCPEC.2006.279292

[185] Richter, A., Glunz, S. W., Werner, F., Schmidt, J., & Cuevas, A. (2012). Improved quantitative description of Auger recombination in crystalline silicon. Physical Review B - Condensed Matter and Materials Physics, 86(16), 1–14. https://doi.org/10.1103/PhysRevB.86.165202

[186] Bonilla, R. S., Woodcock, F., & Wilshaw, P. R. (2014). Very low surface recombination velocity in n-type c-Si using extrinsic field effect passivation. Journal of Applied Physics, 116(5). https://doi.org/10.1063/1.4892099

[187] Bonilla, R. S., Reichel, C., Hermle, M., & Wilshaw, P. R. (2014). On the location and stability of charge in SiO2/SiNx dielectric double layers used for silicon surface passivation. Journal of Applied Physics, 115(14). https://doi.org/10.1063/1.4871075

[188] Dingemans, G., Mandoc, M. M., Bordihn, S., Van De Sanden, M. C. M., & Kessels, W. M. M. (2011). Effective passivation of Si surfaces by plasma deposited SiOx/a-SiNx:H stacks. Applied Physics Letters, 98(22), 3–6. https://doi.org/10.1063/1.3595940

[189] Dingemans, G., Seguin, R., Engelhart, P., Sanden, M. C. M. van de, & Kessels, W. M. M. (2010). Silicon surface passivation by ultrathin Al_2O_3 films synthesized by thermal and plasma atomic layer deposition. Physica Status Solidi (RRL) - Rapid Research Letters, 4(1–2), 10–12. https://doi.org/10.1002/pssr.200903334

[190] Hoex, B., Heil, S. B. S., Langereis, E., Van De Banden, M. C. M., & Kessels, W. M. M. (2006). Ultralow surface recombination of c-Si substrates passivated by plasma-assisted atomic layer deposited Al2O3. Applied Physics Letters, 89(4), 2–5. https://doi.org/10.1063/1.2240736

[191] Hoex, B., Gielis, J. J. H., Van De Sanden, M. C. M., & Kessels, W. M. M. (2008). On the c-Si surface passivation mechanism by the negative-charge-dielectric Al2 O3. Journal of Applied Physics, 104(11). https://doi.org/10.1063/1.3021091

[192] Richter, A., Benick, J., Hermle, M., & Glunz, S. W. (2014). Reaction kinetics during the thermal activation of the silicon surface passivation with atomic layer deposited Al2O3. Applied Physics Letters, 104(6). https://doi.org/10.1063/1.4865901

[193] Dingemans, G., Terlinden, N. M., Pierreux, D., Profijt, H. B., van de Sanden, M. C. M., & Kessels, W. M. M. (2011). Influence of the Oxidant on the Chemical and Field-Effect Passivation of Si by ALD Al[sub 2]O[sub 3]. Electrochemical and Solid-State Letters, 14(1), H1. https://doi.org/10.1149/1.3501970

[194] Dingemans, G., Einsele, F., Beyer, W., van de Sanden, M. C. M., & Kessels, W. M. M. (2012). Influence of annealing and Al_2O_3 properties on the hydrogen-induced passivation of the Si/SiO_2 interface. Journal of Applied Physics, 111(9), 093713. https://doi.org/10.1063/1.4709729

[195] Dingemans, G., & Kessels, W. M. M. (2012). Status and prospects of Al_2O_3 -based surface passivation schemes for silicon solar cells. Journal of Vacuum Science &

Technology A: Vacuum, Surfaces, and Films, 30(4), 040802. https://doi.org/10.1116/1.4728205

[196] Hoex, B., Bosman, M., Nandakumar, N., & Kessels, W. M. M. (2013). Silicon surface passivation by aluminium oxide studied with electron energy loss spectroscopy. Physica Status Solidi (RRL) - Rapid Research Letters, 7(11), 937–941. https://doi.org/10.1002/pssr.201308081

[197] Shin, B., Weber, J. R., Long, R. D., Hurley, P. K., Van De Walle, C. G., & McIntyre, P. C. (2010). Origin and passivation of fixed charge in atomic layer deposited aluminum oxide gate insulators on chemically treated InGaAs substrates. Applied Physics Letters, 96(15), 1–4. https://doi.org/10.1063/1.3399776

[198] Kimoto, K., Matsui, Y., Nabatame, T., Yasuda, T., Mizoguchi, T., Tanaka, I., & Toriumi, A. (2003). Coordination and interface analysis of atomic-layer-deposition Al2O3on Si(001) using energy-loss near-edge structures. Applied Physics Letters, 83(21), 4306–4308. https://doi.org/10.1063/1.1629397

[199] Otto, M., Kroll, M., Käsebier, T., Salzer, R., Tünnermann, A., & Wehrspohn, R. B. (2012). Extremely low surface recombination velocities in black silicon passivated by atomic layer deposition. Applied Physics Letters, 100(19), 1–5. https://doi.org/10.1063/1.4714546

[200] Otto, M., Kroll, M., Käsebier, T., Ziegler, J., Sprafke, A. N., & Wehrspohn, R. B. (2013). Passivation of optically black silicon by atomic layer deposited Al 2O3. Energy Procedia, 38, 862–865. https://doi.org/10.1016/j.egypro.2013.07.357

[201] Repo, P., Haarahiltunen, A., Sainiemi, L., Yli-Koski, M., Talvitie, H., Schubert, M. C., & Savin, H. (2013). Effective passivation of black silicon surfaces by atomic layer deposition. IEEE Journal of Photovoltaics, 3(1), 90–94. https://doi.org/10.1109/JPHOTOV.2012.2210031

[202] van de Loo, B. W. H., Ingenito, A., Verheijen, M. A., Isabella, O., Zeman, M., & Kessels, W. M. M. (2017). Surface passivation of n-type doped black silicon by atomic-layer-deposited SiO2/Al2O3 stacks. Applied Physics Letters, 110(26), 263106. https://doi.org/10.1063/1.4989824

[203] Pasanen, T., Vähänissi, V., Theut, N., & Savin, H. (2017). Surface passivation of black silicon phosphorus emitters with atomic layer deposited SiO2/Al2O3stacks. Energy Procedia, 124, 307–312. https://doi.org/10.1016/j.egypro.2017.09.304

[204] Chen, K., Pasanen, T. P., Vähänissi, V., Savin, H., (2019). Effect of MACE Parameters on Electrical and Optical Properties of ALD Passivated Black Silicon, 9(4), 974–979.

[205] George, S. M. (2010), Atomic Layer Deposition: An Overview, Chem. Rev. 2010, 110, 111-131

[206] Sharma S. K., Handbook of Materials Characterization, Springer International Publishing, 2018

[207] Goldstein J. I., Scanning Electron Microscopy and X-Rays Microanalysis, Springer, Fourth Edition, 2018

[208] Müller, E. W. (1956). Resolution of the atomic structure of a metal surface by the field ion microscope. Journal of Applied Physics, 27(5), 474–476. https://doi.org/10.1063/1.1722406

[209] Müller, E. W. (1956). Resolution of the atomic structure of a metal surface by the field ion microscope. Journal of Applied Physics, 27(5), 474–476. https://doi.org/10.1063/1.1722406

[210] Ward, B. W., Notte, J. A., & Economou, N. P. (2006). Helium ion microscope: A new tool for nanoscale microscopy and metrology. Journal of Vacuum Science and Technology B: Microelectronics and Nanometer Structures, 24(6), 2871–2874. https://doi.org/10.1116/1.2357967

[211] Notte, J., Hill, R., McVey, S., Farkas, L., Percival, R., & Ward, B. (2006). An introduction to helium ion microscopy. Microscopy and Microanalysis, 12(SUPPL. 2), 126–127. https://doi.org/10.1017/S1431927606069820

[212] Bentham Instruments, URL bentham.co.uk, last accessed January 2021

[213] Payne D., Abbott M. D., Claville Lopez A., Zeng Y., Fung T. H.m McIntosh K. R. et al., Rapid optical modelling of plasma textured silicon, 33rd European Photovoltaic Solar Energy Conference and Exhibition, 897-901

[214] Sinton, R. A., & Cuevas, A. (1996). Contactless determination of current-voltage characteristics and minority-carrier lifetimes in semiconductors from quasi-steady-state photoconductance data. Applied Physics Letters, 69(17), 2510–2512. https://doi.org/10.1063/1.117723

[215] Sinton Instruments, URL sintoninstruments.com, last accessed January 2021

[216] Sinton, R. A., Cuevas, A., & Stuckings, M. (1996). Quasi-steady-state photoconductance, a new method for solar cell material and device characterization. Time, 457–460.

[217] Yee, K. (1966). Numerical solution of initial boundary value problems involving Maxwell's equations in isotropic media. Antennas and Propagation, IEEE Transactions On. https://doi.org/10.1109/TAP.1966.1138693

[218] Ansys Lumerical knowledge base, URL lumerical.com, last accessed January 2021

[219] Payne, D. N. R., Charlton, M. D. B., & Bagnall, D. M. (2015). Broadband wavelength and angle-resolved scattering characterization for nanophotonics investigations. Applied Optics, 54(24). https://doi.org/10.1364/AO.54.007224

[220] NKT Photonics, URL nktphotonics.com, last accessed January 2021

[221] Togonal, A. S., He, L., Roca I Cabarrocas, P., & Rusli. (2014). Effect of wettability on the agglomeration of silicon nanowire arrays fabricated by metal-assisted chemical etching. Langmuir, 30(34), 10290–10298. https://doi.org/10.1021/la501768f

[222] Alaeian, H., Atre, A. C., & Dionne, J. A. (2012). Optimized light absorption in Si wire array solar cells. Journal of Optics, 14(2). https://doi.org/10.1088/2040-8978/14/2/024006

[223] Sturmberg, B. C. P., Dossou, K. B., Botten, L. C., Asatryan, A. A., Poulton, C. G., Martijn de Sterke, C., & McPhedran, R. C. (2011). Analysis of enhanced absorption in dense silicon nanowire arrays. Optics InfoBase Conference Papers, 19(September), 1136–1138. https://doi.org/10.1364/iqec.2011.i1062

[224] Cao, L., Fan, P., Vasudev, A. P., White, J. S., Yu, Z., Cai, W., … Brongersma, M. L. (2010). Semiconductor nanowire optical antenna solar absorbers. Nano Letters, 10(2), 439–445. https://doi.org/10.1021/nl9036627

[225] Brönstrup, G., Jahr, N., Leiterer, C., Csäki, A., Fritzsche, W., & Christiansen, S. (2010). Optical properties of individual silicon nanowires for photonic devices. ACS Nano, 4(12), 7113–7122. https://doi.org/10.1021/nn101076t

[226] Perez-Diaz, O., Quiroga-Gonzalez, E., (2020), Silicon conical structures by metal assisted chemical etching, Micromachines 2020, 11, 402; doi:10.3390.mi11040402

[227] Venkatesan, R., Arivalagan, M. K., Venkatachalapathy, V., Pearce, J. M., & Mayandi, J. (2018). Effects of silver catalyst concentration in metal assisted chemical etching of silicon. Materials Letters, 221, 206–210. https://doi.org/10.1016/j.matlet.2018.03.053

[228] Huang, Z. G., Lin, X. X., Zeng, Y., Zhong, S. H., Song, X. M., Liu, C., … Shen, W. Z. (2015). One-step-MACE nano/microstructures for high-efficient large-size multicrystalline Si solar cells. Solar Energy Materials and Solar Cells, 143, 302–310. https://doi.org/10.1016/j.solmat.2015.07.017

[229] Macdonald, D., Rougieux, F., Cuevas, A., Lim, B., Schimdt,J., Di Sabatino, M., Geerligs, L. J., (2009), Light-induced boron-oxygen defect generation in compensated p-type Czochralski silicon, J. of Appl. Phys., 105, 093704

[230] Zubel, I., Rola, K., & Kramkowska, M. (2011). The effect of isopropyl alcohol concentration on the etching process of Si-substrates in KOH solutions. Sensors and Actuators, A: Physical, 171(2), 436–445. https://doi.org/10.1016/j.sna.2011.09.005

[231] Vazsonyi, E., De Clercq, K., Einhaus, R., Van Kerschaver, E., Said, K., Poortmans, J., Nijs, J. (1999). Improved anisotropic etching process for industrial texturing of silicon solar cells. Solar Energy Materials and Solar Cells, 57(2), 179–188. https://doi.org/10.1016/S0927-0248(98)00180-9

[232] Baker-finch, S. C., & Mcintosh, K. R. (2013). Re fl ection distributions of textured monocrystalline silicon : implications for silicon solar cells, 2(March 2012), 960–971. https://doi.org/10.1002/pip

[233] Chen, Q., Liu, Y., Wang, Y., Chen, W., Wu, J., & Zhao, Y. (2019). Optical properties of a random inverted pyramid textured silicon surface studied by the ray tracing method. Solar Energy, 186(January), 392–397. https://doi.org/10.1016/j.solener.2019.05.031

[234] Yang, Y., Green, M. A., Ho-Baillie, A., Kampwerth, H., Pillai, S., & Mehrvarz, H. (2013). Characterization of 2-D reflection pattern from textured front surfaces of silicon solar cells. Solar Energy Materials and Solar Cells, 115, 42–51. https://doi.org/10.1016/j.solmat.2013.03.026

[235] Green, M. A. (2011). Analytical expressions for spectral composition of band photoluminescence from silicon wafers and bricks. Applied Physics Letters, 99(13). https://doi.org/10.1063/1.3645636

[236] Manzoor, S., Filipič, M., Onno, A., Topič, M., & Holman, Z. C. (2020). Visualizing light trapping within textured silicon solar cells. Journal of Applied Physics, 127(6). https://doi.org/10.1063/1.5131173

[237] Fung, T. H., Khan, M. U., Zhang, Y., Western, N. J., Payne, D. N. R., Mclntosh, K. R., & Abbott, M. D. (2019). Improved Ray Tracing on Random Pyramid Texture via Application of Phong Scattering. IEEE Journal of Photovoltaics, 9(3), 591–600. https://doi.org/10.1109/JPHOTOV.2019.2894688

[238] Mäckel, H., Holst, H., Löhmann, M., Wefringhaus, E., & Altermatt, P. P. (2016). Detailed Analysis of Random Pyramid Surfaces with Ray Tracing and Image Processing. IEEE Journal of Photovoltaics, 6(6), 1456–1465. https://doi.org/10.1109/JPHOTOV.2016.2601947

[239] Vogt, M. R., Holst, H., Schulte-huxel, H., Blankemeyer, S., Ahrens, I., Köntges, M., … Brendel, R. (2016). Optical constants of UV transparent EVA and the impact on the PV module output power under realistic irradiation. Energy Procedia, 92, 523–530. https://doi.org/10.1016/j.egypro.2016.07.136

[240] El-Din, N. M. S., & Sabaa, M. W. (1995). Thermal degradation of poly(vinyl butyral) laminated safety glass. Polymer Degradation and Stability, 47(2), 283–288. https://doi.org/10.1016/0141-3910(94)00118-R

[241] Shamim, A., Noman, M., Zubair, M., Khan, A. D., & Saher, S. (2018). A facile approach to determine the unknown refractive index (n) and extinction coefficient (k) of novel encapsulant materials used in back contact PV modules. Applied Physics A: Materials Science and Processing, 124(8), 1–6. https://doi.org/10.1007/s00339-018-1974-x

[242] Meichner, C., Schedl, A. E., Neuber, C., Kreger, K., Schmidt, H. W., & Kador, L. (2015). Refractive-index determination of solids from first-and second-order critical diffraction angles of periodic surface patterns. AIP Advances, 5(8). https://doi.org/10.1063/1.4928654

[243] Kurokawa, Y., Watanabe, Y., Kato, S., Yamada, Y., Yamada, A., Ohta, Y., … Hirota, M. (2013). Observation of Light Scattering Properties of Silicon Nanowire Arrays. 2013 IEEE 39th Photovoltaic Specialists Conference (PVSC), 1880–1884. https://doi.org/10.1109/PVSC.2013.6744510

[244] Procel, P., Ingenito, A., De Rose, R., Pierro, S., Crupi, F., Lanuzza, M., Cocorullo, G., Isabella, O., and Zeman, M. (2017) Opto-electrical modelling and optimization study of a novel IBC c-Si solar cell. Prog. Photovolt: Res. Appl., 25: 452– 469. doi: 10.1002/pip.2874.

[245] Kukli, K., Ritala, M., & Leskelä, M. (2000). Atomic layer deposition and chemical vapor deposition of tantalum oxide by successive and simultaneous pulsing of tantalum ethoxide and tantalum chloride. *Chemistry of Materials*, *12*(7), 1914–1920. https://doi.org/10.1021/cm001017j

[246] Lin, F., Hoex, B., Koh, Y. H., Lin, J. J., & Aberle, A. G. (2012). Low-temperature surface passivation of moderately doped crystalline silicon by atomic-layer-deposited hafnium oxide films. *Energy Procedia*, *15*(2011), 84–90. https://doi.org/10.1016/j.egypro.2012.02.010

[247] Allen, T. G., & Cuevas, A. (2014). Electronic passivation of silicon surfaces by thin films of atomic layer deposited gallium oxide. *Applied Physics Letters*, *105*(3), 3–7. https://doi.org/10.1063/1.4890737

[248] Park, H., & Crozier, K. B. (2013). Multispectral imaging with vertical silicon nanowires. *Scientific Reports*, *3*, 1–6. https://doi.org/10.1038/srep02460

[249] Tucher, N., Eisenlohr, J., Kiefel, P., Höhn, O., Hauser, H., Peters, M., … Bläsi, B. (2015). 3D optical simulation formalism OPTOS for textured silicon solar cells, *23*(24), 302–307. https://doi.org/10.1364/OE.23.0A1720

[250] Eisenlohr, J., Tucher, N., Höhn, O., Hauser, H., Kiefel, P., Goldschmidt, J. C., & Bläsi, B. (2015). Matrix formalism for light propagation and absorption in thick textured optical sheets, *23*(11), 37–49. https://doi.org/10.1364/OE.23.00A502

[251] Oh J., Yuan H., Branz H. (2012). An 18.2% efficient black-silicon solar cell achieved through control of carrier recombination in nanostructures. Nature Nanotechnology, vol. 7.